THE MORPHOLOGY OF BONE MINERAL CRYSTALS

By: S. A. Jackson

A thesis submitted for the degree of Doctor of Philosophy in the department of mechanical engineering at the University of Surrey.

December 1976

Acknowledgements

I would like to express my deep appreciation and sincere thanks to all those people who have helped me over the past few years to reach this goal. I would especially like to thank my supervisor, Dr. Tony Cartwright, for his perseverence, criticism, and constant encouragement for which I am greatly indebted. I would like to give special thanks to my other supervisor, Dr. D. Lewis, also Mr. J. Wheeler, Mr. J. Tucker, Mr. S. Greaves of the chemical physics department, Mr. S. Bennett and Mr. M. Dickens of the mechanical engineering department, and Mr. M. Hepburn of the metallurgy department for their greatly appreciated technical assistance. I would also like to thank my typist, Miss B. Tacy for her continual hard work, and finally I wish to express my thanks to Mr. J. Owen and my wife Jane for their encouragement. To all these people I am eternally grateful.

Summary

This work examines two aspects of bone structure, namely the basic size and form of the bone mineral crystallites, and the three-dimensional orientation of these crystals within the whole bone. X-ray diffraction, and both bright and dark field electron microscopy of bone, strongly suggest the mineral crystals to be irregular plate-like forms, approximately 5.0nm thick, with a variable maximum dimension; these methods also find no significant difference in the shape, size or composition of crystals in fixed and unfixed rabbit femur. The (002) diffracted beam is used to produce dark field images, the measured c-axial length distributions have mean values of 32.6nm, 36.2nm, and 32.4nm for rabbit, ox and human bones respectively. Using the x-ray method of line broadening, it is shown that c-axial measurements consistent with those of the dark field method are produced, provided that lattice strain is accounted for in the theoretical formulation. The x-ray method is used to examine crystal maturation. Results indicate that the crystals of rabbit bone increase in size and perfection from birth until a stable situation is attained after approximately seven weeks, when the crystals exhibit a mean c-axial length of approximately 34.0nm, and a maximum compressive or tensile lattice strain of 0.3% in the (002) direction. An x-ray goniometer is designed and constructed, and used to produce quantitative (002) pole figures of small samples of secondary type human, and primary type ox bones. Results show secondary bone to have a major fibre axis aligned on average with the femoral axis, and the degree of orientation shows rotational symmetry about this axis. Primary bone exhibits the same major axis, but also shows a planar orientation along the laminar direction. The results of this work, their significance, and suggestions for future developments are discussed in the final chapter.

CONTENTS

Introduction

Bone is a specialised form of connective tissue. It is distinguished from other forms of connective tissue by the fact that it is extremely hard, owing to the deposition within a soft organic matrix of a complex mineral substance, largely composed of calcium phosphate. Bone is often thought of as a dead or inert substance, probably because it retains its structure for many thousands of years after death. However, in the body, bone is a viable and very active tissue which is undergoing constant change in response to varying physical and chemical conditions.

The behaviour of bone, as a material and as a living tissue, has been studied for many years. It is known that bone can respond to abnormal mechanical stresses by either removing or depositing tissue, in a way which is thought to accommodate the stresses most effectively. Associated with mechanical deformation, bone exhibits the property of a piezoelectric transducer, that is, it has the ability to transduce mechanical energy into electrical energy, and vice-versa. Whether or not the cellular activity associated with mechanical stressing is a direct result of this electrical effect, or is mediated by other means remains to be shown. Before the behaviour of bone can be understood, in both normal and abnormal situations, there are many aspects of its structure and metabolism which need to be studied. Before the results of tests can be fully interpreted , it is important to have accurate information about the structural features of bone which collectively determine the physical behaviour. This work, which is directed towards this end examines two outstanding aspects of bone structure which have to date, not been well defined.

Firstly, the basic shape and size of the bone mineral crystals have been investigated in the past by two techniques, x-ray diffraction and bright field electron microscopy. The two techniques have not produced

consistent results, nor have they been successful in delineating either the shape or size of the bone mineral crystals. This present work uses these two methods and also the dark field imaging technique (see chapters 2 and 5) which has been applied in an attempt to clarify the past discrepancies, and hence obtain more meaningful measurements of crystal size and shape.

Secondly, the three dimensional orientation of bone mineral reveals the fibrous structure of a sample, and besides the anatomical interest, it is important to be aware of any anisotropy or structural variation which could influence the interpretation of physical tests. In general, past works have tended to assume bone to be homogenous, or with uniaxially oriented fibres, and also measurements of orientation have tended to be qualitative. Consequently, a device to measure bone mineral orientation quantitatively has been designed and used, to enable the fibrous structure of a bone sample to be determined accurately and quickly.

Although it is clear that a great deal of further research has yet to be done in this field, it is believed that the techniques developed and the results obtained in this work clarify the two aforementioned aspects of bone structure, and will lead to a better understanding of bone as a material.

CHAPTER ONE

THE STRUCTURE OF BONE

1.1. The General Anatomy and Histology of Bone

Bone is a multi-functional tissue, in that it provides support and protection to the body, and also acts as a store for the important mineral calcium, which is necessary for most bodily functions. There are two distinct ways in which bones are formed in the embryonic skeleton. Firstly, by the replacement of a cartilagenous model by bone tissue, (endochondral ossification), and secondly where bone is laid down directly, usually within membranous areas, (intra-membranous ossification).

The first type of bone to appear in embryonic development is termed woven, or immature bone, and is characterised by a random orientation of collagen fibres (see section 1.3.). Woven bone also appears at sites of fracture repair.

Before birth, woven bone begins to be replaced by primary bone, which has a layered structure. Figure 1.1. shows a transverse section taken from a bovine femur, and figure 1.2. depicts the same section viewed under polarised light. The laminations are an optical effect caused by the collagen fibres in adjacent layers (Lamellae), having different orientations.

Throughout life, bone is continually being removed and replaced, this process is known as remodelling. As remodelling occurs, primary bone is replaced by secondary bone, which is characterised by systems of osteons. The osteon can be considered as the basic structural unit of secondary bone. Figure 1.3. shows part of a transverse section taken from a human femur, and figure 1.4. shows the laminated appearance of the osteon when viewed under polarised light. In the centre of the osteon, (sometimes termed an Haversian system), lies the Haversian canal which carries blood through the bone. The vessels which connect the Haversian canals laterally are called Volkman's canals, and both are shown in figure 1.5.

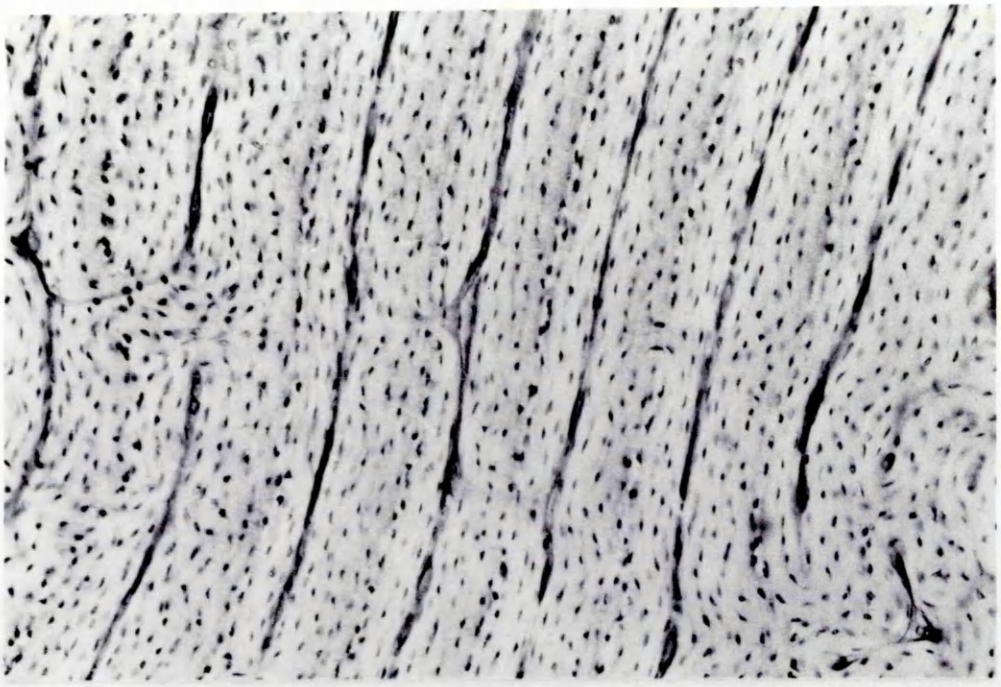

Figure 1.1

Light micrograph of a transverse section of bovine femur, (x 50). The laminated structure is typical of primary type bone.

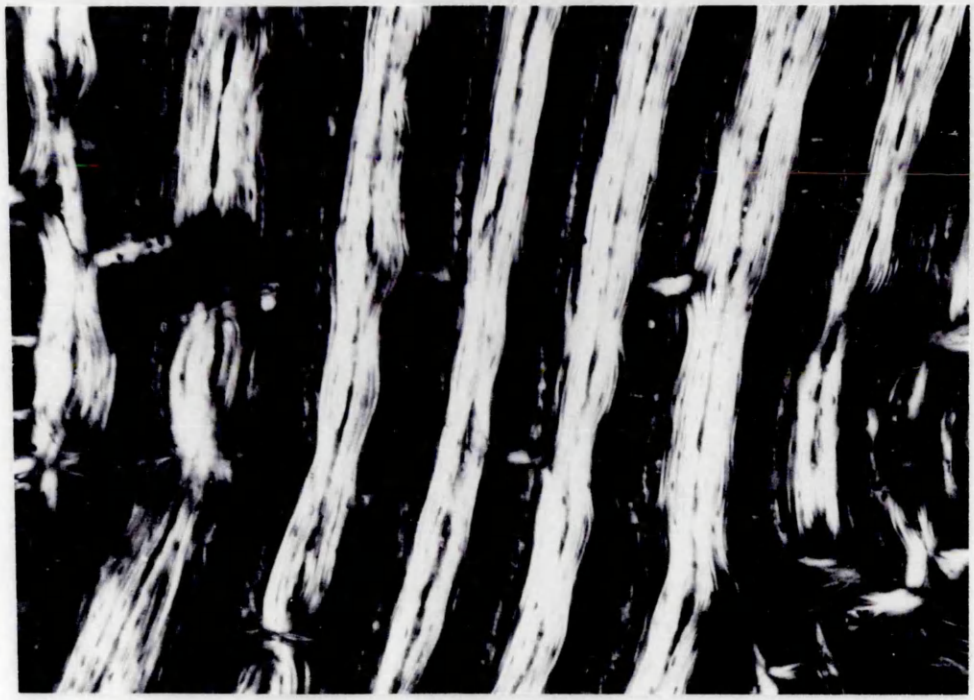

Figure 1.2

The same section of bone as shown above, viewed under polarised light, (x 50).

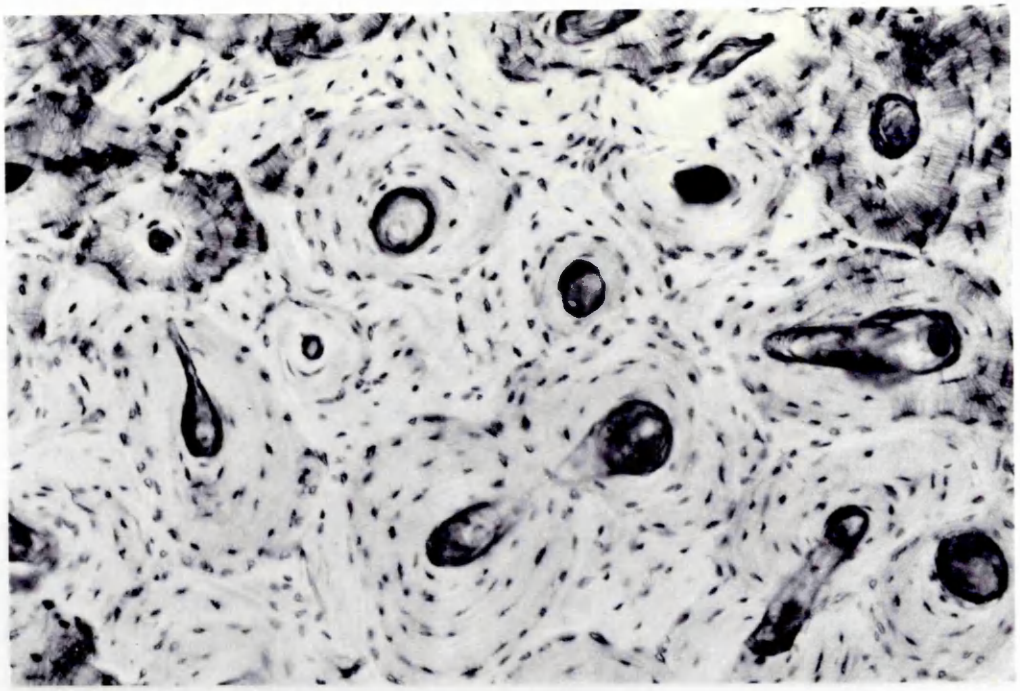

Figure 1.3

Light micrograph of a transverse section of human femur, (x 85). This type of structure is typical of secondary type bone.

Figure 1.4

The same section of bone as shown above, viewed under polarised light. (x 85).

Secondary Type Bone.

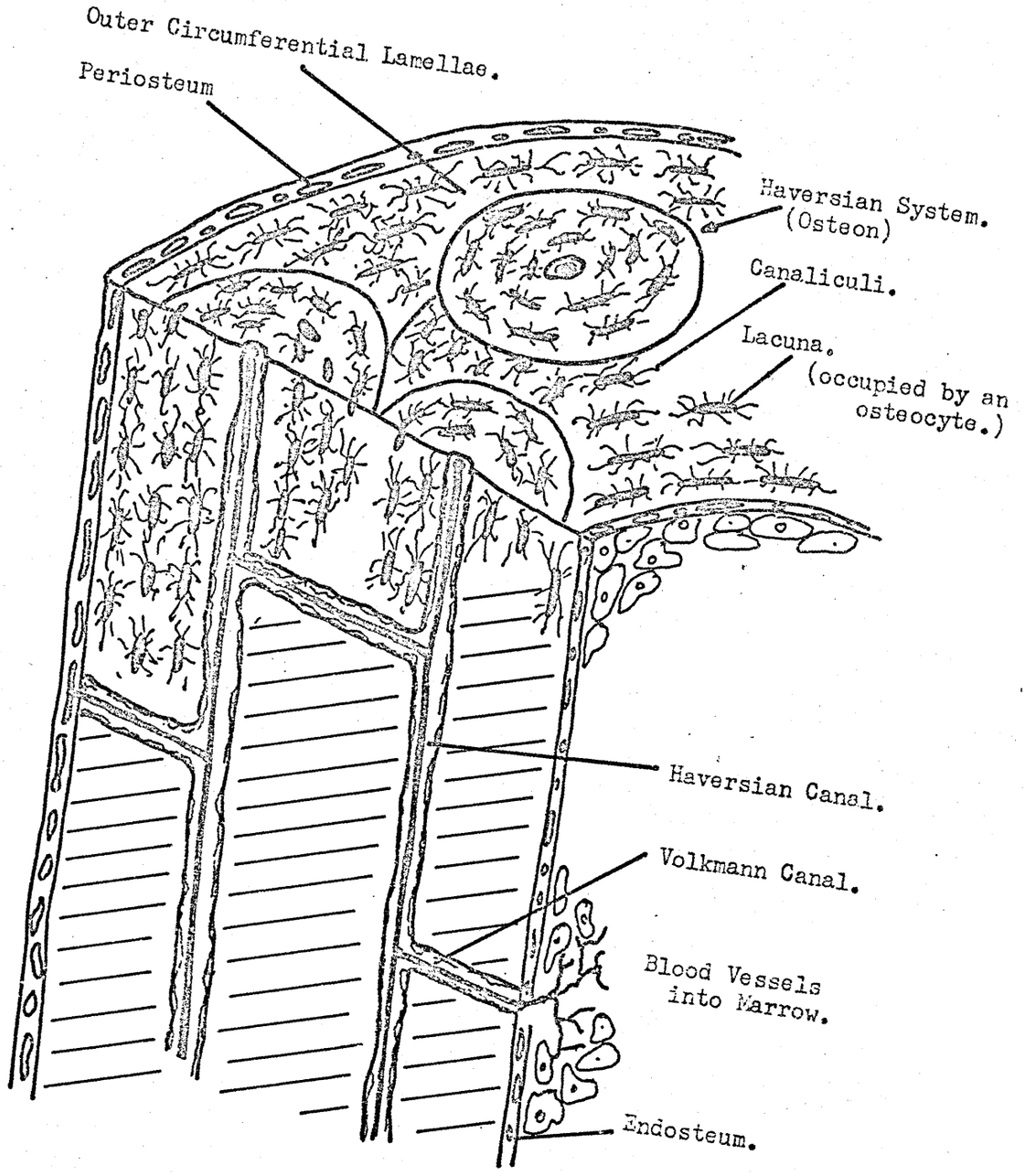

Figure 1.5

Cortical, or compact bone forms the outer surface of bones, and is particularly thick in the central section of the long bones. Cortical bone is in the form of a thin shell at the ends, or epiphyses of the long bones, and around the outer surface of bones such as the vertebrae. Cancellous, or spongy bone is usually found in the interior of bones together with the marrow. The two types of bone are microscopically the same, but the architecture is found to be different. Both types of bone are clearly visible in figure 1.6.

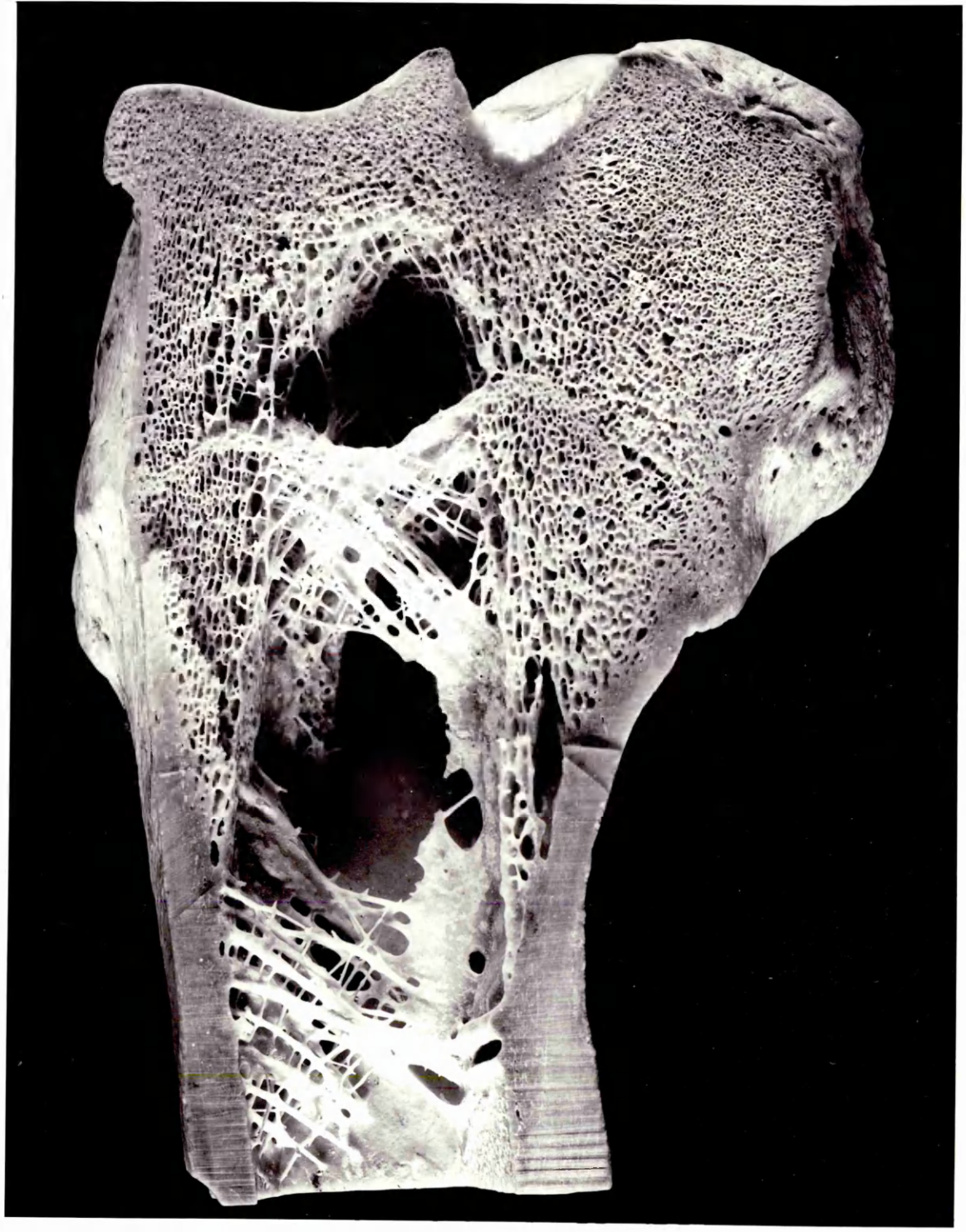

Figure 1.6

Distal end of ox femur, showing both cancellous and cortical bone.

(x 1.5)

1.2. Bone Cells

There are three main types of bone cell, the osteoblast, the osteoclast, and the osteocyte.

The osteoblast is responsible for laying down the bone matrix, (matrix being a general term for the bone tissue excluding the cells). After forming its surrounding matrix the osteoblast either becomes an osteocyte, or remains as an osteoblast lining an Haversian canal, Owen (1963). It has been suggested that the osteoblast may play a part in the deposition of bone mineral, Pautard and Arnott (1967), Bonucci (1971), however, the exact role of the osteoblast in this calcification process is still not clear.

The osteoclast is found on, or near, bone surfaces during the process of resorption, which is the removal of bone for the process of remodelling. Very little is actually known about the resorption process but osteoclasts seem to be concerned with the liberation of calcium into the bloodstream as well as the continual remodelling of bone. Vaughan (1970).

Whilst cellular activity, leading to both bone deposition and resorption are controlled by hormonal influences, mechanical factors also play an important role. These mechanical factors, by influencing cellular activity enable bone to remodel, and adapt to unusual stresses, Fung (1972). Bone turnover, therefore, is probably controlled by a variety of inter-connecting factors, both physical and chemical.

The Osteocytes occupy discus-shaped cavities in the bone matrix, known as lacunae. The cytoplasmic processes of these cells permeate the bone matrix through channels known as the canalicular system. The actual function of the osteocyte is not known. However, it is the osteocyte which is the living part of bone, and osteocyte death is synonymous with the death of the bone. Just how the osteocyte contributes to the complex processes occuring in bone has still to be determined.

1.3. Collagen.

Collagen is the most abundant protein in the human body, it is the major fibrous constituent of skin, tendon, ligament, cartilage and bone. The basic collagen molecule, known as the tropocollagen molecule, is a group of three polypeptide chains, each composed of about a thousand amino acids. The two amino acids, proline and hydroxyproline, make up as much as 25% of the links in the collagen molecule, they prevent easy rotation of the regions in which they are located, thus imparting a certain amount of rigidity to the collagen, Gross (1961). Collagen owes its properties, not only to its chemical composition, but also to the arrangement of its individual molecules. The basic molecular chain is twisted into a left handed helix, and three such helices are wrapped around each other to form a right handed super-helix. The three chains are currently believed to be joined by hydrogen bonds, a structure first proposed by Ramachandran and Kartha (1954).

The tropocollagen molecules which are produced by the osteoblasts in bone, are rod-like units, with dimensions of about 300nm x 1.4nm, and an approximate molecular weight of 300,000. These molecules are arranged into fibres which show a banded structure with a repeat distance of approximately 64nm, see figure 1.7. The fact that the organised fibre shows a pattern repeating at intervals of just less than a quarter of the length of a tropocollagen molecule, was at one time taken to indicate a side by side 'quarter staggered' arrangement. Hodge et al (1965), Petruska and Hodge (1964), see figure 1.8. More recently another model has been proposed, Grant et al (1965), in which the tropocollagen molecules are described as filaments, approximately 280nm in length, which are divided into five bonding, and four non-bonding zones of 26.5nm and 37.5nm in length respectively. The collagen fibre is formed by a random side by side aggregation of the filaments with their bonding regions in register, see figure 1.9.

The Structure of Collagen.

Starting Material —— Amino Acids.

Single chain left handed molecular helix.

3 chain, right handed superhelix.

The tropocollagen molecule.

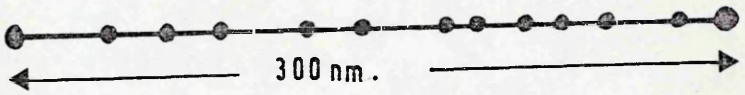

Tropocollagen molecules aggregated to produce collagen fibre.

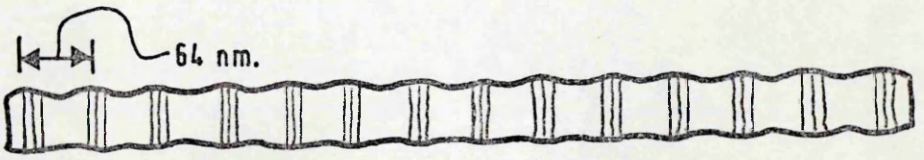

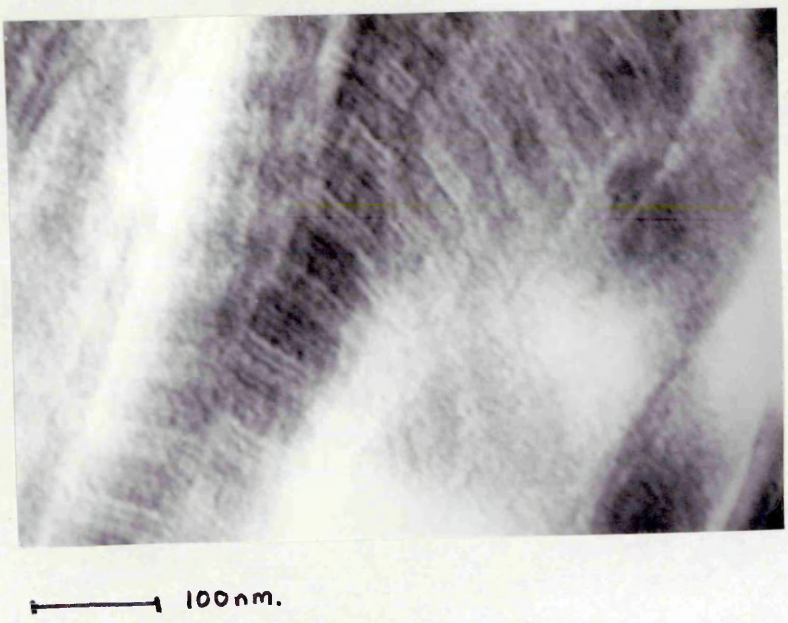

Figure 1·7

figure 1·8

figure 1·9

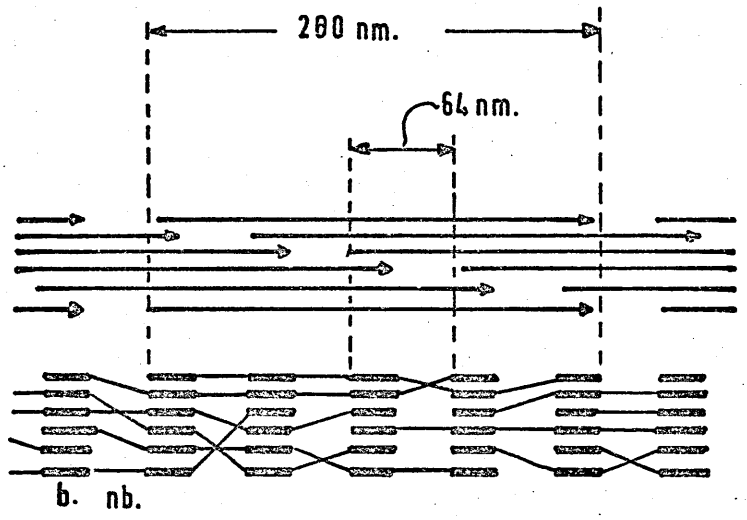

Models for the organisation of tropocollagen molecules into collagen fibres.

Figure 1.8, the 'quarter staggered' arrangement of Hodge et al (1965).

Figure 1.9, the random aggregation model of Grant et al (1965).

b = bonding zone.

nb = non-bonding zone.

1.4. Other Organic Constituents of Bone Matrix.

Increased interest has recently been shown in the non-collagenous constituents of bone. The carbohydrate-protein complexes, which occur in bone in larger amounts than previously suspected, have been termed mucins, mucoids, mucopolysaccharides and mucoproteins. These substances are found between the collagen fibres, and for this reason have generally been called the cementing substance. Interest has been shown in the possibility that the cementing substance has an important role in initial calcification in cartilage, Bonucci (1971). Present knowledge of the carbohydrate-protein complexes suggests classification into two types, proteinpolysaccharides, and glycoproteins.

Proteinpolysaccharides consists of a protein chain, or core, to which are attached a number of polysaccharide chains, which are relatively simple, consisting mainly of a regularly repeating unit of two sugars.

Glycoproteins are similar to the first class, in that they contain carbohydrate linked to protein. In this case however, the carbohydrate chains are relatively short and contain a wide variety of sugars.

Finally, the amount of Lipid in cortical bone is small, (0.3 - 0.5% by wt.), but is of interest since Irving (1965), has suggested that it may be associated with the calcification process.

1.5. Calcification.

Tissue calcification, or mineralisation, is generally considered to be the last step in bone formation, following cellular differentiation and matrix formation. The many theories concerning mineralisation can be divided into three main classes:

1) Theories which propose mechanisms that would raise the ionic concentrations at specific sites, so that the mineral would precipitate spontaneously;

2) Theories which propose mechanisms that would create nucleation sites, so that mineral could precipitate readily from the serum levels of calcium and phosphate;

3) Theories which propose that the crystalline bone mineral does not precipitate directly from serum, but via the transformation of another calcium phosphate mineral which is initially formed.

Robinson (1923) proposed that the enzyme alkaline phosphatase is responsible for producing an excess of free inorganic phosphate at calcification centres. This would raise the local phosphate concentration to a supersaturated level in the tissue serum to such an extent to cause bone mineral to precipitate. The most serious drawback to Robinson's theory being the fact that alkaline phosphatase is present in tissues that do not normally calcify, Bradfield (1949). In the light of this objection interest was focused on the second type of theory, where the organic matrix plays an important part in the calcification process.

Collagen, being the major organic component in bone was favoured as the nucleation site of bone mineral. This hypothesis has received considerable support from electron microscopical studies, where a close relationship between bone crystals and collagen fibres has been seen in developing bone, Fitton-Jackson and Randall (1956), Molnar (1960), Robinson and Watson (1955). The

inference from such observations is that sites exist in, and/or on the collagen fibres, which act as foci for the inception of crystallisation. Glimcher (1959), has demonstrated that only collagen showing the 64nm periodicity in the fibre direction will calcify in vitro. Glimcher suggested that it is the structural arrangement of the tropocollagen molecule which is the important factor in determining the nucleation sites. Various other investigators have noted that specific amino acids may be important in defining these sites. Robinson and Watson (1955), found bone mineral crystals near the crossbands of collagen where basic and acidic amino acids are thought to be more concentrated. According to Bonucci (1971), the locus of initial calcification in both cartilage and bone appears to be structures of cellular origin, which are not found within the cells, but in the matrix between the collagen fibres. Clusters of crystals then appear, attached to these structures or templates, which Bonucci has termed 'crystal ghosts', and suggested that they probably belong to the protein polysaccharide complexes.

There is one difficulty however in considering the matrix as a seed forming agent, namely that the organic components of bone tissue are found in connective tissues that do not normally calcify. No conclusive evidence is available to suggest that there are subtle chemical or conformational differences between mineralising and non-mineralising tissues that explain the ability of the former to calcify.

The third class of theories propose that there is an initial precipitation of a non-crystalline, or amorphous calcium phosphate, which subsequently converts by hydrolysis into hydroxyapatite, which is the crystalline form of bone mineral.

Brushite, ($CaHPO_4.2H_20$) and octacalciumphosphate, ($Ca_8H_2(PO_4)_6.5H_20$), see 1.7.5 and 1.7.7, have both been suggested as the initial mineral phase in bone formation, Neuman and Neuman (1958), Brown (1962), but no direct evidence has been obtained of their existence, Glimcher (1969).

Amorphous calcium phosphate on the other hand, is apparently present in bone to a considerable extent, and it appears to possess many of the properties required of a mineral intermediate to hydroxyapatite. Posner (1969), suggests that the amorphous calcium phosphate is a product of cellular activity, and the amorphous salt, once formed becomes the controlling source of ions for the precipitation of bone apatite crystals. Since it is more soluble than apatite, the amorphous material through dissolution provides the fluid levels of calcium and phosphate needed for the extra-cellular formation of apatite. Bone collagen could still provide the preferential sites for primary nucleation of apatite, secondary nucleation using the apatite crystals themselves as substrates, Eanes and Posner (1965) and (1969). In this model, the primary factor responsible for limiting the formation of apatite crystals to those areas that normally calcify, is a cellularly derived calcium phosphate. Thus the cell ultimately governs the entire calcification process.

1.6. Crystal-Collagen Relationships.

It has long been established that relationships exist between bone mineral and collagen. The orientation of crystallities in bone was first detected in the x-ray diffraction patterns of long bones by Clark (1931), who showed a fibre axis parallel to the long axis of the bones. This was confirmed by Stühler (1936), who, in a subsequent x-ray crystallographic investigation (1938), was able to show that the direction of the crystallite c-axis was parallel to the collagen fibre axis. In their investigations on calcified bird tendon, Engström and Zetterström (1951), demonstrated the well oriented reflections of both collagen and apatite on the same diffraction pattern, the c-axes of both constituents being parallel.

The action of collagen as a nucleation site for bone mineral crystallisation has been mentioned in the previous section. Evidence suggesting a relationship between collagen and crystal formation can be seen in many electron micrographs, where the collagen banding, whilst not being visible itself, is indicated by a variation of crystallite density. See figure 1.10.

Whilst it is generally accepted that the above relationships between bone mineral and collagen do exist, the details of these relationships are still not clear.

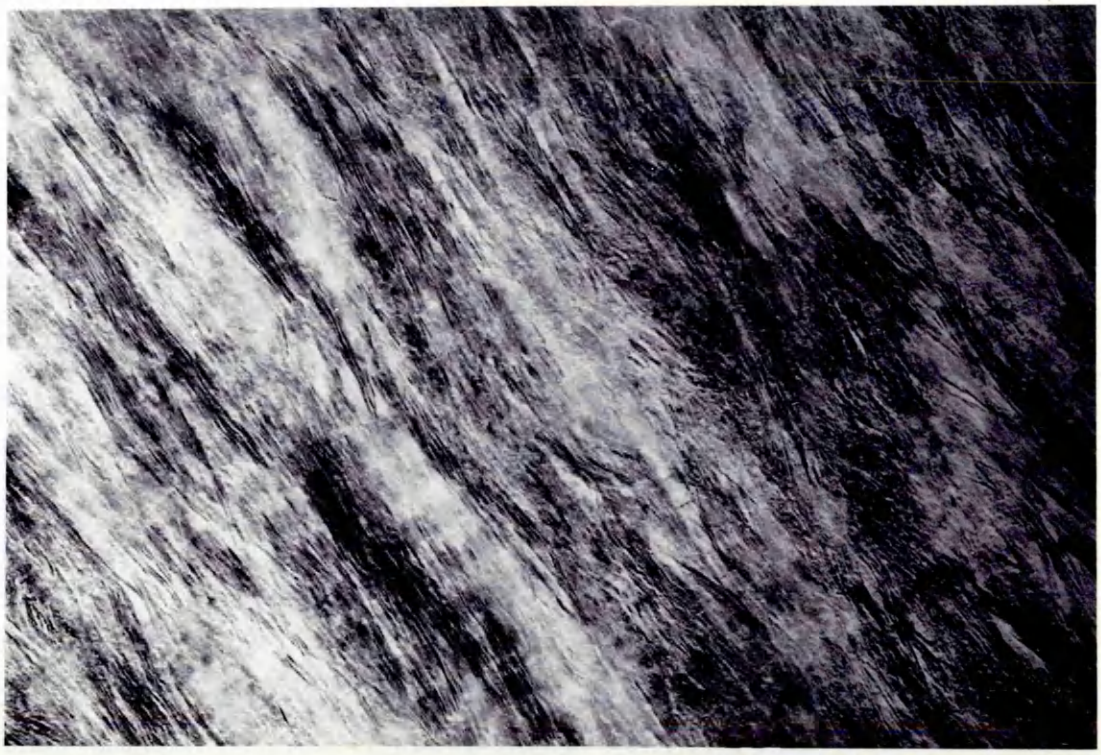

Figure 1.10 ⟵100 nm.

Rabbit femur, fixed in osmium tetroxide, postfixed in glutaraldehyde.

Collagen banding shown by variation in bone mineral density.

1.7. Bone Mineral.

1.7.1. Introduction

The exact chemical and physical characteristics of bone mineral are still not clear. Early work by de Jong (1926), demonstrated the similarity between the x-ray diffraction patterns of untreated bone, and a group of minerals known as apatities. However, because of the extremely small crystal size, in bone (<100nm), the diffraction pattern is diffuse, and so accurate calculations of the lattice parameters are impractical. However, by heating or calcination of the bone, the diffraction pattern can be greatly improved, since temperatures over 500^{o}C cause growth of the crystallites this produces better diffraction conditions. Unfortunately, this also encourages reactions between the apatite and ions outside the lattice, such as organic bound phosphate and calcium. So, although the crystals are larger after heating, their chemical composition may have changed.

Klement (1929), suggested that the major constituent of bone mineral was hydroxyapatite, and in 1932, Klement and Trömel demonstrated the identity between diffraction patterns of hydroxyapatite and bone. As a result of this work it is now widely accepted that hydroxyapatite is the major component of bone mineral.

However, all attempts to account for the composition of bone mineral with one rational chemical formula have been unsuccessful. It seems highly probable therefore, that the chemical composition is variable, and since bone mineral is formed in a dynamic, living system, it is likely that environmental fluctuations will be made manifest in the chemical character of the mineral.

1.7.2. Apatites

Apatites belong to a general classification of crystals known as the hexagonal system, since in the ideal form they appear as hexagonal prisms. These prisms can be described by a principal axis, termed the c-axis, about which there is hexagonal symmetry. Normally, and equally spaced around the c-axis, are the three a-axes, all identical in length, see figure 1.11. These axes are used to describe the symmetry of a crystal, the relationship of the faces, and the position of points, or ions within the crystal. The hexagonal prism is simply one way of describing the crystal, which could equally be described by considering the c-axis and only two of the a-axes. This unit cell is the smallest possible basic unit from which the entire crystal lattice could be constructed.

1.7.3. Hydroxyapatite

The unit cell for hydroxyapatite can be considered to be a right rhombic prism, with a length along each edge of the basal plane, which is described by the a-axes, of 0.9432 nm, and a height described by the c-axis of 0.6881 nm, Posner and Perloff (1958). Atomic constituents of this unit cell are given by the formula - $Ca_{10}(PO_4)_6 \cdot (OH)_2$, and the arrangement of these atoms within the cell is shown in figure 1.12.

1.7.4. Fluorapatite

Fluorapatite has basically the same structure as hydroxyapatite, with the hydroxyl ions replaced by fluorine ions. The conversion of hydroxyapatite to fluorapatite, by the ingestion of fluoride is the basis of the treatment of some dental and bone disorders. It has been shown, Posner etal (1962), (1963), (1965), that fluorine retention leads to an increase in the bone

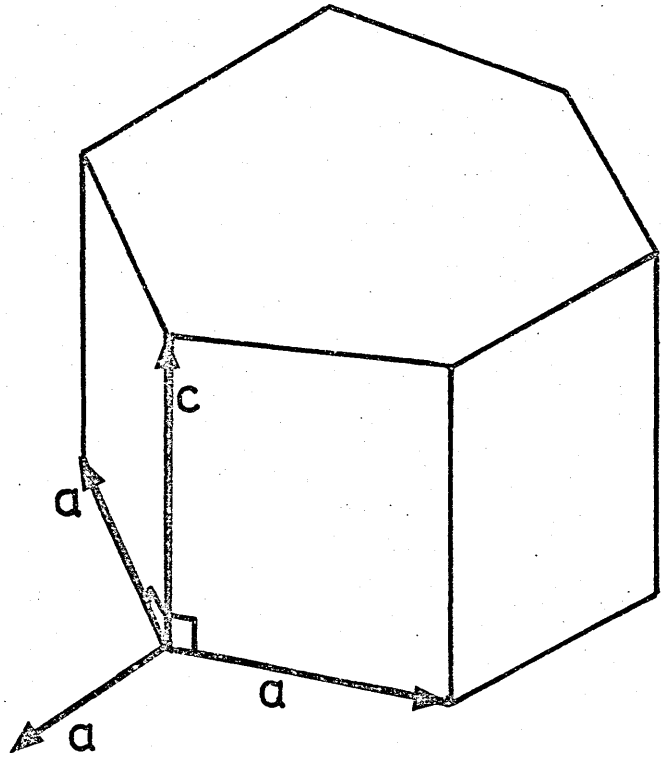

Figure 1·11

Hydroxyapatite Unit Cell Contents.

The structure is shown here projected onto the basal plane, the numbers written in the symbols represent the fractional height within the unit cell.

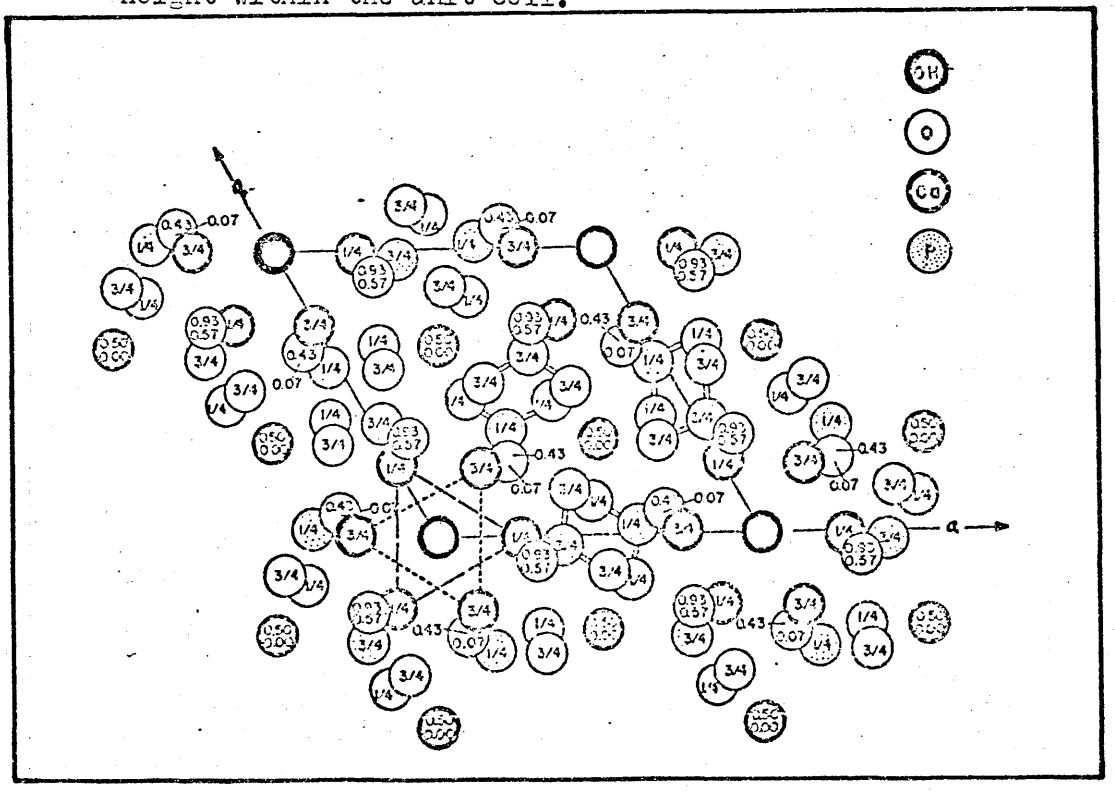

Figure 1·12

mineral crystallite size. The rate of reaction between a solid and solution is affected by the crystal size, the larger crystals reacting more slowly than the smaller ones, and this is at least part of the explanation for the reduction of dental caries associated with fluoride ingestion. Fluoride has also been used as a treatment for both Paget's disease and osteoporosis, Sognnaes (1965). However, excess of fluoride in drinking water, owing to industrial contamination, has led to the development of pathological bone disorders, Johnson (1964).

1.7.5. Octacalciumphosphate

Octacalciumphosphate (OCP), has the chemical composition ($Ca_8 H_2 (PO_4)_6 . 5H_2O$), giving it a calcium to phosphorus mole ratio of 1.33, relative to hydroxyapatite (HA), which is 1.667. There are many structural similarities between OCP and HA, and so there is a high probability of epitaxial crystal overgrowth, that is one crystal acting as a base for the other, so that the two crystals grow together with their axes aligned. Comparison of the crystallographic parameters show the similarity between OCP and HA, see table 1.1.

Note that ($^{a}/2$) for OCP is approximately equal to (a), for HA.

According to Brown (1962), part of the OCP structure is similar to HA and part is rich in water molecules, he refers to these different parts as an apatite layer and a water layer. OCP crystallises as thin triclinic blades, elongated in the c-axial direction, and can be identified through x-ray diffraction by the 1.868 nm and 0.267 nm reflections. However, because of the small size of bone mineral crystallites, and

The Crystallographic Parameters of Hydroxyapatite and Octacalciumphosphate. Brown (1962).

Parameter.	HA.	OCP.
a	0.943 nm.	1.987 nm.
b	0.943 nm.	0.963 nm.
c	0.688 nm.	0.687 nm.
α	90°	89° 17'
β	90°	92° 13'
γ	120°	108° 57'

Table 1.1

(for explanation of parameters see figure 2.1)

consequently the poorly resolved diffraction pattern, it has not been possible to use these reflections as a quantitative measure of OCP in a mixture with HA.

It has been demonstrated by Newesely (1964), that the central part of the OCP unit cell, is much poorer in calcium than the marginal zones, and that in the building of the crystal, the lattice space of a= 1.987 nm may be changed to 2a. The central zone is consequently doubled, so that the whole structure projected down the c-axis, is composed of two dense layers, of about 1.0 nm in thickness, separated by a less dense 2.0 nm thick zone. There is a striking correspondence between this data and structures which are sometimes observed in the electron microscope, D-Steve Bocciarelli (1969). Because of this evidence, and the fact that chemical analysis of bone mineral yields a low calcium to phosphorus ratio, OCP has been favoured as the explanation.

1.7.6. Calcium Deficient Apatites

Synthetic calcium phosphates yield similar x-ray diffraction patterns to hydroxyapatite, but these compounds often have a lower calcium to phosphorus ratio than ideal, or stoichiometric hydroxyapatite. This could be explained by either phosphate groups absorbed onto the surface of stoichiometric hydroxyapatite, or calcium ions missing from the crystal lattice, whilst the remainder of the structure is intact. Several arguments have been advanced against the explanation that the lack of stoichiometry is due solely to surface absorbed phosphate groups, Newman (1953). Thus it seems quite likely that the low Ca/P ratio hydroxyapatites are, in fact, calcium deficient.

Calcium deficient apatites are more reactive thermally and chemically than stoichiometric hydroxyapatite. Temperatures of the order of 300°C cause dehydration, and condensation to pyrophosphate ($P_2O_7^{-4}$) in the apatite structure. Heating above 800°C causes complete dehydration and formation of β - $Ca_3 (PO_4)_2$. Stoichiometric hydroxyapatite will remain unchanged well over 800°C.

Evidence for the existence of calcium deficient apatites in bone and tooth mineral is seen from chemical analyses, and from the formation of pyrophosphate at mild temperatures, Herman & Dallemagne (1961), and β - $Ca_3 (PO_4)_2$ at higher temperatures, Sobel et al (1949).

1.7.7. Monenite and Brushite

Lénárt (1968), has suggested that hydroxyapatite in bone is formed through stages involving brushite (Ca H PO_4 . 2 H_2O), and monenite (Ca H PO_4). In an electron diffraction study of mineralising callus, Lénárt (1971), has detected both monenite and hydroxyapatite. However, it must be emphasised that because of the extremely small size of bone mineral crystallites, diffraction patterns are diffuse, and so evade accurate interpretation.

1.7.8. Amorphous Calcium Phosphate

Evidence from electron miscroscopical studies, Robinson & Watson (1955), Fitton-Jackson and Randall (1956), Höhling et al (1966) and Molnar (1959), suggested that not all bone mineral is crystalline in nature. The above reports showed that in areas, mainly around osteoblasts, there existed mineral-like particles that differed in morphology from apatite crystals and did not produce electron diffraction

patterns. More recently, it has been demonstrated by x-ray diffraction, that the amount of crystalline apatite present in any given bone sample, is insufficient to account for all the bone mineral contained in that sample, Eanes et al (1966), Harper & Posner (1966), Termine (1966). By comparing results from synthetic systems with those from bone samples, these workers calculated that up to about 40% of the total mineral in mature compact bone, was present in the form of an amorphous non-apatitic phase. This percentage was found to be even higher in younger bones, see table 1.2. The amount of amorphous material ~~apparantly~~ found in bone has been criticised, Bachra (1970), who questions the validity of the direct comparison between synthetic and living systems. However, it still remains that a great deal of bone mineral is so poorly crystallised as to appear amorphous to x-ray diffraction, whether this is actually the beginnings of hydroxyapatite, or another distinct phase is difficult to prove.

Since the chemical constituents of bone mineral are predominantly calcium and phosphate ions, this non-crystalline, or amorphous, component which ~~apparantly~~ forms a substantial portion of the total mineral, is thought to be some sort of calcium phosphate compound. Once again the work on synthetic systems has shown that an amorphous calcium phosphate precursor is present in the precipitation of hydroxyapatite from physiological solutions. Unless stabilised in some way, this precursor converts to hydroxyapatite, and it has not yet been determined if some form of stabilising factor is present in the in-vivo situation.

The effect of age upon the crystalline/amorphous mineral composition of whole rat femur. Termine.J.D. and Posner.A.S.(1967)

Age/days.	%. Crystalline Mineral	%. Amorphous Mineral
3	32.8	67.2
5	31.6	68.4
7	34.2	65.8
10	37.5	62.5
13	36.1	63.9
15	39.0	61.0
17	42.5	57.5
20	44.6	55.4
24	44.1	55.9
26	47.1	52.9
30	50.4	49.6
35	53.6	46.4
40	59.8	40.2
50	62.0	38.0
60	62.3	37.7
70	64.5	35.5
80	63.1	36.9

Table 1·2

1.7.9. Mineral Composition. Summary

Investigations into the structure and composition of bone mineral have led to much confusion. Due to inherent difficulties, accurate analyses have so far been impossible. Since bone is formed in a dynamic environment, the fluctuating physical and chemical conditions must, in turn, provide fluctuations in the composition of bone mineral. Thus, unfortunately, from the many investigations on bone mineral it is only possible to draw the following general conclusions:

1) Bone mineral exists in both crystalline and amorphous phases.

2) The crystalline phase appears to be an imperfect form of hydroxyapatite, which is present as extremely small crystals.

3) The amorphous phase is a basic calcium phosphate associated with bone formation, and is thought to be more metabolically active than the crystalline fraction.

1.7.10. The Morphology of Bone Mineral

It was noticed from early x-ray diffraction work on bone, that the OOL reflections (reflections from planes in the crystal which are perpendicular to the c-axis*), were narrower than reflections from other planes. This was taken as indicating an elongation of the bone mineral crystallites in the c-axis direction. Attempts have been made to estimate the dimensions of the crystallites in bone from the broadening of diffraction lines. However, crystal size is not the only factor which can influence the width of a diffraction profile. Internal strain in the crystal, leads to variations in the lattice dimensions, and this leads to a broadening of the diffraction profile.

Carlström and Glas (1959), using fish bones, succeeded in measuring the profiles of the (002), (004), (008) and (130) reflections. (This terminology is explained in the next chapter). From this data they concluded that the line broadening was due to both size and strain effects, and calculated a c-axial length of about 60 nm and width of about 5 nm. Myers and Engström (1965), performed a similar type of measurement on calcified fowl tendon, and calculated dimensions of 35 nm x 5nm. Stühler (1938), in his investigations of various types of bone estimated the c-axial length to lie between 3nm and 29 nm. Carlström (1955), calculated the average c-axial dimension from line broadening of the 002 reflection only, to be 23 nm $\pm$ 2 nm, using various types of bone. Apart from the line broadening method, particle sizes can be estimated by another technique, which uses the diffuse, low angle scattering of x-rays. This method has been applied to the measurement of bone crystal sizes by Engström and Finean (1953), who found that the crystals in various bones were of uniform size and rod-shaped, with dimensions of 21 nm x 7.5 nm,

* Only true when the c-axis is perpendicular to the basal plane, as is the case with hydroxyapatite.

with the elongation in the c-axial direction. Carlström and Finean (1954), confirmed these findings by applying the technique to fish bone, which is a highly oriented structure. They concluded that the crystallites were probably rod-shaped, having dimensions of 22 nm x 6.5 nm. Engström (1972), using the same technique and type of bones calculated dimensions of 33-35 nm x 3-5 nm.

The other main technique by which studies on bone mineral have been performed is electron microscopy. From measurements on 1000 crystals in human bone, Robinson (1952), found an average particle size of 50 nm x 25 nm x 10 nm, with a long direction parallel to the c-axis. In a later investigation on human bone, Robinson and Watson (1952), concluded that the mature crystal length was 35 nm - 40 nm, with a width of about the same value. The thickness of these plates was estimated to lie between 2.5 nm and 5 nm. They found that crystallites with a length of about 18 nm were four times more abundant than those of 40 nm, but thought that these smaller particles were fragments of the larger plates. In an extensive study on the crystal-collagen relationship in human bone, and on changes occuring with age, Robinson and Watson (1955), found that the crystalline phase increased in size, from an unresolvable particle of less than 5 nm diameter in the infant, to plate-like crystals of 150 nm x 50 nm x 10 nm in the senile subject.

It has been suggested by Fernandex-Morán and Engström (1957), that the observed plates are actually lateral aggregations of rods. However, this does not account for

the difference in observed contrast between the two types of structure. The rod-like structures appearing more dense than the plate-like objects.

Steve-Bocciarelli (1969), made a study of ox bone in the electron microscope, and by using a tilting specimen stage, he was able to compare images of the same crystallite taken at $\pm$ 20° to the normal position. He arrived at the following conclusions:

a) Rod-like images of the crystallites were actually edge views of plate-like structures.

b) The plates measured 2-4 nm in thickness and up to 70 nm in length and width.

c) The plates showed no well defined profile, but sometimes an angle of 90° could be observed.

These observations are corroboration of work by Johansen and Parks (1960), who arrived at the same basic conclusions.

1.7.11. Mineral Morphology. Summary

Microscopical observations of the size and shape of bone mineral crystallites have not been in agreement with x-ray diffraction findings. The two prevalent viewpoints consider bone mineral to be either rod-like or plate-like in habit. There appears to be agreement that the smallest dimension of the crystals is about 5 nm, but there is discrepancy in the reported c-axial lengths. X-ray diffraction techniques producing values of about 20 nm - 35 nm, whilst microscopical estimations tend to be two or three times larger. Whilst various hypotheses have been suggested to explain this discrepancy, experimental evidence is still inconclusive in delineating both the size and shape of bone mineral crystallites.

1.8. Piezoelectricity in Bone

It has been well established that bone exhibits the property of a piezoelectric transducer, Bassett (1968). That is, it has the ability to transduce mechanical energy into electrical energy, and vice versa. Indeed, this phenomenon has been shown to be an inherent property of other mineralised structures, and of non-mineralised connective tissue. This property of biological tissue is regarded by some, as being of fundamental importance in supplying the critical transducing step in the initiation of physiological processes by external means.

Although it is clear that bone behaves piezoelectrically when deformed, the origin and significance of the response are not completely understood. It is known that bone has the ability to adapt itself to accommodate new stresses, and it does this by a process of remodelling, Currey (1968). Currey goes on to suggest that an electrical stimulus is the most likely mechanism behind the control of osseous cellular activity. Many workers have shown that when a bone is bowed, the concave periosteal and endosteal surfaces become negatively polarised with respect to the convex endosteal and periosteal surfaces. The negative potential seems to induce osteoblastic activity, whilst the positive potential appears to induce osteoclastic activity. Referring to figure 1.13 it can be seen that this mechanism leads to a drift of the bone over a long period, such that it is remodelled to accommodate the stress. Thus, a negative feedback system appears to operate which controls the remodelling process. It remains to be shown whether this electrical stimulus is directly responsible for the cellular activity, or that the activity is mediated by other means.

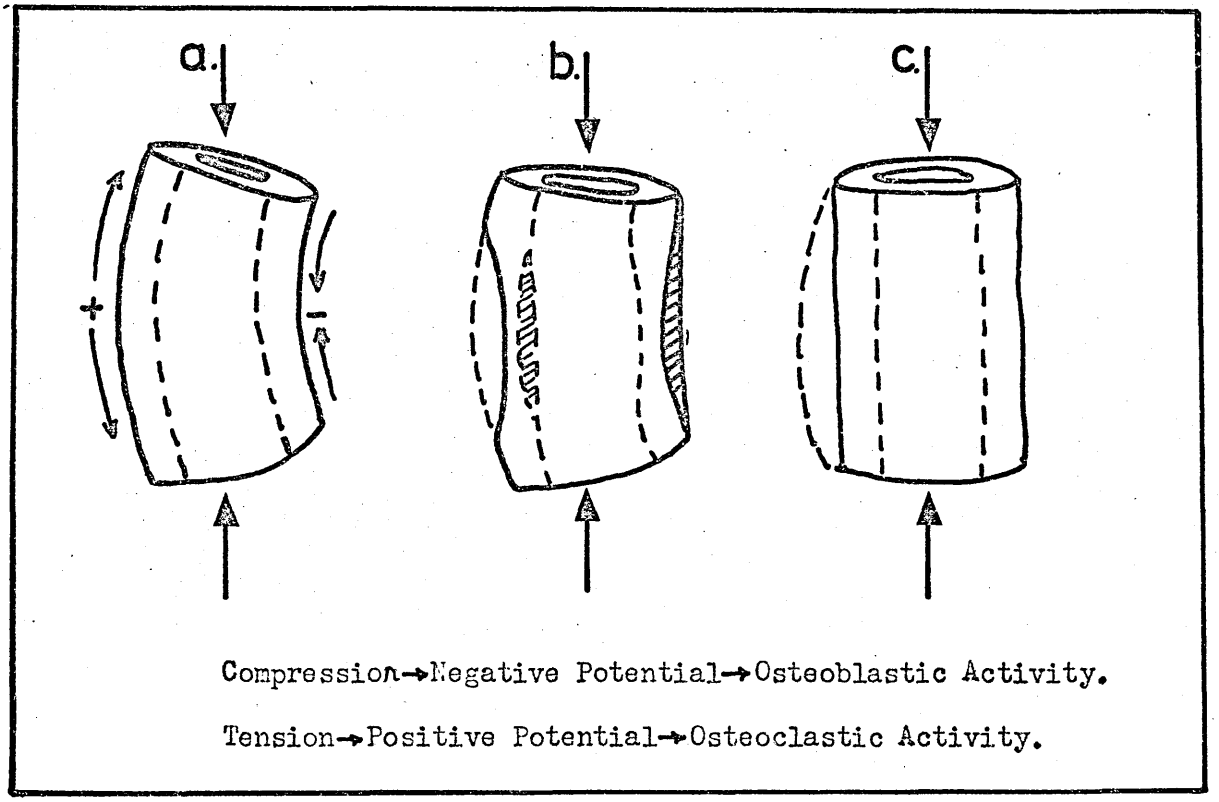
a.
b.
c.
+
−
Compression→Negative Potential→Osteoblastic Activity.
Tension→Positive Potential→Osteoclastic Activity.

Figure 1·13

1.9. The Objectives of this Study

This first chapter has given a brief introduction to the structure of bone and some of the difficulties encountered in its study. Before the physical behaviour of such a complex material as bone, in both normal and abnormal situations, can be understood, it is necessary to have basic information about the structural components. Two outstanding aspects of bone structure which need further study are:

a) The shape and size of bone mineral crystals.

The two methods by which this topic has been studied are x-ray diffraction and electron microscopy. Past results have been inconclusive, and there have been discrepancies between the two methods.

b) Bone mineral orientation.

This particular topic is important since the c-axial orientation of bone mineral is co-axial with the collagen fibres, and hence the mineral orientation indicates the three dimensional fibrous structure of the bone sample. Past results have tended to be qualitative, and techniques need to be developed to obtain a quantitative description of the fibrous structure.

This work is an attempt to develop techniques which will clarify past discrepancies and also provide quantitative information on the shape, size and orientation of bone mineral crystals and hence further the understanding of bone as a material.

CHAPTER TWO

INTRODUCTION TO EXPERIMENTAL TECHNIQUES USED IN THIS STUDY

2.1. Crystal Structure.

A crystal can be defined as a solid, composed of atoms, which are arranged in a pattern periodic in three dimensions. Thus crystals differ in a fundamental way from gases and liquids, which do not have this periodic ordering. Some solids also lack a periodic structure, and are termed amorphous.

The crystal lattice can be considered as a set of points which have a fixed relation in space to the atoms of the crystals, and may be regarded as a framework on which the actual crystal in built. The lattice is chosen, such that the crystal is divided into a large number of cells, the contents of each cell being a representative unit of the crystal. These unit cells are defined by three vectors, a, b and c, which are the crystallographic axes of the cell. Alternatively, the cell may be described by the lengths of these vectors and the angles between them, see figure 2.1.

When x-rays, or electrons, fall on a crystal they can be considered to be reflected from planes of atoms which are defined within the crystal, and in order to label, or index the various sets of planes with respect to the crystal lattice, Miller indices are used. Examples of plane indexing by Miller indices are shown in figure 2.2. The spacings of these planes of atoms, (the d-spacings), can be calculated from a general formula using the respective Miller indices.

For the hexagonal crystal system, the d-spacings are given by:-

$$\frac{1}{d^2} = \frac{4}{3}\left(\frac{h^2 + hk + k^2}{a^2}\right) + \left(\frac{l}{c}\right)^2$$

Crystal Lattice (a), and Unit Cell (b), Showing Lattice Parameters.

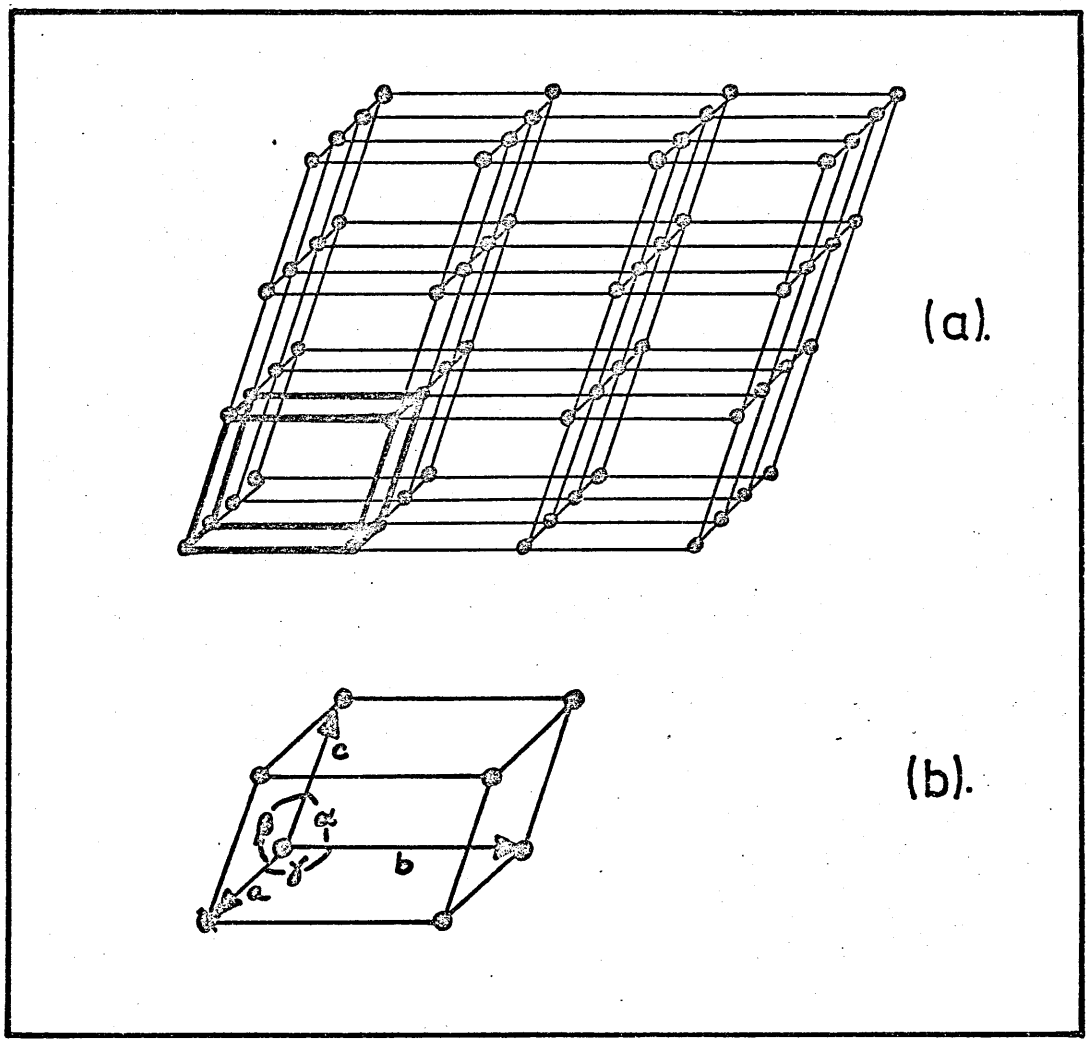

Figure 2·1

Definition:-

Miller indices are reciprocals of the fractional intercepts which the plane makes with the crystallographic axes.

e.g. If the Miller indices of a plane are (hkl), then the plane makes fractional intercepts of a/h,b/k, and c/l as shown below.

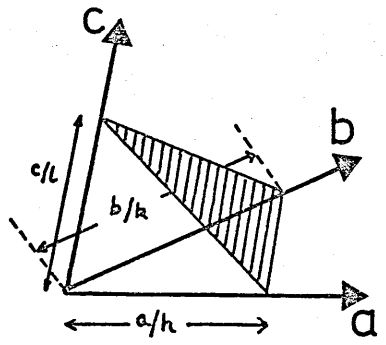

The spacing of a set of crystal planes with Miller indices (hkl), is represented as d_{hkl} , examples are shown below.

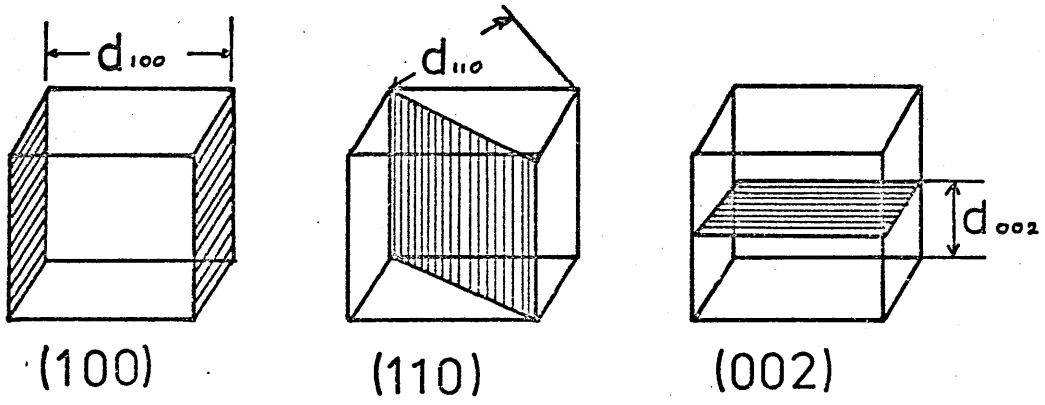

Figure 2·2

2.2. X-rays.

2.2.1. Introduction

X-rays were discovered in 1895 by the German physicist Röentgen. They were quickly put to use in the medical field without a proper understanding of their nature. It was not until 1912 that their exact nature was established. Also in that year, the phenomenon of x-ray diffraction by crystals was discovered and this provided physicists with a new tool with which to probe the fine structure crystals. The wavelength of light is about 600 nm, and this places a limit on the size of objects which can be examined by light. X-rays, on the other hand, have wavelengths of the order of 0.1 nm and so may be used to give detailed information about objects the size of atoms.

2.2.2. X-ray Diffraction

If x-rays are considered to be reflected from the various sets of planes in a crystal, the reflected rays will interfere with each other. Rays from successive planes, will interfere constructively, if their path difference is a whole number of wavelengths. If the crystal is assumed to be infinite, then all the other rays will cancel themselves out by destructive interference. In the case of real crystals, which are by no means infinite, the rays are not completely cancelled out, and the strong reflection becomes less well defined. As the crystal becomes smaller, the more diffuse its diffraction pattern appears. The condition for a strong reflection depends upon the crystal geometry and the wavelengths of the x-rays, and this condition is expressed by Braggs Law, see figure 2.3.

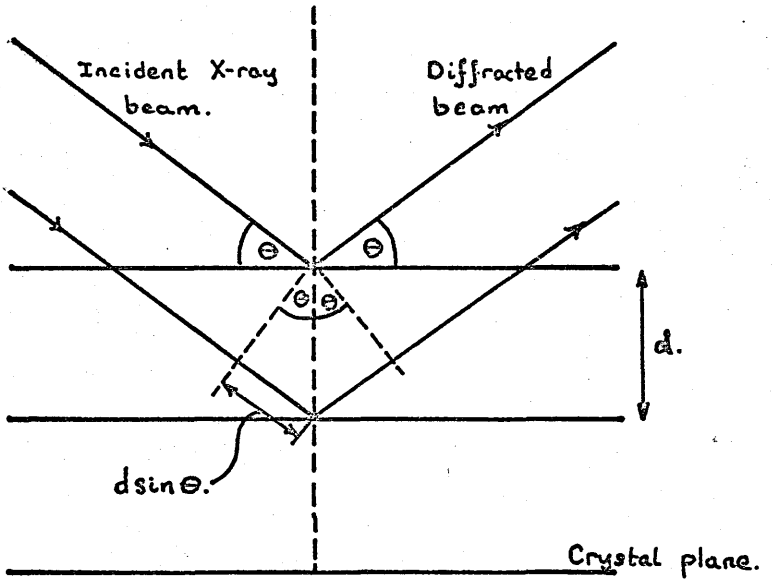

Constructive interference of X-rays occurs when the path difference between rays diffracted from successive crystal planes is a whole number of wavelengths, i.e.

$$2d.Sin\theta = n\lambda$$

Figure 2.3

2.2.3. The Powder Method

This method is probably the most commonly used technique in crystallography. The crystals to be examined are first reduced to a fine powder, if not in that condition already. The powder is then loaded into a thin glass capilliary, which is presented to the x-ray beam. Each particle of powder being a tiny crystal, oriented at random, with respect to the incident beam. Statistically, some of the particles will be arranged to give a certain Bragg reflection, and because of their random orientation about the x-ray beam, that reflection will form a cone of x-rays. A series of cones will be produced for all possible Bragg reflections, see figure 2.4. The powder technique is alternatively called the Debye-Scherrer method, and the apparatus used is a short cylinder with the powder specimen placed on the axis. A thin strip of film is fitted into the cylinder in such a manner that all the diffraction cones strike the film, as shown in figure 2.5. By measuring the spacings of the lines on the film, and knowing the geometry of the apparatus the cyrstal d-spacings can be determined. The two pieces of apparatus commonly used for obtaining information from x-ray films are:-

a) An illuminated graticule with a sliding cursor which allows accurate measurement of the diffraction line diameters;

b) A microdensitometer, which is a device to translate the optical density along the film into a graphical form. In this manner, information concerning the profile of the diffraction lines, together with their relative strengths can be obtained, see figure 2.5.

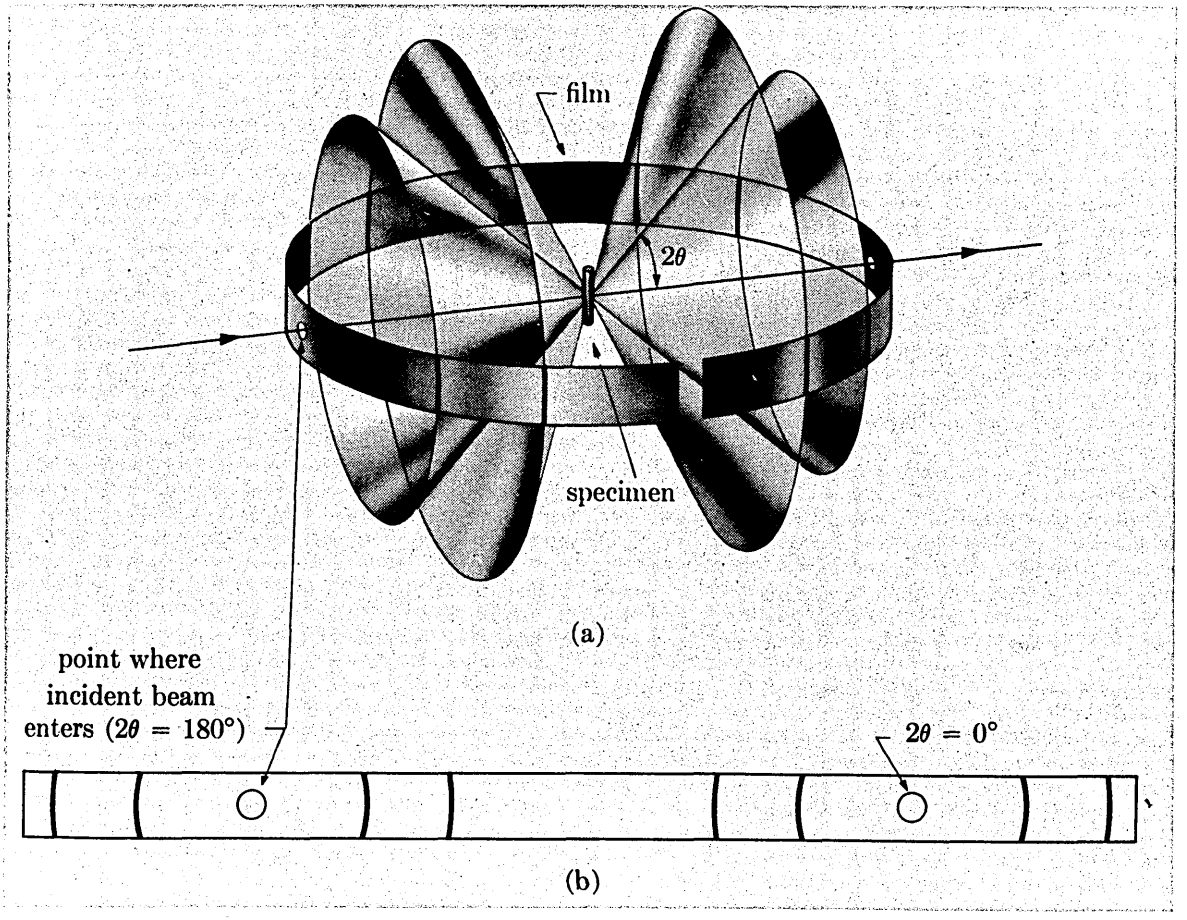

Figure 2.4

The Debye-Scherrer powder method.

(a) relation of film to specimen and incident beam.

(b) appearance of film when laid out flat.

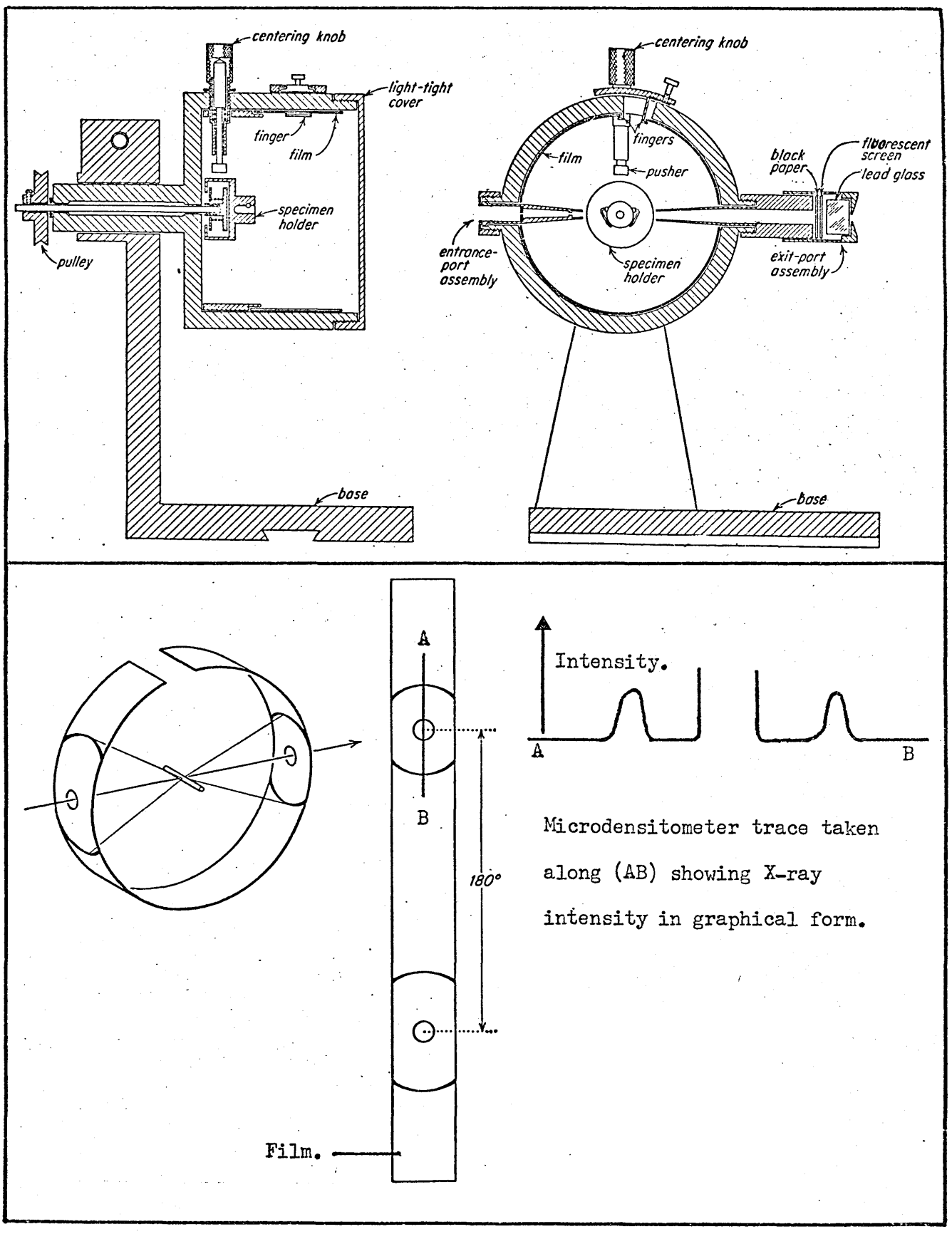
centering knob
light-tight cover
finger
film
specimen holder
pulley
base
centering knob
fingers
film
pusher
black paper
fluorescent screen
lead glass
entrance-port assembly
specimen holder
exit-port assembly
base
A
B
180°
Film.
Intensity.
A
B
Microdensitometer trace taken along (AB) showing X-ray intensity in graphical form.

Figure 25

2.2.4. The Flat Film Method

In this method, the specimen is simply placed in the x-ray beam, and the diffracted beams are detected on a flat plate film which is placed in front of the specimen, or behind if back reflections are to be studied, as shown in figure 2.6. This method does not give a complete coverage of the 2θ values as with the Debye-Scherrer method. However, it does give a complete picture of the diffraction cones, so that orientation effects can be studied.

If the crystals in a polycrystalline specimen are perfectly oriented in one direction, then the diffracted beams would appear as spots on a film. If the orientation is completely random, diffraction rings would be observed. If the orientation lies between these two extremes, then the spots spread into arcs, the distribution of which give information about the degree of orientation. Figure 2.7. demonstrates the effect of orientation upon the diffraction pattern.

2.2.5. The X-ray Diffractometer

Basically, a diffractometer is designed somewhat like a Debye-Scherrer camera, except that a movable counter replaces the strip of film. In both instruments essentially manochromatic radiation is used, and the x-ray detector (film or counter) is placed on the circumference of a circle centred on the specimen. The intensity of a diffracted beam is measured in a diffraction camera, by the amount of blackening it produces on an x-ray film. This is usually converted to a graphical form by using a microdensitometer. In the diffractometer however, the intensity is measured directly by the counter, and can be monitored continuously on a chart recorder, or at selected discreet points.

The Flat Film Method.

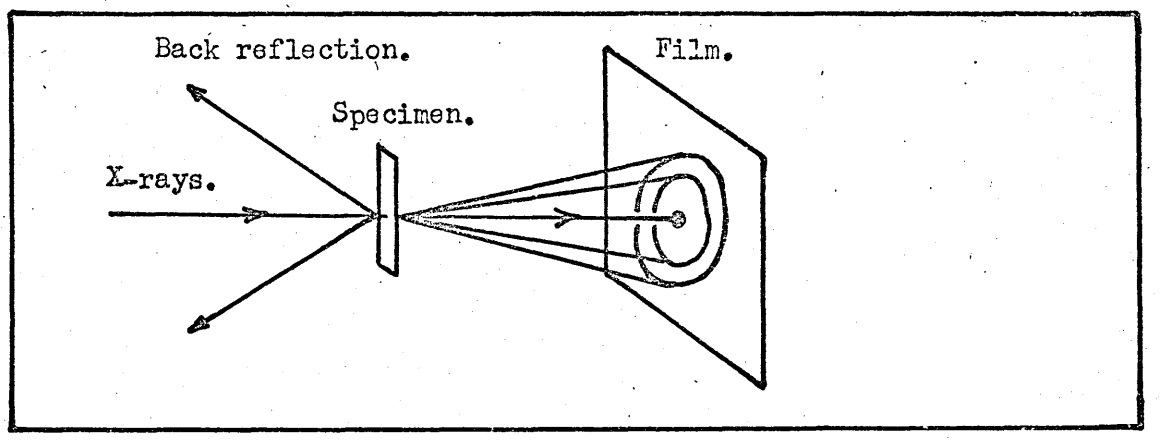

Figure 2.6

The Effect of Crystal Orientation on the Diffraction Pattern.

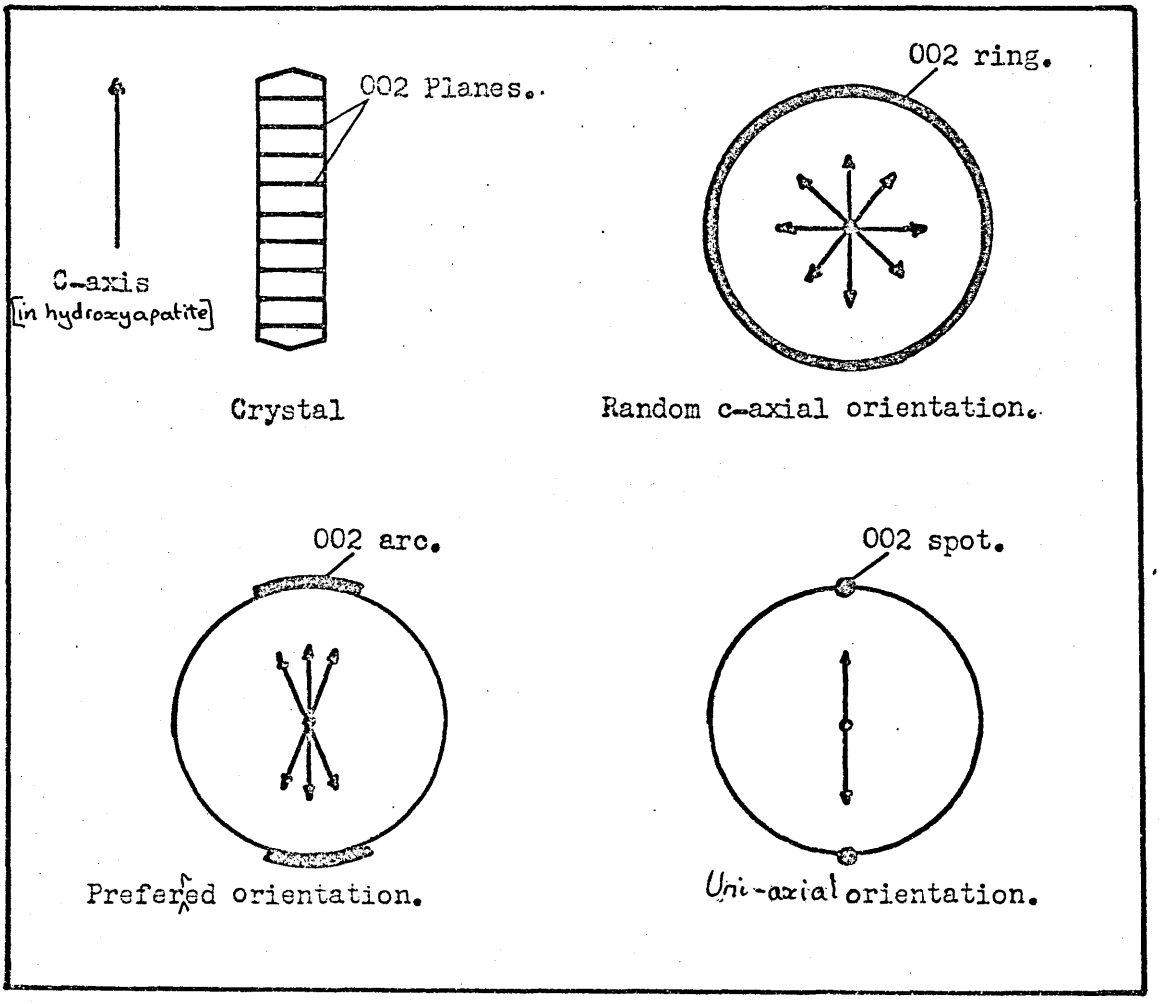

Figure 2.7

This method provides accurate detailed information about the diffraction peak intensities and shape, and it will be seen later, that the shape of the diffraction envelope is an important factor when determining the crystallite size by this method.

As mentioned previously, the x-ray beam should ideally be monochromatic, and this is achieved by filtering. The x-rays generated by a copper target x-ray tube, consist of two high intensity peaks. These are the result of electronic transitions in the copper atoms. By passing the beam through a metal which has an absorption edge between the two peaks, only one high intensity peak will emerge. If this peak is sufficiently greater than the background radiation, it may be considered to be monochromatic. Nickel is the filter used with copper radiation, see figure 2.8.

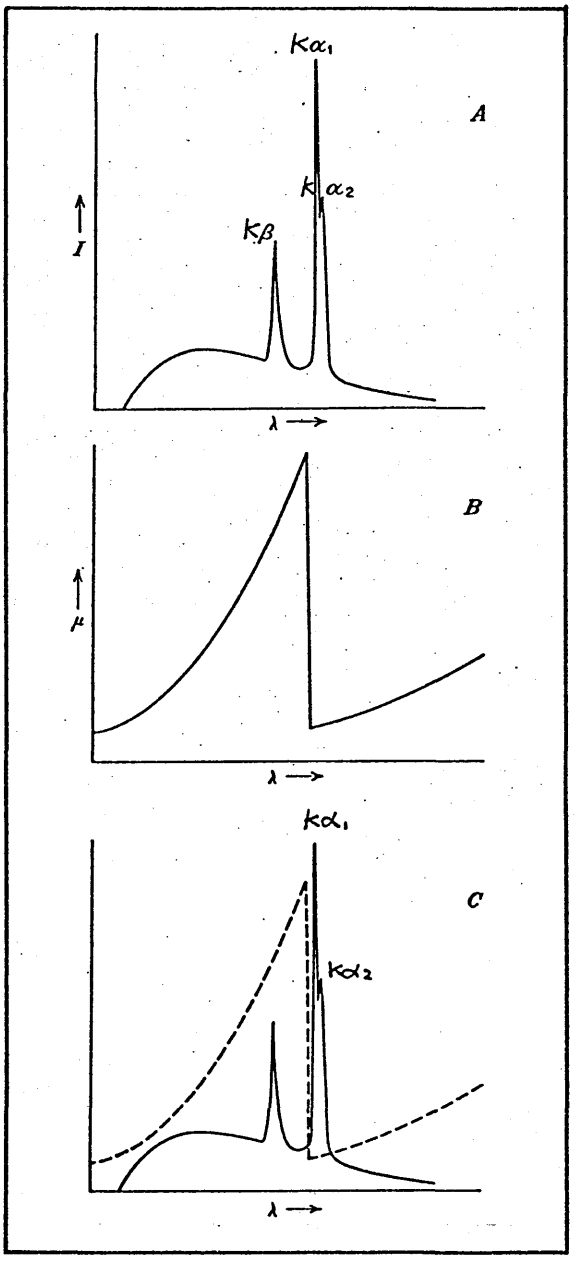

A. Characteristic X-ray spectrum emitted by an X-ray tube.

B. The variation of X-ray absorption with wavelength for an element such as nickel, which is used to filter copper radiation.

C. When the X-ray spectrum of A. is filtered by the element indicated in B. , the resulting radiation is approximately monochromatic, consisting almost entirely of the strong $K\alpha$ peak.

Figure 2.8

2.3. Electron Microscopy

The elctron microscope is a versatile instrument, and can be used in a variety of different modes. The image contrast is formed in two distinct ways, a) by absorption, b) by diffraction.

2.3.1. Absorption Contrast

The specimen used for transmission electron microscopy is usually in the form of a thin section, 20-100nm. thick. As electrons pass through the specimen, they are scattered and absorbed to varying degrees, depending upon the composition of the specimen, Electrons emerging from the lower surface, are focused to form the final image, which correspondingly varies in contrast with the electron density of the specimen.

Whilst absorption contrast occurs in all types of specimen, the second method of contrast formation occurs only with crystalline objects.

2.3.2. Diffraction Contrast

When electrons, passing through a specimen encounter a crystalline substance, which is so oriented as to produce a diffracted beam, then the transmitted beam will be reduced in intensity, by the amount diffracted away. The diffracted beam is usually stopped by the objective aperture, which is placed directly below the specimen holder, and so does not continue down the microscope column to contribute to the final image. Both types of contrast formation are shown diagramatically in figure 2.9.

2.3.3. Bright Field Operation

In this mode of operation, the image is formed by electrons which are transmitted through the specimen, and therefore both methods of image contrast formation come into effect. Figure 2.10. shows the typical construction

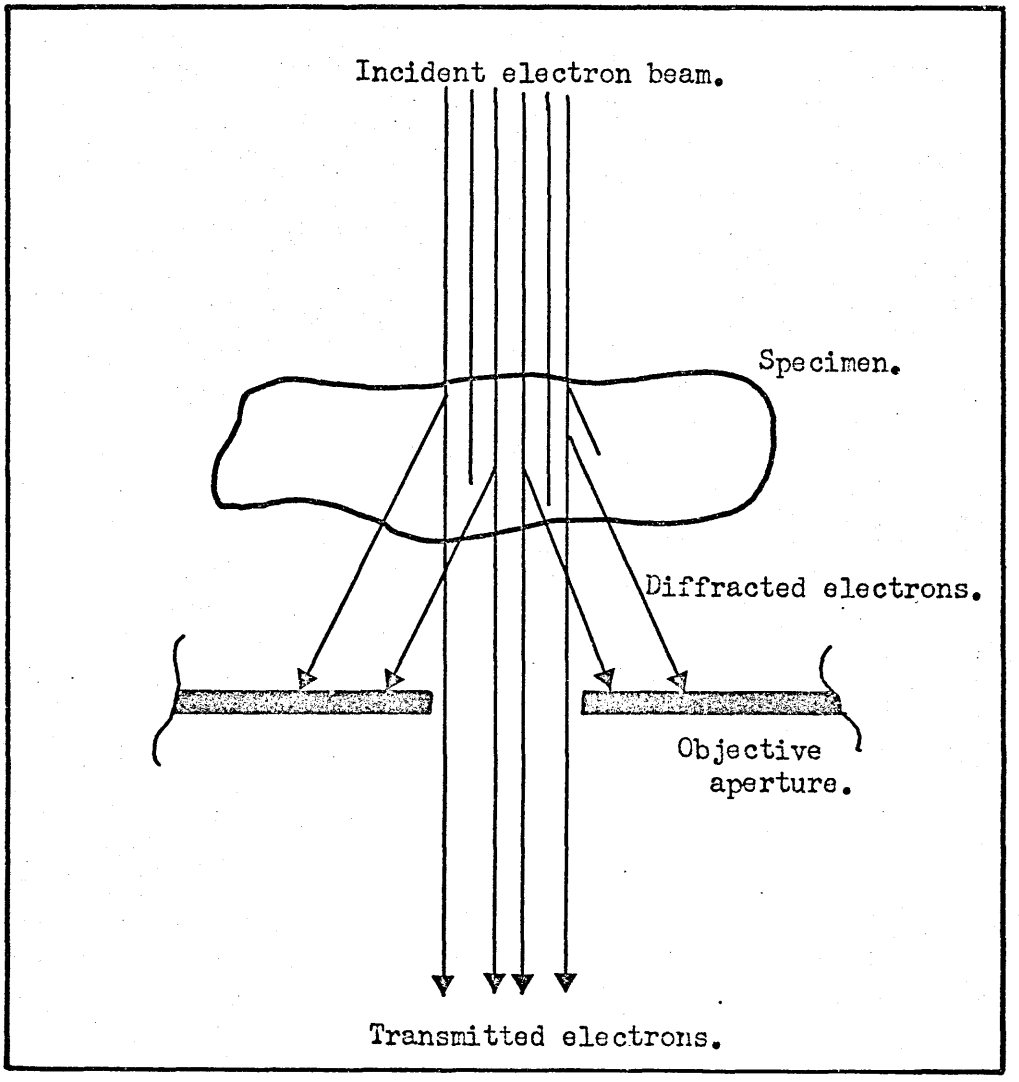

Figure 2.9

Both absorption and diffraction of the incident beam lead to image contrast.

and lens arrangement of a modern electron microscope.

The type of information which can be obtained by this method is mainly concerned with the morphology of the specimen, and structural relationships. Various techniques can be used to increase the amount of information obtainable from bright field images. For instance, by tilting the specimen from its normal position two or more images of a certain structure can be obtained, and these, when viewed in a suitable stereo viewer, can give a pseudo three dimensional image.

With biological specimens it is often required to localise certain substances, and this is achieved by staining the specimen with heavy metal salts, which attach themselves preferentially to various substances within the specimen.

These are just two of the ways in which the bright field mode can be enhanced to give specific information.

2.3.4. Electron Diffraction

Since electrons exhibit wave properties, like x-rays, they form a diffraction pattern when transmitted through crystalline objects. In the electron microscope, the diffraction pattern is focused in the back focal plane of the objective lens, see figure 2.11. This pattern can be brought into focus at the image plane by changing the focal lengths of the lenses, which is done electrically. Thus, areas of interest can be selected whilst in the image mode, and analysed by diffraction, by switching from one mode to the other. An electron diffraction pattern can be easily formed from an area only 1 μm. in diameter, requiring a photographic exposure

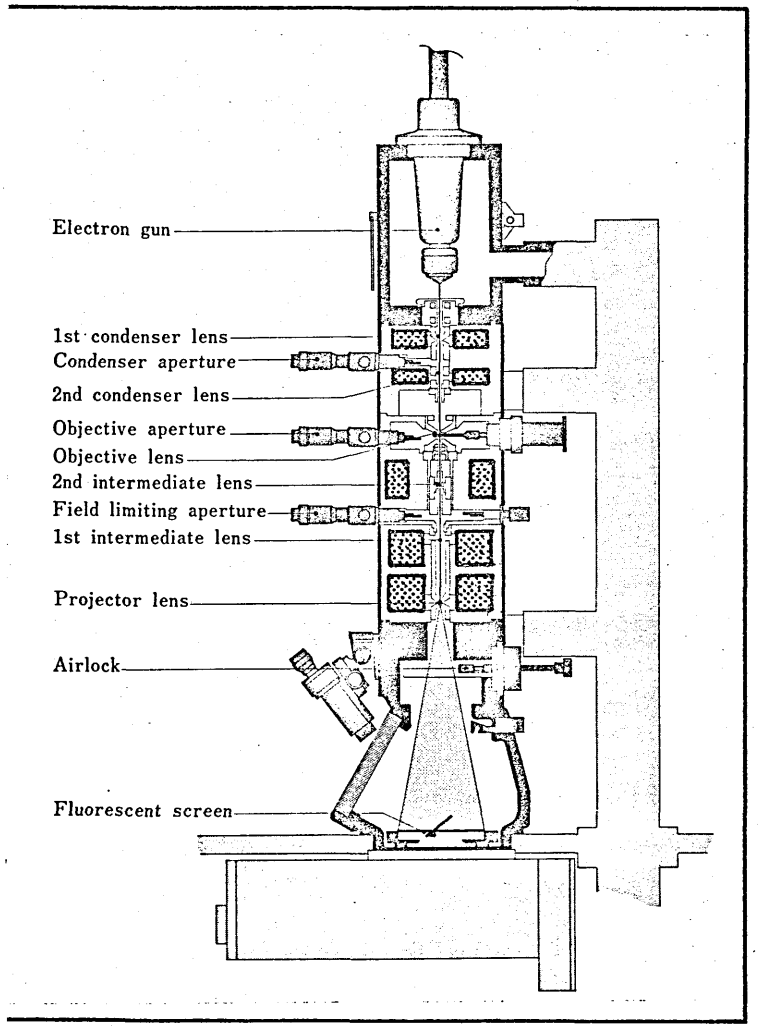

Figure 2.I0

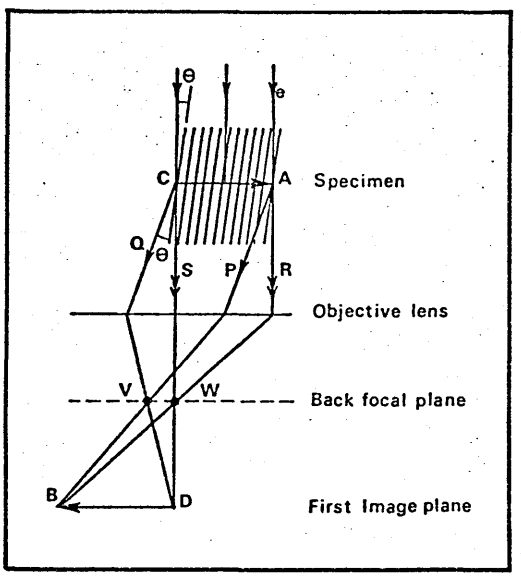

Figure 2.II

Figure 2.I0 shows the crossection of a modern electron microscope.

Figure 2.II is a ray diagram showing how electrons emerging parallel from the specimen are focused in the back focal plane. The diffraction pattern is produced in the final image by focusing on the back focal plane instead of the first image plane.

of a few seconds. By comparison, the minimum area selectable for x-ray diffraction analysis is between 20 and 100 times larger, and requires much longer exposure times. However, specimen preparation for x-ray analysis is usually far simpler than that for electron microscopy.

The information obtainable from electron diffraction relates to the specimen composition, structure, and orientation effects in polycrystalline samples.

2.3.5. Dark Field Operation

In this mode of operation, the final image is formed from diffracted rather than transmitted beams, figure 2.12 shows how this is achieved.

Method A involves moving the objective aperture away from the optical axis, and this introduces spherical aberration into the image. To overcome this problem, the diffracted beam is aligned with the optical axis, as shown in B, and under these conditions, only objects which diffract beams through the objective aperture will appear bright, everything else appears dark.

The particular use of dark field microscopy to the problems of calcified tissue will become evident in the following chapters.

Formation of a Dark Field Image.

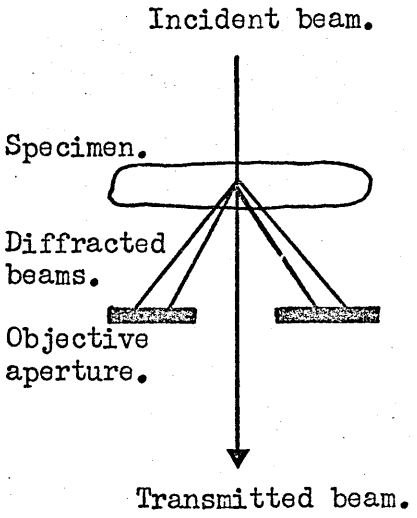

Method A. Objective aperture moved to stop the main beam and transmit the diffracted beam.

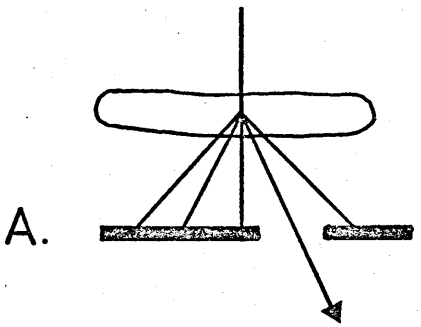

Method B. Main beam tilted so that the diffracted beam passes through the objective aperture.

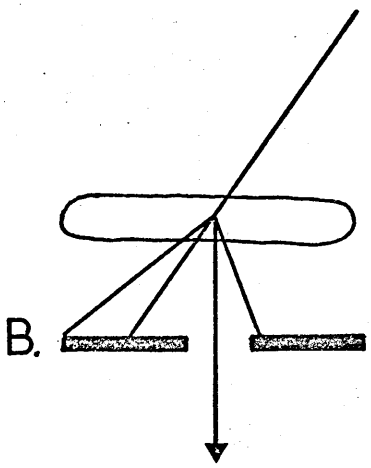

Figure 2.12

CHAPTER THREE

SPECIMEN PREPARATION FOR ELECTRON MICROSCOPY

3.1. Specimen Preparation and Analysis.

3.1.1. Introduction

Since bone is a biological material it undergoes autolytic changes after death. Autolysis being the self-destruction of tissue by enzyme action, causing the breakdown of protein and the eventual liquefaction of the cells. Bone matrix is a unique tissue, in that it apparently remains stable for many thousands of years. However, to gain information about in-vivo situations, by studying bone in-vitro, it is necessary to know what changes have occured after death.

The first step in tissue preparation is usually fixation. This process halts any autolytic activity and crosslinks protein, to make a more permanent structure. Fixation is an attempt to preserve the tissue as near as possible to the in-vivo state. However, by the very nature of the process it cannot do this. It is, therefore, important to be aware of any changes brought about by fixation, and if indeed they are significant. The problem is a difficult one, and the only reasonable way in which it can be investigated is to use various, and if possible, widely differing preparation techniques and compare results. In this study bone mineral has been investigated by using two methods:-

a) X-ray diffraction, which provides information on structural and chemical changes;

b) Electron microscopy, which provides more qualitative information on structural features, such as gross changes to crystallites due to dissolution and re-precipitation.

3.1.2. Review

Experiments on the structure of bone mineral under different experimental conditions have been performed by Ascenzi et al (1968). X-ray diffraction, electron diffraction and electron microscopy all indicated no apparent change in the structure and form of bone mineral prepared by various standard techniques and bone which was unfixed and unembedded. Johansen and Parks (1960), found that the crystallite morphology appeared unchanged between hydroxyapatite crystals in dentine which had been sectioned without previous treatment, and dentine which had undergone routine fixation and embedding.

One point to be considered is the effect of specimen preparation on the amorphous fraction of bone mineral. It has been suggested by Pautard (1970), that all bone mineral could exist in an amorphous form in-vivo, and only becomes crystalline after death. This idea has been investigated by the author and dismissed. The reader is referred to Appendix I for this topic.

From their work on synthetic systems, Termine and Posner (1967), (1972), conclude that whilst the majority of bone mineral is present in the crystalline form, the amorphous fraction appears to be stabilised in-vivo and can convert to the crystalline form after death, but it can also be removed by prolonged aqueous processing during specimen preparation.

It appears therefore, that the crystalline fraction, which forms the majority of bone mineral is unaltered in morphology and chemical composition by standard tissue preparation techniques. The amorphous fraction on the other hand appears to be very susceptible to alteration.

However, since this work relates to structural features defined by the crystalline portion of bone mineral, the amorphous fraction is unimportant in this case.

Despite previous investigations, during the preliminary stages of this work it was decided to check for preparation artefacts by using electron microscopy and x-ray diffraction, since techniques and materials were being used which had not specifically been used in the past.

3.1.3. The Choice of Specimen

Work in the past has been performed on many types and species of bone, so it was decided initially, in an attempt to standardise experiments, to use the same bone and specie of animal. Cortical bone from the mid-femural region of the female dutch rabbit was chosen, and the animals, which were fed on a standard diet, were obtained from the university animal breeding unit.

3.1.4. Experimental method

A femur was removed from a female dutch rabbit, aged approximately six months, immediately after death. The epiphyseal growth plate was still present, indicating that the animal had not reached maturity. The mid-section of the femur was cut into 1mm thick slices as shown diagramatically in figure 3.1., using a Metals Research macrotome, fitted with a sintered diamond wheel. Distilled water was used as a lubricant except for the specimen which was to be untreated, and this was cut dry.

The samples were then treated as follows:-

The Bone Sample.

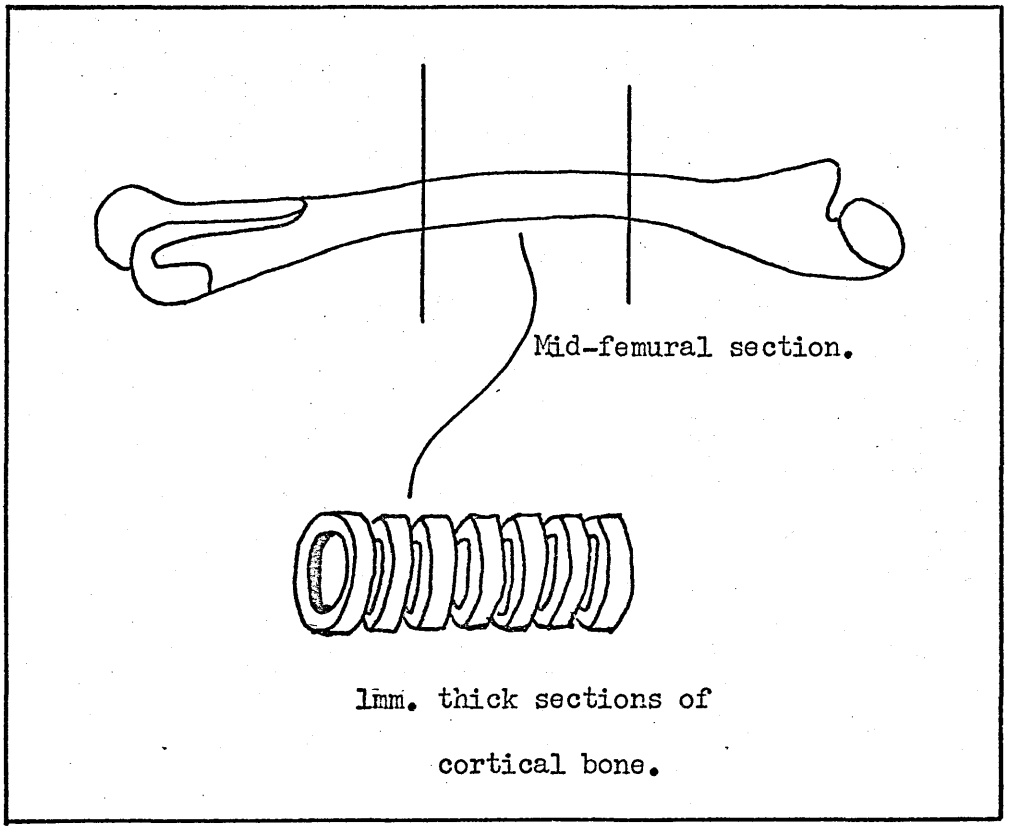

Figure 3.1

a) Fixed in Ethyl Alcohol

Ethyl alcohol (ethanol) is a powerful dehydrating agent, and causes shrinkage and hardening of biological tissue. Fixation was carried out in a 250 ml conical flask, at room temperature for seven days, after which the sample was powdered by filing, and used for x-ray analysis.

b) Fixed in Neutral Buttered Formal Saline

Neutral buttered formal saline is composed of:-

Formalin	:	100ml
Tap water	:	900ml
Acid Sod. Phosphate Monohydrate	:	4.0g
Anhydrous Disodium Phosphate	:	6.5g

This mixture is a common histological fixative and fixation was carried out in a 250ml conical flask, at room temperature for seven days. The sample was then washed in distilled water for ten minutes, and then powdered for x-ray analysis.

c) Freeze Dried

Freeze drying is a method of arresting tissue decomposition without chemically altering any of the constituents of the sample, and ideally only water is removed. The sample is however not fixed, and can deteriorate if allowed to absorb moisture. The sample was first of all quenched in Arcton 12, which had been cooled to -158^{o}C by Liquid nitrogen. Arcton 12 was used in preference to liquid nitrogen since it has a higher thermal conductivity and does not form bubbles around the specimen which would impede the cooling. It is important to have a rapid

cooling rate so that ice crystals do not form and disrupt the structure. The frozen specimen was then transferred to a vacuum chamber at less than 0.01mm Hg pressure and -40°C. Under these conditions the ice in the specimen sublimes, and is absorbed by a tray of phosphorus pentoxide. After twenty-four hours the sample was slowly brought to room temperature and pressure and then powdered for x-ray analysis.

d) Fixed in Glutaraldehyde

Glutaraldehyde is a rapidly penetrating fixative and is in common use. Fixation was carried out in a 250ml conical flask at 40°C for 3½ hours, after which the specimen was washed in distilled water, dried in air and then powdered for x-ray analysis.

e) Untreated

This specimen was left to dry in air for a period of two weeks, after which it was powdered for x-ray analysis.

3.1.5. X-ray Analysis

The various bone powders were loaded into 0.3mm glass capiliaries and irradiated with nickel filtered copper radiation in a Debye-Scherrer powder camera for a period of 2½ hours. The exposed film was then developed and measurements taken of the ring diameters using an illuminated graticule. A change in these diameters, or the appearance of new rings would indicate a change in the crystal composition.

3.1.6. Calculation of the d-spacings

The dimensions of the Debye-Scherrer powder camera, are such that 1mm measured on the film represents 1^{o} (2θ). A ring diameter subtends an angle of 4θ at the specimen, as shown in figure 3.2. Thus, by using the measured values of θ, and the Bragg Law, the various d-spacings which characterise the specimen were calculated.

3.1.7. Plane Indexing

The d-spacings for the various (hkl) planes of bone mineral were calculated by using the hexagonal crystal model, as mentioned in 2.1., and lattice constants for bone mineral of:-

$$a = 0.9432 \text{ nm}$$
$$c = 0.6881 \text{ nm}$$

(Posner and Perloff - 1958)

The calculated spacings were then compared to those measured experimentally and Miller indices assigned to the various rings on the film.

3.1.8. Results

The following figures and tables show the microdensitometer trace of each film, together with measured d-spacings for the peaks indicated.

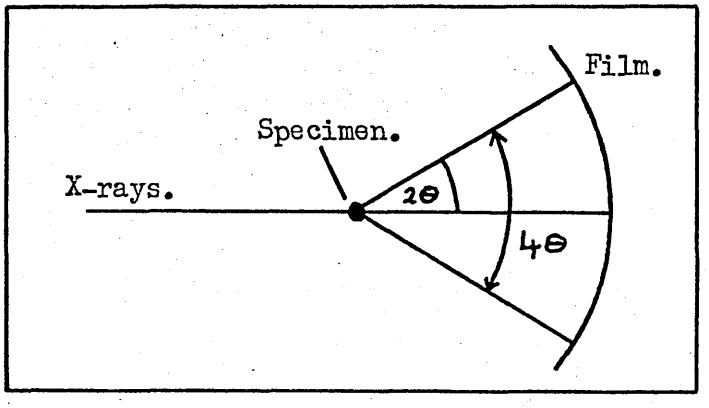

Figure 3.2

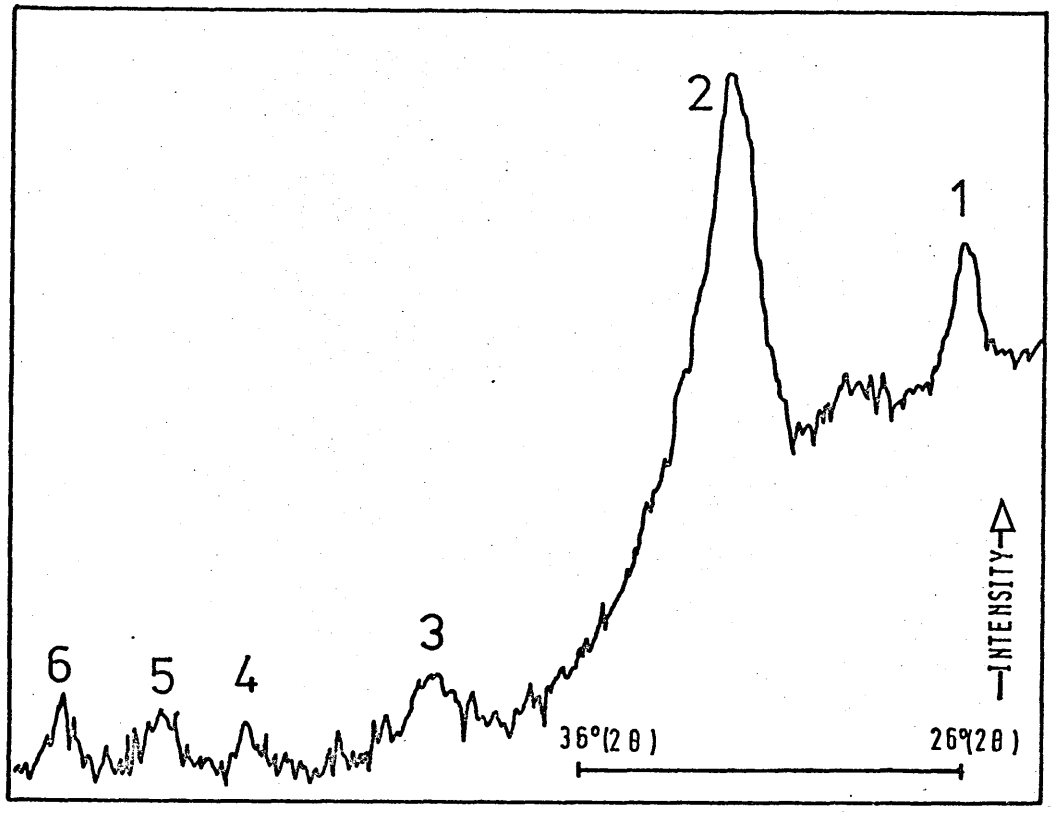

TRACE. 3.I

SPECIMEN S1A. ABSOLUTE ETHANOL.

PEAK	d-SPACING. nm.	MILLER INDICES.	INTENSITY.
1	0.3431 ± 0.0010	002	Good.
2	0.2798 ± 0.0010	121/112	V.Good.
3	0.2271 ± 0.0010	130	Poor.
4	0.2030 ± 0.0010	113/203	V.Poor
5	0.1951 ± 0.0010	222	V.Poor.
6	0.1835 ± 0.0010	123.	V.Poor.

TABLE 3.1

SPECIMEN S1B. N.B.F.S.

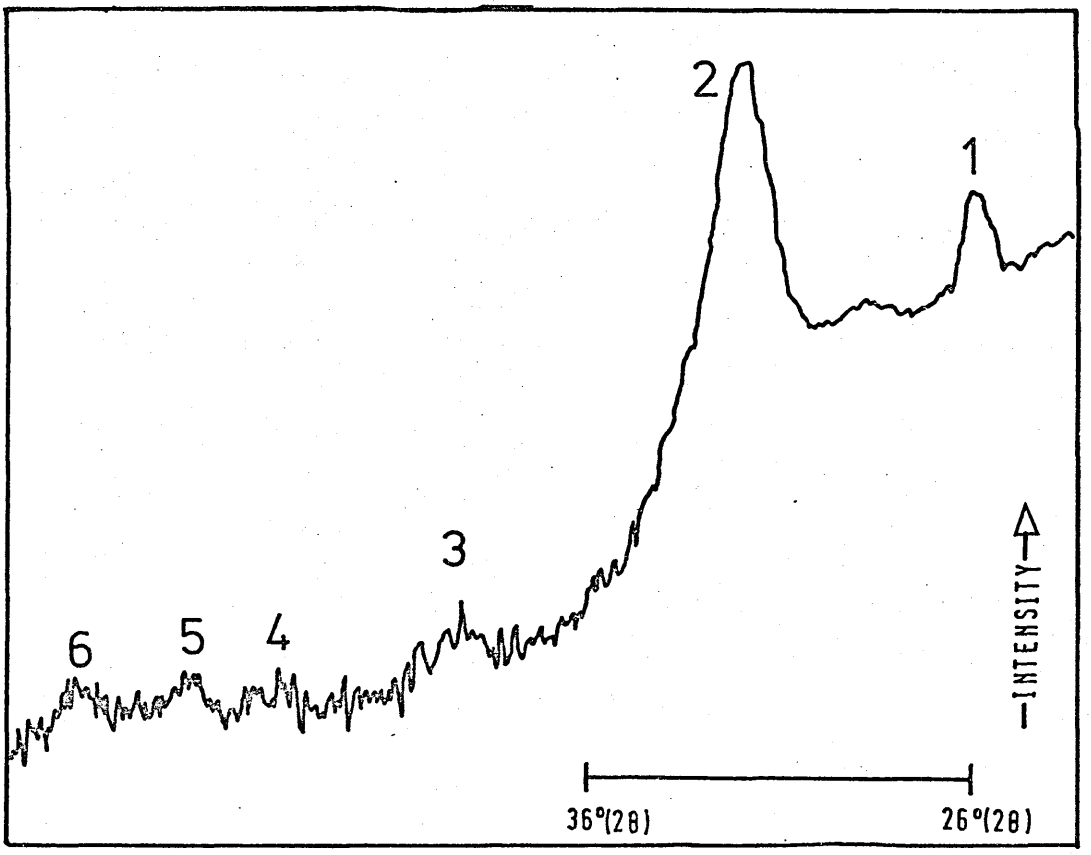

TRACE. 3.2

SPECIMEN S1B. N.B.F.S.

PEAK	d-SPACING.nm.	MILLER INDICES.	INTENSITY.
1	0.3440±0.0010	002	Good.
2	0.2801±0.0010	121/112	V.Good.
3	0.2276±0.0010	130	Poor.
4	0.2032±0.0010	113/203	V.Poor.
5	0.1947±0.0010	222	V.Poor.
6	0.1843±0.0010	123	V.Poor.

TABLE 3.2

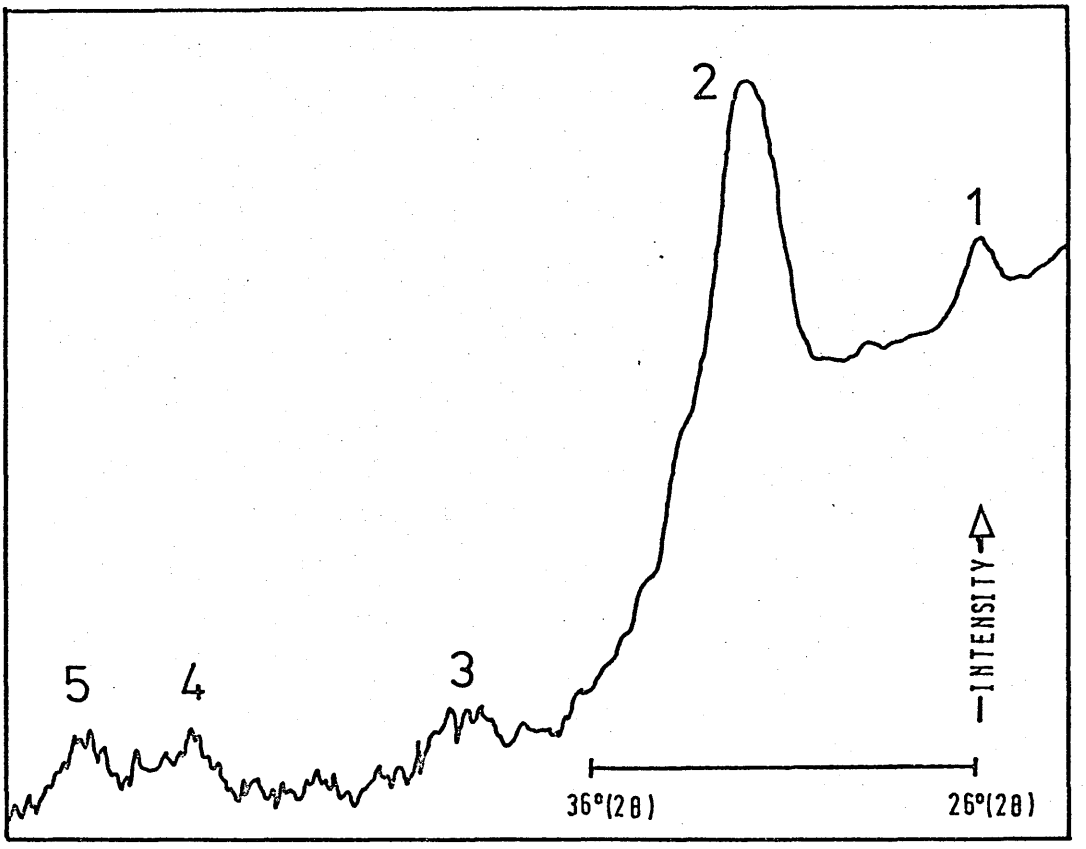

TRACE. 3.3

SPECIMEN S1C. FREEZE DRIED.

PEAK	d-SPACING. nm.	MILLER INDICES.	INTENSITY.
1	0.3421± 0.0010	002	Good.
2	0.2797±0.0010	121/112	V.Good.
3	0.2265±0.0010	130	Poor.
4	0.1939±0.0010	222	V.Poor.
5	0.1838±0.0010	123	V.Poor.

TABLE 3.3

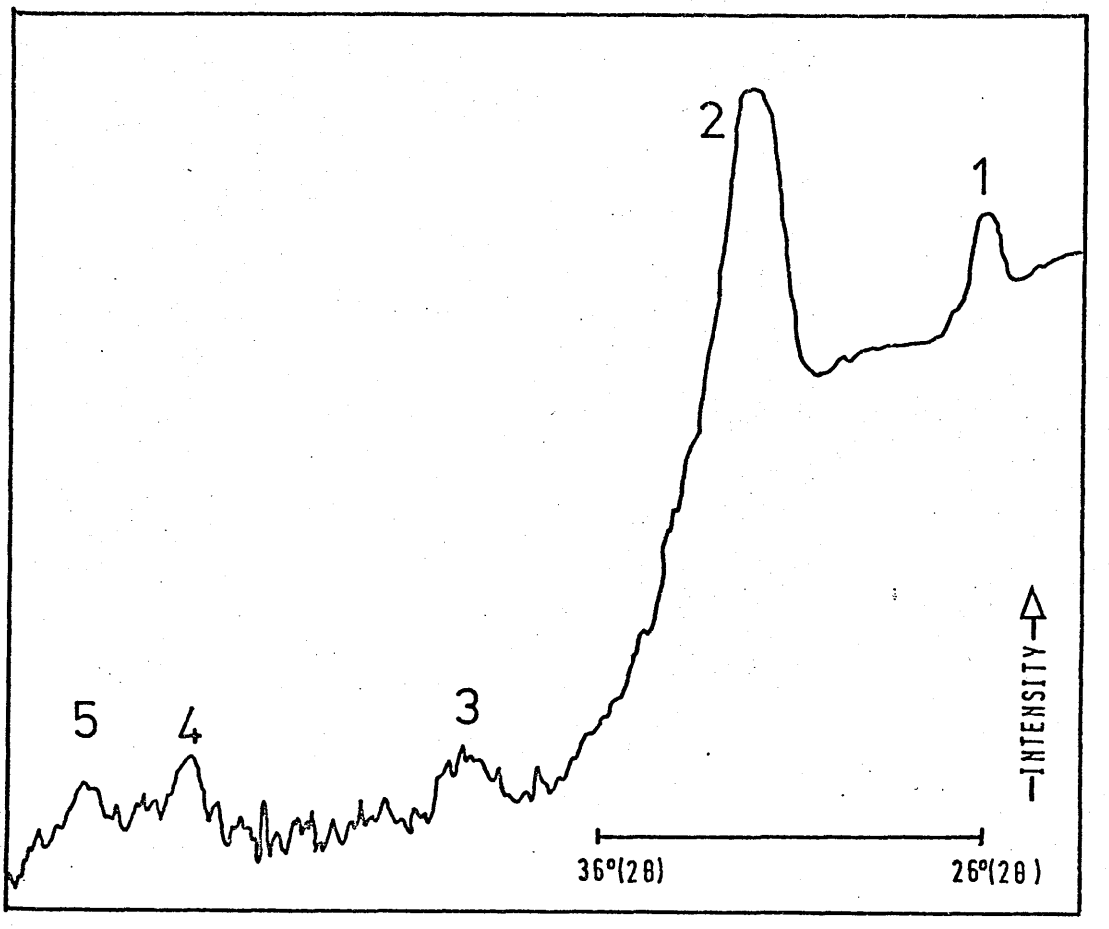

TRACE.. 3.4

SPECIMEN S1D. GLUTARALDEHYDE.

PEAK	d-SPACING. nm.	MILLER INDICES.	INTENSITY.
1	0.3440±0.0010	002	Good.
2	0.2801±0.0010	121/112	V.Good.
3	0.2279±0.0010	130	Poor.
4	0.1949±0.0010	222	V.Poor.
5	0.1845±0.0010	123	V.Poor.

TABLE 3.4

SPECIMEN SIE. UNTREATED.

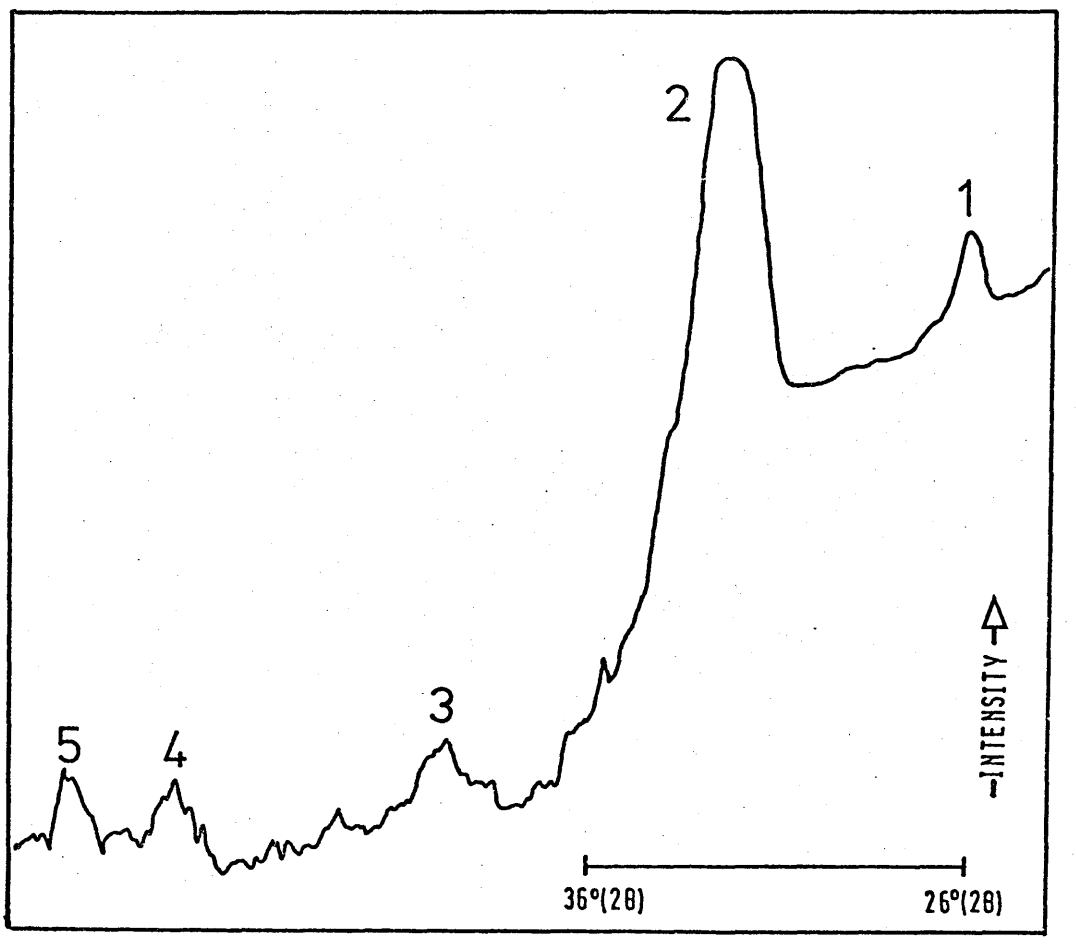

TRACE. 3.5

SPECIMEN SIE. UNTREATED.

PEAK	d-SPACING. nm.	MILLER INDICES.	INTENSITY.
1	0.3438±0.0010	002	Good.
2	0.2795±0.0010	121/112	V.Good.
3	0.2273±0.0010	130	Poor.
4	0.1943±0.0010	222	V.Poor.
5	0.1842±0.0010	123	V.Poor..

TABLE 3.5

3.1.9. Comparison of Results

To compare the measured d-spacings for each sample, the following method was adopted. The errors indicated in the various values of d , were estimated from the precision of measurement on the film. The mean value of each d-spacing and its limits were considered as three readings, so that a mean and standard deviation could be calculated. Then a comparison was made between the same peaks of each of the five samples, by using the t-test. Table 3.6 shows results of the test using only the maximum and minimum measured values for each set of d-spacings.

Comparison of d-spacings

Peak	Minimum Mean Value of d.(nm)	Standard Deviation (nm)	Maximum Mean Value of d.(nm)	Standard Deviation (nm)	T-statistic
002	0.3421	0.001	0.3440	0.001	2.45
121/112	0.2795	0.001	0.2801	0.001	0.73
130	0.2265	0.001	0.2279	0.001	1.71
113/203	0.2030	0.001	0.2032	0.001	0.24
222	0.1939	0.001	0.1951	0.001	1.47
123	0.1835	0.001	0.1845	0.001	1.22

Table 3.6.

For this test, the tabulated value of t at the 5% level of significance = 2.78. Therefore, since none of the calculated t values are greater than 2.78, there is no significant difference between the respective d-spacings as measured for each sample. Since this test has been made between the maximum and minimum of each set of values the same result applies to the intermediate values of d.

3.1.10. Conclusions

No significant differences were found, at the 5% level, between the diffraction patterns of the fixed and unfixed samples. Since the measured d-spacings for each sample showed no significant difference, this indicated that the lattice parameters were unaltered by the different preparation techniques. Lines were not detected in the diffraction pattern, other than those arising from the assumed model, which indicated that the various preparations did not permanently introduce new material into the bone matrix.

The (002) reflection was identified as a sharp and well isolated line, and this property is used in the following dark field and orientation work. One possible interpretation of these results is that changes have been made to the bone mineral, but have not been detected. Consequently, throughout the rest of this work where new techniques are introduced and developed, samples are prepared differently and accessed by these techniques for preparation artefacts.

3.2. Ultrathin Sectioning

3.2.1. Introduction

Before any specimen can be examined by transmission electron microscopy, it has to be reduced to a thickness of the order of 10 nm - 100 nm. If the specimen is too thick, the electron beam will not be transmitted sufficiently to produce an image, if it is too thin, the specimen will break up under the pressure of the electron beam. The most widely used method of producing ultrathin sections of biological material is ultramicrotomy. Before the sample can be sectioned it has to be supported in a rigid medium so that there is a minimal amount of deformation during the sectioning. The process of infiltration with a supporting medium such as Araldite is known as embedding.

3.2.2. Embedding and Sectioning

In the preparation of soft biological materials it is normal practice to embed the sample by the following procedure:-

1) Dehydration : by using ascending grades of ethanol in water.

2) Infilteration with propylene oxide : which, being a solvent for both Araldite* and ethanol acts as a link reagent.

* Araldite resin type CY212, hardener type HY964.

3) Gradual replacement of propylene oxide with Araldite.

4) Curing the Araldite in an oven at 60°C.

Initially, this process was used to prepare the bone samples, however, it was found unnecessary to infiltrate the specimen since the bone matrix was sufficiently rigid to withstand the sectioning process. Good sections were obtained from unembedded bone simply cemented into an araldite block for support in the ultratome jig, the arrangement of which is shown diagramatically in figure 3.3. The main arm of the ultratome moves up and down in a cutting action while the specimen is advanced towards the knife edge. Mechanical advances serve to adjust the instrument but the final advance onto the knife is made by thermal expansion of the arm, which is controlled by an electrical heater. The rate of advance can be adjusted to just a few nonometers between cutting strokes.

For most biological materials knives made from glass are adequate. However, because bone is hard, it blunts the edge of a glass knife after only a few strokes, and so a diamond cutting edge has to be used. Glass knives are used to trim the face of the bone sample so that only a small block, approximately one tenth of a millimeter square, is presented to the diamond knife, see figure 3.4. A diamond knife and glass knife are shown for comparison in figure 3.5. Behind the knife edge is a small trough which is filled with a liquid, so that as the sections are cut they float in a serial fashion onto the liquid. Once sufficient sections are floating in the trough they are picked up, together with a drop of liquid by placing a copper grid, held in a pair of fine tweezers, on top of them. The liquid is removed by inverting the grid onto a filter paper, and the sections are left firmly adhered to the grid. Various sizes of grid mesh are available, and it was found that a grid of mesh size 400 provided adequate support to the bone sections.

The Ultramicrotome.

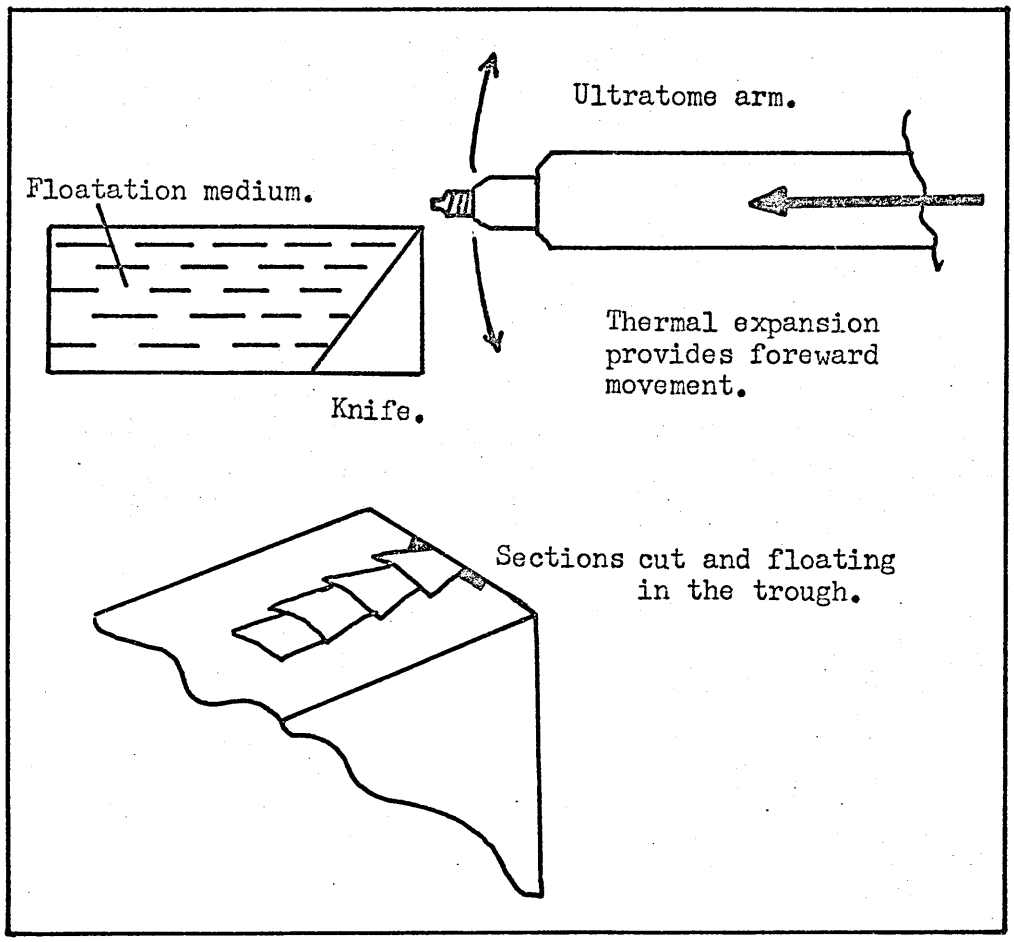

Figure 3.3

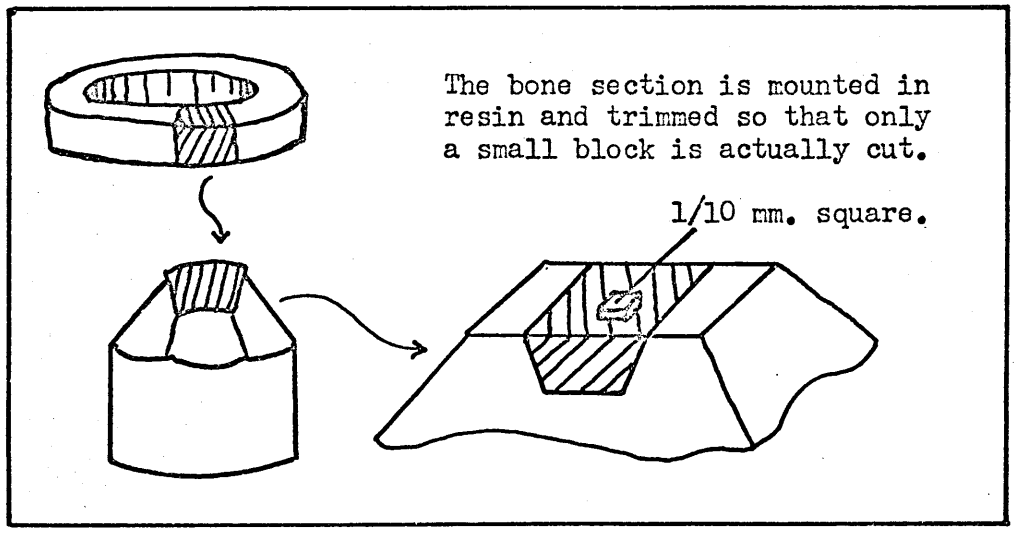

Figure 3.4

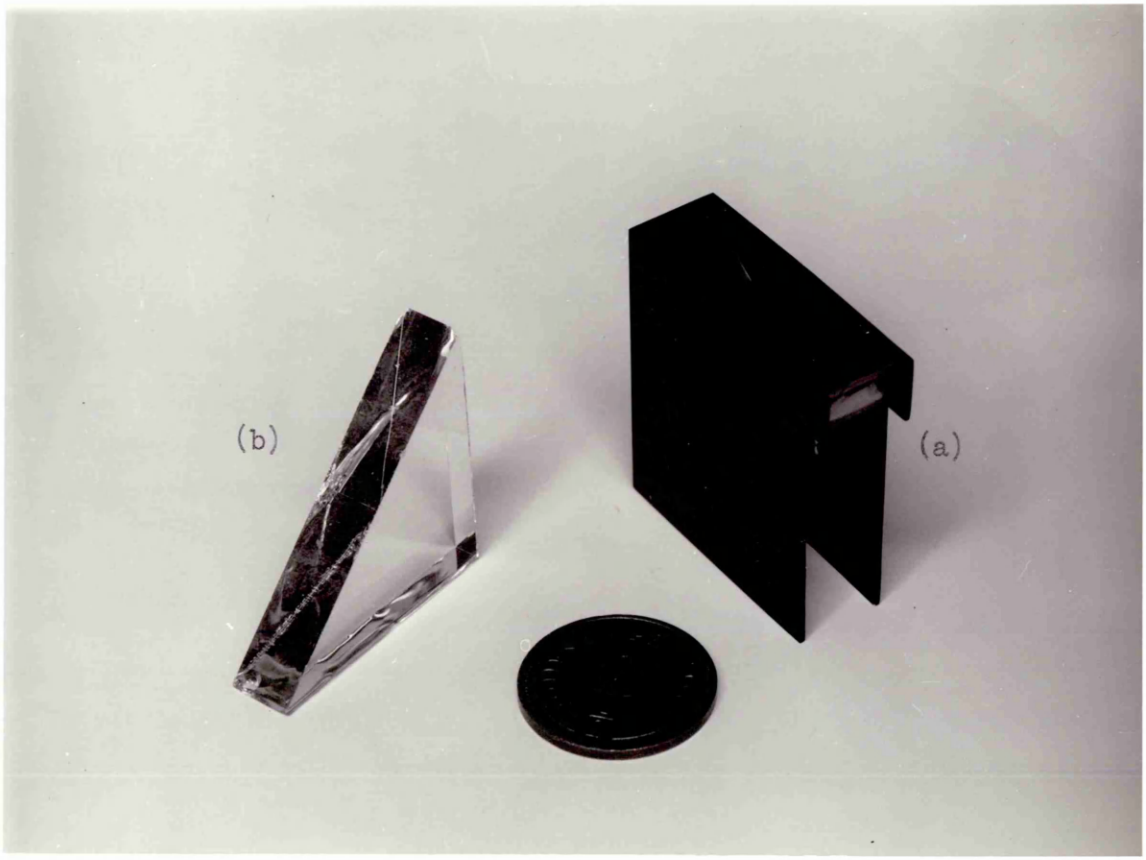

Figure 3.5
Diamond Knife (a), and Glass Knife (b).

The floatation medium used for this work has been distilled water, as it was found that buffered media contaminated the specimen with salt crystals, and since washing is necessary to remove them, distilled water was used in preference.

In order to test whether a short exposure to distilled water affected the bone sections, some bone was prepared anhydrously by fixing in ethanol, and the sections removed from the knife edge in a drop of ethanol. The appearance of these sections was the same as those prepared by floatation on distilled water, and so distilled water was used throughout this work as the floatation medium.

It was found by practice that the best thin sections of bone were obtained when cutting in a plane perpendicular to the radial direction of the femur, with a cutting speed of 5cm/sec., and a feed rate of 60nm - 80 nm per cutting stroke. Although sections were obtained by cutting in the two other mutually perpendicular directions, the best sections were always obtained by cutting in this plane. This finding was partly expected, since the plane, perpendicular to the radial direction is coincident with the laminar arrangement of primary type bone, and all rabbit femora examined had a primary type structure, see figure 3.6.

Once the entire preparation procedure had been developed, the total time from the removal of a bone sample, to the examination in the microscope was as little as 3-4 hours for unfixed samples.

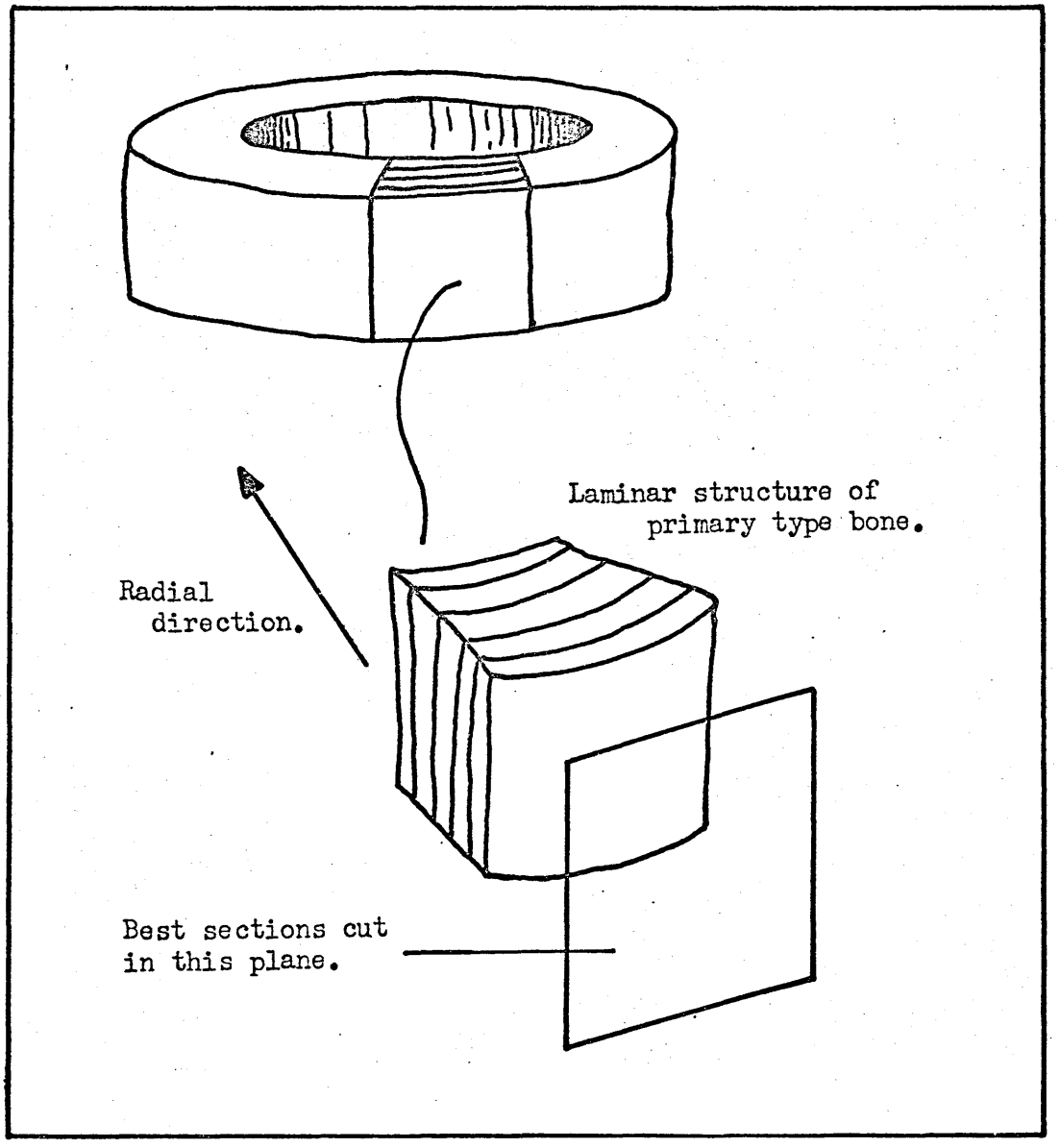
Laminar structure of
primary type bone.
Radial
direction.
Best sections cut
in this plane.

Figure 3.6

CHAPTER FOUR

BRIGHT FIELD ELECTRON MICROSCOPY

4.1. Microscope Calibration

In order to interpret bright field images it is important to calibrate the microscope for (a) magnification, (b) diffraction pattern rotation, and it is worth considering these before discussing any of the following micrographs.

a) Calibration of magnification

Initially a magnification calibration chart was constructed for the JEM.100b electron microscope by examining polystyrene latex particles at different magnifications. These particles have a uniform size and so are commonly used as a magnification standard. In the later part of this work, because of service alterations to the microscope it was necessary to re-calibrate the magnification, and beef catalase was used. Beef catalase is a substance which crystalises in a two dimensional regular array, showing a strong repeat interval of 8.75nm, see figure 4.1. This standard is mounted on a copper grid so that it can be used each time measurements are taken, thus allowing for short term fluctuations in the microscope which could affect the magnification.

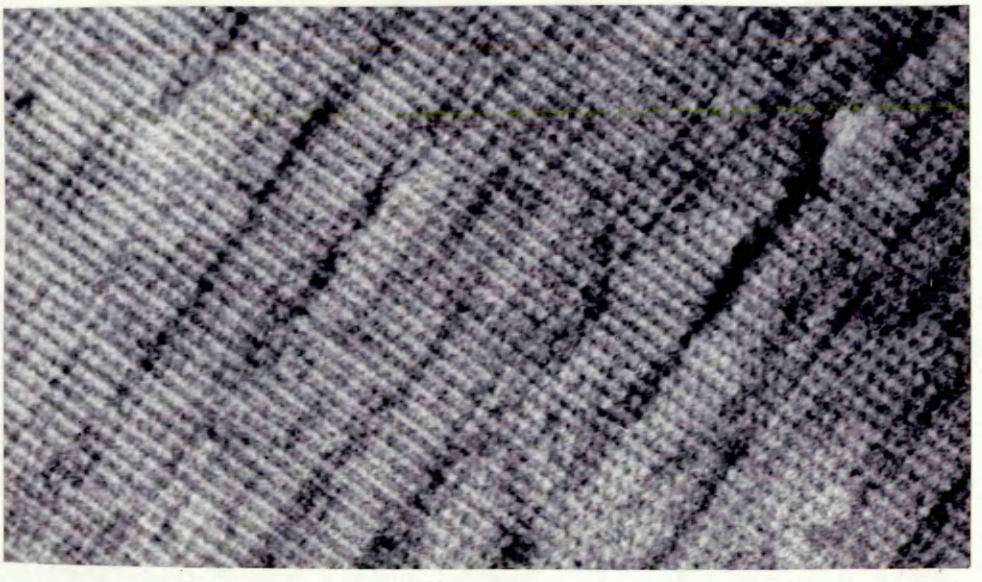

Beef catalase

100 nm.

Figure 4.1

b) Calibration of Diffraction Pattern Rotation

This type of calibration is important to enable the orientation of crystalline objects to be determined. The image in the microscope is rotated with respect to the object by the action of the lenses. The lens configuration is different in the diffraction mode to the image mode, and thus the diffraction pattern and image are rotated by different amounts, and this difference varies with magnification. An accurate way to measure this rotation uses a crystal such as molybdenum trioxide. When viewed in the electron microscope, these crystals are seen with long straight edges, which are perpendicular to the (100) direction in the crystal. A superimposed diffraction pattern and image allow a direct measurement of the difference in rotation so that diffraction patterns and images of the same object can be accurately aligned.

4.2. Examination of Bone Samples

4.2.1. Bright Field Imaging

The following series of micrographs have been selected as showing features typical of those found by using the bright field imaging mode.

All samples of bone have been taken from the mid-femoral section of female dutch rabbits, aged approximately six months. The samples have been fixed by different techniques for the detection of possible artefacts due to preparation. Sections were cut as described in 3.5. Details of the sample preparation and notes on the appearance of the sample in the microscope are given on the page immediately following the micrograph.

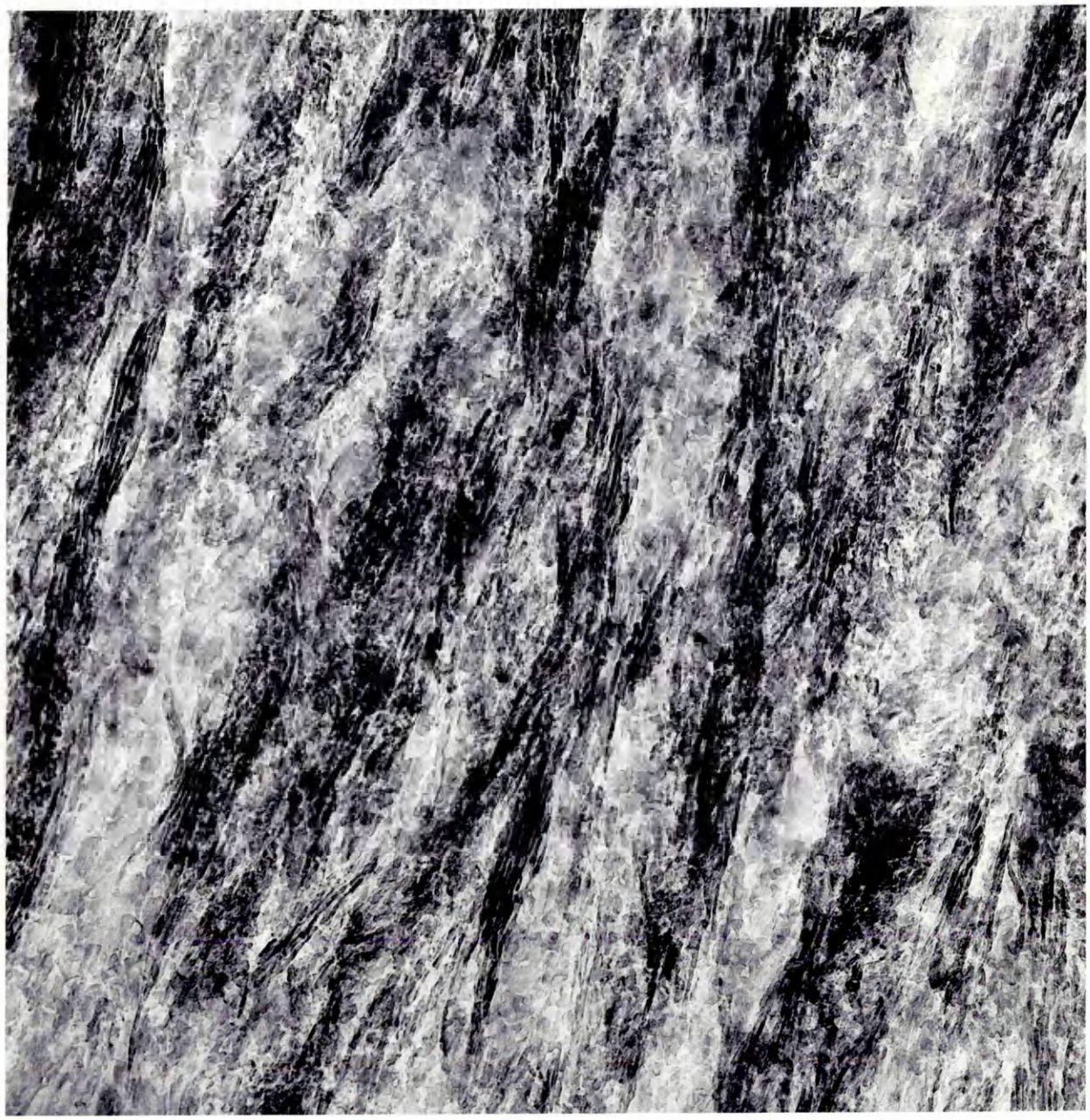

100nm.

Figure 4.2

Fig. 4.2

Sample No. S5D

Preparation:

Fixed in 5% Glutaraldehyde with bicarbonate buffer for five hours at $4^{o}C$.

Washed in physiological medium TC.199 with bicarbonate buffer at pH 7.2.

Post fixed in osmium tetroxide with veronal acetate buffer.

Dehydrated in ascending grades of ethanol in water, and embedded in araldite using propylene oxide as a link reagent.

Sectioned in a radial direction as described in 3.5.

Notes on appearance:

Both long thin dark objects and less dense irregular plate-like objects can be seen in the same section. This means that either the rod-like objects are actually the plate-like objects viewed on edge, or that two types of structure are present.

Collagen cannot be seen in this section since unstained collagen is electron transparent.

There is a wide variation in the size and shape of the objects in the micrograph which are in fact, the bone mineral crystals. Because of the dense nature of fully calcified bone, single crystals are difficult to isolate as their outlines tend to merge and overlap. This dense nature is one of the reasons why work in the past

has tended to have been carried out on less calcified systems, such as embryonic bone and calcified tendon. Whether results from these materials are directly comparable with fully calcified and mature bone, is open to question. However, since diamond knives have become available, it has been possible to obtain good thin sections of fully calcified bone.

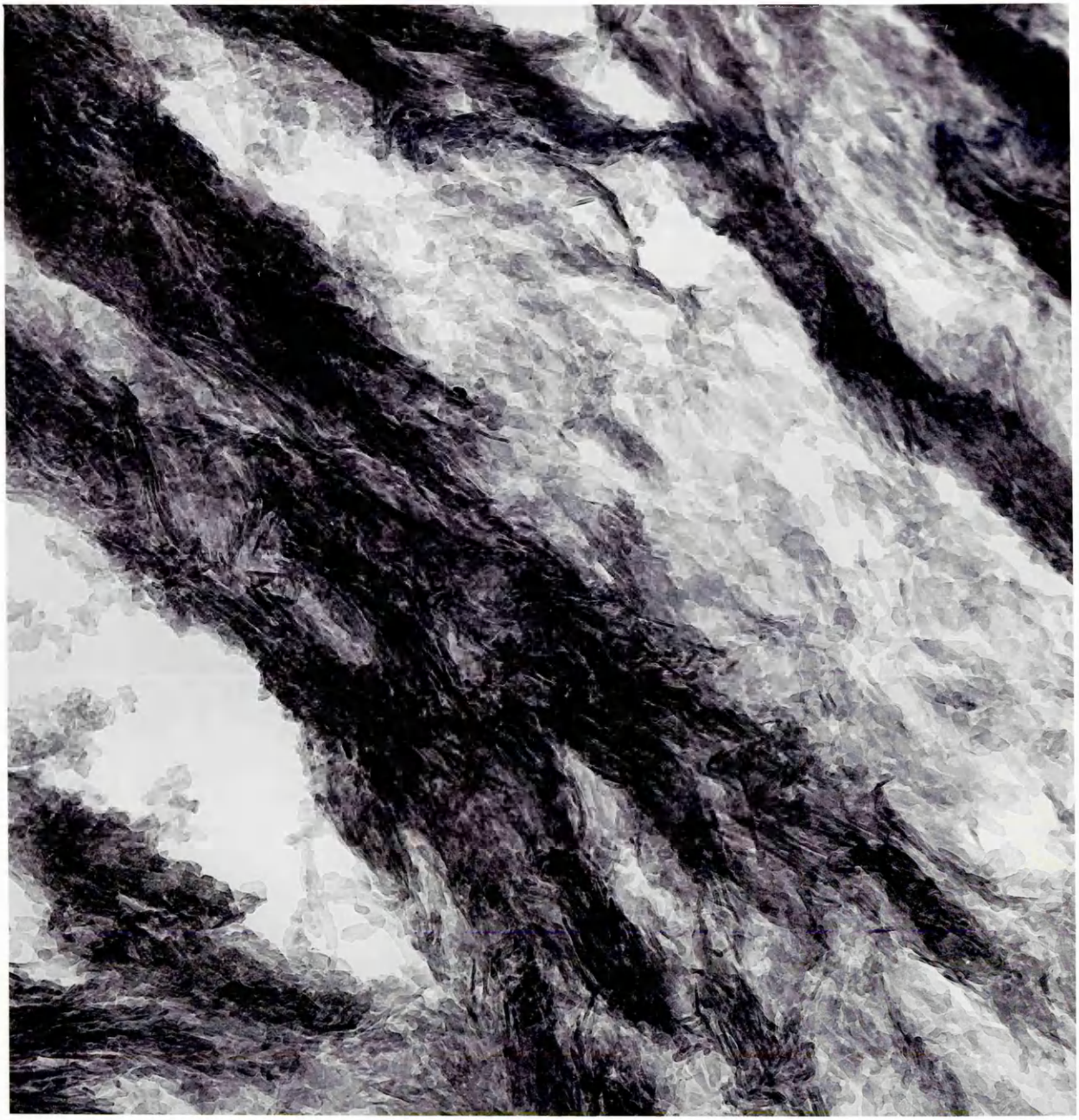

100nm.

Figure 4.3

fig. 4·3

Sample No. S5B2

Preparation:

Fixed in glutaraldehyde with bicarbonate buffer to pH 7.2, for five hours at 4°C. Dehydrated in ascending grades of ethanol in water, then embedded in araldite using propylene oxide as a link reagent.

Sectioned in a radial direction as described in 3.5.

Notes on appearance:

This section has cut unevenly and the dark areas are parts of the section which have buckled.

Basically the appearance of this micrograph is the same as figure 4.2.

Irregular plate-like forms can be seen in the thinner regions and what could be rod-like forms can be seen in the thicker parts of the section.

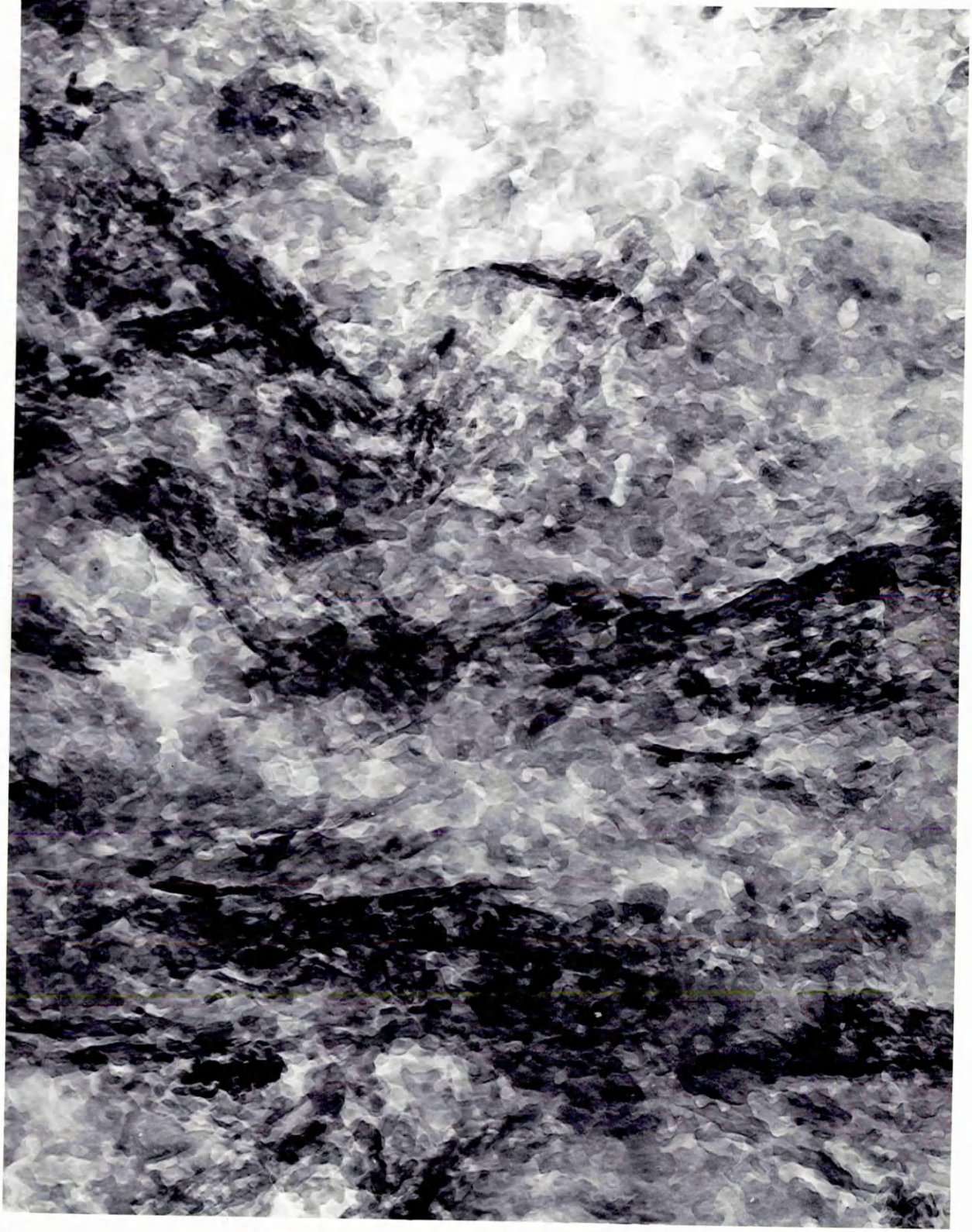

100nm.

Figure 4.4

fig. 4·4

Sample No: S3B3

Preparation:

This sample was unfixed and allowed to dry in air for twenty-four hours before being sectioned in a radial direction as described in 3.5.

Notes on appearance:

This micrograph shows an area of bone where the crystals appear predominantly as irregular plate-like forms. Once again, because of the dense nature of this material, individual crystals are difficult to isolate since their outlines tend to merge and overlap.

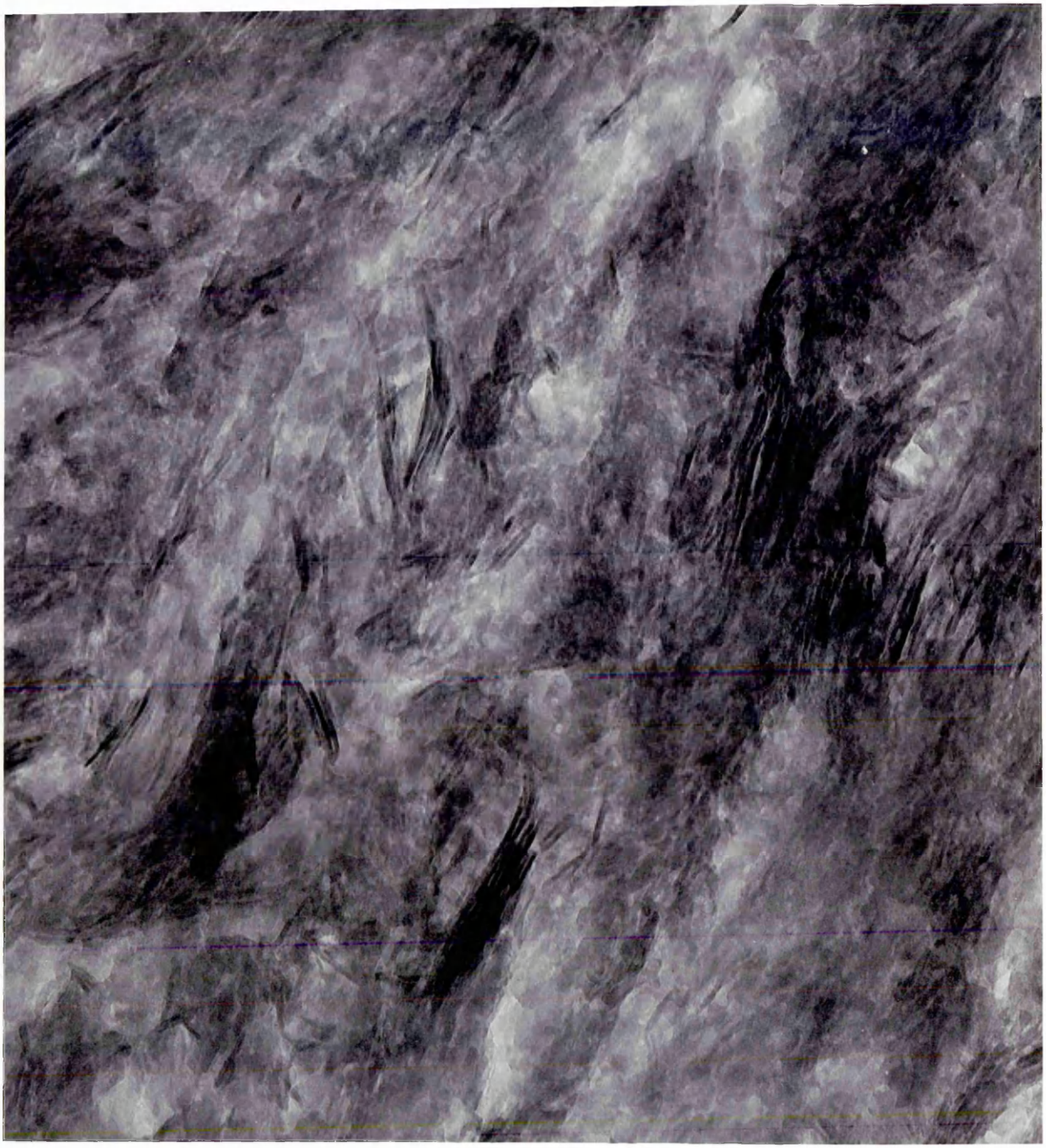

100nm.

Figure 4.5

fig. 45

Sample No. S5B4

Preparation:

Same as figure 4.3.

Sections cut in a longitudinal direction as described in 3.5.

Notes on appearance:

This micrograph shows features which could indicate the presence of octacalcium-phosphate, as described by D. Steve-Bocciarelli (1969). These 'double lined' structures could also be interpreted as two thin plate-like crystals viewed on edge. Other features of this micrograph are basically the same as the previous examples. showing densely packed irregular shaped cyrstals.

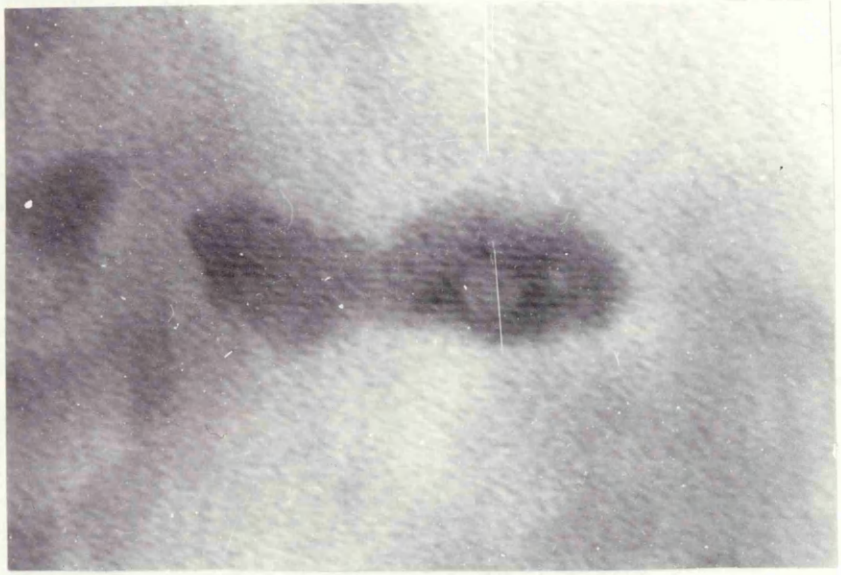

10 nm.

Figure 4.6

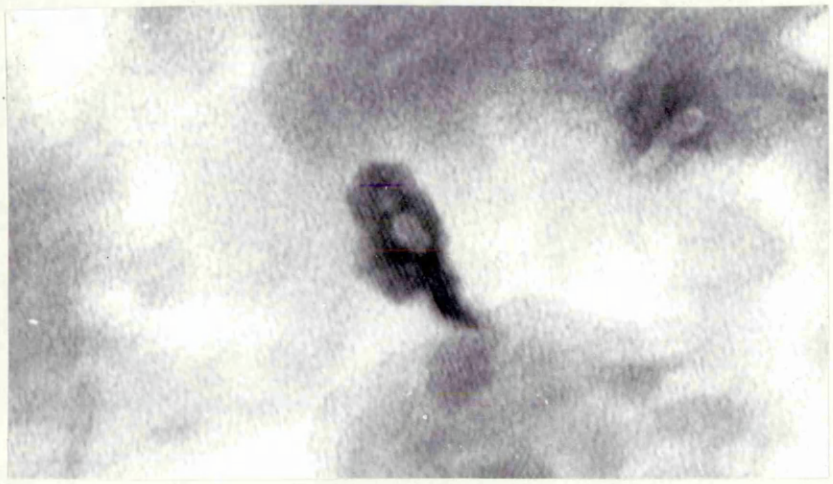

10 nm.

Figure 4.7

fig. 4·6 & 4·7

Sample No: S5C3

Preparation:

Fixed in ethanol for six days at room temperature. Embedded in araldite using propylene oxide as a link reagent.

Sectioned in a transverse direction as described in 3.5.

Notes in appearance:

These two micrographs, taken at high magnification, show two crystals which appear isolated from the background and the crystals themselves show a regular array of lines. These crystals have irregular outlines although part of figure 4.7 shows an angular feature, and apparent areas of lower density within the body of the crystals could indicate some kind of imperfection in structure. The crystals appear darker than others which are in the background because of the diffraction contrast effect. The general spotty appearance is due to the carbon film which is used in this case to support the specimen on the grid.

The lines within the crystal are caused by an interference effect. When a diffracted beam from a certain set of planes in the crystal manages to pass through the objective aperture, it recombines with the undeviated beam at the image to produce an interference pattern. The spacing of lines in this pattern is the same as the actual lattice planes from which the diffracted beam originated and this effect is known as lattice plane resolution. It is possible to determine which lattice planes are being imaged by measurement of the spacing,

provided the magnification is known accurately. Additional information can also be gained by imaging the objective aperture with the diffraction pattern to see which diffracted beams can pass through. Figure 4.8 shows a microdensitometer trace of the electron diffraction pattern, on which is marked the positions of the objective aperture and the (100) diffracted beams, which are actually combined in the large undeviated beam. The (100) planes in bone mineral have the largest d-spacing of the crystal and hence the lowest diffraction angle. No other diffracted beam can pass through the 20 μm aperture and this suggests that the imaged planes are actually the (100) planes, which have a spacing of 0.8169nm. One possible configuration of the crystal and (100) planes is shown in figure 4.9.

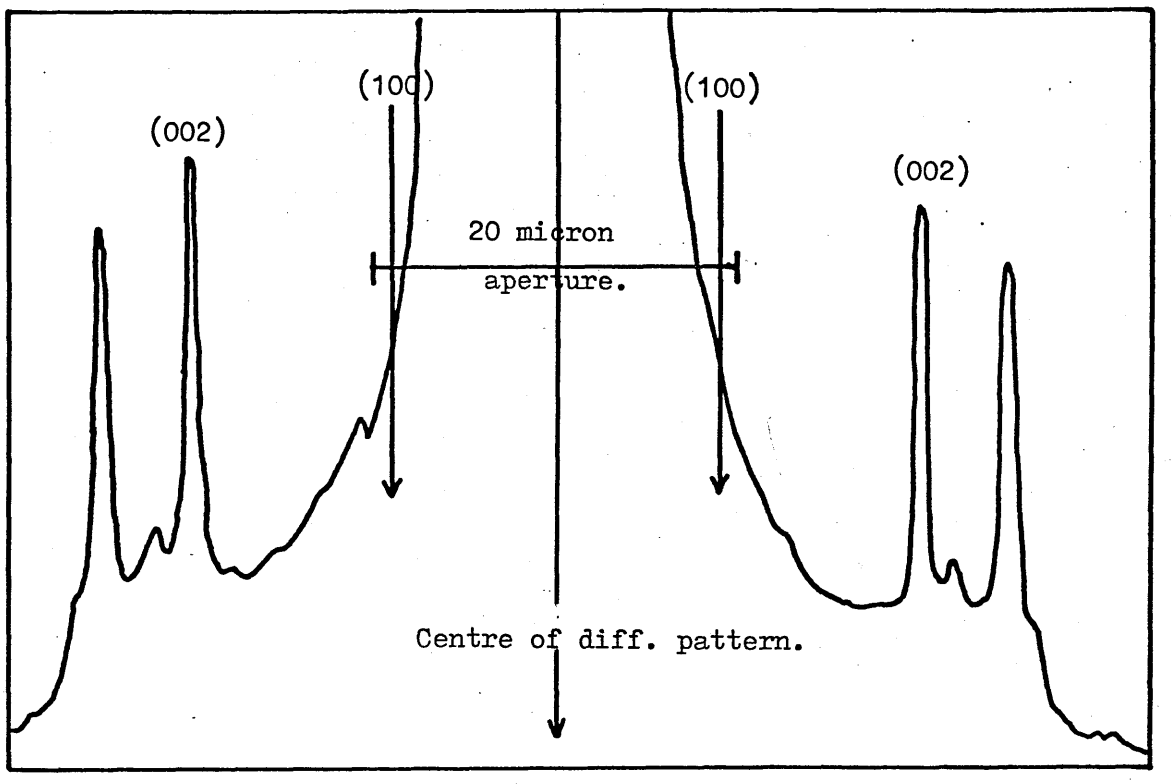

Figure 4.8

A microdensitometer trace across the diameter of the electron diffraction pattern of a radial section of rabbit femur.
The (100) reflection has a d-spacing of 0.8169 nm. and is able to pass through the 20 micron objective aperture in bright field conditions, as indicated above.
Shown below is a possible configuration of the (100) planes within the bone mineral crystal.

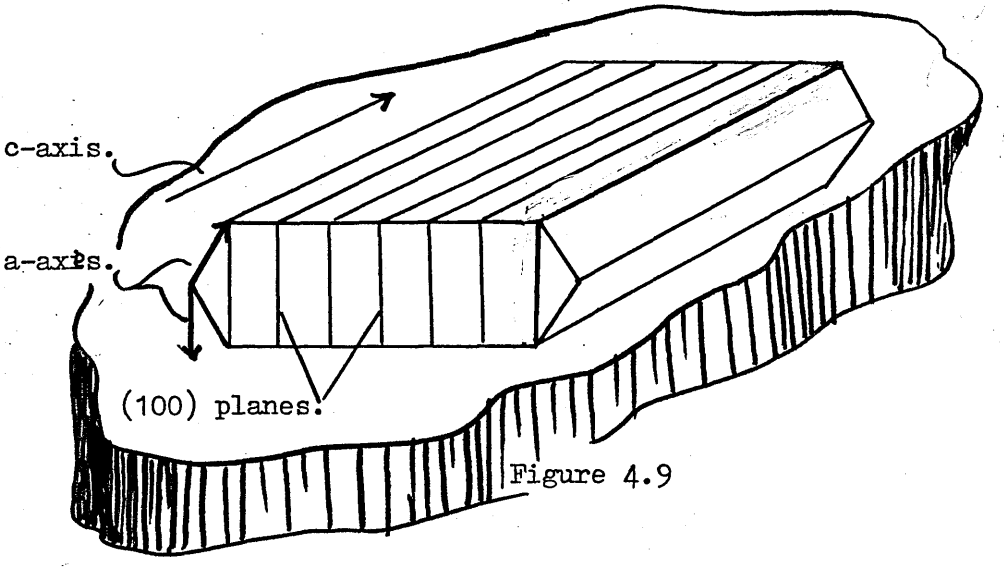

Figure 4.9

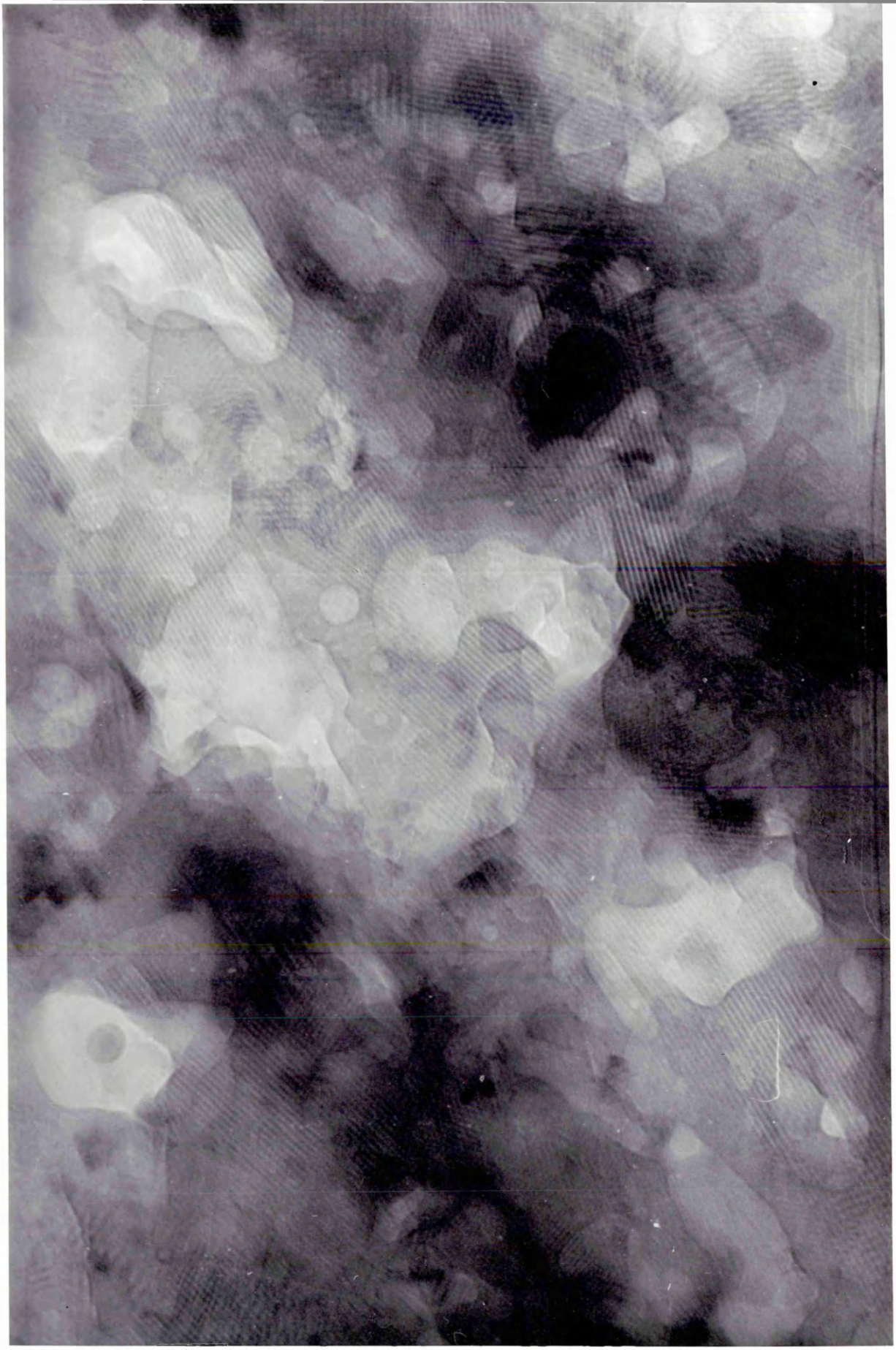

10nm.

Figure 4.10

fig. 4·10

Sample No: S5D

Preparation:

Same as 4.2.

Notes on appearance:

In this micrograph, which was taken at the maximum magnification of the microscope, the majority of the fringe patterns are due to (100) lattice plane resolution. A few of the fringes are due to effects between overlapping crystals and are dealt with in the next chapter. The lattice lines can be followed easily over distances of a few tens of namometers, indicating that crystals of this size are in fact single crystals and not composed of aggregations of smaller units. The crystals themselves are almost impossible to isolate since their outlines overlap and are difficult to follow, thus making any form of size measurement extremely difficult.

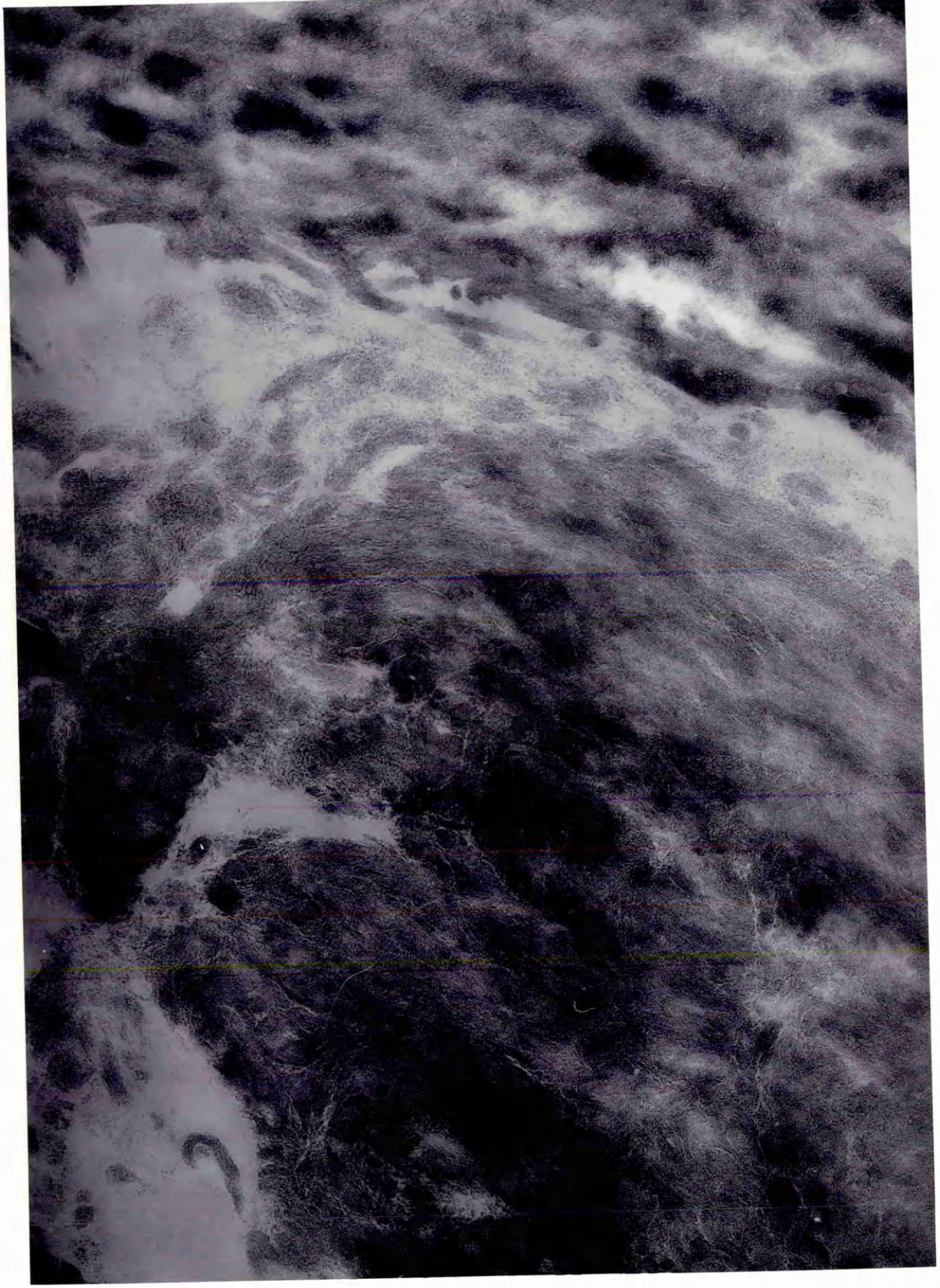

1μm.

Figure 4.11

Fig. 4.11

Sample No: S5D

Preparation:

Same as 4.2.

Notes on appearance:

This micrograph shows an area of bone matrix immediately surrounding a bone cell. The mineral deposits surrounding the cell do not have the usual crystalline appearance and do not produce a crystalline diffraction pattern. The amorphous nature gradually changes and within 3 -4 μm from the cell border crystalline structures begin to appear in the matrix.

4.2.2. Electron Diffraction

X-ray work has shown quite conclusively that the crystal c-axes of bone mineral are aligned in the direction of the collagen fibres. This feature can be observed in micrographs taken at low magnifications (100Kx). Figure 4.12 shows a micrograph of unfixed, unembedded bone in which the crystals are elongated and aligned in one general direction. The collagen banding can also be seen to lie in this general direction. Figure 4.13 is an electron diffraction pattern of the area shown in figure 4.12, and the (002) arcs show how the crystal c-axes are distributed about the collagen fibre axis.

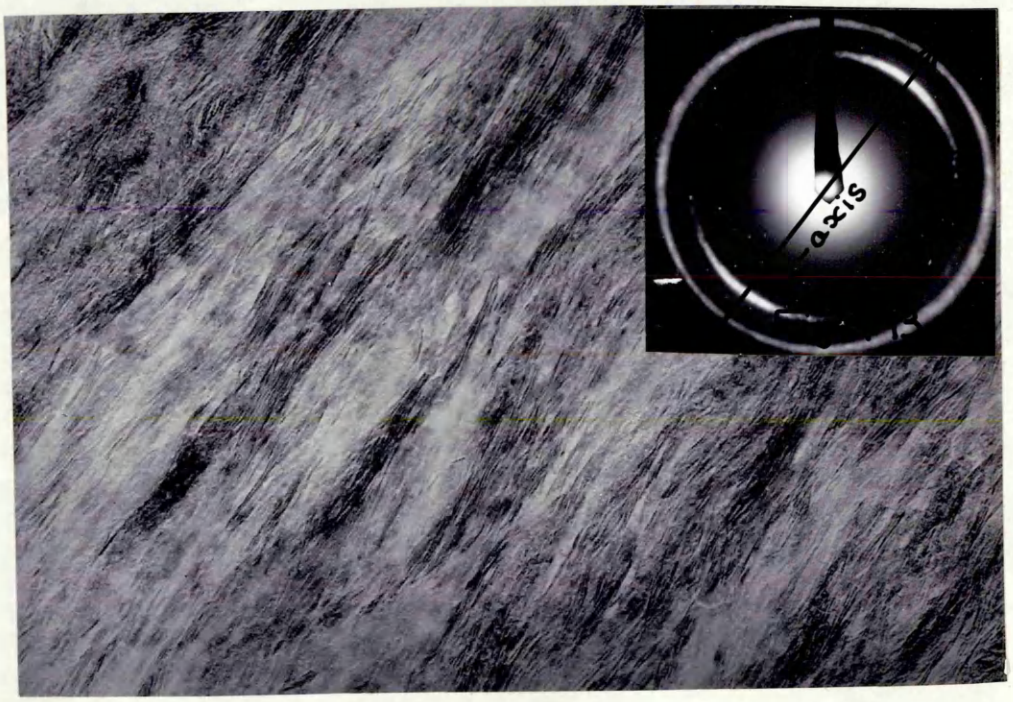

100 nm.

Figure 4.12

It was mentioned in Section 3.3.3. that the best sections were always obtained when cutting in a radial plane. Initially sections were cut in three mutually perpendicular directions, as shown below.

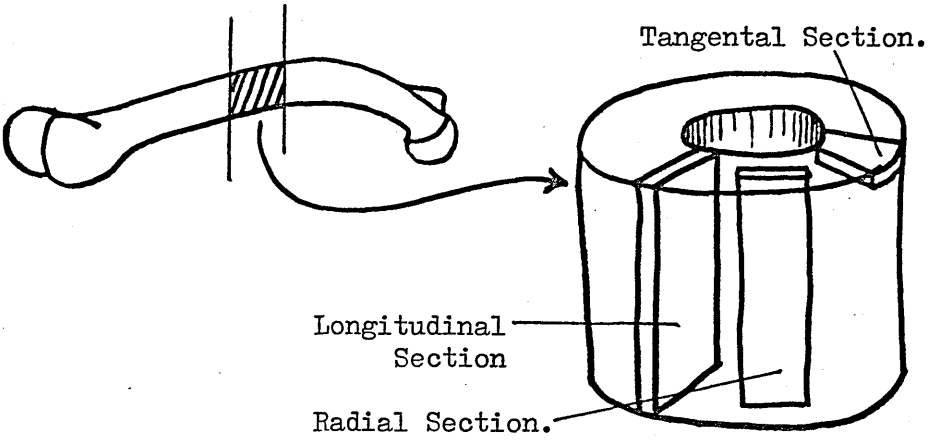

Figure 4.14

The electron diffraction patterns of these three types of section show one important feature, namely the absence of an (002) diffraction peak in the transversely cut sections, see figure 4.15. This means that the crystal c-axes and hence the collagen fibres, are aligned, in general along the long axis of the femur.

Electron Diffraction Patterns of Rabbit Bone Sections.

The sections have been cut mutually perpendicular to each other.
Note the absence of an (002) diffracted beam in the tangental section.

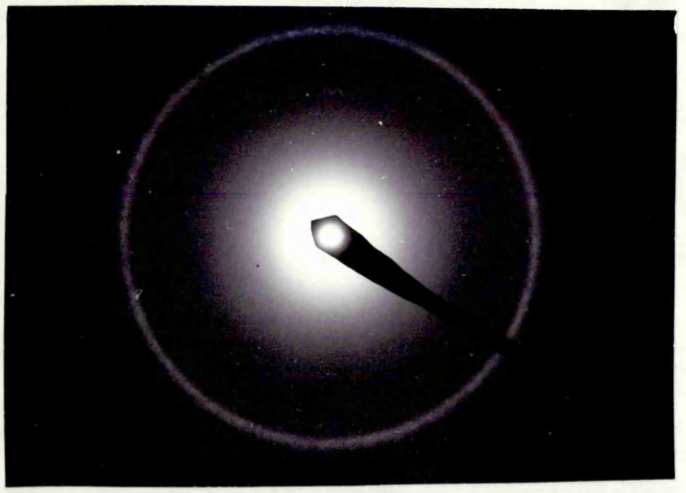

Tangental Section.

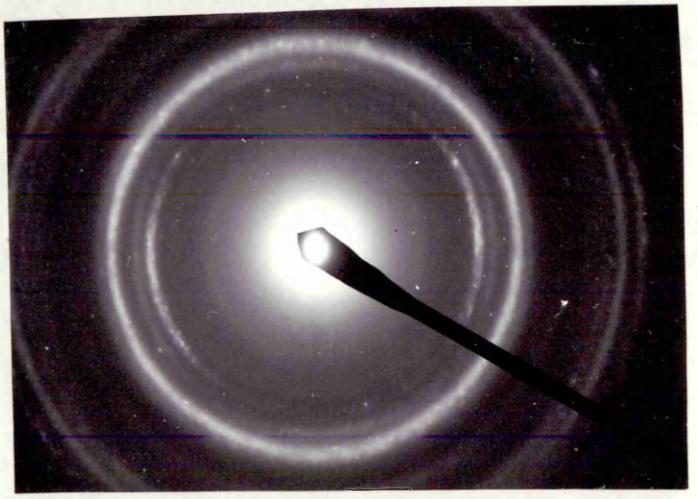

Radial Section.

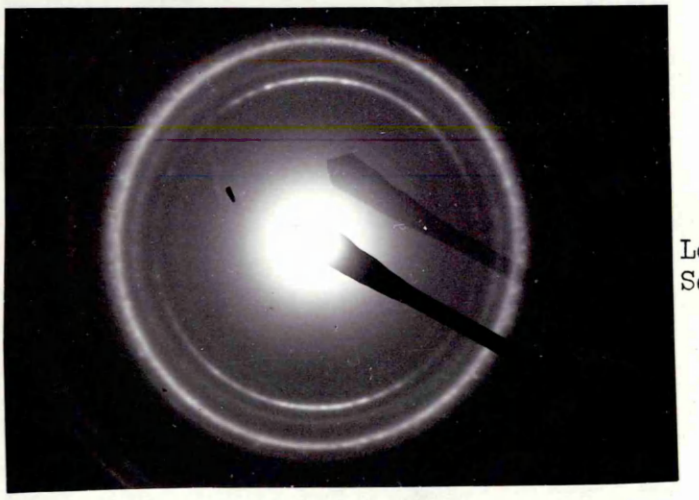

Longitudinal Section.

Figure 4.15

4.2.3. Conclusions

From the selection of micrographs presented here, typical of many others which have been examined throughout this work, the following conclusions can be drawn.

a) No features have been found which could indicate damage to the specimen caused by any of the preparation techniques used.

b) Both crystalline and amorphous bone mineral have been visualised. The bone matrix itself consisting mainly of collagen and crystalline mineral, and the amorphous form being associated with bone cells.

c) Figure 4.4. shows crystals whose edges parallel to the long axis appear more electron dense than the central region. This feature has been noted by D. Steve-Bocciarelli (1969), although its exact nature has still to be determined.

d) Both rod-like and plate-like images have been seen in many micrographs, although as mentioned in Section 1.7.10, the long dark objects have been shown, by tilting the specimen, to be edge views of the plate-like objects. Thus it would appear that bone mineral has a plate-like form.

e) High magnification micrographs have shown images of many overlapping crystals with irregular shapes and sizes. Variation of electron density within some of the crystals could indicate imperfections in the structure. The fact that lattice resolution lines can be followed over distances of some tens of nanometers means that crystals of this size are not composed of aggregations of smaller units.

f) It has been shown by selected area electron diffraction that the crystal c-axes are aligned, in general with the collagen fibre axis. This axial orientation tends to be longitudinal in the mid-femural section.

g) Probably the most important conclusion to be drawn from this evidence is that measurements of crystal dimensions from bright field images have little value. Because of the dense nature of bone, micrographs show images of many overlapping crystals, with widely varying shapes and sizes, thus making the isolation of individual crystals almost impossible. Even if this isolation could be achieved the orientation of the crystal axes are not known in any bright field micrograph, and so measurements have little relation to the crystal lattice.

However, these difficulties have been overcome by using the technique of dark field imaging, which has not been applied to this problem before and is described in the next chapter.

CHAPTER FIVE

DARK FIELD ELECTRON MICROSCOPY

5.1. Development of the Dark Field Technique

5.1.1. Introduction

One of the most important modes of operation of the modern electron microscope, when used with crystalline specimens, is dark field imaging. This technique, which has been briefly described in chapter two, uses diffracted, rather than transmitted, beams to form the final image. Hence, only structures which produce the required diffracted beams appear bright in the image, everything else appears dark. This condition is an ideal solution to the problems involved with the crystal size measurement of bone mineral. The dense nature of bone mineral means that many crystals are overlapping, but only a few are oriented to produce certain diffracted beams and only these few crystals will appear bright in the dark field image. Thus the problem of the isolation of individual crystals can be overcome. Furthermore, if the diffracted beam is chosen so that the crystal orientation is known, then accurate measurements, which are related to the crystal axes can be made.

5.1.2. Dark Field Imaging

Initial attempts at producing dark field images gave confusing results. The main beam in the microscope was tilted, so that only diffracted beams could pass through the objective aperture, as shown below in figure 5.1.

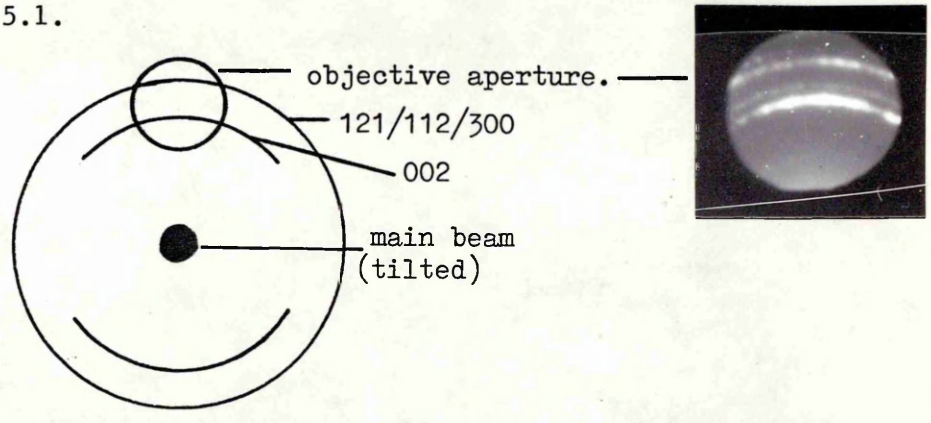

Figure 5.1

The diffracted beams which were used to form the image, were visualised by leaving the objective aperture in position and switching to diffraction mode. Initially, the smallest objective aperture, as supplied with the microscope was 20/^{um} in diameter and this allowed many diffracted beams through to form the image, with the following results.

Figures 5.2. and 5.3. show the corresponding bright field and dark field images respectively. The dark field image was formed using diffracted beams as shown in figure 5.1. The bright field image is typically confused, consisting of many overlapping crystals. The dark field image consists of many systems of fringes and bears little resemblence to its bright field counterpart.

These fringes have been reported by Braddock (1973) and Kauffman (1973). Braddock postulates that the fringes are images of crystals aligned on collagen fibres, but suggests that they could be some form of interference effect. Kauffman measured the fringe period and area dimensions, finding a typical period of 2-3nm, and an area of 7.0nm x 20.0nm. Kauffman ruled out lattice images as an explanation since the smallest observed fringe period was 1.5nm and the largest lattice spacing of bone mineral is 0.8169nm.

Periodic fringes can be produced in the electron microscope by various forms of crystal fault, such as dislocations and stacking faults. However, crystal faults do not produce fringes of such great area and variation in spacing as the observed fringes and are thus an unlikely explanation.

Thickness fringes are another form of periodic image which is observed in thin crystals, however these are unlikely to be observed fringes since thickness fringes

Corresponding Bright and Dark Field Images from an Area of Unfixed Rabbit Femur.

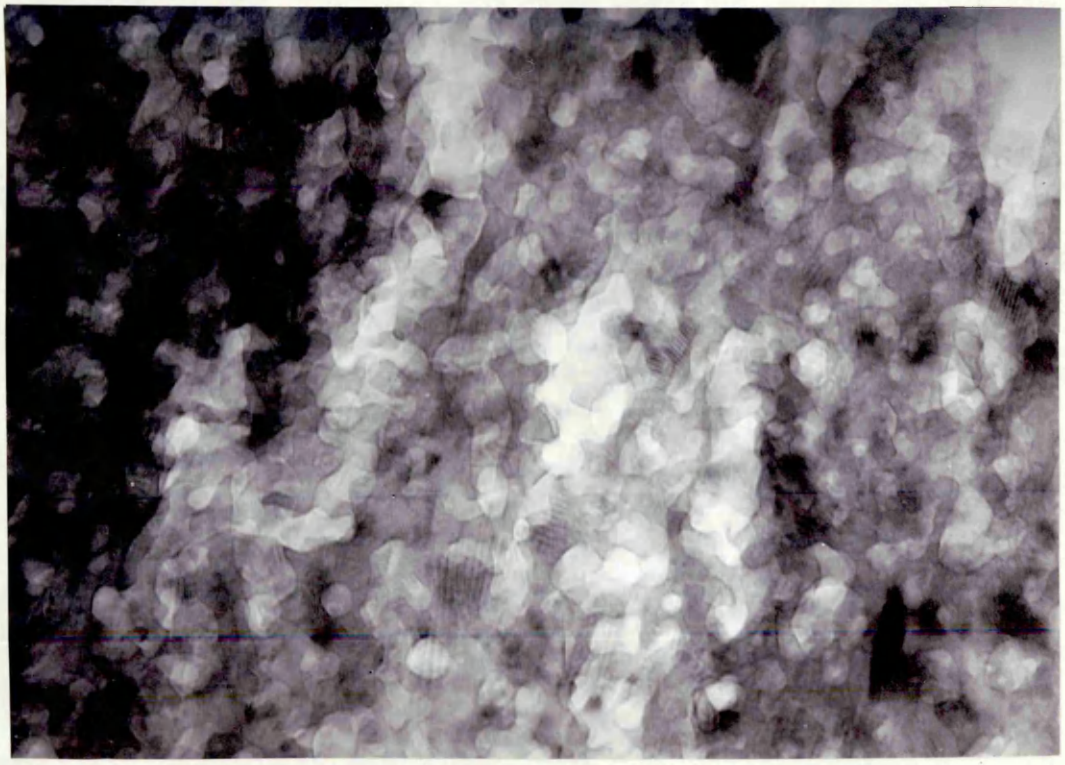

Figure 5.2 (Bright Field Image)

100nm.

Figure 5.3 (Dark Field Image)

100nm.

have only four or five peaks which decrease in intensity quite rapidly.

The most likely explanation for the observed fringes is that they are, in fact, Moiré fringes. Moiré fringes are formed when two crystals overlap and diffraction takes place in both crystals. The diffracted beams interfere at the image to produce the fringes, which in effect map out the region of crystal overlap.

Essentially, the fringes which are produced as a result of overlapping crystal planes are described by the following equations, which have been derived for optical Moiré patterns.

a) Fringe spacing (D) $= \dfrac{d1 \cdot d2}{|d1-d2|}$

For parallel overlapping planes of spacing d1 & d2.

b) Fringe spacing (D) $= \dfrac{d}{2 \text{ Sin } (\frac{1}{2}\alpha)}$

For overlapping planes with the same spacing and a small relative twist (α).

c) Fringe spacing (D) $= d1 \cdot d2 / \left[(d1-d2)^2 + d1 \cdot d2 \cdot \alpha^2\right]^{\frac{1}{2}}$

For overlapping planes with different spacing and small relative rotation.

One of the most useful properties of Moiré fringes is to produce a magnified image of crystal lattice imperfections. Figure 5.4. shows an optical analogue of the effect produced by a dislocation in one set of planes, on the formation of the Moiré pattern. The pattern shows a magnified image of the dislocation. Figure 5.5. shows a dislocation in bone mineral observed by this effect.

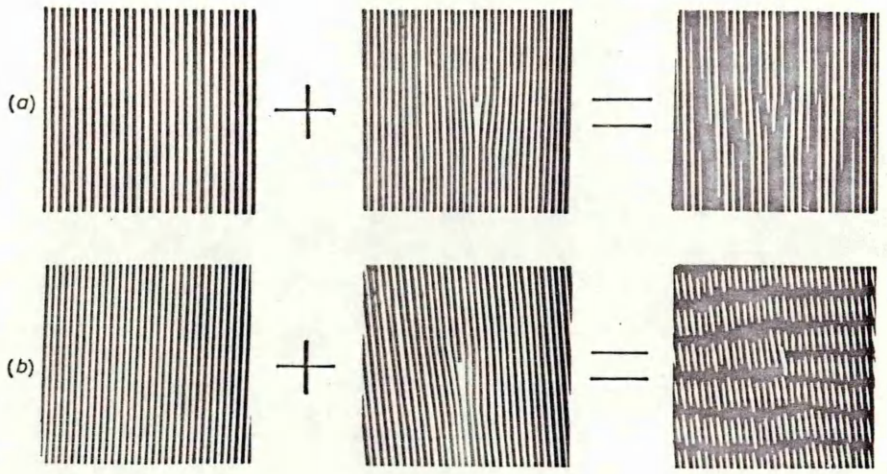

Figure 5.4

An optical analogue showing the effect of a dislocation in one grating on the formation of Moiré patterns,(a) parallel Moiré pattern, (b) rotation Moiré pattern.

⟵⟶10 nm.

Figure 5.5

A dislocation observed by a Moiré pattern in the dark field image of a section of unfixed rabbit femur.

5.1.3. Discussion

Dark field images, formed by using many diffracted beams have little value, for the following reasons:

a) Moiré fringes are formed which impair the isolation of individual crystals for measurement. These fringes do not give any information which can be used to determine the c-axial length of bone mineral crystals.

b) When many diffracted beams are used to form the image it is impossible to know which beam produces a certain image and thus, the crystal orientation cannot be determined.

It is, therefore, important to eliminate, as far as possible, the Moiré fringes and to use only one set of diffracted beams, i.e., from the same set of planes in different crystals, to form the dark field image.

5.1.4. Improved Dark Field Technique

A small objective aperture was specially obtained which contained 5, 10, 20 and 40 μm diameter holes. It was found in practice that the 10 μm aperture was sufficient to isolate the (002) diffracted beams and good dark field images were produced, with a drastic reduction in the number of Moiré fringes. The (002) beams were chosen because the (002) planes of bone mineral have a simple relationship to the c-axis, also these beams are strong and well isolated, a condition which is necessary for the formation of good dark field images. Figure 5.6 shows how the (002) beams produce dark field images of crystals whose c-axes all lie within the plane of the section and in a direction within that plane determined by the position of the objective aperture on the diffraction pattern.

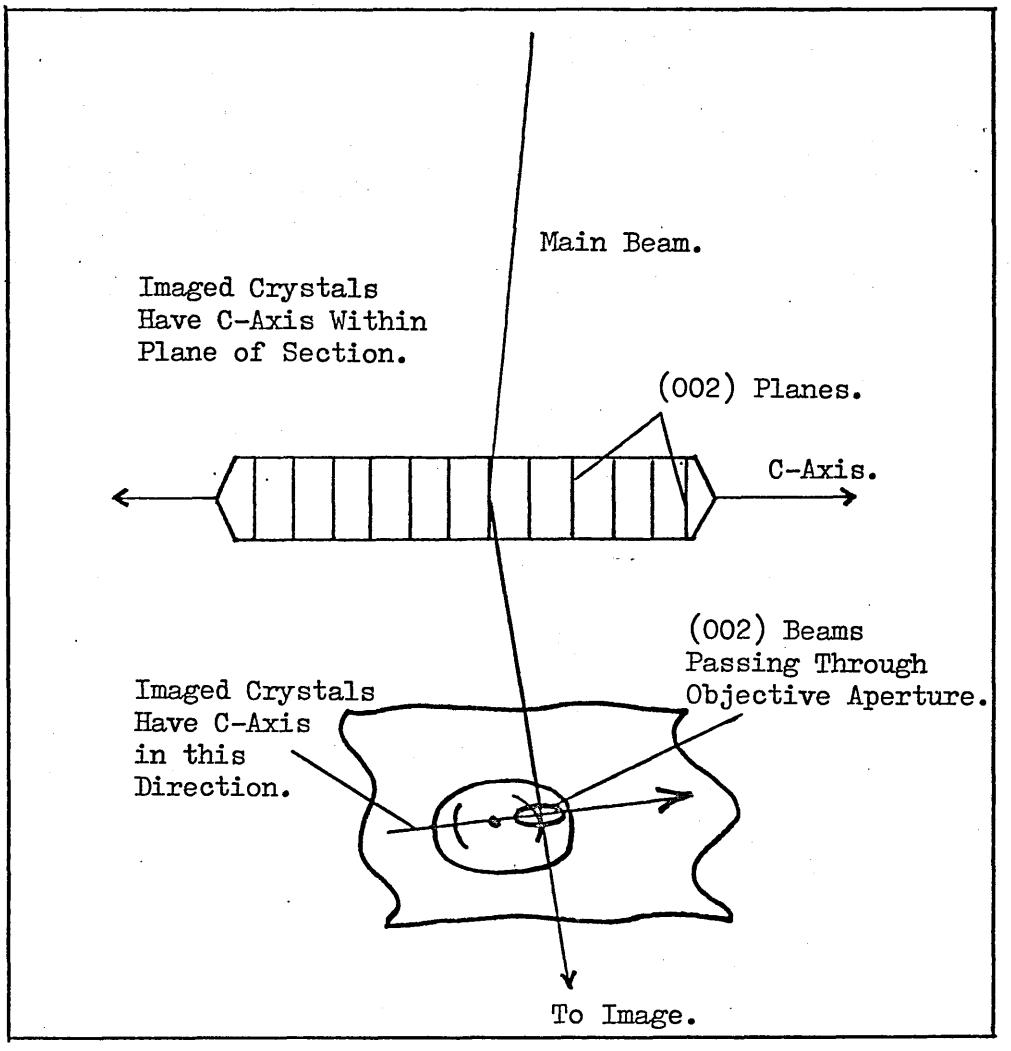

Figure 5.6

Because of the reduced image intensity associated with the dark field method, long photographic exposure times were found to be necessary (30s - 60s). Over this length of time specimen drift due to bending of the section under the pressure of the electron beam was found to be a problem and this was overcome by using copper grids with an evaporated carbon support film. Although reducing the clarity of the micrograph, this support film proved to be invaluable in stopping specimen drift.

Figure 5.7. shows a good dark field image formed by using the small aperture and (002) diffracted beams only. The c-axial direction is indicated.

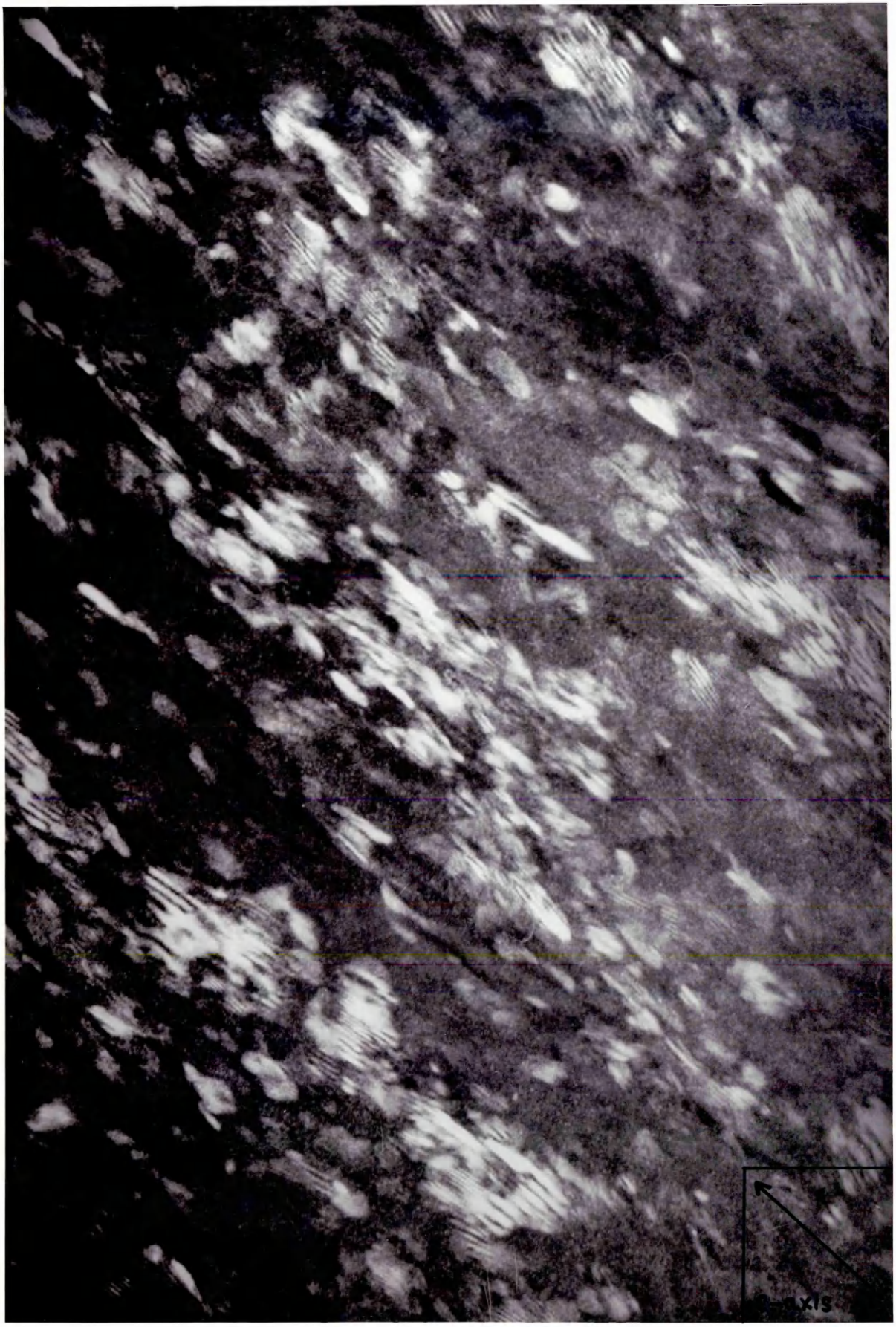

Figure 5.7

5.2. C-axial Length Measurement Using The Dark Field Method

5.2.1. Introduction

The bone sample was taken from the mid-femural section of a female Dutch rabbit, aged approximately six months, removed and prepared immediately after death. Since the dark field technique had not previously been used for this work, different specimen preparation techniques were used to detect possible preparation artefacts.

Three sections, 1mm thick, were cut from the bone sample using a Metals Research macrotome fitted with a diamond wheel and prepared by the following techniques.

A. Fixed in 5% glutaraldehyde with bicarbonate buffer for five hours at $4^{o}C$. Washed in T.C.199 with bicarbonate buffer, pH 7.2. Post fixed in osmium tetroxide with veronal acetate buffer.

Dehydrated in ascending grades of ethanol in water and embedded in araldite.

B. Fixed in absolute ethanol for twenty hours at room temperature.

Embedded in araldite.

C. Air dried for a period of eight weeks.

Sample not embedded but supported in an araldite block for sectioning.

Procedure A represents a high quality biological preparation, B represents an inferior preparation and C involves no preserving technique at all.

Sections were cut as described in 3.5., mounted on 400 mesh carbon coated copper grids and examined without further treatment.

The dark field images were formed using only (002) diffracted beams and the 10/^{um} diameter objective aperture. The c-axial direction of the crystals appearing brightly in the dark field images was determined from the superposition of the diffraction pattern and the objective aperture image, as shown in figure 5.8., account being taken of the rotation factor mentioned in Section 4.1.2.

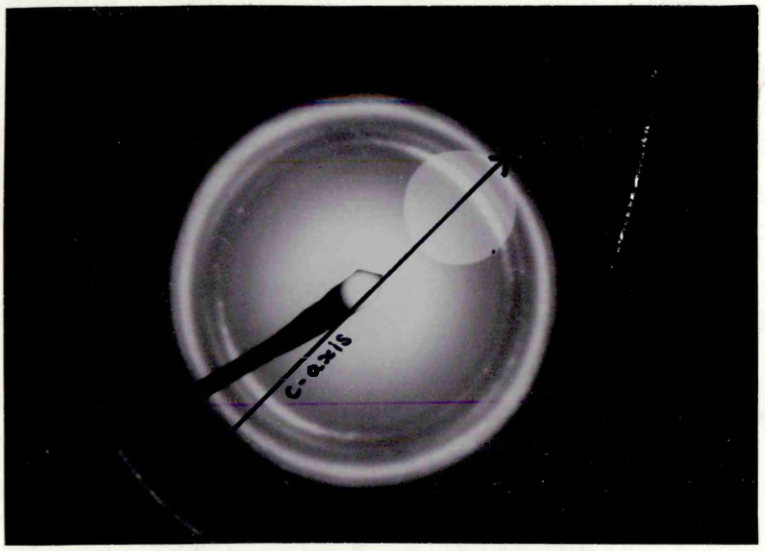

Electron Diffraction Pattern and Objective Aperture.

Figure 5.8

The micrographs were photographically enlarged to a convenient size before measurements were made. Only crystals which appeared bright and well isolated were chosen for measurement. From many micrographs, 400 measurements of the c-axial length were taken for each of the three samples using a magnified graticule and the data was analysed statistically.

5.2.2. Results

The actual measurements taken from the enlarged micrographs are tabulated in the following pages. The numerical data has units of centimetres and the scale factor is such that:-

Crystal Size (c-axial length) = Size measured (in centimetres) x 42 nm

Each set of data was anlaysed statistically by computer programme, see Appendix II and the analysis is presented after each set of tabulated data.

GLUTARALDEHYDE/OSMIUM FIXED

0.23	0.31	0.34	0.37	0.42
0.25	0.32	0.35	0.38	0.43
0.25	0.32	0.35	0.38	0.45
0.26	0.32	0.35	0.38	0.45
0.27	0.32	0.35	0.40	0.45
0.27	0.32	0.35	0.40	0.45
0.28	0.32	0.35	0.40	0.45
0.28	0.32	0.35	0.40	0.45
0.30	0.33	0.37	0.41	0.45
0.30	0.34	0.37	0.42	0.45
0.56	0.59	0.60	0.62	0.65
0.57	0.60	0.60	0.62	0.65
0.57	0.60	0.60	0.62	0.65
0.57	0.60	0.61	0.62	0.65
0.57	0.60	0.61	0.62	0.65
0.58	0.60	0.61	0.62	0.65
0.58	0.60	0.62	0.63	0.66
0.58	0.60	0.62	0.63	0.66
0.59	0.60	0.62	0.64	0.66
0.59	0.60	0.62	0.64	0.66
0.75	0.77	0.80	0.81	0.84
0.75	0.77	0.80	0.81	0.85
0.76	0.77	0.80	0.81	0.85
0.76	0.78	0.80	0.81	0.85
0.76	0.78	0.80	0.81	0.85
0.76	0.78	0.80	0.82	0.85
0.76	0.78	0.80	0.83	0.85
0.76	0.79	0.80	0.83	0.85
0.77	0.79	0.80	0.83	0.85
0.77	0.80	0.81	0.83	0.85
0.98	1.03	1.07	1.11	1.15
0.98	1.05	1.07	1.12	1.15
0.98	1.05	1.08	1.12	1.15
0.99	1.05	1.10	1.12	1.16
0.99	1.05	1.10	1.13	1.16
1.00	1.05	1.10	1.13	1.17
1.00	1.05	1.10	1.14	1.17
1.00	1.06	1.10	1.14	1.18
1.00	1.07	1.10	1.15	1.20
1.02	1.07	1.10	1.15	1.20

TABLE 5.1

GLUTARALDEHYDE/OSMIUM FIXED

0.46	0.48	0.51	0.53	0.55
0.46	0.49	0.51	0.53	0.55
0.46	0.50	0.52	0.53	0.55
0.47	0.50	0.52	0.54	0.55
0.47	0.50	0.52	0.54	0.55
0.48	0.50	0.52	0.54	0.55
0.48	0.50	0.52	0.54	0.55
0.48	0.50	0.52	0.54	0.55
0.48	0.50	0.52	0.55	0.56
0.48	0.51	0.53	0.55	0.56
0.66	0.68	0.70	0.70	0.73
0.67	0.68	0.70	0.70	0.73
0.67	0.68	0.70	0.71	0.74
0.67	0.68	0.70	0.71	0.74
0.67	0.68	0.70	0.72	0.75
0.67	0.69	0.70	0.72	0.75
0.67	0.69	0.70	0.72	0.75
0.67	0.69	0.70	0.72	0.75
0.67	0.69	0.70	0.73	0.75
0.68	0.69	0.70	0.73	0.75
0.85	0.88	0.90	0.92	0.95
0.85	0.88	0.90	0.93	0.95
0.85	0.88	0.90	0.93	0.95
0.85	0.88	0.90	0.93	0.95
0.86	0.88	0.91	0.94	0.95
0.86	0.88	0.92	0.94	0.95
0.86	0.89	0.92	0.94	0.95
0.87	0.89	0.92	0.94	0.96
0.87	0.90	0.92	0.95	0.97
0.87	0.90	0.92	0.95	0.97
1.20	1.26	1.30	1.50	1.81
1.20	1.27	1.34	1.58	1.93
1.20	1.27	1.35	1.58	1.95
1.20	1.28	1.35	1.60	1.95
1.22	1.29	1.36	1.66	1.95
1.23	1.30	1.36	1.69	2.10
1.23	1.30	1.38	1.73	2.15
1.23	1.30	1.38	1.75	2.40
1.24	1.30	1.39	1.77	2.70
1.25	1.30	1.45	1.77	2.70

TABLE 5.2

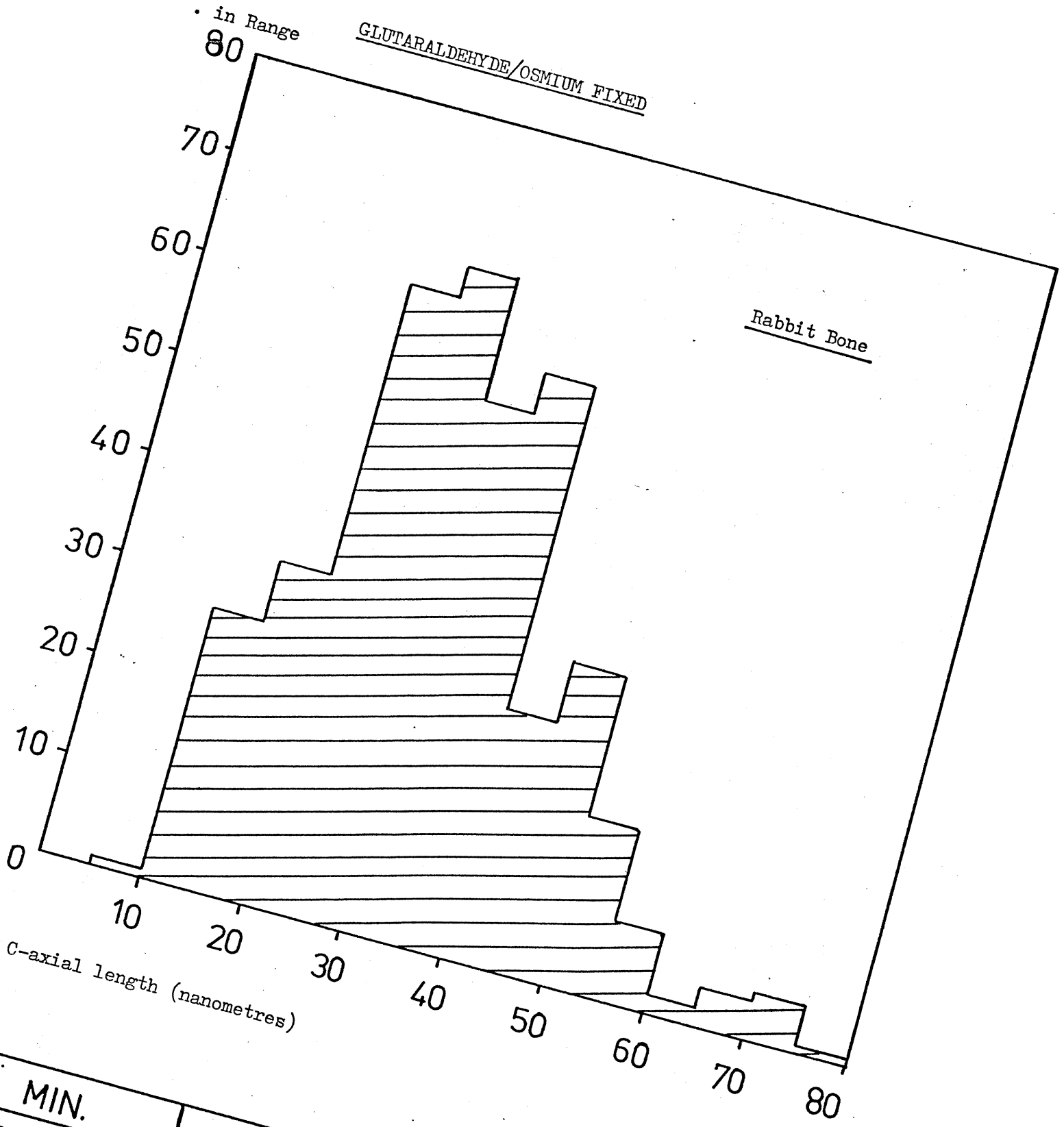

MIN.	MAX.	MEAN.	S. D.
9·7 nm.	113·0nm.	34·0nm.	15·5nm.

Figure 5.9

ALCOHOL FIXED

0.28	0.37	0.40	0.40	0.45
0.28	0.37	0.40	0.42	0.45
0.30	0.37	0.40	0.43	0.45
0.30	0.38	0.40	0.43	0.45
0.32	0.38	0.40	0.43	0.45
0.34	0.38	0.40	0.43	0.46
0.35	0.38	0.40	0.44	0.46
0.35	0.39	0.40	0.44	0.46
0.35	0.39	0.40	0.45	0.47
0.36	0.40	0.40	0.45	0.47
0.55	0.55	0.57	0.60	0.60
0.55	0.55	0.57	0.60	0.60
0.55	0.55	0.58	0.60	0.60
0.55	0.55	0.58	0.60	0.60
0.55	0.55	0.58	0.60	0.60
0.55	0.56	0.58	0.60	0.61
0.55	0.56	0.58	0.60	0.62
0.55	0.56	0.59	0.60	0.62
0.55	0.56	0.59	0.60	0.62
0.55	0.56	0.60	0.60	0.62
0.74	0.75	0.78	0.80	0.80
0.74	0.75	0.78	0.80	0.81
0.74	0.75	0.78	0.80	0.81
0.74	0.75	0.78	0.80	0.81
0.75	0.75	0.78	0.80	0.81
0.75	0.76	0.79	0.80	0.82
0.75	0.76	0.79	0.80	0.82
0.75	0.76	0.80	0.80	0.82
0.75	0.77	0.80	0.80	0.82
0.75	0.78	0.80	0.80	0.83
0.99	1.02	1.06	1.10	1.13
1.00	1.02	1.07	1.10	1.13
1.00	1.04	1.07	1.10	1.15
1.00	1.04	1.08	1.10	1.15
1.00	1.05	1.08	1.10	1.15
1.00	1.05	1.08	1.11	1.16
1.00	1.05	1.08	1.12	1.16
1.00	1.05	1.09	1.12	1.16
1.01	1.05	1.09	1.12	1.16
1.02	1.05	1.10	1.12	1.17

TABLE 5.3

0.47	0.49	0.50	0.51	0.53
0.47	0.49	0.50	0.51	0.53
0.47	0.49	0.50	0.51	0.53
0.48	0.49	0.50	0.52	0.53
0.48	0.49	0.50	0.52	0.54
0.48	0.50	0.50	0.52	0.54
0.48	0.50	0.50	0.52	0.54
0.48	0.50	0.50	0.53	0.54
0.49	0.50	0.50	0.53	0.54
0.49	0.50	0.50	0.53	0.55
0.62	0.64	0.65	0.69	0.71
0.62	0.64	0.66	0.70	0.71
0.62	0.64	0.66	0.70	0.72
0.62	0.64	0.67	0.70	0.72
0.63	0.65	0.68	0.70	0.72
0.63	0.65	0.68	0.70	0.72
0.63	0.65	0.68	0.70	0.72
0.63	0.65	0.68	0.70	0.73
0.63	0.65	0.68	0.70	0.73
0.63	0.65	0.68	0.70	0.73
0.83	0.85	0.88	0.90	0.94
0.83	0.85	0.88	0.91	0.94
0.83	0.85	0.88	0.91	0.95
0.84	0.86	0.88	0.92	0.95
0.84	0.86	0.89	0.92	0.95
0.84	0.87	0.90	0.92	0.95
0.85	0.87	0.90	0.92	0.95
0.85	0.87	0.90	0.93	0.96
0.85	0.87	0.90	0.93	0.97
0.85	0.87	0.90	0.94	0.98
1.18	1.25	1.38	1.42	1.60
1.18	1.25	1.38	1.42	1.70
1.18	1.25	1.38	1.44	1.72
1.19	1.26	1.39	1.46	1.78
1.20	1.30	1.40	1.48	1.79
1.20	1.32	1.40	1.49	1.82
1.20	1.32	1.40	1.50	1.90
1.22	1.34	1.40	1.50	1.96
1.23	1.35	1.40	1.53	2.00
1.24	1.37	1.42	1.58	2.02

TABLE 5.4

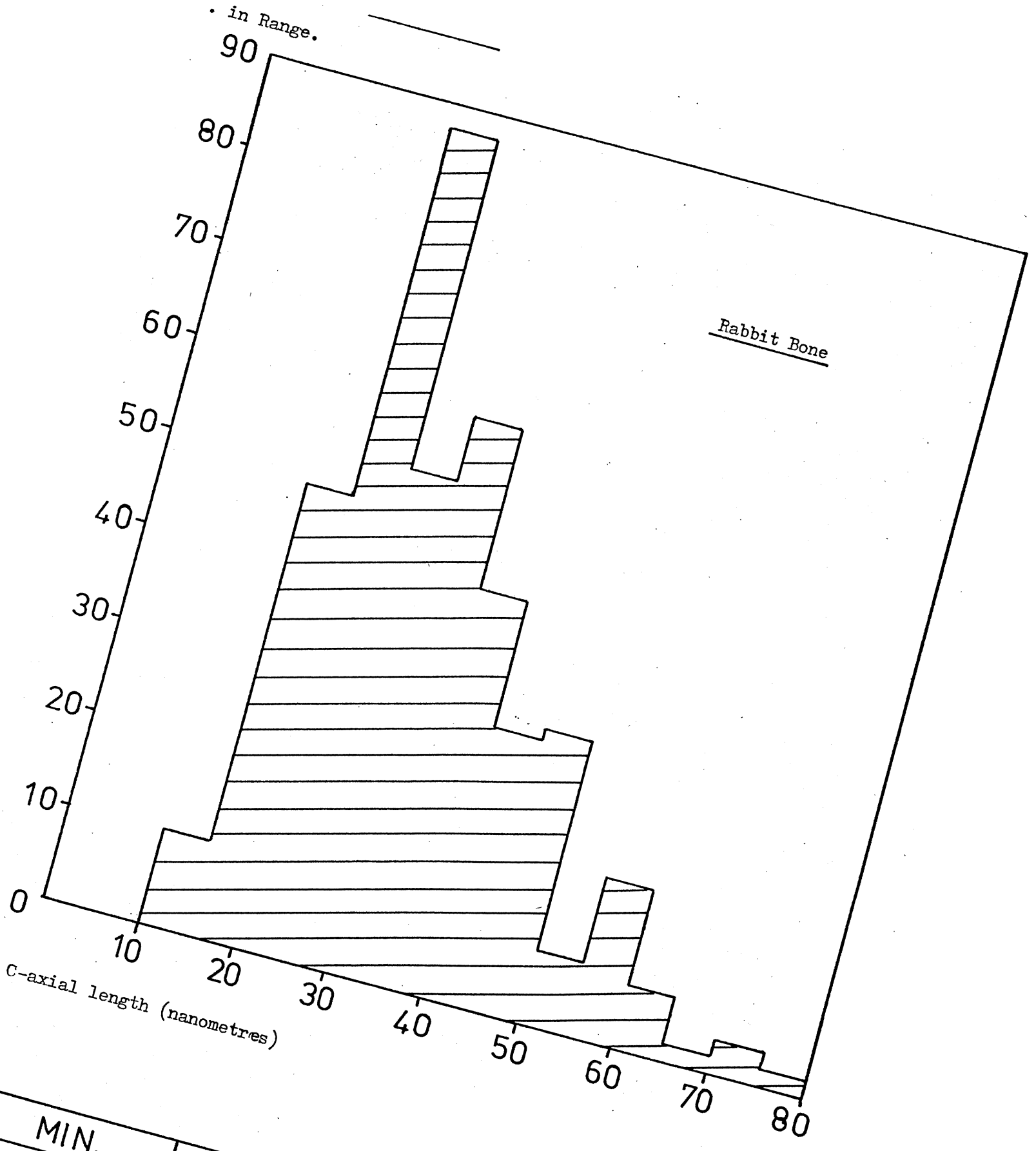

MIN.	MAX.	MEAN.	S.D.
11·8 nm.	99·0 nm.	33·5 nm.	14·2 nm.

Figure 5.10

0.24	0.32	0.35	0.38	0.42
0.24	0.33	0.36	0.39	0.42
0.26	0.33	0.36	0.39	0.43
0.26	0.33	0.36	0.39	0.43
0.27	0.33	0.36	0.40	0.44
0.30	0.33	0.36	0.40	0.44
0.30	0.33	0.37	0.41	0.44
0.31	0.34	0.37	0.41	0.44
0.31	0.35	0.37	0.42	0.44
0.32	0.35	0.38	0.42	0.44
0.55	0.56	0.58	0.60	0.60
0.55	0.56	0.58	0.60	0.60
0.56	0.56	0.58	0.60	0.60
0.56	0.56	0.58	0.60	0.60
0.56	0.57	0.58	0.60	0.60
0.56	0.57	0.58	0.60	0.60
0.56	0.57	0.59	0.60	0.61
0.56	0.57	0.59	0.60	0.61
0.56	0.58	0.59	0.60	0.61
0.56	0.58	0.59	0.60	0.61
0.69	0.71	0.72	0.74	0.76
0.69	0.72	0.72	0.74	0.76
0.69	0.72	0.73	0.75	0.77
0.69	0.72	0.73	0.75	0.77
0.70	0.72	0.74	0.75	0.77
0.70	0.72	0.74	0.75	0.77
0.71	0.72	0.74	0.75	0.77
0.71	0.72	0.74	0.75	0.77
0.71	0.72	0.74	0.75	0.77
0.71	0.72	0.74	0.76	0.77
0.89	0.94	0.98	1.02	1.09
0.89	0.94	0.98	1.03	1.10
0.90	0.95	0.98	1.03	1.11
0.91	0.95	0.99	1.05	1.11
0.91	0.97	0.99	1.05	1.11
0.92	0.97	1.00	1.06	1.11
0.93	0.97	1.00	1.07	1.14
0.94	0.97	1.00	1.08	1.15
0.94	0.97	1.01	1.08	1.16
0.94	0.97	1.02	1.09	1.17

TABLE 5.5

0.44	0.46	0.49	0.50	0.53
0.44	0.47	0.50	0.51	0.53
0.44	0.47	0.50	0.51	0.53
0.44	0.47	0.50	0.52	0.53
0.44	0.47	0.50	0.52	0.54
0.45	0.48	0.50	0.52	0.54
0.45	0.48	0.50	0.52	0.54
0.46	0.48	0.50	0.52	0.55
0.46	0.49	0.50	0.52	0.55
0.46	0.49	0.50	0.53	0.55
0.61	0.63	0.65	0.65	0.67
0.61	0.63	0.65	0.66	0.67
0.61	0.63	0.65	0.66	0.67
0.61	0.63	0.65	0.66	0.67
0.62	0.63	0.65	0.66	0.67
0.62	0.63	0.65	0.66	0.67
0.62	0.64	0.65	0.66	0.68
0.62	0.64	0.65	0.67	0.68
0.62	0.64	0.65	0.67	0.68
0.63	0.64	0.65	0.67	0.69
0.77	0.80	0.81	0.83	0.85
0.78	0.80	0.81	0.83	0.86
0.78	0.80	0.81	0.83	0.87
0.78	0.80	0.81	0.83	0.87
0.78	0.80	0.82	0.84	0.88
0.78	0.80	0.82	0.84	0.88
0.78	0.81	0.82	0.84	0.88
0.79	0.81	0.82	0.85	0.88
0.80	0.81	0.83	0.85	0.88
0.80	0.81	0.83	0.85	0.89
1.17	1.22	1.29	1.44	1.66
1.17	1.22	1.30	1.47	1.71
1.18	1.22	1.30	1.47	1.80
1.19	1.23	1.30	1.50	1.80
1.20	1.23	1.32	1.51	1.80
1.20	1.24	1.33	1.52	1.90
1.20	1.25	1.34	1.55	1.95
1.20	1.26	1.39	1.60	1.98
1.21	1.27	1.40	1.61	2.02
1.21	1.28	1.43	1.65	2.70

TABLE 5.6

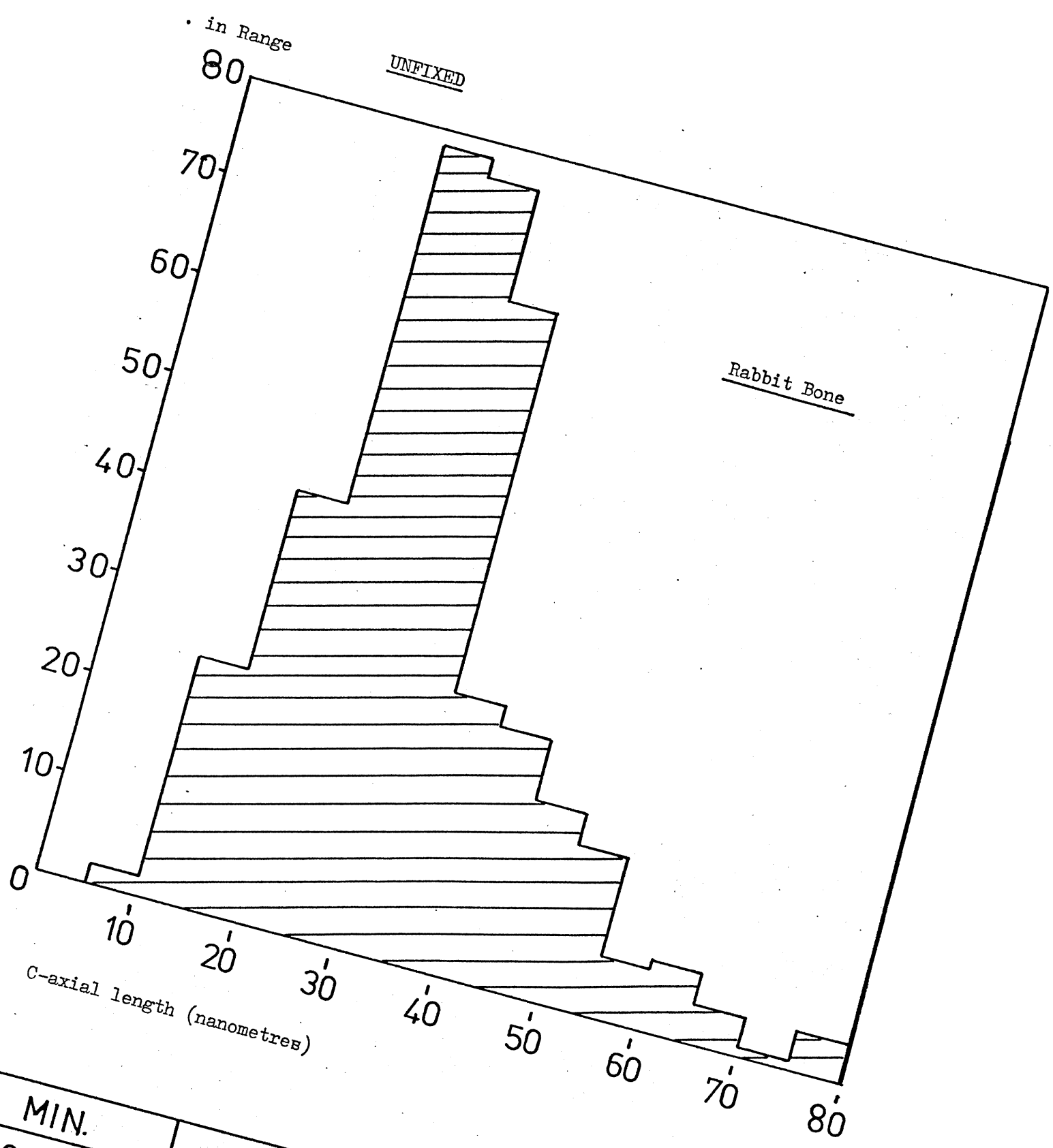

MIN.	MAX.	MEAN.	S.D.
10·0 nm.	113·0 nm.	32·0 nm.	14·0 nm.

Figure 5.11

5.2.3. Conclusions

a) The dark field technique proved a most effective method for measuring the c-axial length of bone mineral crystals.

b) The (002) diffracted beam was strong and well isolated so that good dark field images were formed. Unfortunately, no other diffracted beam fulfilled this condition, so it was not possible to measure dimensions other than the c-axial one.

c) The three groups of measurements were compared by using a one-way analysis of variance and no significant difference was found between the three sets of data the the 5% level. Hence, at this level of significance, the method of specimen preparation was shown to have no effect upon the crystal size distribution.

d) Since Moire fringes are best formed in thin crystals and large areas of these fringes were found, a thin plate-like form for bone mineral is strongly suggested.

e) The dark field images showed a wide variation in the crystal size and shape. There appears to be agreement with the bright field observations, that the crystals are in the form of irregular plates. The apparent 'width' perpendicular to the c-axial direction, varied in the dark field images from about 4nm to dimensions approaching that of the c-axial length in some crystals. Since the crystals would still produce dark field images when rotated about the c-axis, the small 'width' probably corresponds to the thickness of the plate-like crystals.

f) Attempts were made to be as unbiased as possible when chosing crystals for measurement, in an effort to obtain a representative sample of the crystal size population. However, it is possible that small crystals, which do not produce strong diffracted beams were not detected, thus giving an artificially high average to the mean c-axial length.

At this stage of the work it was felt that the dark field technique had been developed into a useable form. The specimen preparation experiments had failed to show that any artefacts were produced by the preparation technique, which meant that untreated bone could be used for the remainder of this work. The next chapter, therefore, deals with the main part of this investigation, which is an attempt to use the dark field technique to explain the past discrepancies of c-axial measurement between x-ray diffraction and bright field methods. It is, therefore, hoped, using the dark field technique to obtain a more accurate estimation of bone mineral crystal size and size distribution than has previously been possible.

CHAPTER SIX

A COMPARISON OF DARK FIELD AND X-RAY METHODS IN MEASURING C-AXIAL LENGTH

6.1. Introduction

In this chapter the dark field technique is compared with the x-ray method of line broadening for measuring the c-axial length of bone mineral.

It has been mentioned in chapter one that discrepancies have arisen in the past, between x-ray and bright field electron microscopical determinations of the c-axial length. It has also been stated in 4.2.3. that the bright field measurements have little validity, since they cannot be related to the crystal axes, whereas the dark field measurements can. Thus it is hoped that the dark field method can help explain past discrepancies and enable the true c-axial length to be estimated.

Three different bone types have been used for this experiment, rabbit, ox and human, as a preliminary investigation into the variation of crystal size between bone types. All samples were of cortical bone taken from the mid-femural region. Details of these bones and their preparation are given in the following sections.

6.2. The X-ray Method of Line Broadening

When x-rays are diffracted by a crystal, for the Bragg Law to be true, the following conditions have to hold.

a) The crystal structure is perfect.
b) The x-ray beam is parallel and monochromatic.
c) The crystal lattice is infinite.

The first condition is difficult to prove, so initially it was assumed that the crystal structure was perfect.

The second condition was achieved by using standard x-ray diffraction apparatus incorporating a nickel filter and a beam collimator.

The third condition was known not to hold and the broadening of the x-ray diffraction lines from bone mineral has been attributed in the past to the small crystal size.

It is the spread of the diffraction line which provides a method of estimating the crystal size. Figure 6.1. shows diagramatically a diffraction peak profile.

Diffraction Peak Profile.

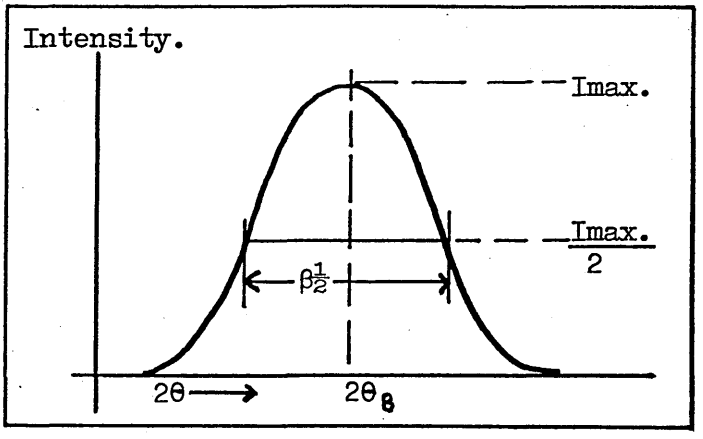

Figure 6.1

The maximum intensity occurs at $2(\Theta_B)$, the Bragg angle and falls to zero at either side. The angular width measured at half the maximum intensity is known as the beta half width ($\beta_{\frac{1}{2}}$) and it is this factor which is usually measured experimentally.

Scherrer (1918) was the first person to show that the mean dimension, t, of crystals comprising a powder is related to $\beta_{\frac{1}{2}}$ by the equation:

$$\beta_{\frac{1}{2}} = \frac{0.9\lambda}{t.\ \mathrm{Cos}\,\Theta_B} \qquad (1)$$

where:- $\beta_{\frac{1}{2}}$ = pure diffraction breadth (in radians)

λ = x-ray wavelength

t = mean crystal thickness, in a direction perpendicular to the planes from which the diffracted beam arises. In the case of the (002) diffracted beam t represents the mean c-axial length.

$\beta_{\frac{1}{2}}$ has been assumed to be the pure diffraction breadth, i.e., free from any broadening due to instrumental effects. In his original investigation, Scherrer proposed that the pure breadth ($\beta_{\frac{1}{2}}$) could be obtained from the experimentally observed breadth ($B_{\frac{1}{2}}$) of a diffraction line, by subtracting from it the breadth ($b_{\frac{1}{2}}$) of a line produced under similar geometrical conditions by a material with a crystallite size well in excess of 100nm, which produces negligible broadening, i.e.,

$$\beta_{\frac{1}{2}} = B_{\frac{1}{2}} - b_{\frac{1}{2}} \qquad (2)$$

However, Scherrer's postulate concerning the additivity of ($\beta_{\frac{1}{2}}$) and ($b_{\frac{1}{2}}$) has been found to have no general validity. It has been shown by Warren (1938, 1941) that if both instrumental and measured profiles are approximately gaussian in shape, following relationship holds:

$$(B_{\frac{1}{2}})^2 = (\beta_{\frac{1}{2}})^2 + (b_{\frac{1}{2}})^2 \qquad (3)$$

This formula has now become widely used for correcting observed line widths for the effect of instrumental broadening.

6.3. Experimental Techniques

6.3.1. The Bone Samples

Since it was shown in Chapter 5 that the method of specimen preparation had no significant effect upon the crystal c-axial length, no special preserving techniques were used. Details of the three bone types are given below.

a) Rabbit Bone

The femur was taken from a female Dutch rabbit, aged approximately six months, immediately after death and allowed to dry in air. The mid-femural section was then used for x-ray analysis and dark field examination.

b) Ox Bone

This sample of cortical bone was taken from the mid-femural section of a Red Devon Ox, aged between two to three years. The bone had been deep frozen but otherwise untreated.

c) Human Bone

This sample of cortical bone was taken at post mortem from the mid-femural section of a sixty-five year old male. Death was not caused by a primary bone disorder and the sample was untreated.

6.3.2. The X-ray Technique

The x-ray diffractometer has been described briefly in Chapter two and since it is now standard laboratory equipment no details of its operation will be discussed.

The sample shape required for the diffractometer is in the form of a small flat slab, approximately 10mm x 20mm x 1mm. Obviously with rabbit bone, whole bone samples of this size are out of the question, so a sample had to be fabricated. The femur was cut into 1mm thick sections perpendicular to its length and these sections were placed in a 10mm x 20mm mould which was filled with araldite. After the araldite had cured, the slab was polished flat and trimmed to the shape required. Since the diffracted beams produced by bone are not very strong, long experimental times normally result. However, by aligning the bone sections, as shown in figure 6.2., such that the majority of c-axes are aligned, the (002) diffracted beam was strongly enhanced.

The diffractometer produced a direct output of x-ray intensity versus (2θ), which was recorded on a strip chart from which measurements were taken. In order to obtain the peak profile showing only instrumental broadening, a sample of rabbit bone was heated in air to $800^{o}C$ for two hours. Under these conditions the crystals grow to dimensions in excess of 100nm, a fact verified by electron microscopy. The heated bone was then powdered in an agate mortar and compressed flat into the sample holder before being examined.

To check that equation (3) was applicable to this work, each peak profile was tested for normality. This was achieved by plotting the peak profile as a probability function on normal probability graph paper. A straight line was produced in every case, indicating that the peaks were gaussian in shape and consequently validating equation (3) in terms of its application to correct observed peak widths for instrumental factors in this work.

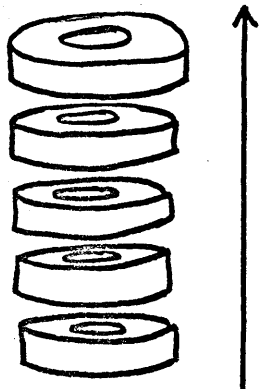

Mid-femural section cut into 1mm. thick slices.

Long axis of femur.
(main c-axial direction).

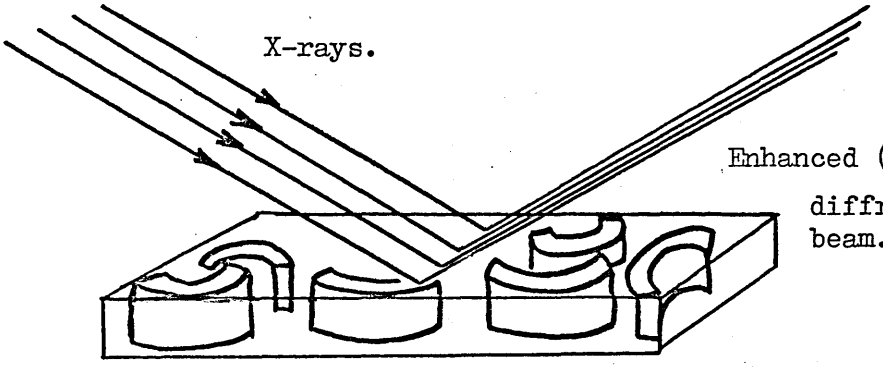

Sections embedded in araldite such that the majority of crystal c-axes are oriented perpendicular to the face of the slab.

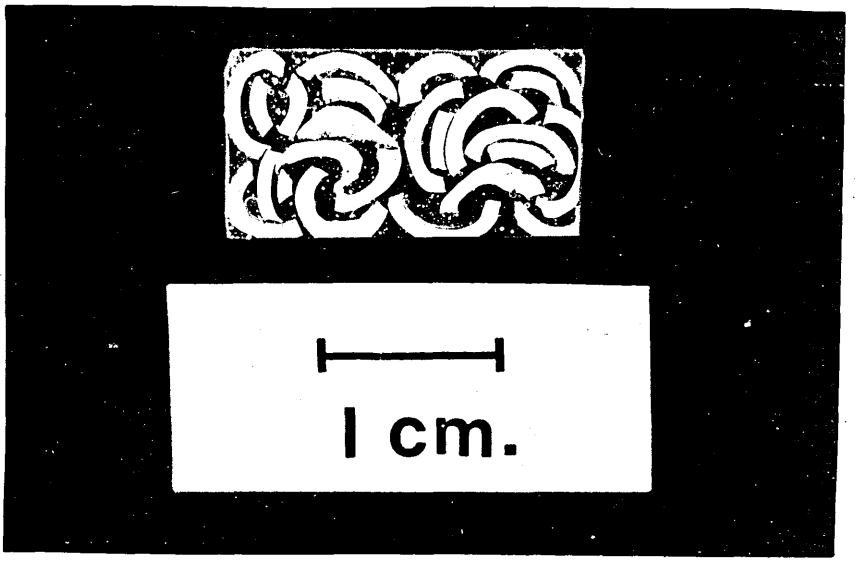

Figure 6.2

6.3.3. The Dark Field Method

The three bone types were examined by the dark field technique as described in 5.1.4. Results of both techniques are presented in the next section.

6.4. Results

6.4.1. X-ray Line Broadening Results

Three separate measurements were made of each peak width so that experimental variation could be estimated. Some of the variation in the $2\theta_B$ values was attributed to a slight warping of the specimen slab within the specimen holder, thus shifting the peak position. Measured $B\frac{1}{2}$ widths for both (002) and (004) peaks are listed in the following tables, and the reason for taking the (004) measurements will become evident shortly.

Rabbit Bone S9
Preparation - Heated to 800°C for 2 hours.
This sample used as calibration for instrumental broadening

Peak	002	004
$b\frac{1}{2}$ (degrees)	0.138 0.133 0.142	0.238 0.217 0.229
$b\frac{1}{2}$ mean Standard Deviation	0.138 0.005	0.228 0.010
$2\theta_B$ (degrees)	25.923 25.931 25.925	53.208 53.221 53.242
$2\theta_B$ mean Standard Deviation	25.926 0.004	53.220 0.020

Table 6.1.

Rabbit Bone S9 - Untreated

Peak	002	004
$B\frac{1}{2}$ (degrees)	0.329 0.317 0.323	0.500 0.481 0.513
$2\theta_B$ (degrees)	25.92 25.92 25.91	53.213 53.225 53.225

Table 6.2.

Ox Bone - Untreated

Peak	002	004
$B\frac{1}{2}$ (degrees)	0.325 0.323 0.313	0.525 0.500 0.494
$2\theta_B$ (degrees)	25.975 25.950 25.963	53.250 53.260 53.240

Table 6.3.

Human Bone - Untreated

Peak	002	004
$B_{\frac{1}{2}}$ (degrees)	0.335 0.342 0.329	0.513 0.488 0.519
$2\theta_B$ (degrees)	25.981 26.000 25.994	53.260 53.250 53.260

Table 6.4.

6.4.2. Calculation of C-Axial Length

The pure diffraction breadth ($\beta_{\frac{1}{2}}$) was calculated from the formula:-

$$(B_{\frac{1}{2}})^2 = (\beta_{\frac{1}{2}})^2 + (b_{\frac{1}{2}})^2$$

Where:-

$B_{\frac{1}{2}}$ = measured peak half width

$b_{\frac{1}{2}}$ = half width from heated bone sample

The Scherrer formula:-

$$\beta_{\frac{1}{2}} = \frac{0.9\lambda}{t.\ \text{Cos}\ \Theta_B}$$

was then used to calculate t, the c-axial length using the $\beta_{\frac{1}{2}}$ values for the (002) diffracted beam only. The results are presented below in table 6.5.

C-Axial Lengths Using (002) Line Broadening

Sample	Rabbit	Ox	Human
C-axial length (nanometers)	27.3 28.5 27.9	27.8 28.0 29.0	26.6 26.1 27.3
Mean C-axial Length (nanometers)	27.9	28.3	26.7
Standard Deviation (nanometers)	0.6	0.6	0.6

Table 6.5.

6.4.3. Dark Field Results

Results are presented as in the previous chapter. Tables of actual measurements for each bone type are followed by a histogram and statistical analysis which summarises the data. The tabulated values are measurements taken from enlarged micrographs and have the dimensions of centimetres. The scale factor is such that 1cm = 33.3nm (object size) .

Note that the magnification factor is slightly different to that used previously. This change was brought about by servicing alterations to the microscope, consequently a recalibration was necessary and beef catalase was used.

C-AXIAL LENGTH MEASUREMENTS

RABBIT BONE

0.25	0.43	0.51	0.55	0.60
0.30	0.45	0.52	0.55	0.60
0.30	0.45	0.52	0.57	0.60
0.34	0.45	0.53	0.57	0.62
0.35	0.49	0.54	0.58	0.63
0.40	0.50	0.55	0.60	0.63
0.40	0.50	0.55	0.60	0.64
0.40	0.50	0.55	0.60	0.64
0.42	0.50	0.55	0.60	0.65
0.42	0.50	0.55	0.60	0.65
0.80	0.85	0.90	0.92	0.96
0.80	0.85	0.90	0.92	0.97
0.80	0.86	0.90	0.93	0.98
0.80	0.86	0.90	0.93	0.98
0.80	0.87	0.90	0.93	0.98
0.82	0.88	0.90	0.94	0.98
0.82	0.90	0.90	0.94	0.98
0.83	0.90	0.90	0.95	1.00
0.84	0.90	0.90	0.95	1.00
0.85	0.90	0.92	0.95	1.00
1.20	1.25	1.30	1.40	1.52
1.20	1.25	1.30	1.40	1.55
1.20	1.25	1.30	1.42	1.55
1.20	1.25	1.32	1.45	1.57
1.20	1.25	1.32	1.45	1.60
1.20	1.25	1.33	1.47	1.60
1.20	1.25	1.35	1.48	1.62
1.24	1.25	1.35	1.48	1.62
1.25	1.27	1.37	1.50	1.62
1.25	1.27	1.40	1.50	1.65

Table 6.6

C-AXIAL LENGTH MEASUREMENTS

RABBIT BONE

0.65	0.69	0.70	0.75	0.78
0.65	0.70	0.70	0.75	0.78
0.65	0.70	0.72	0.75	0.79
0.65	0.70	0.72	0.75	0.80
0.66	0.70	0.73	0.75	0.80
0.66	0.70	0.74	0.75	0.80
0.67	0.70	0.75	0.75	0.80
0.68	0.70	0.75	0.76	0.80
0.68	0.70	0.75	0.76	0.80
0.69	0.70	0.75	0.78	0.80
1.00	1.05	1.10	1.12	1.16
1.00	1.05	1.10	1.13	1.17
1.00	1.05	1.10	1.13	1.17
1.00	1.05	1.10	1.13	1.18
1.00	1.05	1.10	1.15	1.18
1.04	1.05	1.10	1.15	1.19
1.04	1.08	1.10	1.15	1.20
1.05	1.09	1.10	1.15	1.20
1.05	1.10	1.10	1.15	1.20
1.05	1.10	1.12	1.15	1.20
1.65	1.80			
1.65	1.80			
1.65	1.81			
1.65	1.90			
1.65	1.90			
1.65	2.10			
1.67	3.30			
1.70				
1.70				
1.75				

Table 6.7

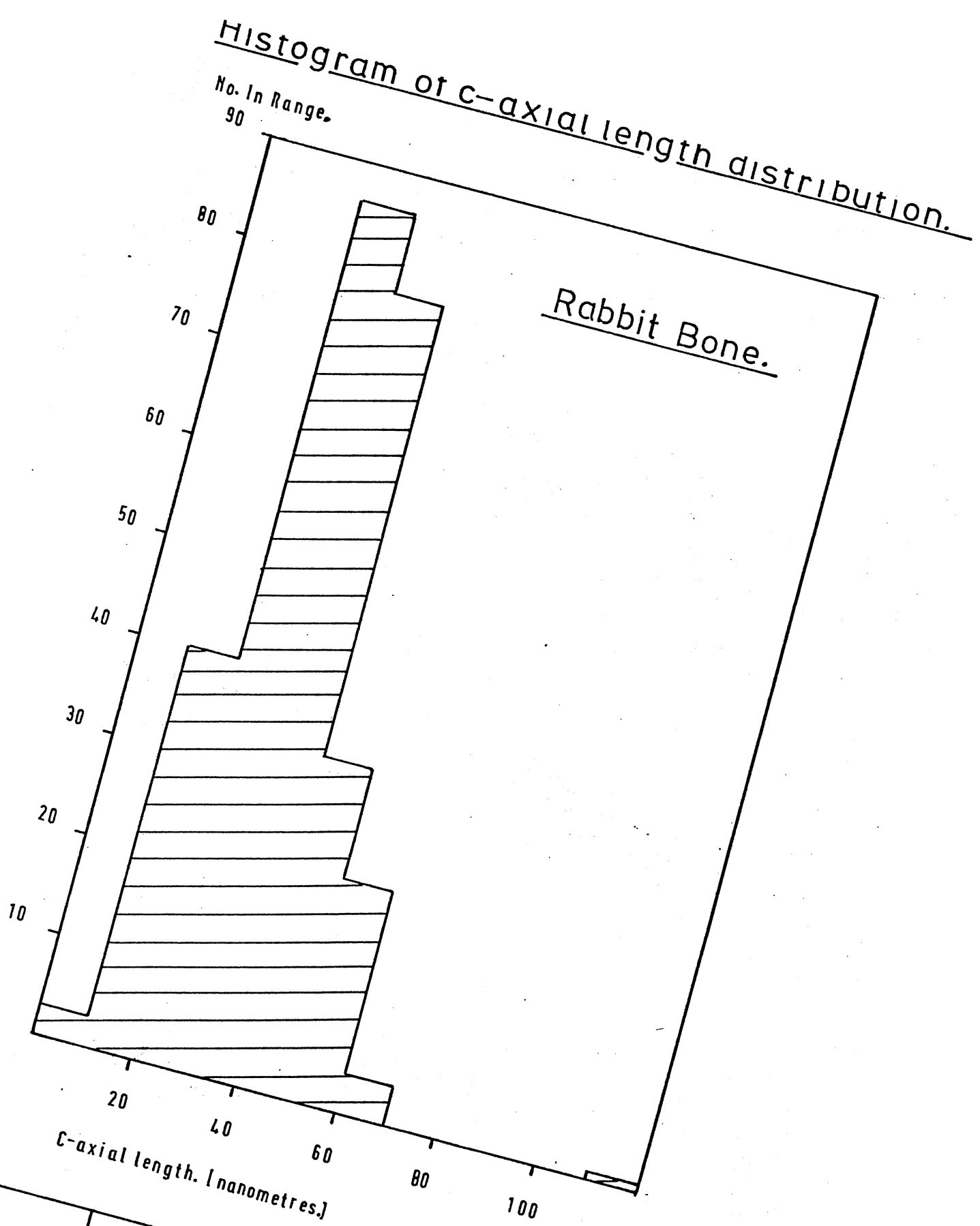

Min.	Max.	Mean.	S. D.
8·3 nm.	110·0nm.	32·6nm.	12·8nm.

Figure 6.3
137.

0.20	0.29	0.32	0.38	0.45
0.21	0.30	0.34	0.40	0.45
0.22	0.30	0.34	0.40	0.45
0.23	0.30	0.35	0.40	0.47
0.24	0.30	0.35	0.40	0.48
0.27	0.32	0.35	0.40	0.48
0.27	0.32	0.35	0.40	0.50
0.28	0.32	0.35	0.42	0.50
0.28	0.32	0.35	0.43	0.50
0.29	0.32	0.35	0.43	0.50
0.77	0.80	0.83	0.87	0.90
0.78	0.80	0.83	0.88	0.90
0.78	0.80	0.85	0.88	0.90
0.80	0.80	0.85	0.88	0.92
0.80	0.80	0.85	0.90	0.92
0.80	0.80	0.85	0.90	0.92
0.80	0.82	0.85	0.90	0.93
0.80	0.82	0.85	0.90	0.95
0.80	0.82	0.86	0.90	0.95
0.80	0.83	0.87	0.90	0.95
1.15	1.23	1.25	1.32	1.40
1.15	1.23	1.30	1.34	1.40
1.16	1.23	1.30	1.35	1.43
1.16	1.25	1.30	1.35	1.44
1.17	1.25	1.30	1.40	1.45
1.17	1.25	1.30	1.40	1.45
1.20	1.25	1.30	1.40	1.45
1.20	1.25	1.30	1.40	1.45
1.20	1.25	1.30	1.40	1.45
1.20	1.25	1.30	1.40	1.45
1.90	2.10	2.45		
1.90	2.10	2.50		
1.90	2.12	2.55		
1.90	2.20	2.70		
1.90	2.25	2.70		
1.95	2.25	2.90		
1.97	2.30	2.95		
2.00	2.30	3.40		
2.05	2.35			
2.10	2.40			

Table 6.8

C-AXIAL LENGTH MEASUREMENTS

OX BONE

0.50	0.58	0.62	0.70	0.75
0.50	0.60	0.62	0.70	0.75
0.53	0.60	0.62	0.70	0.75
0.55	0.60	0.63	0.70	0.75
0.55	0.60	0.65	0.70	0.75
0.55	0.60	0.65	0.70	0.75
0.55	0.60	0.65	0.70	0.75
0.57	0.60	0.67	0.70	0.76
0.58	0.60	0.67	0.71	0.76
0.58	0.60	0.70	0.72	0.77
0.95	1.00	1.05	1.10	1.15
0.95	1.00	1.05	1.10	1.15
0.95	1.00	1.05	1.10	1.15
0.95	1.00	1.05	1.10	1.15
0.95	1.00	1.05	1.10	1.15
0.95	1.00	1.05	1.10	1.15
0.95	1.00	1.08	1.10	1.15
0.95	1.02	1.08	1.12	1.15
0.97	1.03	1.10	1.13	1.15
0.99	1.05	1.10	1.15	1.15
1.50	1.60	1.65	1.72	1.85
1.50	1.60	1.65	1.75	1.85
1.50	1.62	1.68	1.77	1.85
1.50	1.63	1.70	1.77	1.85
1.50	1.65	1.70	1.78	1.85
1.55	1.65	1.70	1.80	1.85
1.57	1.65	1.70	1.80	1.85
1.58	1.65	1.70	1.80	1.86
1.60	1.65	1.70	1.80	1.88
1.60	1.65	1.70	1.82	1.90

Table 6.9

Histogram of c-axial length distribution.

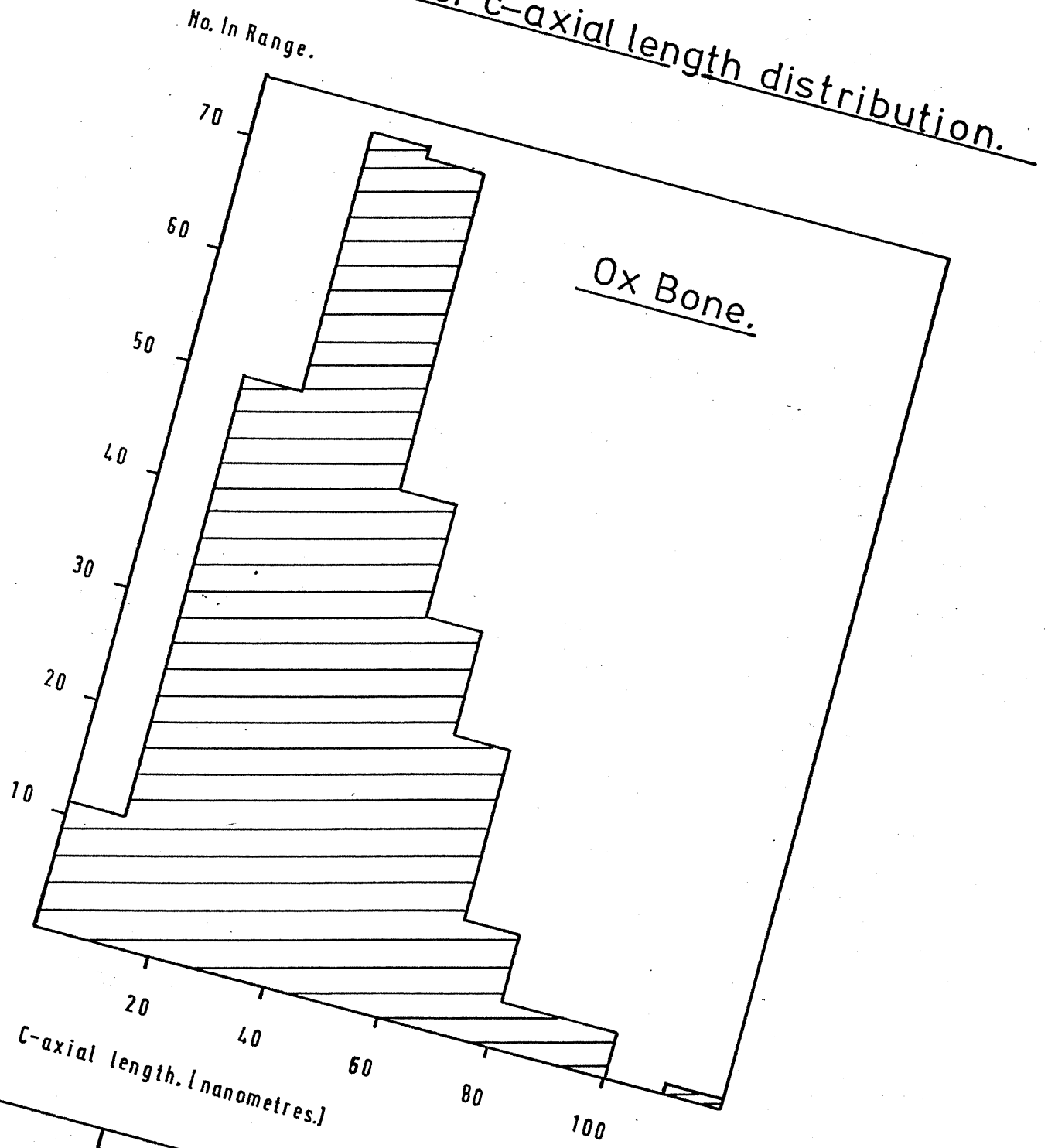

Min.	Max.	Mean.	S. D.
6·7nm.	113·0 nm.	36·2 nm.	19·0nm.

Figure 6.4

C-AXIAL LENGTH MEASUREMENTS

HUMAN BONE

0.18	0.25	0.30	0.34	0.40
0.20	0.25	0.30	0.35	0.43
0.20	0.25	0.30	0.35	0.43
0.20	0.27	0.30	0.36	0.43
0.22	0.27	0.30	0.38	0.45
0.23	0.27	0.30	0.38	0.45
0.24	0.29	0.33	0.38	0.45
0.24	0.29	0.33	0.38	0.45
0.25	0.29	0.34	0.38	0.45
0.25	0.30	0.34	0.39	0.46
0.72	0.75	0.80	0.83	0.88
0.74	0.75	0.80	0.83	0.88
0.74	0.75	0.80	0.84	0.88
0.74	0.77	0.80	0.84	0.88
0.75	0.78	0.81	0.84	0.88
0.75	0.80	0.82	0.85	0.90
0.75	0.80	0.82	0.85	0.90
0.75	0.80	0.82	0.85	0.90
0.75	0.80	0.82	0.85	0.90
0.75	0.80	0.83	0.85	0.90
1.10	1.15	1.20	1.23	1.30
1.10	1.15	1.20	1.24	1.30
1.10	1.15	1.20	1.24	1.30
1.10	1.15	1.20	1.25	1.30
1.12	1.15	1.20	1.25	1.30
1.12	1.15	1.20	1.25	1.32
1.12	1.17	1.20	1.26	1.33
1.13	1.18	1.20	1.27	1.34
1.15	1.18	1.22	1.29	1.35
1.15	1.20	1.22	1.29	1.35
2.00	2.70			
2.00	2.80			
2.00	3.00			
2.03				
2.05				
2.10				
2.10				
2.12				
2.15				
2.40				

Table 6.10

C-AXIAL LENGTH MEASUREMENTS

HUMAN BONE

0.47	0.53	0.58	0.65	0.70
0.47	0.54	0.58	0.65	0.70
0.48	0.54	0.60	0.65	0.70
0.48	0.55	0.60	0.65	0.70
0.48	0.55	0.62	0.67	0.70
0.50	0.55	0.62	0.68	0.70
0.50	0.55	0.62	0.68	0.70
0.50	0.56	0.65	0.68	0.70
0.50	0.57	0.65	0.69	0.70
0.52	0.57	0.65	0.70	0.72
0.90	0.90	0.95	1.00	1.07
0.90	0.91	0.96	1.00	1.07
0.90	0.93	0.97	1.00	1.07
0.90	0.94	0.97	1.02	1.08
0.90	0.94	0.99	1.04	1.08
0.90	0.94	1.00	1.05	1.10
0.90	0.95	1.00	1.05	1.10
0.90	0.95	1.00	1.05	1.10
0.90	0.95	1.00	1.05	1.10
0.90	0.95	1.00	1.06	1.10
1.35	1.40	1.50	1.57	1.75
1.35	1.40	1.50	1.57	1.80
1.35	1.40	1.50	1.59	1.80
1.35	1.40	1.50	1.60	1.85
1.37	1.40	1.50	1.60	1.85
1.38	1.40	1.50	1.64	1.90
1.38	1.43	1.53	1.64	1.93
1.40	1.44	1.54	1.65	1.97
1.40	1.45	1.55	1.70	2.00
1.40	1.47	1.55	1.70	2.00

Table 6.11

Histogram of c-axial length distribution.

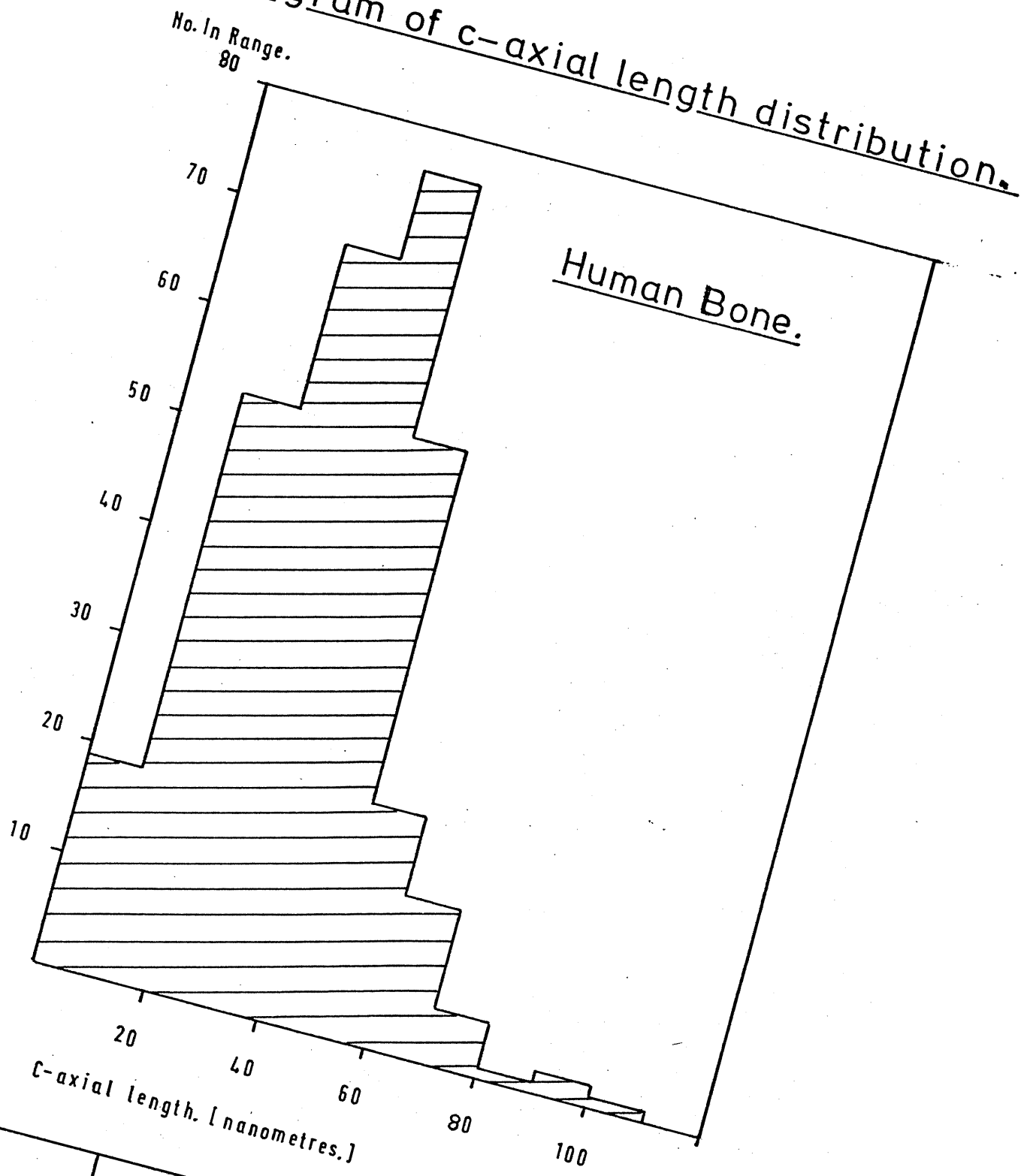

Min.	Max.	Mean.	S. D.
6·0nm.	100·0nm.	32·4nm.	16·3nm.

Figure 6.5

6.4.4. Comparison of Results

To compare the dark field measurements with the x-ray results, the following method was adopted.

From each set of dark field measurements, ten sub-sets of data were randomly selected, each sub-set containing twenty-five measurements. The mean values for the c-axial length calculated from these sub-sets, are normally distributed about the true mean. Hence, the average mean value calculated from the sub-sets could be compared with the x-ray measurements by the 't'-test.

Data Calculated From Dark Field Measurements

Rabbit Bone Mean of Sub-set	Ox Bone Mean of Sub-set	Human Bone Mean of Sub-set
0.91 (Cm)	1.12 (Cm)	0.98 (Cm)
1.02	1.17	1.22
0.97	1.17	1.05
1.03	1.04	0.99
0.99	1.15	0.90
0.74	0.91	0.95
1.05	1.02	0.96
0.97	1.14	1.01
1.06	1.02	0.97
0.91	1.06	0.87

Average of mean	Standard Deviation	Average of mean	Standard Deviation	Average of mean	Standard Deviation
0.97	0.09	1.08	0.08	0.99	0.10

Scale Factor. 1cm = 33.3 nm

Sample	Rabbit	Ox	Human
Average of Mean	32.3 nm	36.0 nm	33.0 nm
Standard Deviation	3.0 nm	3.0 nm	3.0 nm

Table 6.12.

The following test is a comparison of the two techniques which were used to measure the mean c-axial lengths of the three types of bone mineral.

Mean C-Axial Lengths

	X-ray Line Broadening		Dark Field E.M.	
Sample	Mean	Standard Deviation	Mean	Standard Deviation
Rabbit	27.9 nm	0.6 nm	32.3 nm	3.0 nm
Ox	28.3 nm	0.6 nm	36.0 nm	3.0 nm
Human	26.7 nm	0.6 nm	33.0 nm	3.0 nm

Table 6.13.

't' - Test on Means

Sample	Calculated 't' - statistic	Tabulated value of 't', at 5%. Level of significance. 't' = 2.201
Rabbit	2.44	
Ox	4.28	
Human	3.50	

Table 6.14

*The value of 't' was taken from Table III of Fisher & Yates: Statistical Tables for Biological, Agricultural and Medical Research, published by Oliver and Boyd Limited, Edinburgh.

The three 't'-statistics were calculated for each bone type using the respective means and standard deviations produced by the two techniques.

Since all the calculated 't'-values are greater than 2.201 for each bone type, the mean c-axial lengths, as measured by the two techniques are significantly different.

6.5. Revision of Techniques

6.5.1. Discussion

The two techniques, dark field electron microscopy and (002) line broadening produced estimations of the mean c-axial length of the same order, however, it has been shown that results are significantly different.

To explain the discrepancy it is necessary to examine the techniques more closely. The dark field method is relatively simple and does not involve any assumptions which could influence the result. However, it was assumed originally that the x-ray line broadening effect was due solely to crystal size. If another factor was involved and not accounted for, the value of $\beta_{\frac{1}{2}}$ would be larger than that obtained purely by the size effect. Hence an average size, smaller than the true mean would be calculated. The x-ray results are, in fact, smaller than the dark field results, thus indicating that another factor is influencing the width of the diffraction peak profile.

Since bone mineral is thought to be variable in its composition, probably due to the dynamic environment in which it is formed, it would seem likely that imperfections could arise in the lattice structure. In fact, dislocations have been visualised in some micrographs, see figure 5.5. These dislocations and other kinds of crystal fault produce internal strain on the crystal lattice, thereby producing variations in the d-spacing, and hence a spread of the diffracted peak profile, see figure 6.6. Hence, this strain effect, which some previous works have not allowed for, must be taken into account before accurate results can be obtained.

The Effect of Lattice Strain on the Diffracted Peak Profile.

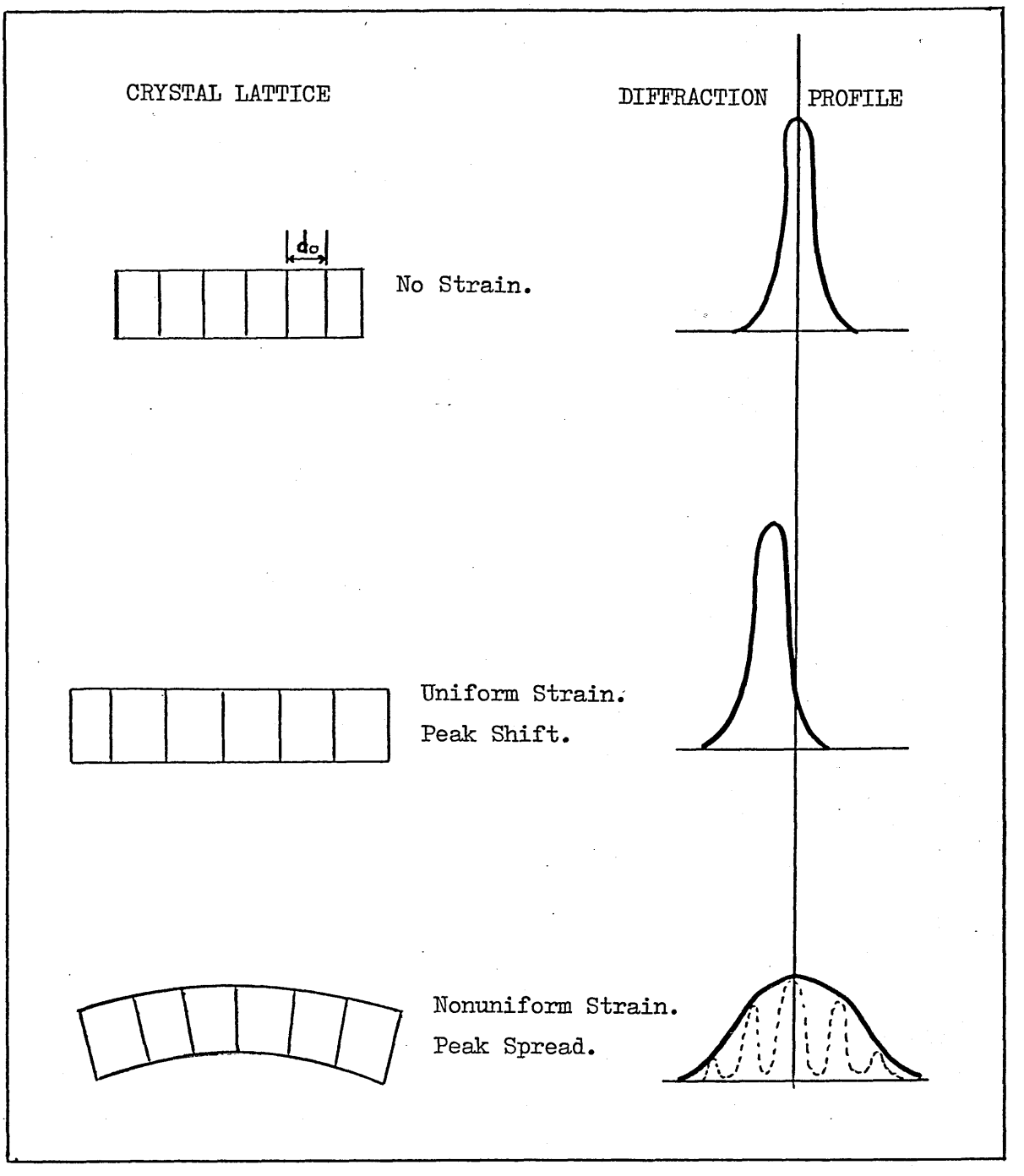

Figure 6.6

6.5.2. Derivation of the Strain Effect.

From the Bragg Law:-

$$2d\sin\theta = \lambda$$

$$\frac{\lambda}{d} = 2\sin\theta$$

Taking logs and differentiating

$$\frac{\Delta d}{d} = \cot\theta.\Delta\theta$$

Lattice strain is defined as $\varepsilon = \frac{\Delta d}{d}$

Also, $\beta_{\frac{1}{2}} = \Delta 2\theta = 2\Delta\theta$

$$\therefore 2\varepsilon = \cot\theta.\beta_{\frac{1}{2}}$$

$$\beta_{\frac{1}{2}} = 2\varepsilon\tan\theta \qquad (4)$$

ε, includes both tensile and compressive components, and if assumed equal, maximum tensile strain equals maximum compressive strain $= \frac{\varepsilon}{2}$

Using the formula for the addition of gaussian peaks,

$$(\beta_{\frac{1}{2}})^2 = (\beta_{\frac{1}{2}}\ \text{SIZE})^2 + (\beta_{\frac{1}{2}}\ \text{STRAIN})^2$$

Also: $$(\beta_{\frac{1}{2}})^2 = (B_{\frac{1}{2}})^2 - (b_{\frac{1}{2}})^2$$

$$\beta_{\frac{1}{2}}\ \text{SIZE} = \frac{0.9\lambda}{t\ \cos\theta_B}$$

$$\beta_{\frac{1}{2}}\ \text{STRAIN} = 2\varepsilon\tan\theta_B$$

$$\therefore (\beta_{\frac{1}{2}})^2\cos^2\theta_B = \left[\frac{(0.9\lambda)}{(t)}\right]^2 + 4\varepsilon^2\sin^2\theta_B \qquad (5)$$

If two diffraction peaks were used which originated from the same crystal planes, i.e., had the same t, but different values of $\beta_{\frac{1}{2}}$ and Θ_B, it would be possible to form two simultaneous equations and solve for t and ε. This has, in fact, proved to be possible by using the (002) and (004) diffracted beams.

The (004) beam being a second order reflection from the (002) planes, i.e., n = 2 in the Bragg Law.

$$2d\sin\Theta_B = n\lambda$$

Therefore, assigning β_1, Θ_1, β_2, Θ_2, to the (002) and (004) peak profiles respectively, and solving equation ⑤ for t and ε:-

$$t = 0.9\lambda \left[\frac{\sin^2\Theta_2 - \sin^2\Theta_1}{\beta_1^2 \cos^2\Theta_1 \sin^2\Theta_2 - \beta_2^2 \cos^2\Theta_2 \sin^2\Theta_1} \right]^{\frac{1}{2}} \qquad ⑥$$

$$\varepsilon = \tfrac{1}{2} \left[\frac{\beta_1^2 \cos^2\Theta_1 - \beta_2^2 \cos^2\Theta_2}{\sin^2\Theta_1 - \sin^2\Theta_2} \right]^{\frac{1}{2}} \qquad ⑦$$

6.5.3. Comparison of Results - 2

The new values of mean c-axial length were calculated using equation ⑥, which accounts for the small crystal size and also the internal lattice strain as line broadening effects. The results are shown in table 6.15 and compared by means of the t-test in table 6.16.

Mean C-Axial Lengths

	X-ray Line Broadening		Dark Field E.M.	
Sample	Mean	Standard Deviation	Mean	Standard Deviation
Rabbit	33.2nm	1.1nm	32.3nm	3.0nm
Ox	36.1nm	1.1nm	36.0nm	3.0nm
Human	32.2nm	1.1nm	33.0nm	3.0nm

Table 6.15

't' - Test on Means Produced by the Two Techniques

Sample	Calculated t-statistic	Tabulated value of 't'
Rabbit	0.840	't' at 5% = 2.201
Ox	0.093	
Human	0.712	

Table 6.16

Since the calculated 't'-values are less than the tabulated value at the indicated level of significance, the two methods used to measure the mean c-axial length produce values which show no significant difference.

Calculated values of the lattice strain factor (ε) are listed below in Table 6.17, their significance is mentioned later.

Calculated Values of (ε)

Sample	Mean (ε)	Standard Deviation
Rabbit	0.0061	0.0005
Ox	0.0064	0.0005
Human	0.0061	0.0007

Table 6.17

A 't'-test on the above values shows that there is no significant difference at the 5% level between the strain factors (ε) for the three bone types.

6.6. Conclusions

1. The mean c-axial length of bone mineral from three bone types has been measured by the dark field method, and by x-ray line broadening. It has been shown that when both lattice strain and crystal size are taken into account, the two techniques produce consistent results.

2. The lattice strain factor (ε) has been calculated, giving values for the maximum tensile or compressive strain in all samples of approximately 0.3%. This means that the crystals are basically straight in the direction of the c-axis, and hence the dark field images of bone mineral have been of the whole crystal and not just a small section of a large curved crystal.

3. Although not directly used in this work it may be of interest to note that of the three bone types examined, the mean c-axial lengths of rabbit and human bone mineral were not significantly different at the 5% level, but both were different to ox bone mineral.

The results presented here suggest that two factors could be responsible for discrepancy between x-ray and bright field electron microscopical estimations of c-axial length. Firstly, that lattice strain needs to be allowed for in line broadening measurements, and secondly that bright field estimations of c-axial length have little validity because crystal orientation is not known. The dark field technique, although lengthy to perform has proved valuable in two respects: it has helped to clarify past discrepancies and it has also provided a direct way to measure crystal size and size distribution.

At this stage it was felt that since consistent results could be obtained by both dark field and line broadening methods, that either technique could be used to investigate problems involving

bone mineral. Because interest has recently been shown in variation of the crystalline/amorphous composition of bone mineral, Termine and Posner (1967), it was decided to investigate this problem with one of the techniques developed in this work. Since the x-ray technique is relatively quick and easy to perform, and since it also gives information on crystal perfection it was the obvious choice. This topic is covered in the next chapter.

CHAPTER SEVEN

CRYSTALLITE VARIATION WITH AGE

7.1. Introduction

One interesting and important part of the many crystallographic studies of bone is the development and changes of bone mineral with age. Both the crystal morphology and crystalline-amorphous relationships of bone mineral will affect the physical, mechanical and chemical behaviour of bone tissue, and of course, it is necessary to be aware of any factors which could influence treatment required in pathological cases.

Hodge, (1949) suggested that bone mineral crystals might be smaller in newly formed, than in stable mature bone. He made this suggestion as a possible explanation of the more rapid uptake of radioactive phosphorus by traebecular bone in-vitro, when compared to compact shaft bone. Zetterström, (1952) also suggested that crystals in newly formed bone are probably smaller, less perfect in their crystal structure, and less stable than those in long established bone. Robinson and Watson, (1955) in an electron microscope study, found bone mineral in a two day old human infant, to have an irregular form with an average maximum dimension of less than 10nm, whilst a bone section taken from an 80 year old male contained crystals with a maximum dimension of approximately 150nm. These workers also suggested that since diffraction patterns of newly formed bone were considerably more diffuse than those produced by mature bone, this not only confirmed the finding of smaller crystals in new bone, but could also indicate that part of the mineral was not in a crystalline form. This latter point has been investigated extensively by Termine and Posner (1967), as mentioned previously in 1.7.8. They found that the crystalline fraction of bone mineral increases with age, as shown in figure 7.1., at the expense of the amorphous fraction. It can be seen from figure 7.1. that approximately 7 weeks after birth, a stable situation is reached and the amorphous-crystalline composition remains constant. This observation could be interpreted as a gradual maturation of the crystalline mineral via a transformation of the amorphous phase.

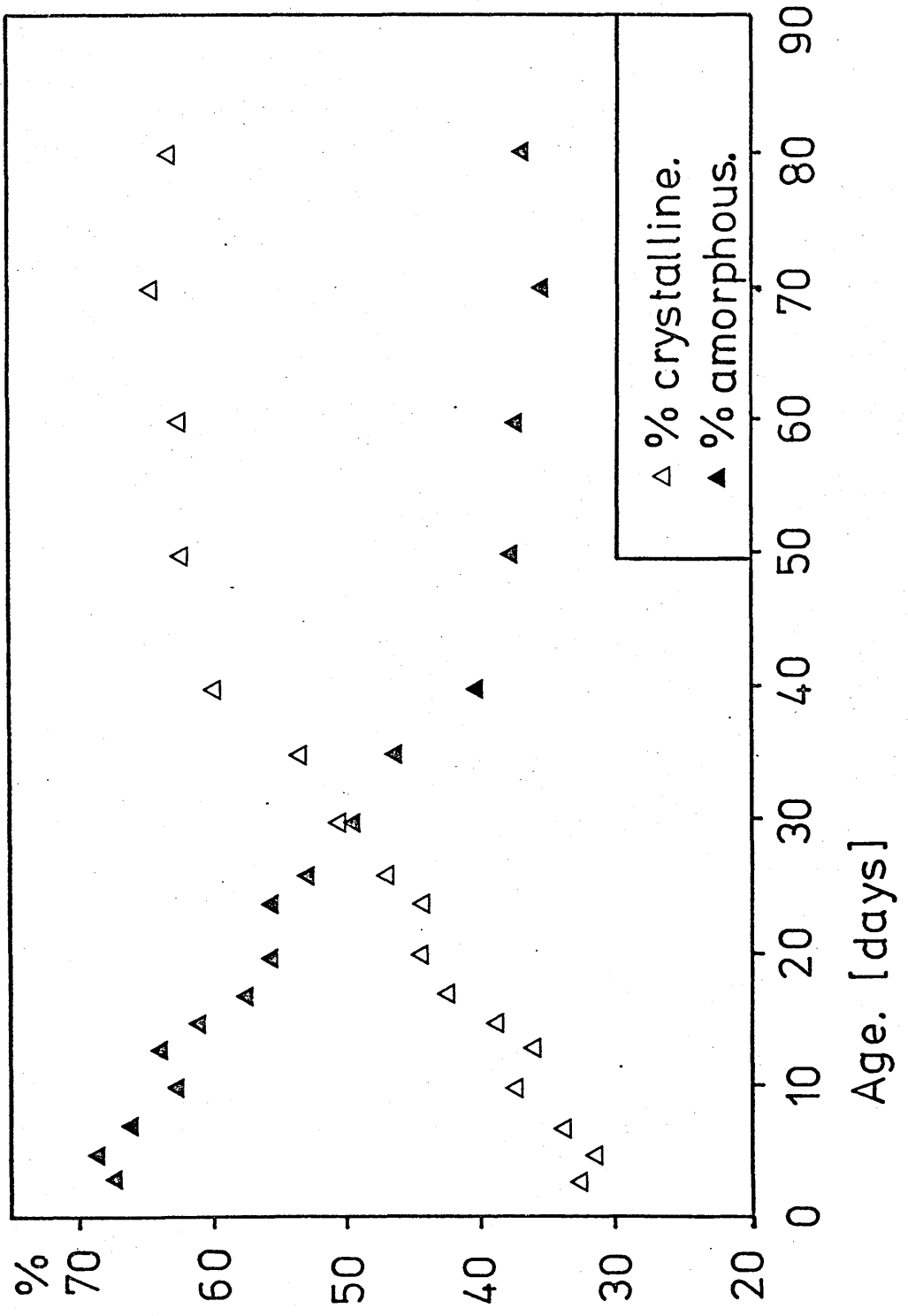

Figure 7·1

The crystalline-amorphous relationship of bone mineral as a function of age. Termine and Posner (1967).

The way in which crystal maturation takes place is still unclear, and it is the aim of this chapter to show how one of the techniques developed in this work can be used to investigate this particular problem. Since it has been shown in the previous chapter that the x-ray method of line broadening gives results which are consistent with dark field electron microscopy, only the x-ray method has been used. This method has the advantage of being relatively quick, producing an average result over a large sample of bone. Two types of information have been obtained, firstly details of the crystal size as indicated by the mean c-axial length, and secondly the crystal perfection is indicated by the lattice strain factor (ε). If the crystal structure has many defects in the form of unfilled lattice sites, and/or ionic substitutions, the crystal lattice becomes deformed, the amount of deformation being indicated proportionally by the strain factor (ε).

7.2. Materials and Method

The sample blocks for x-ray analysis were all prepared from the femora of female Dutch rabbits with ages as listed below, using only one femur for all except the first two cases where it was necessary to use both femora to fill the specimen slab.

Sample	Preparation
1. Age 1 week	Killed by barbiturate overdose. Deep frozen for 1 week, otherwise untreated.
2. Age 2 weeks	Treatment as above.
3. Age 7 weeks	Killed by breaking neck. Femur removed and used immediately without further treatment.
4. Age 6 months	Treatment as above.
5. Age 12 months	Treatment as above.

7.3. Results

As in the previous chapter three separate measurements were made of the experimentally observed half width $B_{\frac{1}{2}}$ and the peak position ($2\theta_B$) for both the (002) and (004) diffracted beams.

Sample 1. (Age 1 week)

Peak	002	004
$B_{\frac{1}{2}}$ (degrees)	0.563 0.575 0.588	1.00 1.06 1.06
$2\theta_B$ (degrees)	26.13 26.09 26.10	53.55 53.51 53.46

Table 7.1.

Sample 2. (Age 2 weeks)

Peak	002	004
$B_{\frac{1}{2}}$ (degrees)	0.438 0.450 0.450	0.838 0.838 0.850
$2\Theta_B$ (degrees)	26.06 26.09 26.10	53.51 53.51 53.50

Table 7.2.

Sample 3. (Age 7 weeks)

Peak	002	004
$B_{\frac{1}{2}}$ (degrees)	0.342 0.317 0.325	0.517 0.492 0.533
$2\Theta_B$ (degrees)	26.02 26.02 26.03	53.36 53.38 53.38

Table 7.3.

Sample 4. (Age 6 months)

Peak	002	004
$B_{\frac{1}{2}}$ (degrees)	0.333 0.342 0.325	0.558 0.508 0.483
$2\Theta_B$ (degrees)	26.01 26.02 26.00	53.29 53.28 53.31

Table 7.4.

Sample 5. (Age 12 months)

Peak	002	004
$B_{\frac{1}{2}}$ (degrees)	0.308 0.325 0.342	0.500 0.525 0.558
$2\Theta_B$ (degrees)	26.03 26.04 26.04	53.33 53.31 53.32

Table 7.5.

Calculation of (t) and (ε)

The values for the c-axial length and strain factor (ε), have been calculated exactly as in the previous chapter, and results are tabulated below in table 7.6.

Figures 7.2 and 7.3 show the results for all samples in graphical form, the mean values for each parameter being plotted with one standard deviation.

Calculated values of (t) and (ε)

Sample	t (mean c-axial length) namometres	(ε) lattice strain (%)
1	22.4 22.4 22.4	1.55 1.68 1.66
2	36.9 32.6 34.5	1.34 1.32 1.35
3	32.6 34.5 36.9	0.68 0.62 0.72
4	36.9 30.9 32.6	0.78 0.60 0.60
5	36.9 34.5 34.5	0.66 0.70 0.76

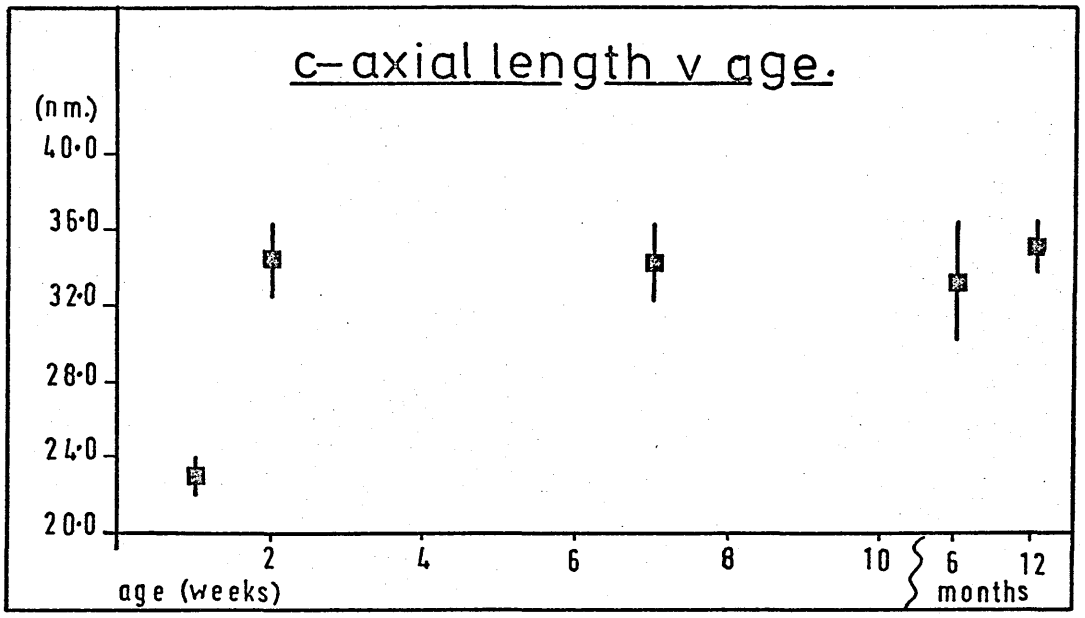

Figure 7·2

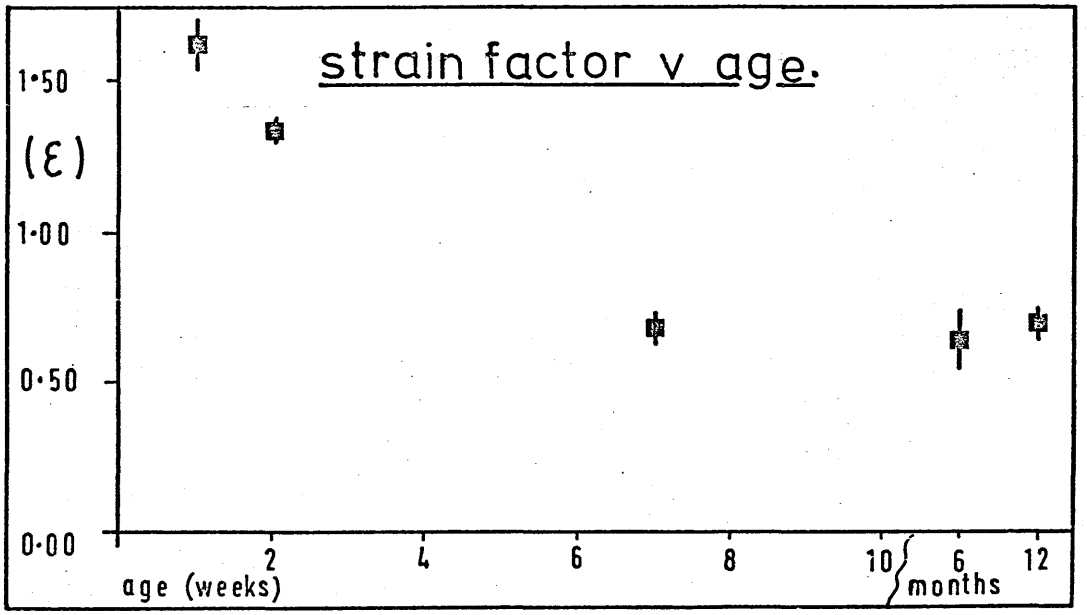

Figure 7·3

7.4. Summary

a) The samples aged 7 weeks and above show no significant difference at the 5% level, between their mean c-axial lengths or their mean values of the lattice strain factor (ε).

b) The two weeks old sample exhibits the same mean c-axial length as the older samples but has a strain factor which is significantly different to both the younger and older bones.

c) The one week old sample exhibits a mean c-axial length significantly smaller than the other four samples, and also a significantly higher value of the strain factor (ε).

From these preliminary results, the following conclusions can be tentatively drawn.

These results would be consistent with a crystal maturation process in which the full crystal size is reached within two weeks from birth, but the actual crystal structure not reaching its stable form until a later date, up to seven weeks, when both the mean crystal c-axial length and lattice strain factor appear to stabilise.

It was noted that the one and two week old samples produced diffraction peaks which were considerably weaker than those produced by the other samples, and this would be consistent with the results shown in figure 7.1., where the amount of crystalline mineral gradually increases until approximately 7 weeks after birth, when a stable situation is attained.

This chapter has illustrated one possible application of the x-ray technique to the study of bone mineral, however, the results are clearly very tentative and further work is needed to confirm these findings.

CHAPTER EIGHT

BONE MINERAL ORIENTATION

8.1. Introduction

Bone mineral is seen to impart strength and rigidity to an otherwise flexible substance, and therefore changes in the mineral size, shape, or composition are almost certain to affect the physical properties of bone. The work so far has been concerned with a determination of these factors using both new and old techniques. Exactly how physical and structural parameters are related in a complex material such as bone is a topic requiring a great deal of further research, and this work forms only one part of that topic. Furthermore, the remainder of this work, which is directed towards the same end as the first part, is concerned with the development of a technique for the determination and study of bone structure but this time on the macrosopic level.

It is generally accepted that bone mineral crystals have their c-axes aligned, on average, with the collagen fibre axes. Thus a study of the crystallite orientation enables the fibrous structure of bone to be determined. X-ray diffraction provides a rapid technique for measuring the crystal orientation, both qualitatively and quantitatively.

There have been many studies of the physical properties of bone, in particular its anisotropic piezoelectric and elastic properties have been investigated, Fukada and Yashuda (1957), Bassett and Becker (1962), Lang (1970). These studies have assumed that the crystallites of bone are all uniformly oriented in a homogenous, regular structure. In fact, by examining most x-ray diffraction photographs of laminar bone, it is found that the crystal c-axes are distributed about one general direction, and since the physical properties of a material such as bone are bound to be dependent upon its crystalline structure, it is important that details of its structure be determined as accurately as possible.

It is the aim of this work to determine the three dimensional crystal orientation, and thereby the complete fibrous structure of bone quantitatively, in an endeavour to aid the interpretation of physical tests, and thereby help in the understanding of the behaviour and function of bone tissue.

8.2. The Stereographic Projection

When studying three dimensional orientation, (of bone mineral crystals in this case), it is important to be able to represent the information in a two dimensional form, and this is accomplished by using the stereographic projection. A single x-ray diffraction photograph can only give two dimensional information, and figure 8.1. shows how the (002) arcs from a sample of bone describe the orientation of crystals which are aligned in a cone of semi-angle $(90-\Theta)$ in the bone section. Several diffraction patterns, taken with the sample in different positions would be necessary to determine the entire three dimensional orientation, and a convenient way of compressing this information onto a single diagram is via the stereographic projection.

If the bone sample is considered to be at the centre of a reference sphere, and the c-axes of the crystals are extended to intersect this sphere, thereby producing a c-axial density distribution over the surface, contour lines could be plotted connecting points of equal density. Thus the entire c-axial orientation can be represented as a density function on the surface of a sphere. The information contained on the reference sphere is then projected onto a plane parallel to the N-S axis as shown in figure 8.2. The result of projecting a sphere ruled with parallels of latitude and longitude is also shown in figure 8.2., and the particular importance of this projection will become apparent in the following chapters. When used to describe crystal orientation in this way, the resulting stereographic projection is known as a pole figure. The pole of a certain set of crystal planes is the intersection of a line drawn perpendicular to those planes, and the reference sphere, and hence the c-axial density distribution for bone mineral represents the (002) pole figure of bone.

To give the reader 'a feel' for pole figures, three examples are given in figure 8.3., showing possible orientations of bone mineral crystals and their respective (002) pole figures.

Diffraction Geometry for the Flat Film Method.

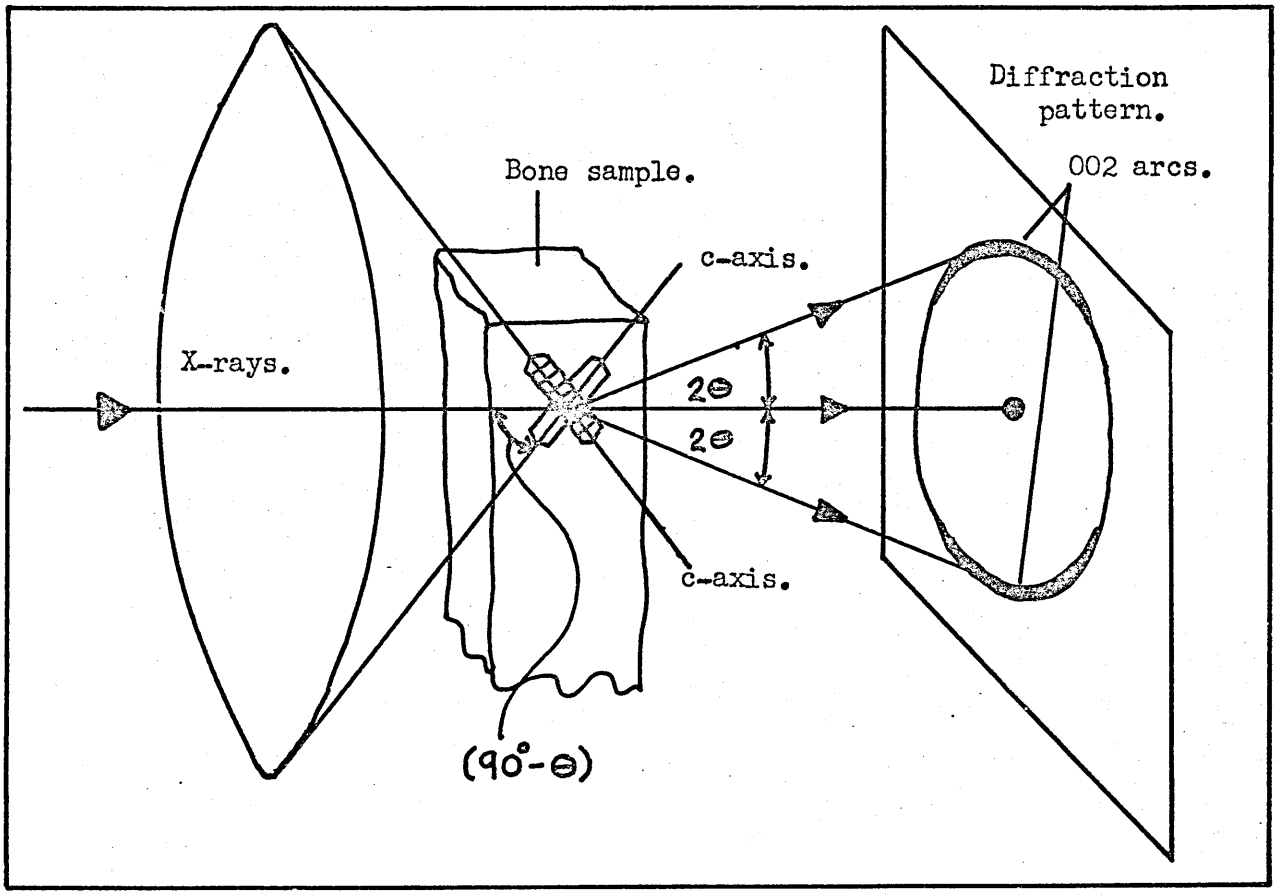

Figure 8.1

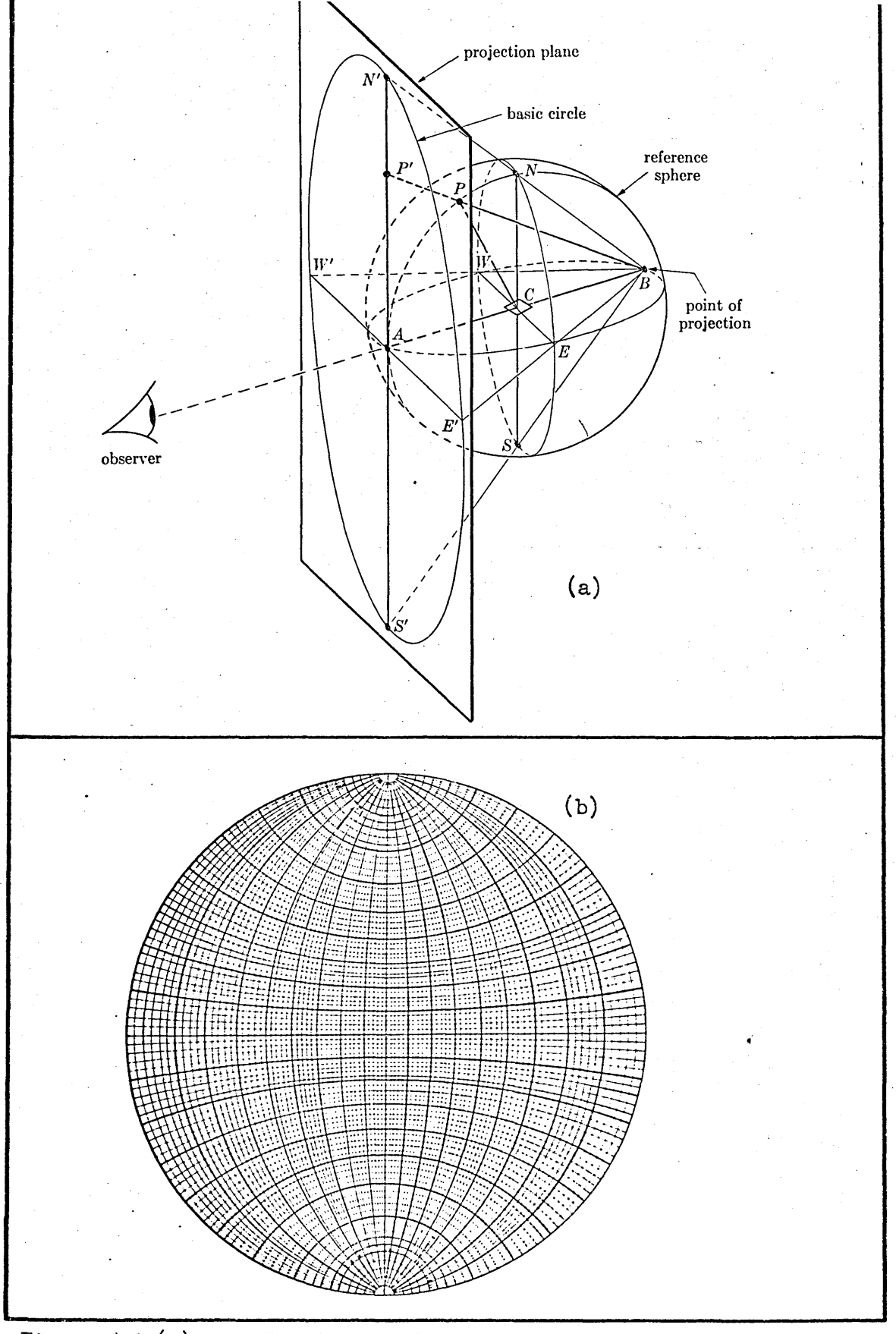

Figure 8.2 (a), construction of the stereographic projection. (b), stereographic projection of a reference sphere ruled with lines of latitude and longitude.

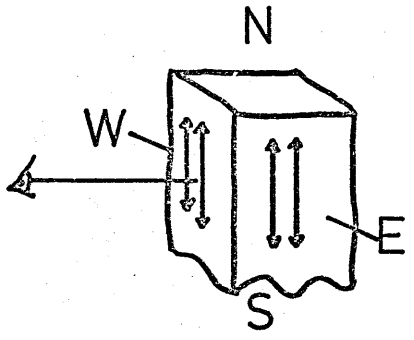

All crystal c-axes perfectly aligned in N/S direction.

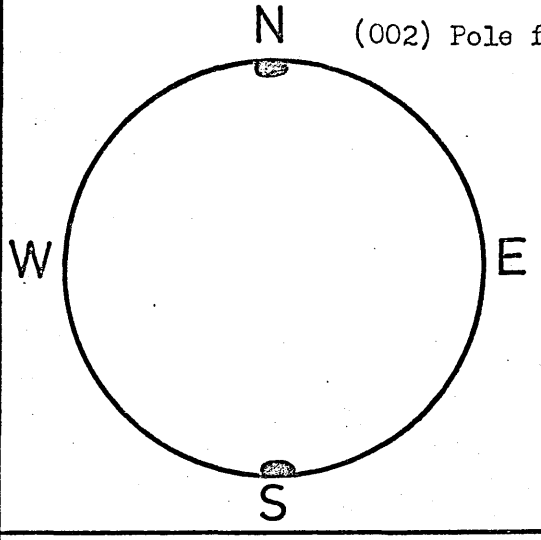

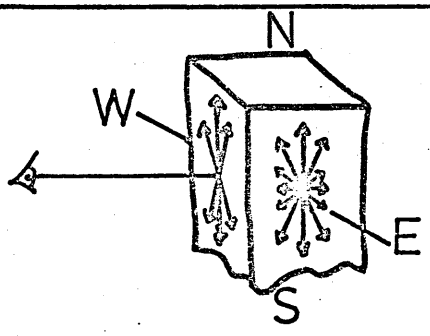

Main c-axial orientation still N/S, but spreading as shown.

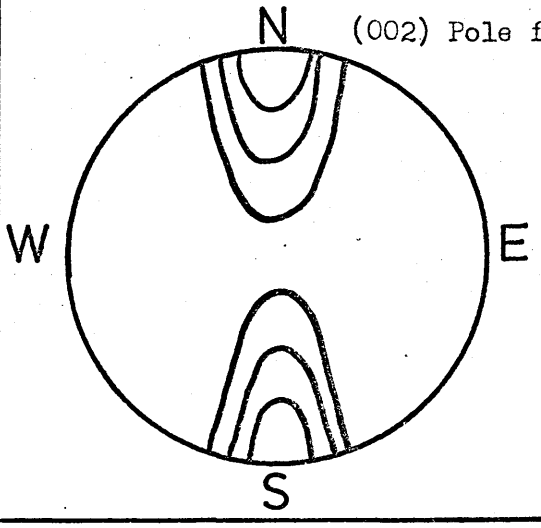

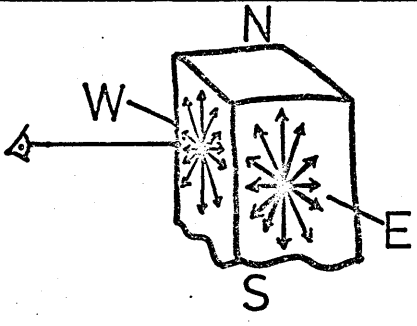

Main c-axial orientation still N/S, but spread about this direction as shown.

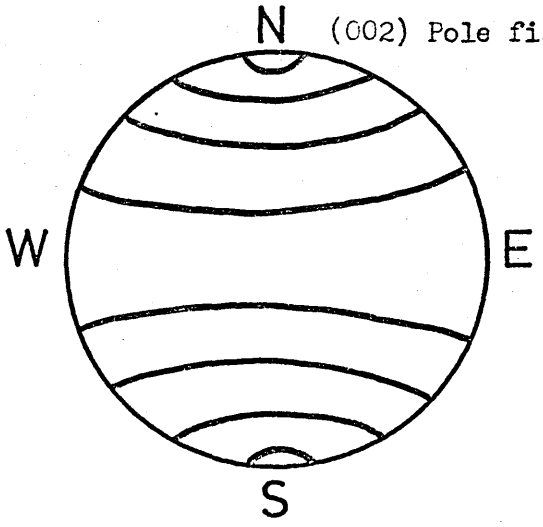

Figure 8·3

8.3. Preliminary Film Work

A preliminary investigation into crystallite orientation was performed by the author, M.Sc. Thesis (1973). In this work, cortical bone samples from the mid-femural section of goat femur were examined by x-ray diffraction using the flat film method. Bone slices, approximately 70 microns thick were cut from the femora using a Metals Research macrotome, and the x-ray diffraction patterns were compared with light microscope pictures taken using both normal and polarised light illumination, the polarised light micrographs indicating the laminar arrangement of the samples. Figure 8.4. shows one such comparison.

By comparing micrographs and diffraction patterns of bone slices cut in three mutually perpendicular directions it was possible to obtain a qualitative idea of the three dimensional arrangement of bone mineral within the sample.

The collagen fibre orientation was also examined directly by x-ray diffraction of decalcified bone slices. The type of diffraction pattern produced is shown in figure 8.5. A full interpretation of this pattern is complex, however, the strong equatorial reflection near the centre arises from an interplanar spacing of 1.05nm - 1.40nm; and is thought to originate from the lateral packing of the tropocollagen molecules, Rich and Crick (1961). Unfortunately, this reflection is affected by the water content of the sample, Ramachandran and Kartha (1955), thereby making collagen unsuitable for a quantitative study of the fibrous orientation. However, as was mentioned earlier, the c-axes of bone mineral crystals are aligned, on average, with the collagen fibre axes, and thus provide a possible method for a quantitative structure determination.

As an initial attempt to produce semi-quantitative results, the diffraction patterns of bone slices were analysed in the following way. Microdensitometer traces were taken across the

Cont. P175

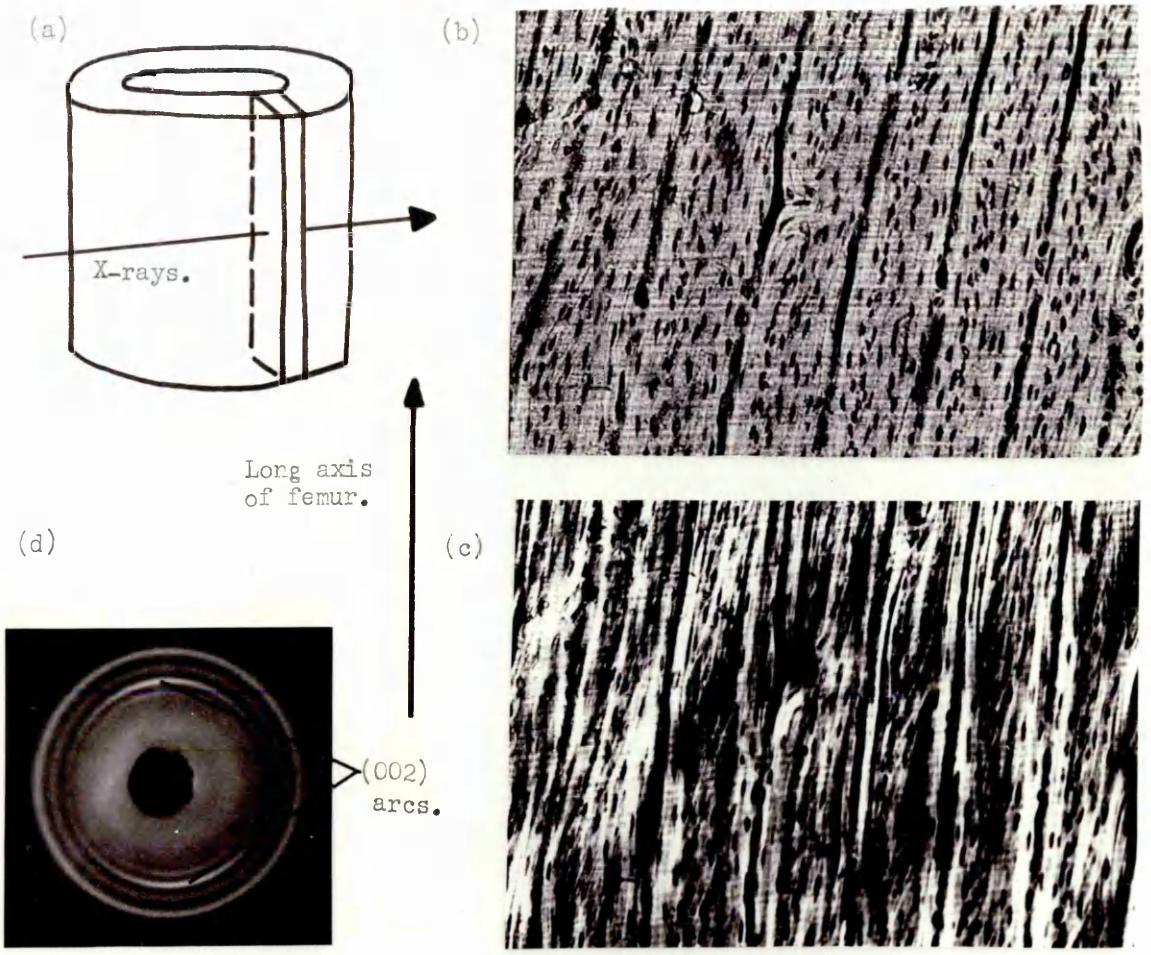

Figure 8.4

(a) Longitudinal section of goat bone taken from the mid-femural region.

(b) Sample examined using ordinary illumination. (x 50).

(c) Sample examined using polarised light illumination,(x 50).
From this and other micrographs of this sample it can be seen that the collagen fibres are laminated circumferentially around the bone shaft.

(d) The (002) arcs in the X-ray diffraction pattern indicate a c-axial alignment on average with the long axis of the femur.

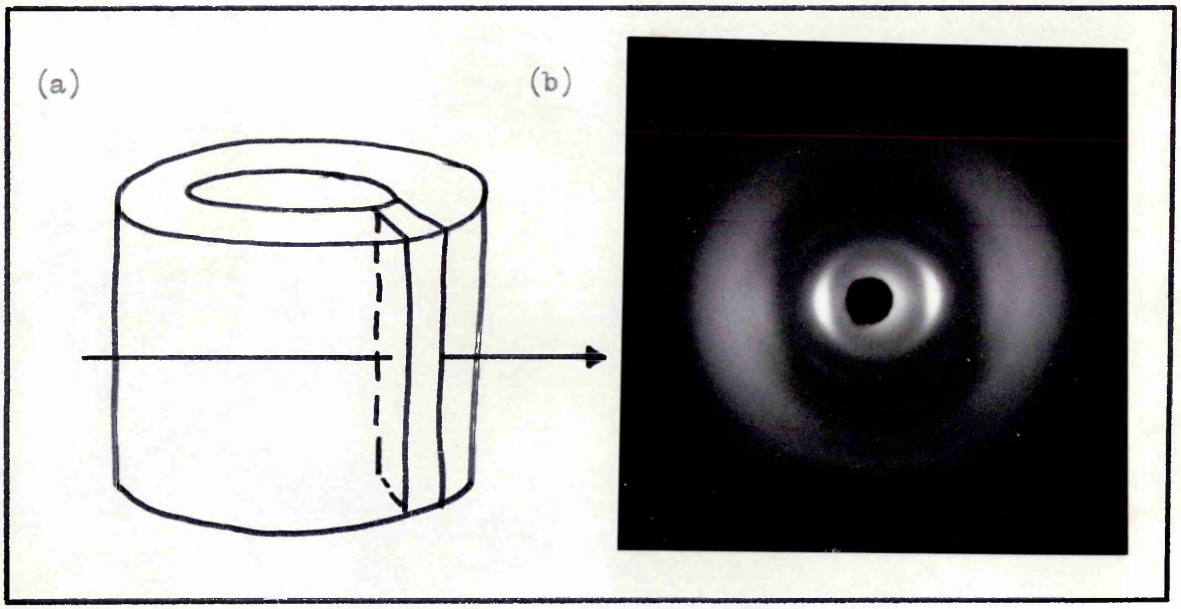

Figure 8.5

(a) The bone sample was cut as shown, approximately 1mm. thick, from the mid-femural region of a goat femur and demineralised in dilute nitric acid.

(b) The diffraction pattern of bone collagen. The two strong reflections near the centre of the pattern correspond to a d-spacing of approx. 1nm., and are thought to arise from the lateral aggregation of the tropocollagen molecules. This pattern indicates a fibre orientation along the long axis of the femur.

diameter of the diffraction pattern, and then the pattern was rotated in ten degree steps, until a full 360^{o} had been covered. The areas under the (002) peaks produced by the microdensitometer for each scan were proportional to the number of crystals aligned in that direction. These areas were measured and plotted as shown diagramatically in figure 8.6. This method however, suffers from three major disadvantages:

1) Because of the geometrical arrangement of a flat plate camera, the (002) arcs show the orientation of crystals aligned in a cone of semi-angle $(90-\theta)$, and not in the plane of the section as would be desired, see figure 8.1.

2) The analysis is lengthy to perform.

3) The data is processed many times and this leads to inaccuracies.

From the qualitative results obtained from this preliminary work, it could be seen that primary bone and secondary type bone possessed different fibrous arrangements. Secondary bone having a rotational symmetry about the main fibre direction which was on average the long axis of the femur, while primary bone exhibits a more planar fibrous structure, with the planar orientation in the direction of the laminar arrangement.

It was decided that in order to pursue this work further and to obtain useful information, it was necessary to obtain quantitative results. Consequently, an x-ray goniometer was designed which would provide the facility for an automatic, quantitative determination of the three dimensional crystallite orientation of small bone samples, and this is described in the next section.

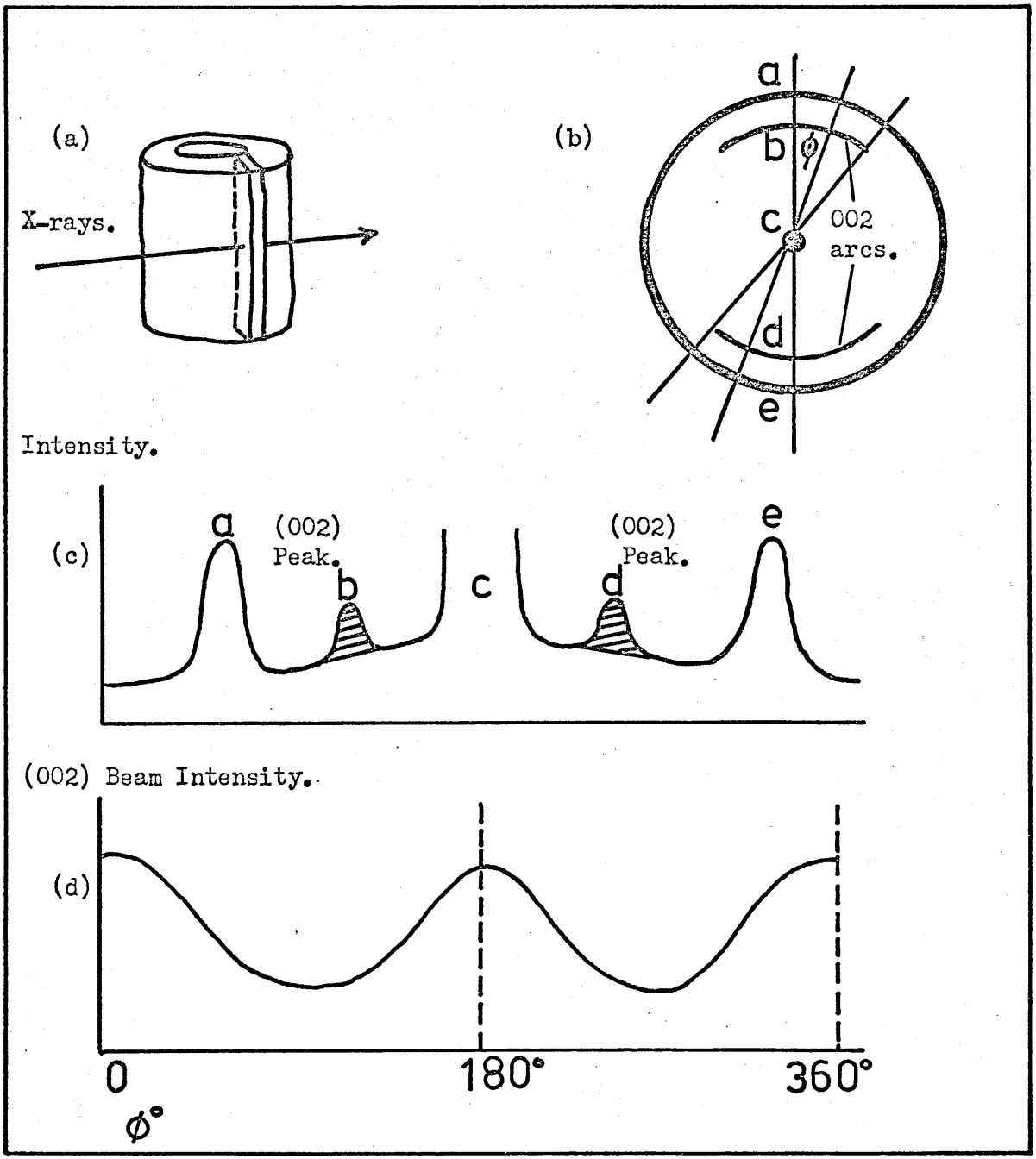

Figure 8.6

(a) Bone sample cut from the femur and X-ray diffraction pattern produced.

(b) The diffraction pattern is scanned in lines as shown, using a microdensitometer.

(c) The microdensitometer trace.

(d) The (002) beam intensity, (peak area) versus ϕ, for $\phi = 0°$-$360°$.

8.4. The X-ray Goniometer

A goniometer is basically a device to hold and position a specimen with relation to a beam of x-rays. Since it was envisaged that very small samples of bone, such as traebeculae would be examined in this work, accurate machining was necessary to keep the sample accurately aligned within the x-ray beam as its position was changed. This condition was one of the basic reasons why small pieces of bone could not be examined using existing goniometers which were designed for larger samples. Figure 8.7. shows diagramatically the geometrical arrangement and movement of the proposed goniometer.

The x-ray beam and counter are each inclined at Θ_B, the Bragg angle to the base line (X), and thus the (002) diffracted beams which are detected by the counter arise from bone mineral crystals whose c-axes are oriented in the (Y) direction. The counter remains fixed as the sample is rotated about the (X) direction. The angle of acceptance of the counter was such that the full width of the (002) diffracted beam was measured, and therefore the beam intensity, as indicated by the counter output, was directly proportional to the number of crystals with their c-axes aligned in the (Y) direction. Only 180° rotation through the angle (ϕ) was necessary to determine a full two dimensional c-axial orientation in the plane Y, XX, since diffracted beams in the second 180° (ϕ) arise from inverted crystals of the first 180° (ϕ) section.

Very small bone samples only produce weak diffracted beams, and therefore samples have to be rotated in a stepwise fashion to allow sufficient counts to be recorded. Since the stepping facility was not incorporated into any standard goniometers, this proved to be another reason for the construction of a special instrument.

The completed goniometer is shown in figure 8.8. The entire construction is mounted on a standard goniometer base plate which enables the device to be positioned accurately on the

Geometrical Arrangement of the Goniometer.

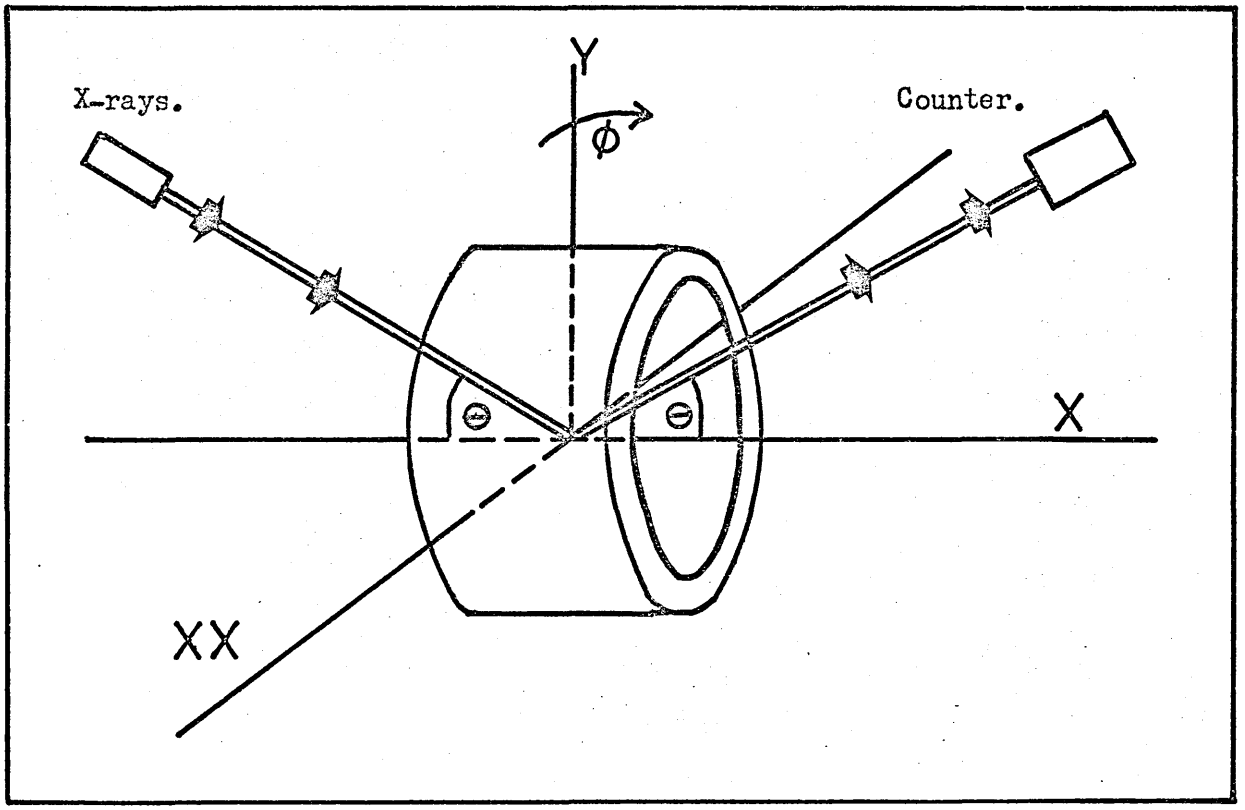

Figure 8.7

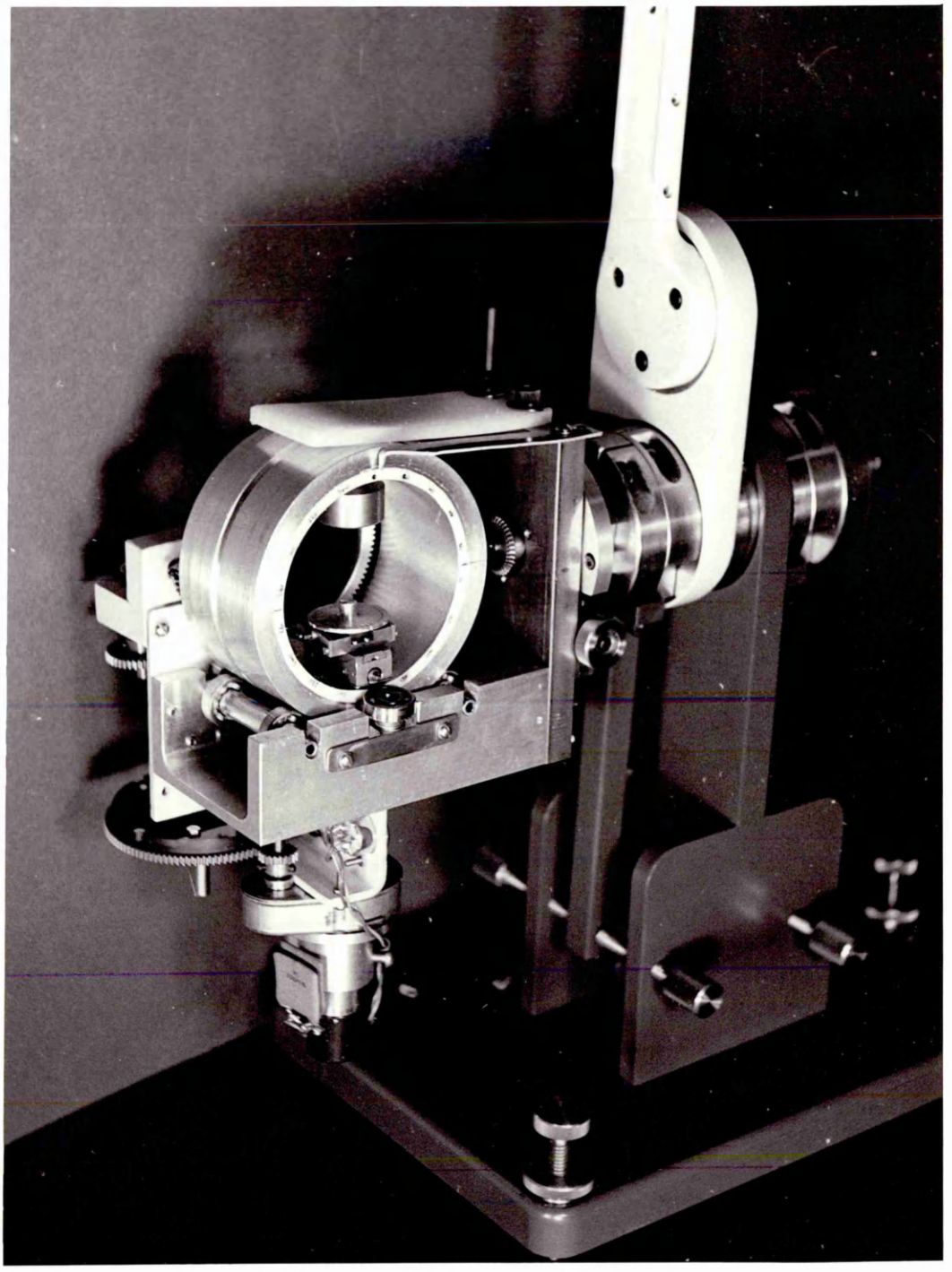

Figure 8.8a

The X-ray Goniometer, Frontal Aspect.

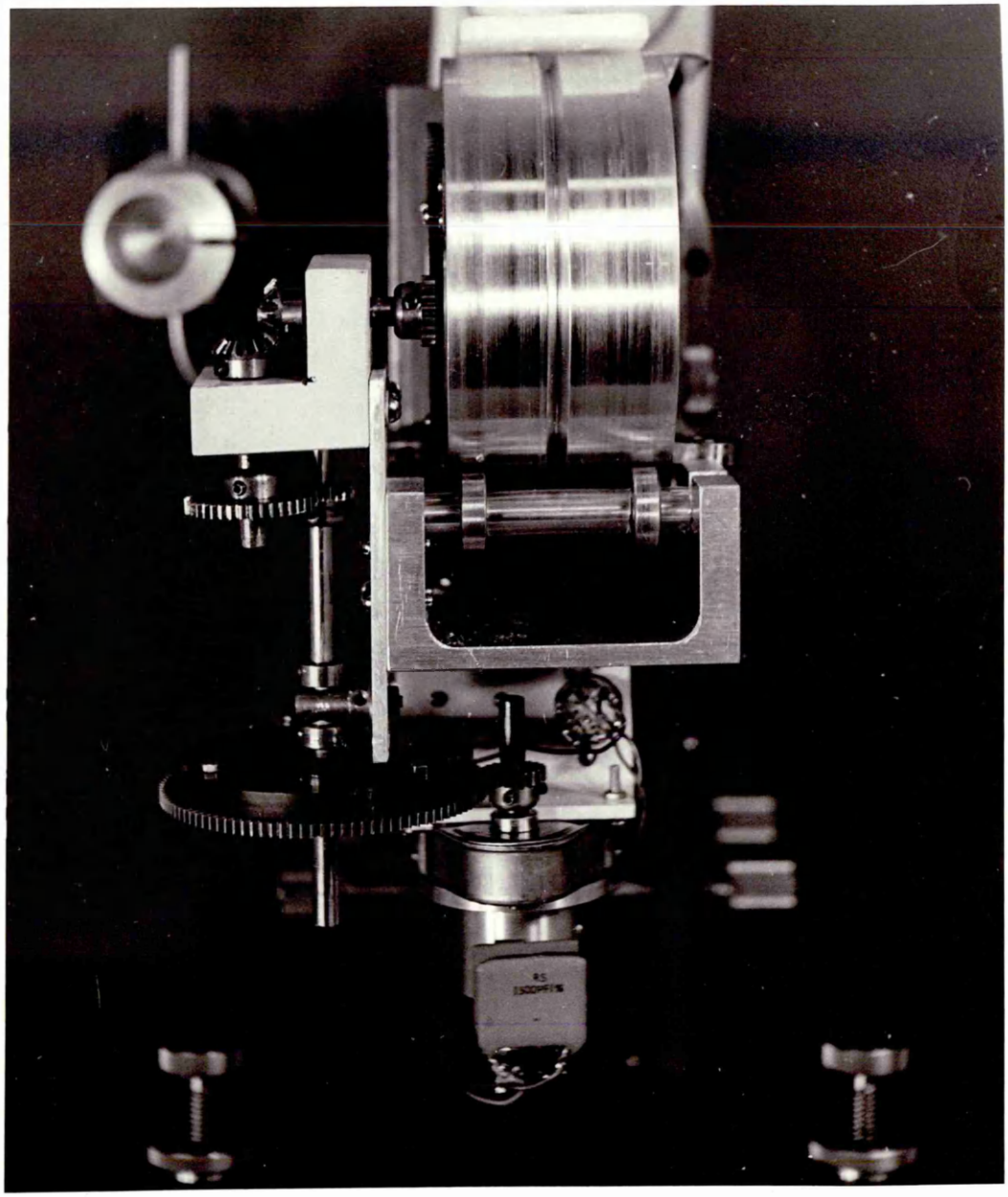

Figure 8.8b

The X-ray goniometer, side aspect, showing the indexing ring and the drive mechanism.

x-ray set. Since cost was an important factor in the design, the instrument was assembled from readily available components. The short cylinder, which contains the specimen mount and counter balance, is supported in a channel section on four small ball races, a nylon pressure finger keeping the cylinder firmly located whilst allowing smooth rotation. The specimen mount provides the facility for fine adjustment of the specimen position, and also rotation about its own axis, see figure 8.9. The cylinder is driven by a 6 volt D.C. motor, via a system of gears which provide a suitable reduction of motor speed. Mounted onto one of the gears is an indexing ring which operates a microswitch, and via this method, which is described fully below, the cylinder can be rotated in a stepwise fashion.

To gain maximum benefit from the goniometer it was decided to automate the movement of the sample, since stepwise coverage of 180^{o} (ϕ) at low count rates could prove to be a lengthy process. It was also planned to be able to vary the angular step and counting time per step, to suit the sample. Since a commercial stepping motor was impractical for financial reasons, the stepping motion was accomplished in the following way.

A 6 volt D.C. motor was pulsed from the control unit, which is described later, sufficiently to move the indexing ring to switch on the microswitch, and once this motion had been started, it stopped only when the microswitch fell into the next groove on the indexing ring. Thus the angular step was determined by the gearing ratio between the indexing ring and cylinder, and the spacing of the grooves on the ring. In practice, it was found satisfactory to have four grooves equally spaced on the indexing ring, providing an angular step of 9^{o} (ϕ) for the specimen, see figure 8.10. The pulse used to initiate a step was derived from existing equipment. The output from the counter was fed into a commercial scaler/timer

The Goniometer Specimen Holder.

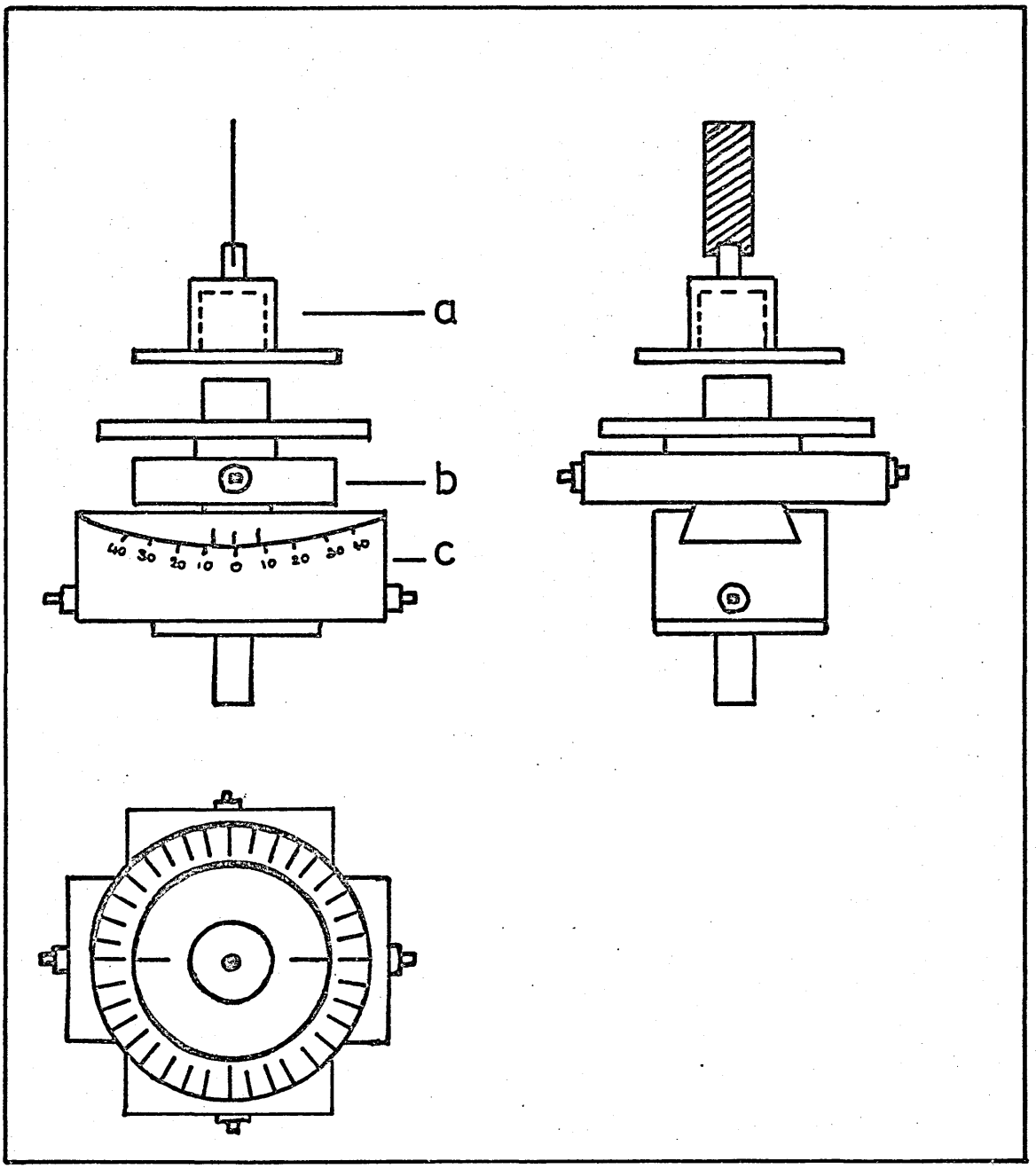

Figure 8.9

Section (a) allows rotation of the specimen about the vertical axis.

Section (b) allows fine lateral adjustment of the sample with respect to the X-ray beam.

Section (c) allows the specimen tilt to be adjusted.

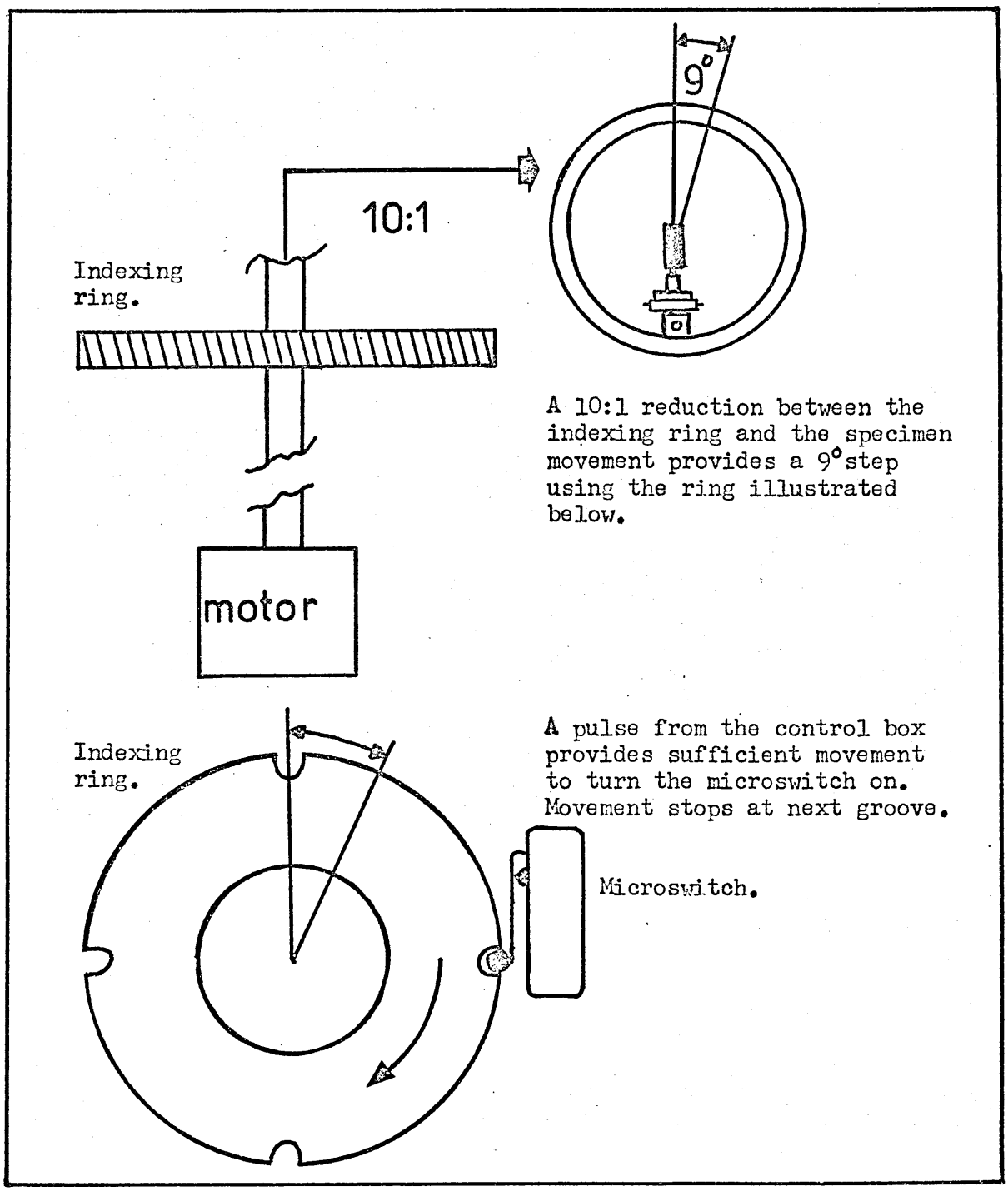
9°
10:1
Indexing ring.
motor
A 10:1 reduction between the indexing ring and the specimen movement provides a 9° step using the ring illustrated below.
Indexing ring.
A pulse from the control box provides sufficient movement to turn the microswitch on. Movement stops at next groove.
Microswitch.

Figure 8.10

unit which allowed either a pre-set count, or pre-set time of count to be selected, and also either analogue output on a strip chart, or numerical output via teletype. The scaler/timer unit also had the provision for repeat counts, and this was utilised in the following manner.

When the numerical output and repeat count mode was selected, the count was made, and then stopped whilst the output was being typed, and when completed the timer/scaler was re-set and the next count started automatically. An electronic pulse was required to initiate the goniometer movement when each count was completed, and this was extracted from the control electronics which started the teletype motor. The time delay between counts, i.e., the time taken to type out the result was approximately 4 seconds. Normally it would be necessary to re-set the scaler/timer after the specimen movement was completed, however, with a 9^{o} step, the movement was completed in less than 4 seconds and so it was unnecessary to provide an extra re-set line to the counter. The extracted pulse used to initiate the specimen movement had to be shaped electronically to fulfill its function, figure 8.11 shows the initial pulse and the final shaped pulse, together with the electronic shaping circuit. To eliminate the base-line ripple of the input pulse, a voltage comparator consisting of R1, R2 and A is used. The inverting (-) input of the 741 operational amplifier is held at +5 volts, if the non-inverting input (+) is below 5 volts, then the output is saturated at -15 volts, and if the (+) input rises above 5 volts the output saturates at +15 volts. Hence the base-line ripple of the input pulse will have no effect upon the state of the output. Only when a pulse greater than 5 volts is applied to the non-inverting input will the output change state. The -15v to +15v pulse is converted to a -2.5v to +2.5v pulse by the potential divider R3, R4, and this resulting pulse is sufficient to trigger the monostable circuit (SN74121N), which was set with a time constant of approximately 1 second, and is non-retriggerable.

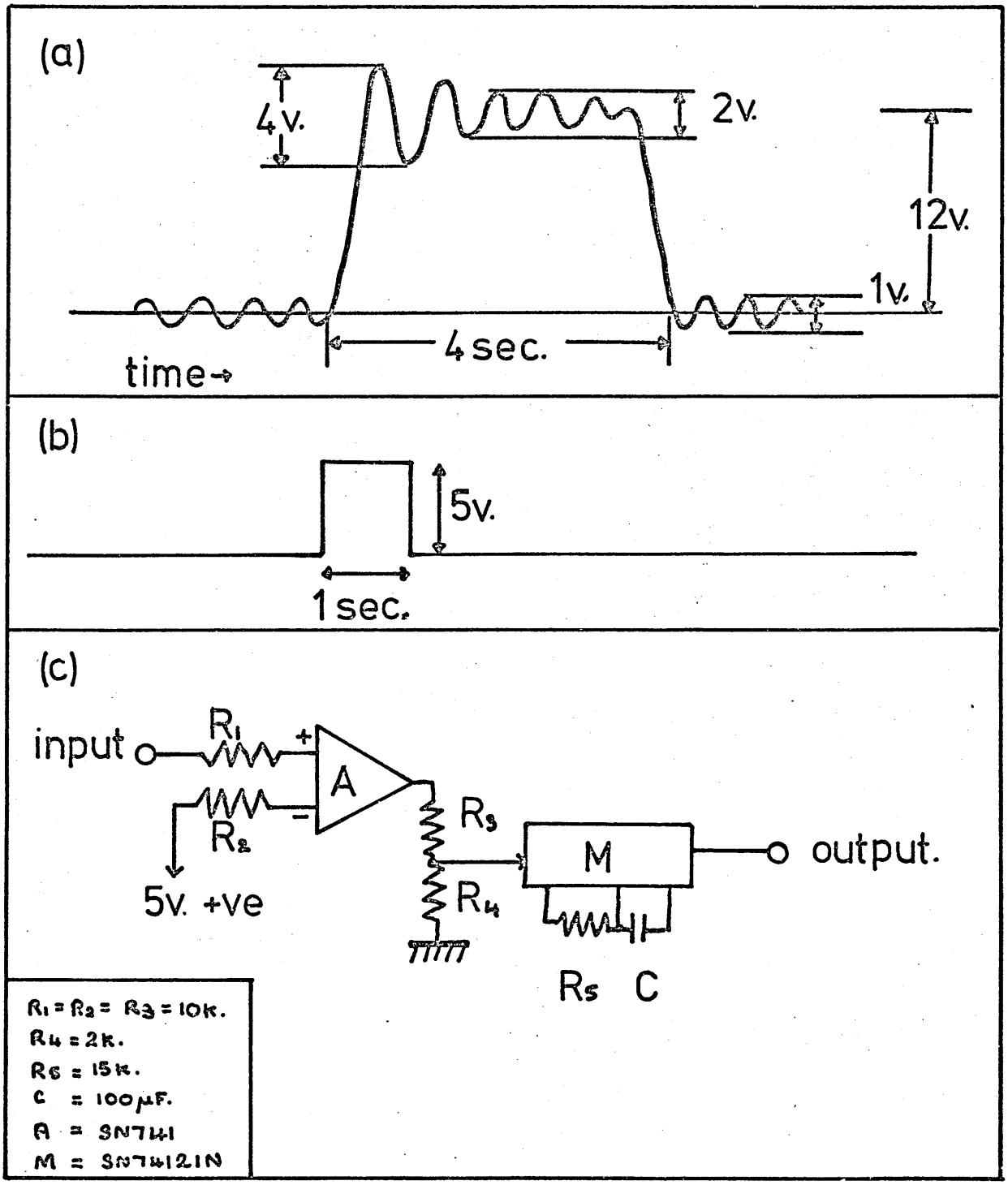

Figure 8.11

(a) The 'motor start' pulse, extracted from teletype.

(b) Desired output to pulse the goniometer motor.

(c) The electronic shaping circuit which converts (a) to (b).

The Goniometer Circuit Diagram.

Block Diagram.

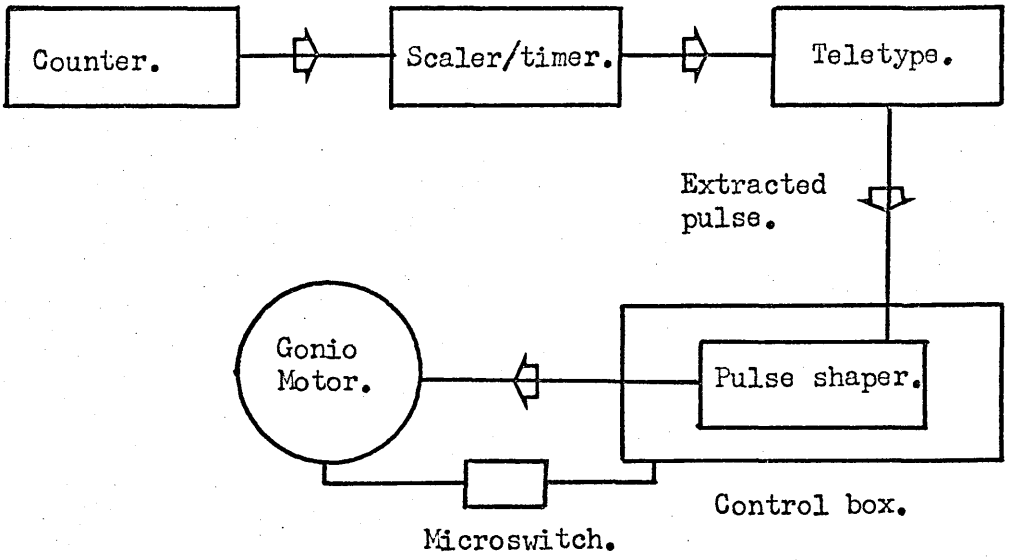

Control Box

Wiring Diagram.

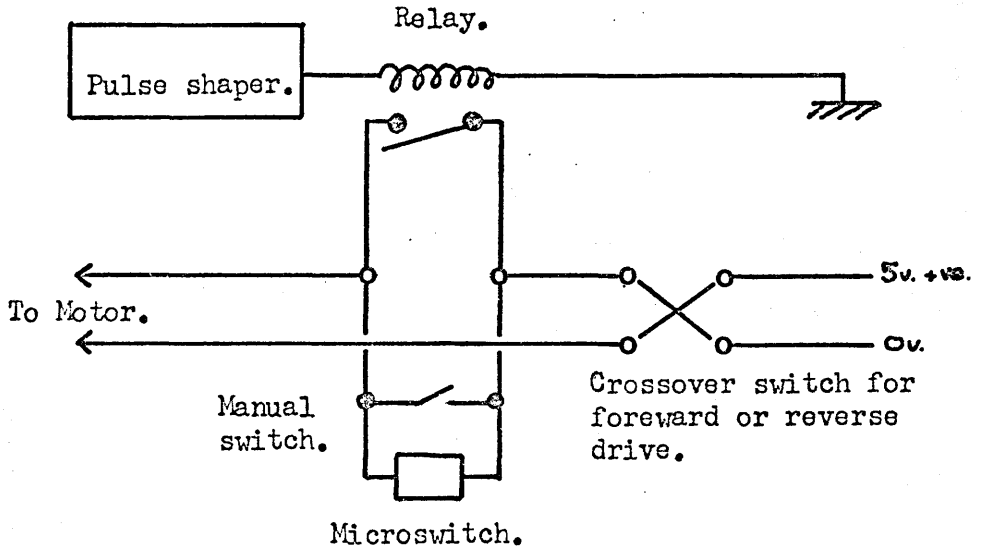

Figure 8.12

Hence the required 1 second, 5 volt pulse is obtained each time the teletype motor is started.

The full wiring circuit for the goniometer is shown in figure 8.12, and a photograph of the apparatus in operation is shown in figure 8.13.

A sample of bone, 50 microns thick was mounted in the specimen support and viewed on edge through a telescope. When adjusted to a central position, the sample was found to remain accurately aligned on the crosswires of the telescope through a full 360^{o} (ϕ) rotation, thus satisfying the design requirement in this respect. The automation proved to be reliable and typical times for a full 180^{o} (ϕ) rotation in the following analyses were of the order of 20-30 minutes. A typical output printout is shown in figure 8.14., the first four figure number showing the step position, the second six figure number showing the present count, and the final six figure number showing the counting time in seconds.

Thus, quantitative analyses of diffraction rings were obtained in a matter of minutes rather than hours, in a single operation, and the following chapters show how the goniometer was utilised to examine various aspects of bone structure.

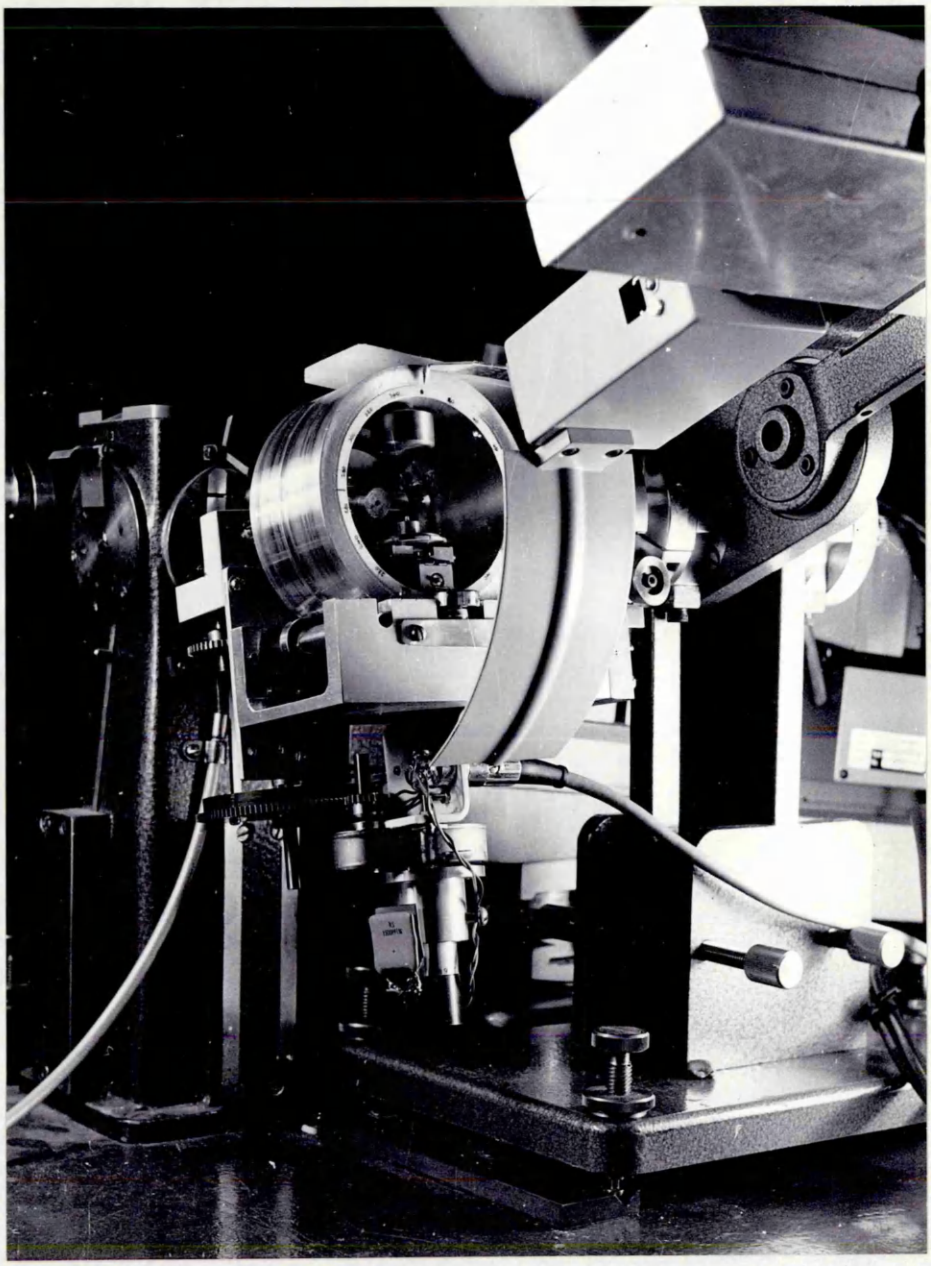

Figure 8.13a

The goniometer mounted in position on the X-ray generator.

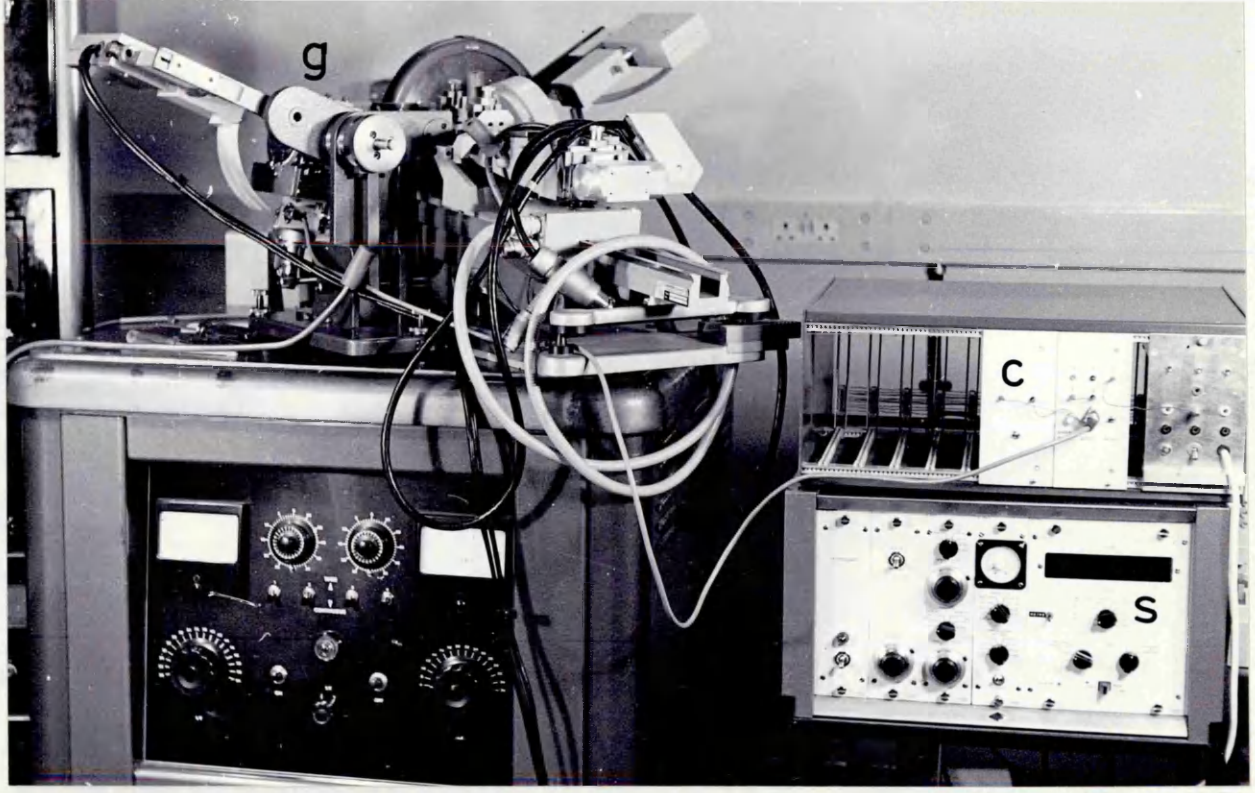

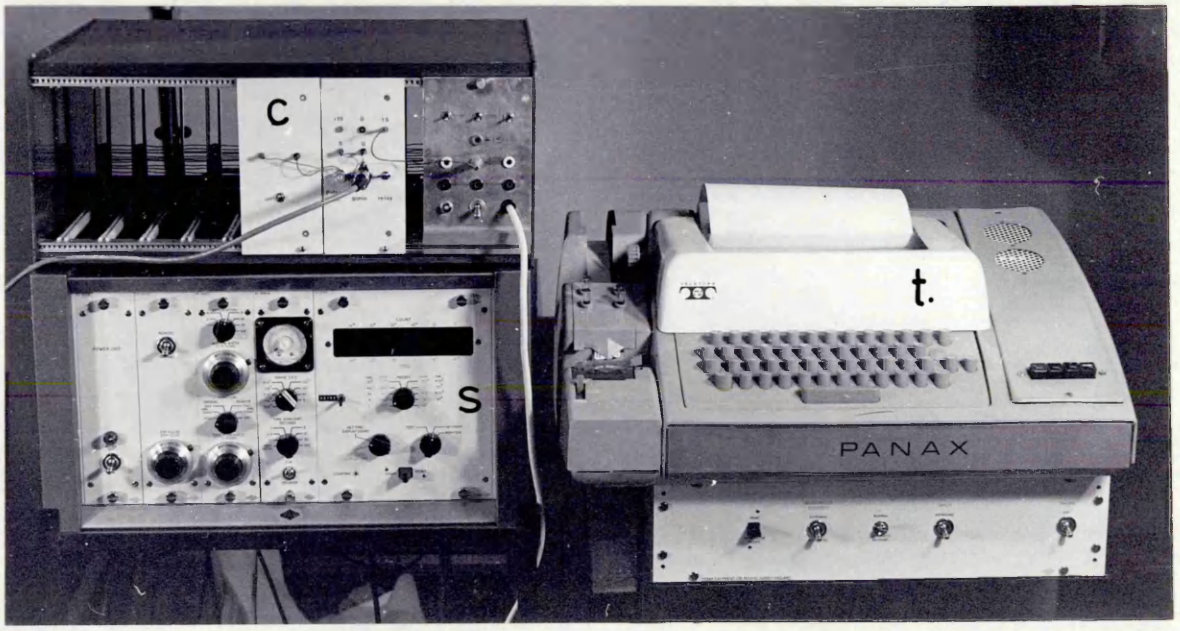

Figure 8.13b

The goniometer (g), control box (c), scaler/timer (s), and teletype (t).

Goniometer Output Format.

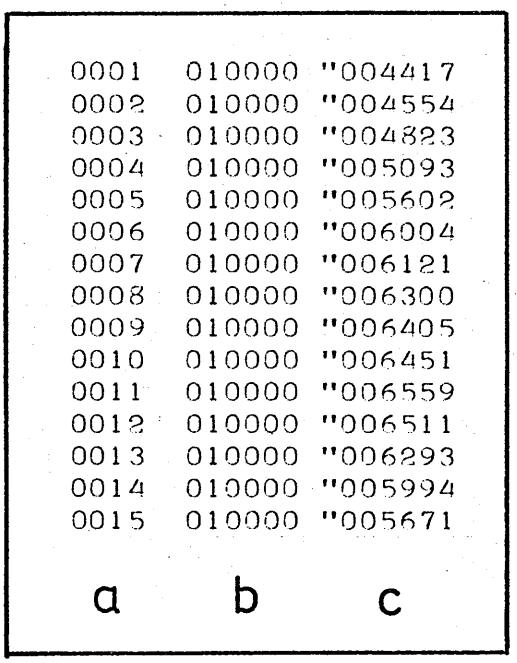

Figure 8.14

a Position number.

b Preset count.

c Time of count (in seconds), showing two places of decimals.

CHAPTER NINE

EXPERIMENTS WITH THE GONIOMETER

9.1. Primary Type Bone

9.1.1. Introduction

As mentioned in the previous chapter, preliminary film work suggested that primary and secondary type bone exhibit different fibrous structures, and so this topic was chosen initially for further investigation. Also in the preliminary work, some apparent variation in the crystallite orientation was attributed to the narrow x-ray beam, (0.1mm - 1.0mm) dia., being affected by local histological variation, and thus the results did not represent a true average for the bone sample. Consequently, the x-ray beam on the goniometer was collimated to 2mm diameter at the specimen, so to produce results more representative of the sample as a whole.

9.1.2. Material and Method

The bone section was taken from the mid-femural region of a Red Devon Ox, aged 2-3 years. The bone had been deep frozen but otherwise untreated. The mid-femural region was chosen since the cortical bone is particularly thick and well defined in terms of histology.

Three slices were cut, approximately 70 microns thick, mutually perpendicular to each other at three different sites within the sample, as shown in figure 9.1. Before x-ray diffraction, the bone slices were examined by light microscopy using both ordinary and polarised light to determine the histological structure. Figures 9.2 and 9.3 show ordinary and polarised light micrographs of a transverse section taken from the ox femur, the laminar structure is evident and this is characteristic of primary type bone.

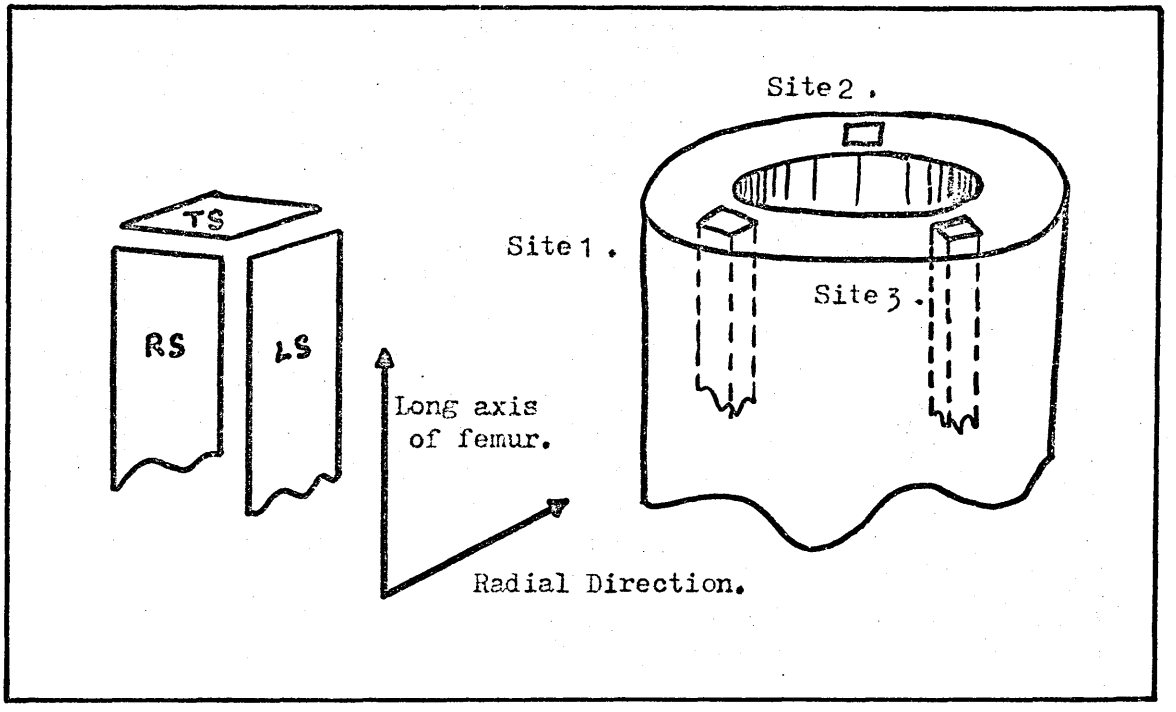

Figure 9.1

Samples of cortical bone were cut from the mid-femural region at three equally spaced sites as shown.

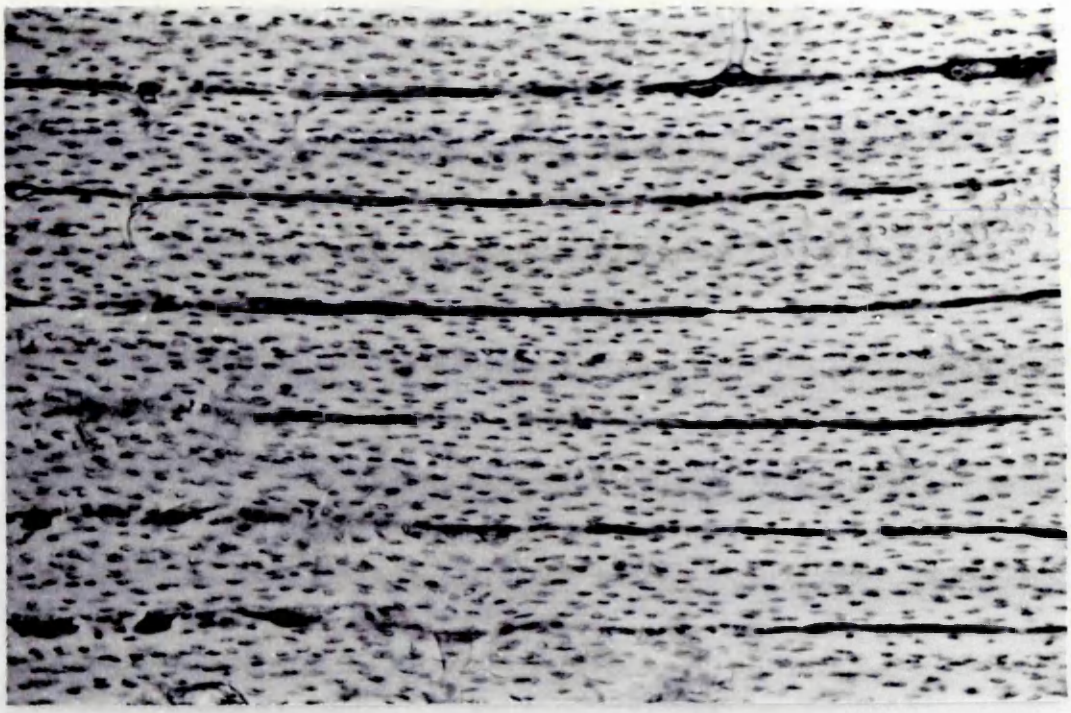

Figure 9.2

Light micrograph of a transverse section of ox femur, (x 50).

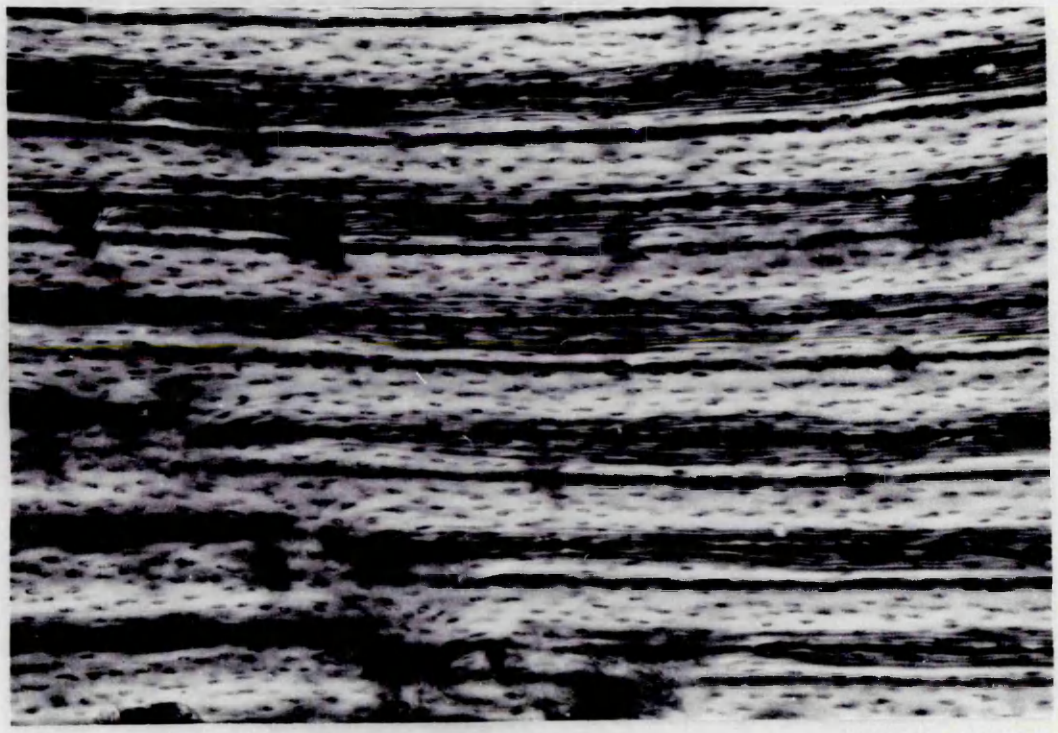

Figure 9.3

The same section of bone as shown above, viewed under polarised light (x 50).

The following operating conditions were used for the x-ray goniometer.

a)	Radiation	:	Cu unfiltered
b)	Pre-set count	:	10,000
c)	Angular Step	:	9^{o}
d)	Diffracted beam used ($2\Theta_B = 26^{o}$)	:	(002)

To determine the absolute intensity of the diffracted x-ray beam it was necessary to subtract the background radiation, and this was measured for each counting position by taking the mean of readings at either side of the (002) beam.

9.1.3. Results

Results are presented in both graphical and tabular form. The tabulated figures show the (002) beam intensity (in counts per second) above the background radiation, with relation to the angle (ϕ), as indicated for each section diagramatically in figure 9.4. The graphical representation shows superimposed results of the three similar sections taken from different sites.

Because the sample thickness was subject to variation, this affected the amount of diffracting volume and x-ray absorption, and hence the (002) beam intensity. Therefore to aid comparison, scales of intensity have been multipled by a constant factor such that (ϕ = o) readings have equal values.

Variation in the mean count rate was estimated by taking repeat measurements for different values of (ϕ). A two standard deviation spread in one direction was covered by approximately 5 c.p.s.

The Relation of (ϕ) to Each Bone Section.

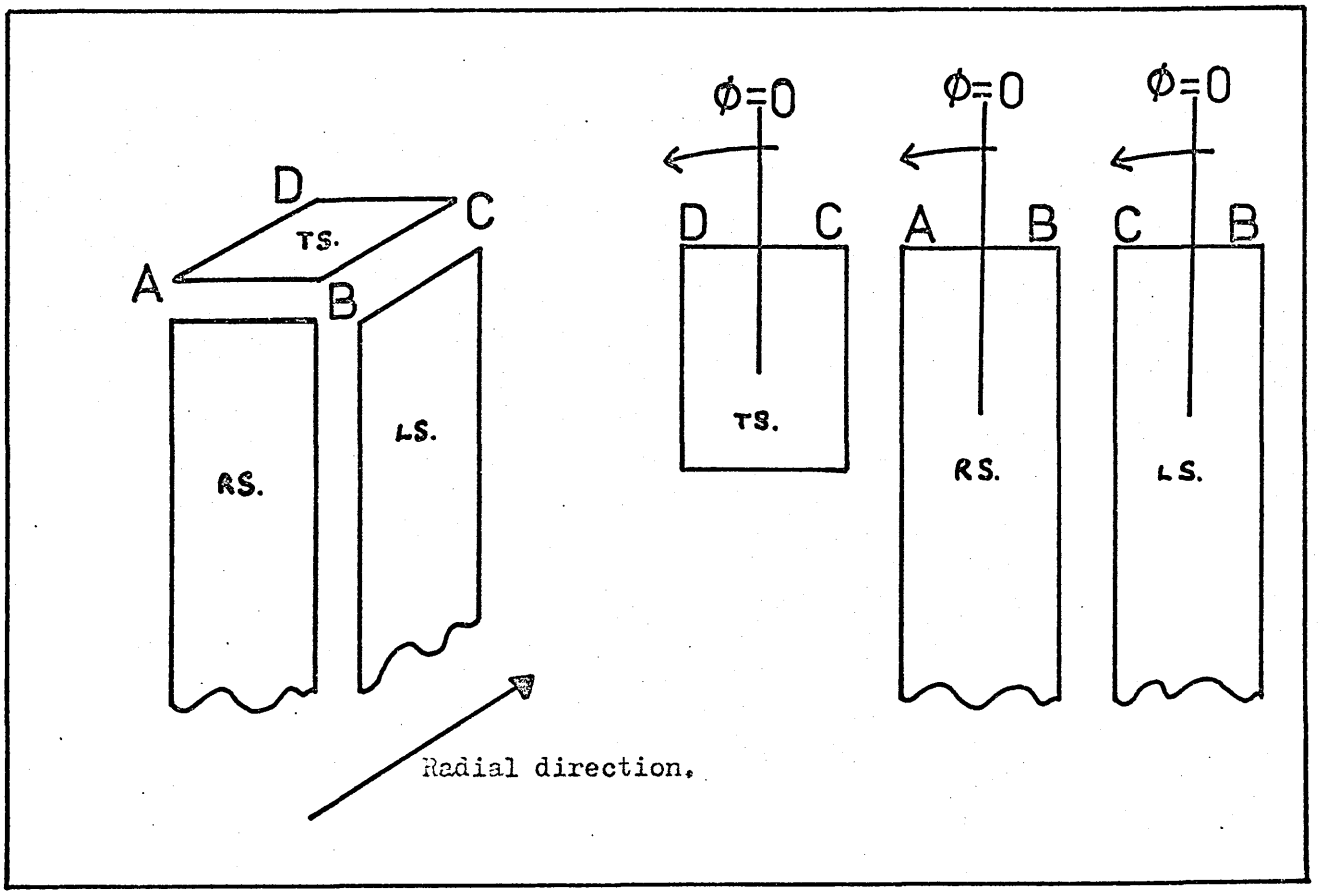

Figure 9.4

(002) Diffracted Beam Intensity v (Ø)

Longitudinal Sections Primary Bone

Angle (Ø)°	(002) Diffracted Beam Intensity, Above Background (c.p.s.)		
	LS1	LS2	LS3
0	174.5	174.5	174.5
9	157.2	165.9	173.0
18	132.0	136.3	149.5
27	94.7	100.2	111.3
36	69.2	68.2	78.2
45	47.1	50.6	42.4
54	35.2	35.4	28.4
63	27.5	29.3	20.0
72	26.8	27.8	17.3
81	24.6	23.3	18.0
90	23.2	24.1	17.3
99	23.9	26.9	16.0
108	26.0	27.0	15.0
117	27.4	30.9	15.5
126	34.8	35.7	18.3
135	46.9	47.1	25.5
144	68.3	64.8	39.7
153	99.2	94.9	62.0
162	132.0	127.8	104.5
171	170.5	163.9	149.0

Table 9.1

Longitudinal Sections.

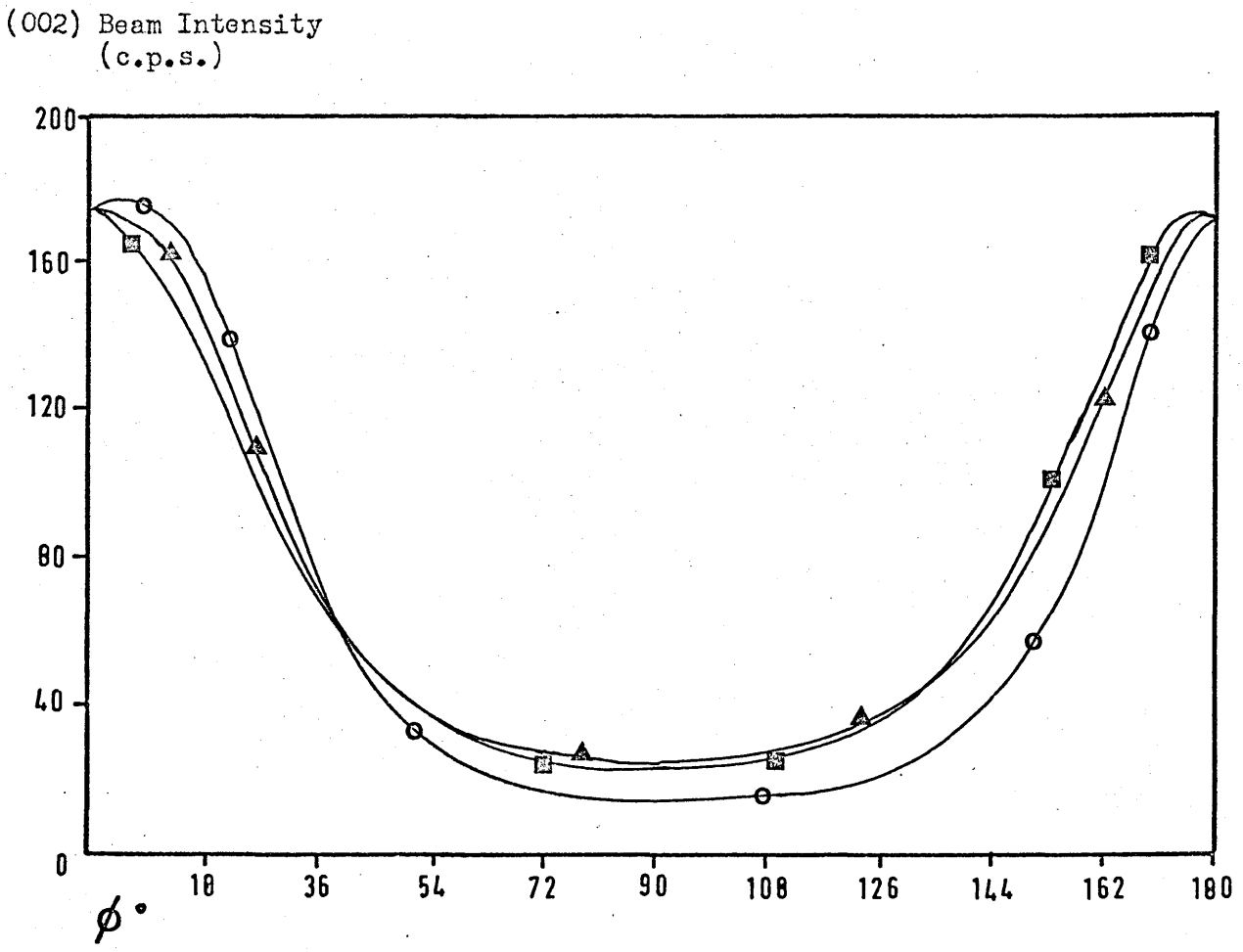

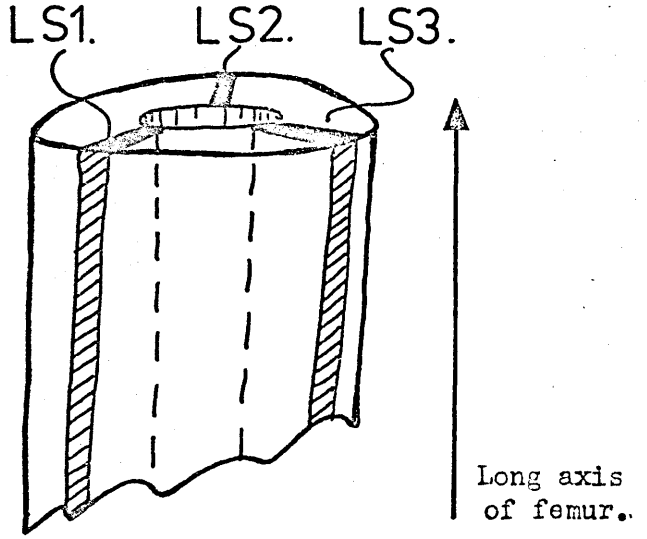

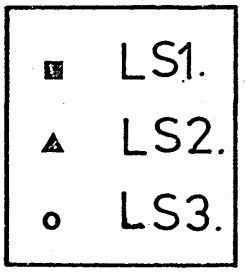

Figure 9·5

(002) Diffracted Beam Intensity v (Ø)

Radial Sections Primary Bone

Angle (Ø)°	(002) Diffracted Beam Intensity, Above Background (c.p.s.)		
	RS1	RS2	RS3
0	146.0	146.0	146.0
9	134.0	130.5	132.6
18	121.1	108.9	115.8
27	99.3	85.1	93.7
36	86.1	64.5	73.4
45	72.8	50.5	58.5
54	63.9	44.6	47.0
63	56.8	37.8	40.8
72	53.1	35.9	33.7
81	52.1	36.3	32.5
90	52.9	37.1	31.0
99	54.0	35.8	30.5
108	57.1	45.5	32.4
117	62.2	54.7	37.6
126	70.6	66.4	47.0
135	86.4	78.4	57.2
144	102.8	106.0	76.7
153	119.0	124.5	99.1
162	132.8	140.2	125.0
171	144.5	149.9	147.2

Table 9.2

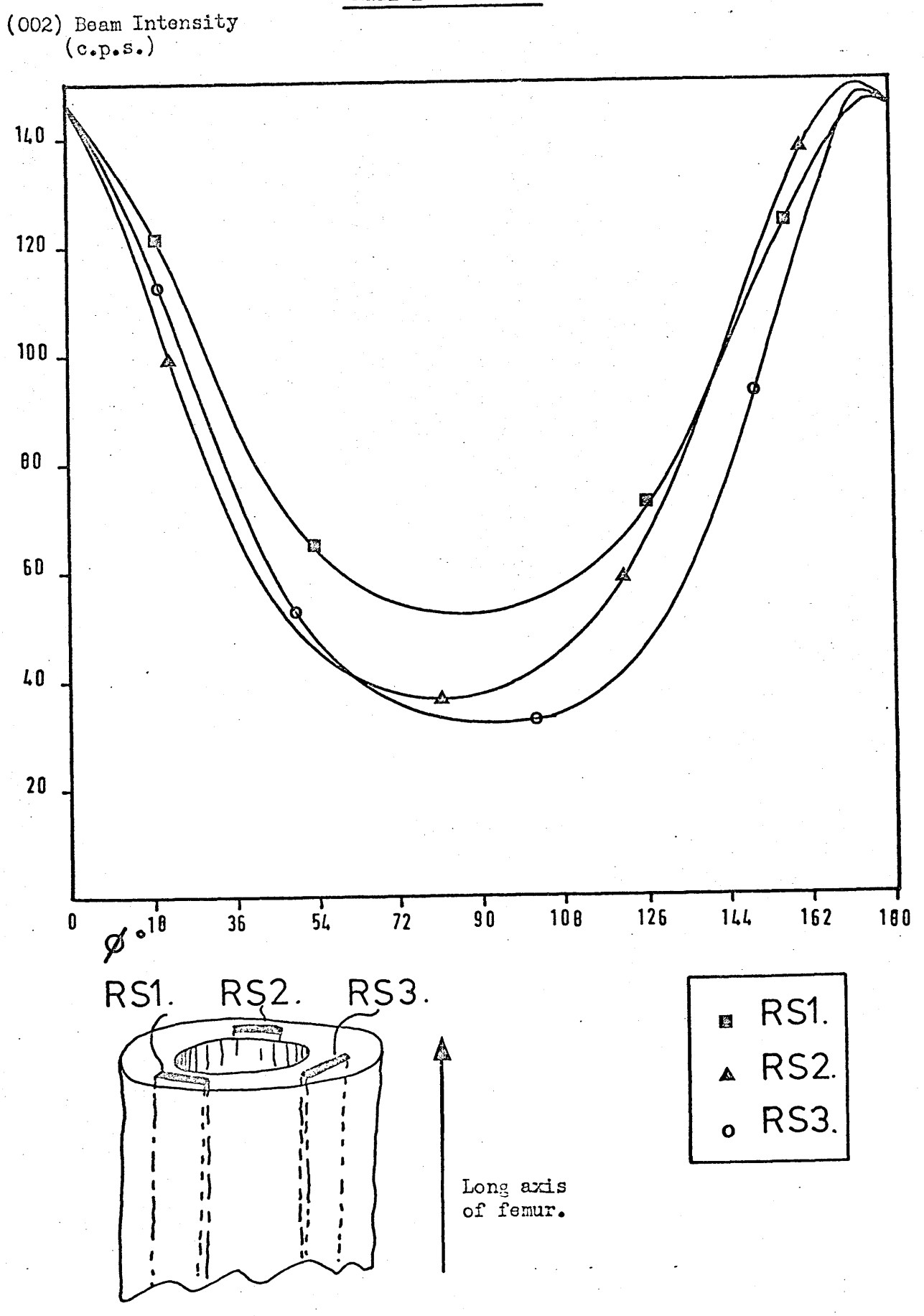
(002) Beam Intensity
(c.p.s.)
140
120
100
80
60
40
20
0
18
36
54
72
90
108
126
144
162
180
Ø°
RS1.
RS2.
RS3.
RS1.
RS2.
RS3.
Long axis
of femur.

Figure 9.6

(002) Diffracted Beam Intensity v (Ø)

Transverse Sections Primary Bone

Angle (Ø)°	(002) Diffracted Beam Intensity, Above Background (c.p.s.)		
	TS1	TS2	TS3
0	23.1	23.1	23.1
18	21.9	19.9	19.8
36	24.4	21.9	19.0
54	23.9	25.9	23.2
72	29.7	37.8	35.1
90	31.2	46.3	48.4
108	31.3	44.0	49.0
126	23.6	38.9	36.7
144	18.5	27.2	21.2
162	18.0	20.9	15.0

Table 9.3

Bone Mineral c-axial Orientation. Primary Bone.

Transverse Sections.

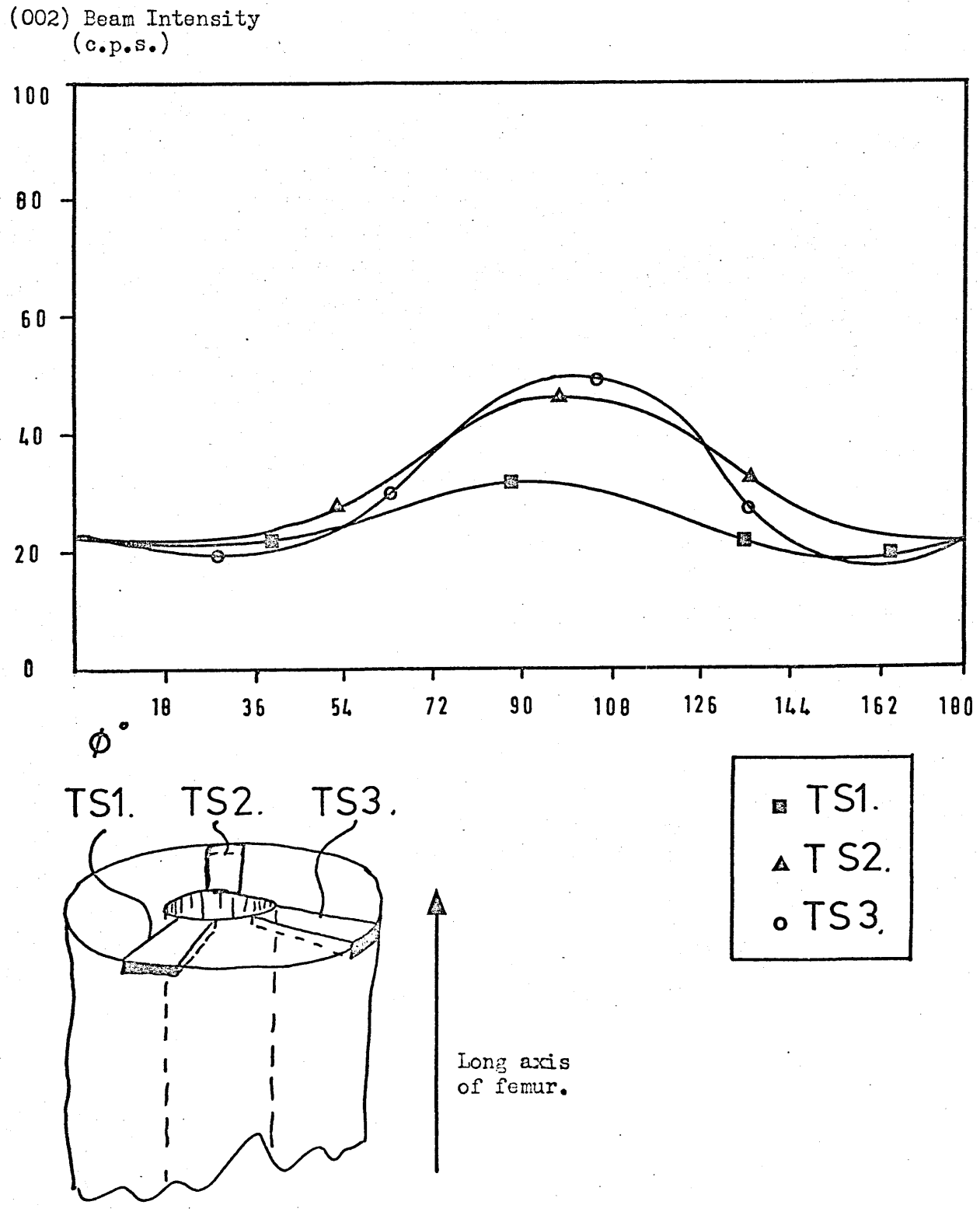

Figure 9·7

The LS and RS sections show basically the same type of orientation pattern, i.e., with the majority of crystal c-axes aligned with the long axis of the bone ($\phi = 0^{o}$ and 180^{o}). This pattern is typical of most diffraction photographs of bone sections where the (002) arcs are distributed about the long axis of the femur. No evidence has been found in this type of bone to suggest any other kind of orientation. pattern. The TS sections produced a pattern which shows an orientation of c-axes parallel to the laminar arrangement of the bone structure.

The information contained in these orientation patterns can be presented in the form of an (002) pole figure, which combines the information of the LS, RS, and TS sections for each sample. Figure 9.8 is the stereographic projection of a reference sphere ruled with parallels of latitude and longitude. If the bone sample is considered as being represented by a LS, RS and TS section placed at the centre of the reference sphere, the orientation patterns produced, when drawn on the reference sphere and projected in the stereographical form, correspond to the lines indicated in figure 9.8, the N-S direction representing the long axis of the femur. Taking the three sets of intensity v (ϕ) readings for each sample, and multiplying two of the sets by constant factors so that intensities at points of intersection of the three lines agree, the pole figure can be drawn by joining points of equal intensity. The scale of the numbers used to label contours of equal intensity is arbitrary since relative orientations can be deduced from any scale. In this work the scale has been taken from the x-ray intensity (c.p.s.) of the diffracted beam for each particular case.

Stereographic Projection of

Reference Sphere.

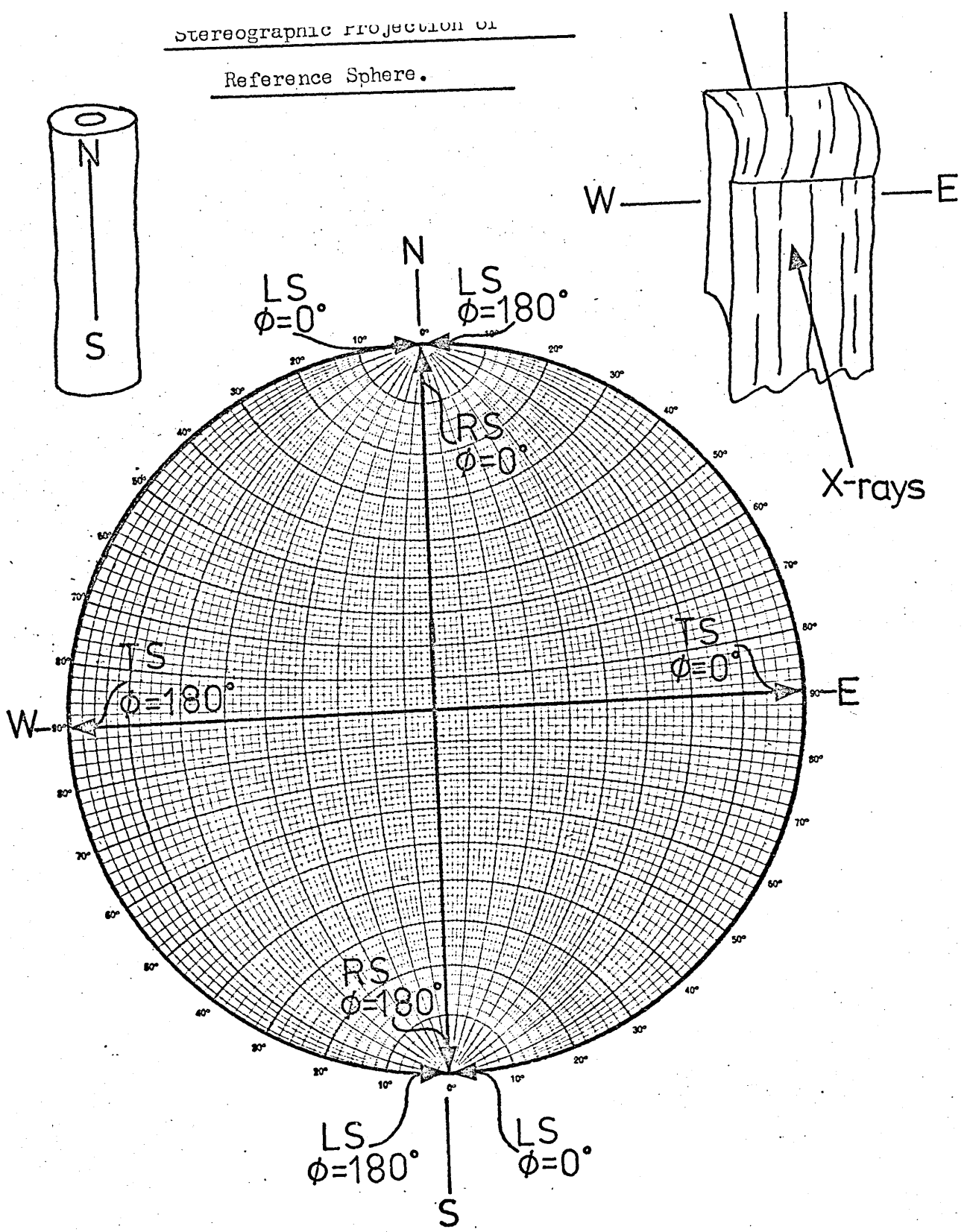

Figure 9·8

Sample 1.

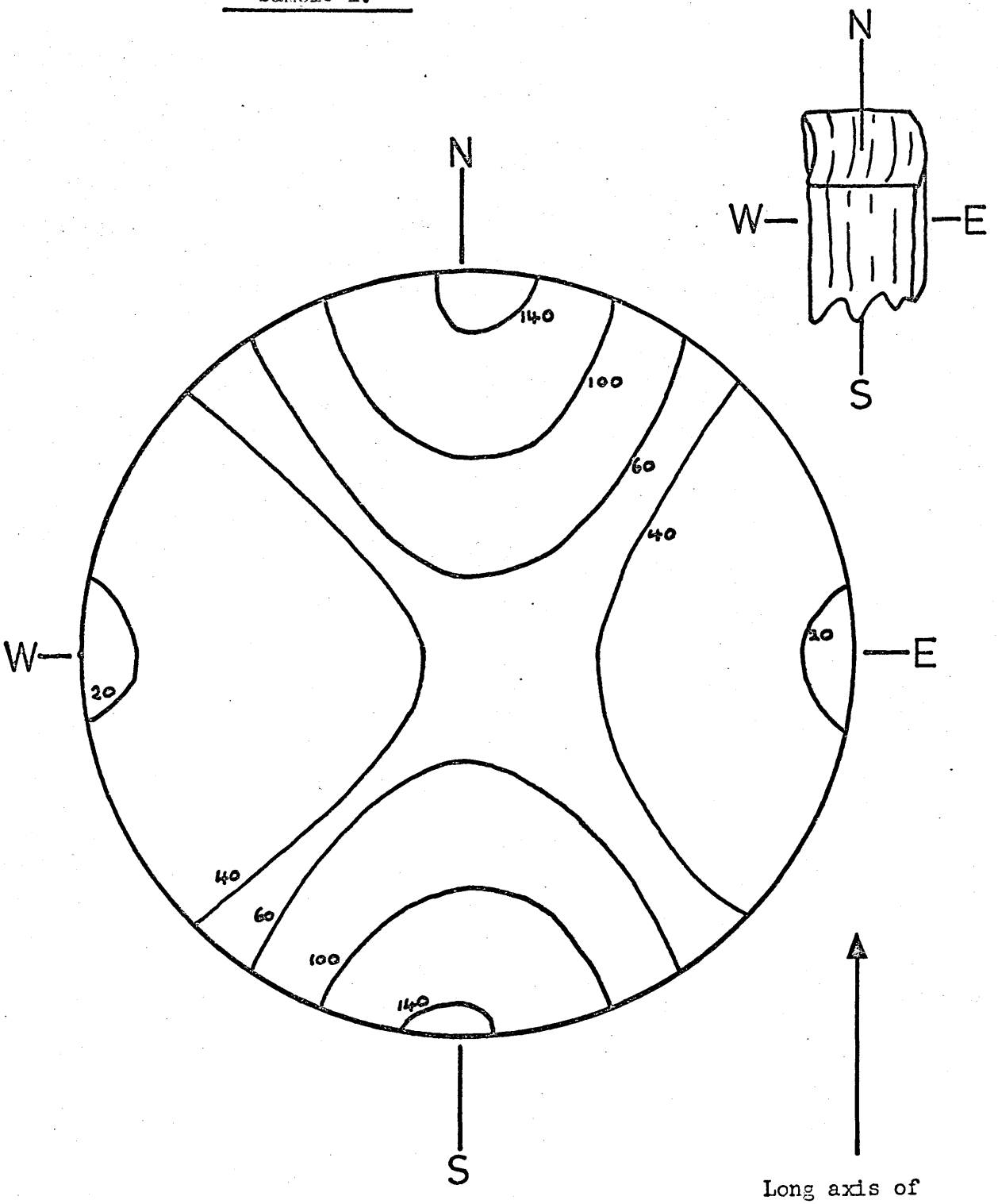

Figure 9.9

(002) Pole Figure. Primary Type Ox Bone.

Sample 2.

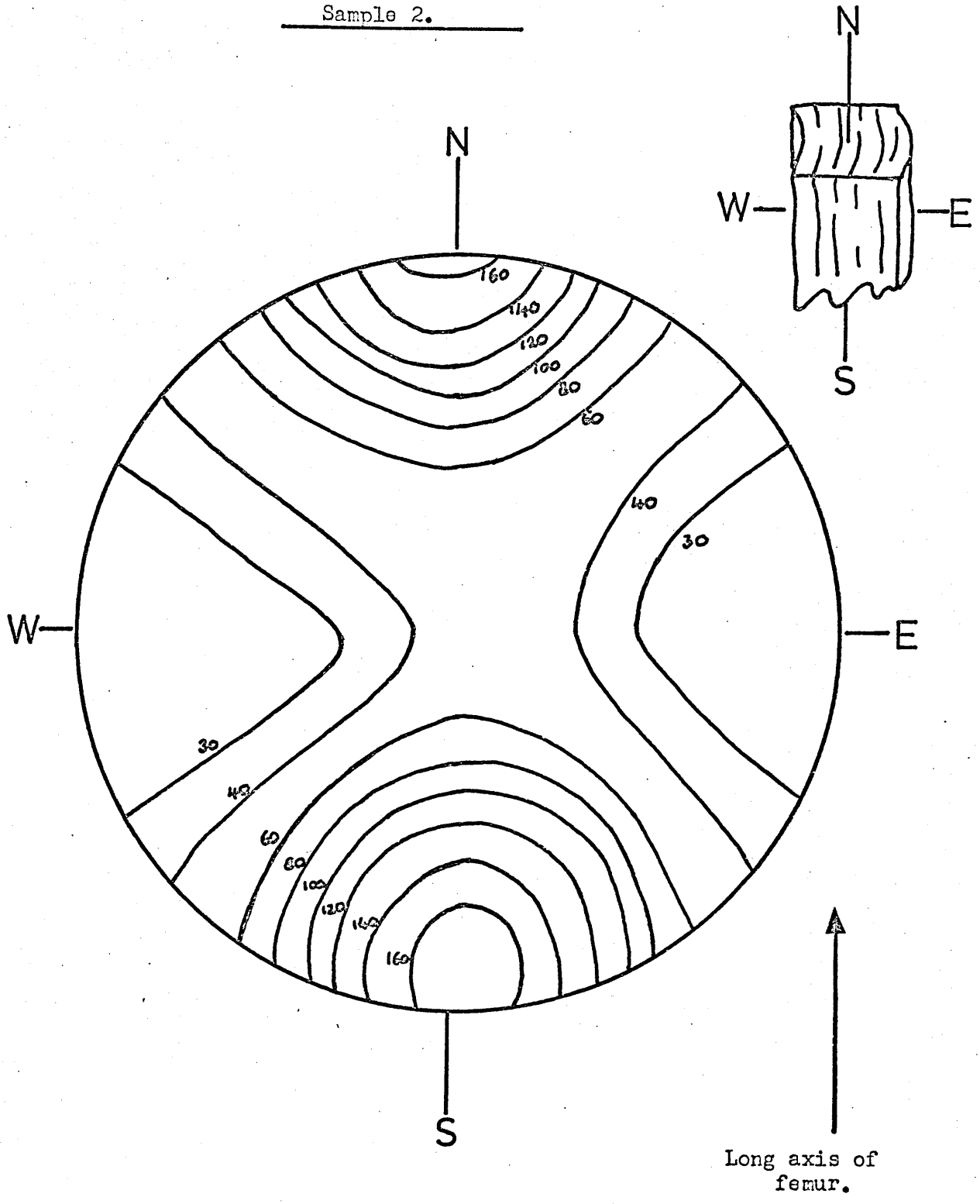

Figure 9·10

(002) Pole Figure. Primary Type Bone.

Sample 3.

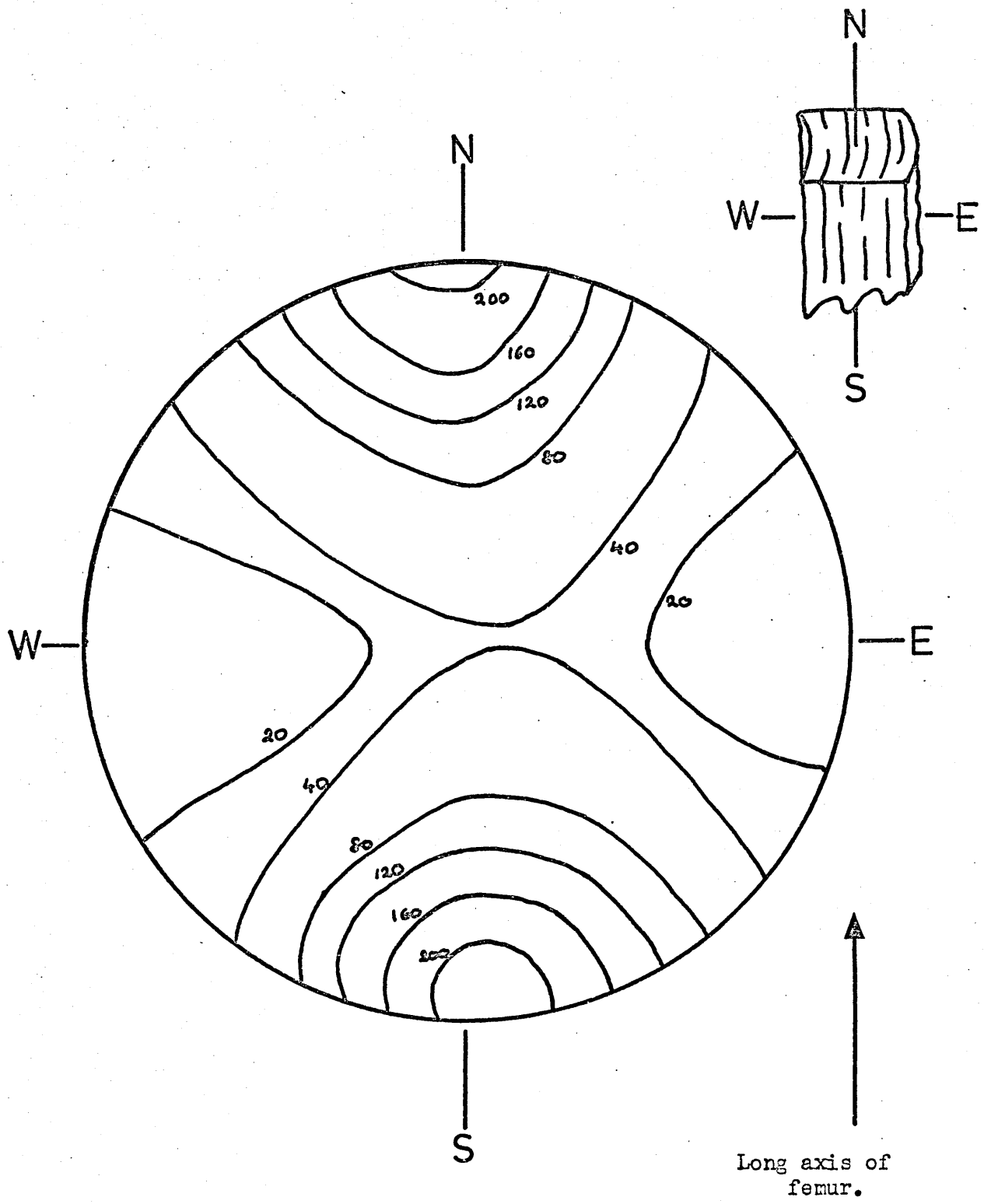

Figure 9·11

9.1.4. Primary Bone - Summary

It must be emphasised that these pole figures are approximate figures since the contours have been determined from only three lines on the projection. The justification for joining the points of equal intensity in this way is based on the observation of many diffraction photographs produced in preliminary work which show that only one major orientation direction exists in this type of bone and so the contours can be drawn with a fair degree of confidence that no other high intensity peaks are present. This point is covered further in the next chapter.

These three pole figures represent the three dimensional orientation of bone mineral c-axes in three separate samples taken from the mid-femural region of an ox femur. Light microscopy has shown the bone to have a laminar structure characteristic of primary type bone and this is reflected in the pole figures, each figure showing essentially the same features.

a) The main fibrous (c-axial) orientation is aligned with the long axis of the femur.

b) If the crystal c-axial orientation was evenly distributed about the main fibre axis, the contour lines of equal intensity would follow the ruled lines of latitude. An uneven distribution is indicated by deviation of the contours from these lines of latitude, and this appears to be the case with primary type bone. There is less orientation in the plane of the laminations than perpendicular to it.

This observation would be consistent with a fibrous layered structure where the fibres spread more within the layers than across the layer boundary into the next layer.

9.2. Secondary Type Bone

9.2.1. Material and Method

A sample of bone taken from the mid-femural region of a 65 year old human male was obtained at a local post-mortem examination. Sections were cut from three different sites within the sample as described for the primary bone. A light microscopic examination of a transverse section revealed a structure characterised by many osteons, and this sample was therefore, typical of secondary type bone, see figures 9.11b and 9.11c.

9.2.2. Results

The results are presented in tabular form and (002) pole figures constructed as described in the previous section.

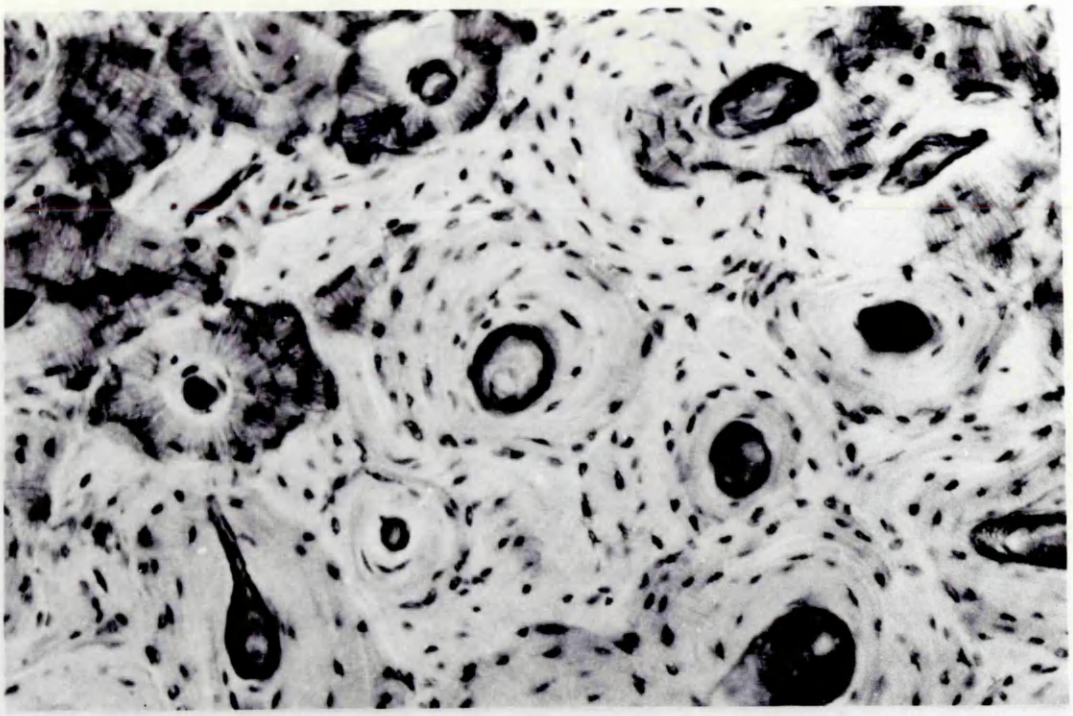

Figure 9.11b

Light micrograph of a transverse section of human femur, (x 100).

Figure 9.11c

The same section of bone as shown above, viewed under polarised light, (x 100).

(002) Diffracted Beam Intensity v (ø)

Longitudinal Sections Secondary Bone

Angle (ø)°	(002) Diffracted Beam Intensity, Above Background (c.p.s.)		
	LS1	LS2	LS3
0	150.0	150.0	150.0
9	133.7	142.9	159.1
18	115.6	125.8	147.8
27	100.6	108.2	135.5
36	86.6	92.7	108.5
45	75.7	76.9	90.0
54	68.9	66.7	76.0
63	63.2	59.7	65.9
72	61.2	56.5	57.9
81	60.1	53.1	53.3
90	61.2	50.1	52.5
99	65.3	51.7	49.6
108	72.6	59.8	52.7
117	81.9	60.2	55.8
126	94.3	73.7	60.8
135	111.4	83.7	77.8
144	130.6	96.6	87.3
153	146.2	113.3	105.6
162	155.5	130.0	126.9
171	157.6	143.3	144.8

Table 9.4

(002) Diffracted Beam Intensity v (Ø)

Radial Sections Secondary Bone

Angle (Ø)°	(002) Diffracted Beam Intensity, Above Background (c.p.s.)		
	RS1	RS2	RS3
0	150.0	150.0	150.0
9	134.5	151.4	139.4
18	117.4	146.8	106.9
27	100.3	134.4	84.7
36	84.3	128.2	60.8
45	70.3	106.7	47.8
54	63.1	96.2	37.2
63	57.9	82.3	30.8
72	54.8	70.8	29.5
81	54.8	69.3	28.9
90	55.9	63.7	28.2
99	59.0	63.0	30.6
108	65.2	65.9	41.8
117	76.6	67.7	51.0
126.	91.0	75.2	67.4
133	109.7	79.6	95.9
144	128.3	85.4	121.0
153	142.8	101.9	146.3
162	153.1	116.5	161.9
171	156.2	132.7	168.0

Table 9.5

(002) Diffracted Beam Intensity v (Ø)

Transverse Sections Secondary Bone

Angle (Ø)°	(002) Diffracted Beam Intensity, Above Background (c.p.s.)		
	TS1	TS2	TS3
0	48.8	48.8	48.8
18	44.6	50.0	47.7
36	49.9	47.5	50.8
54	46.1	50.1	48.0
72	52.0	48.3	53.6
90	54.1	48.8	49.8
108	51.1	51.0	55.1
126	53.3	49.8	53.8
144	50.1	47.0	49.2
162	49.2	48.2	49.0

(002) Pole Figure. Secondary Type Bone.

Sample 1.

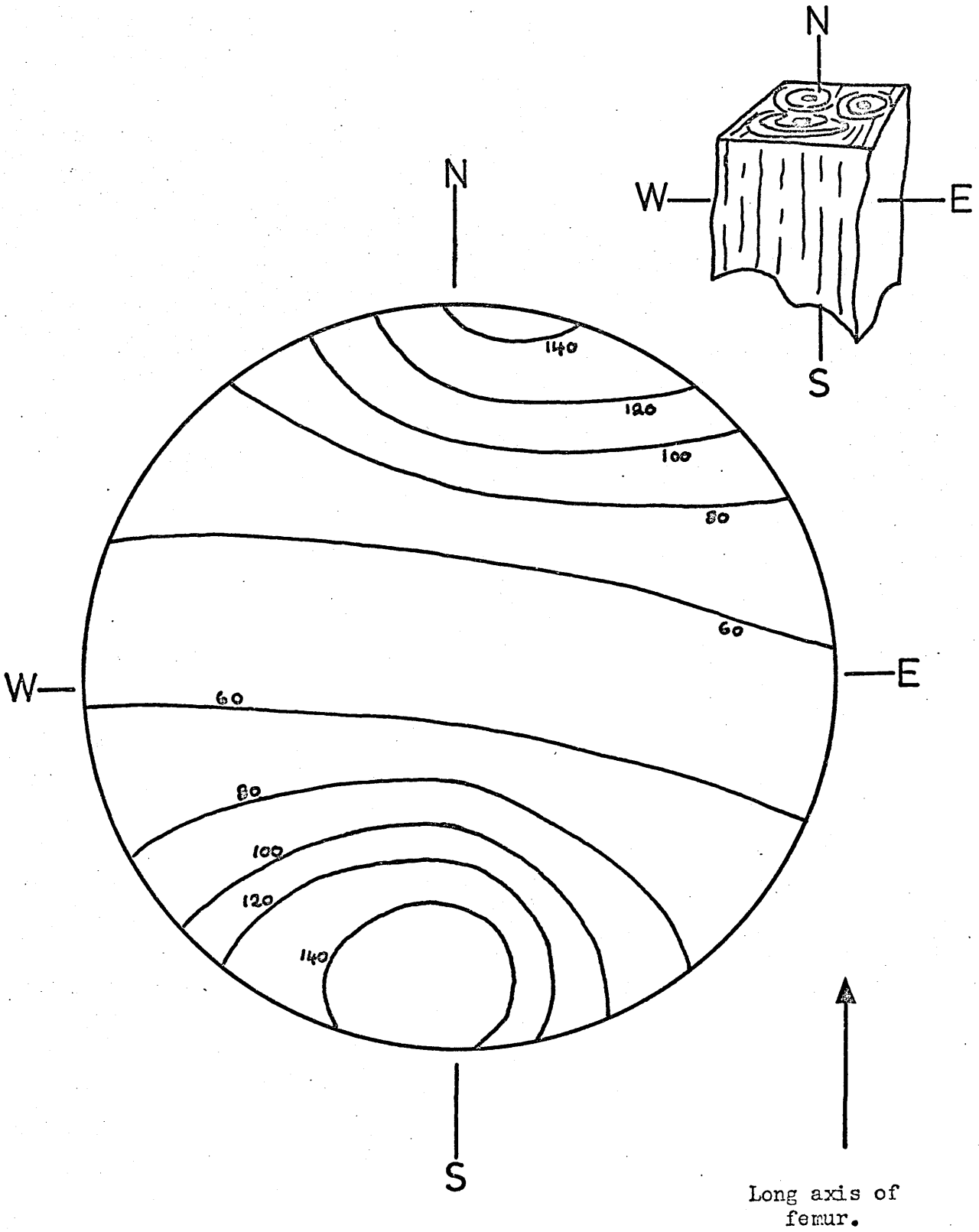

Figure 9·12

(002) Pole Figure. Secondary Type Bone.

Sample 2.

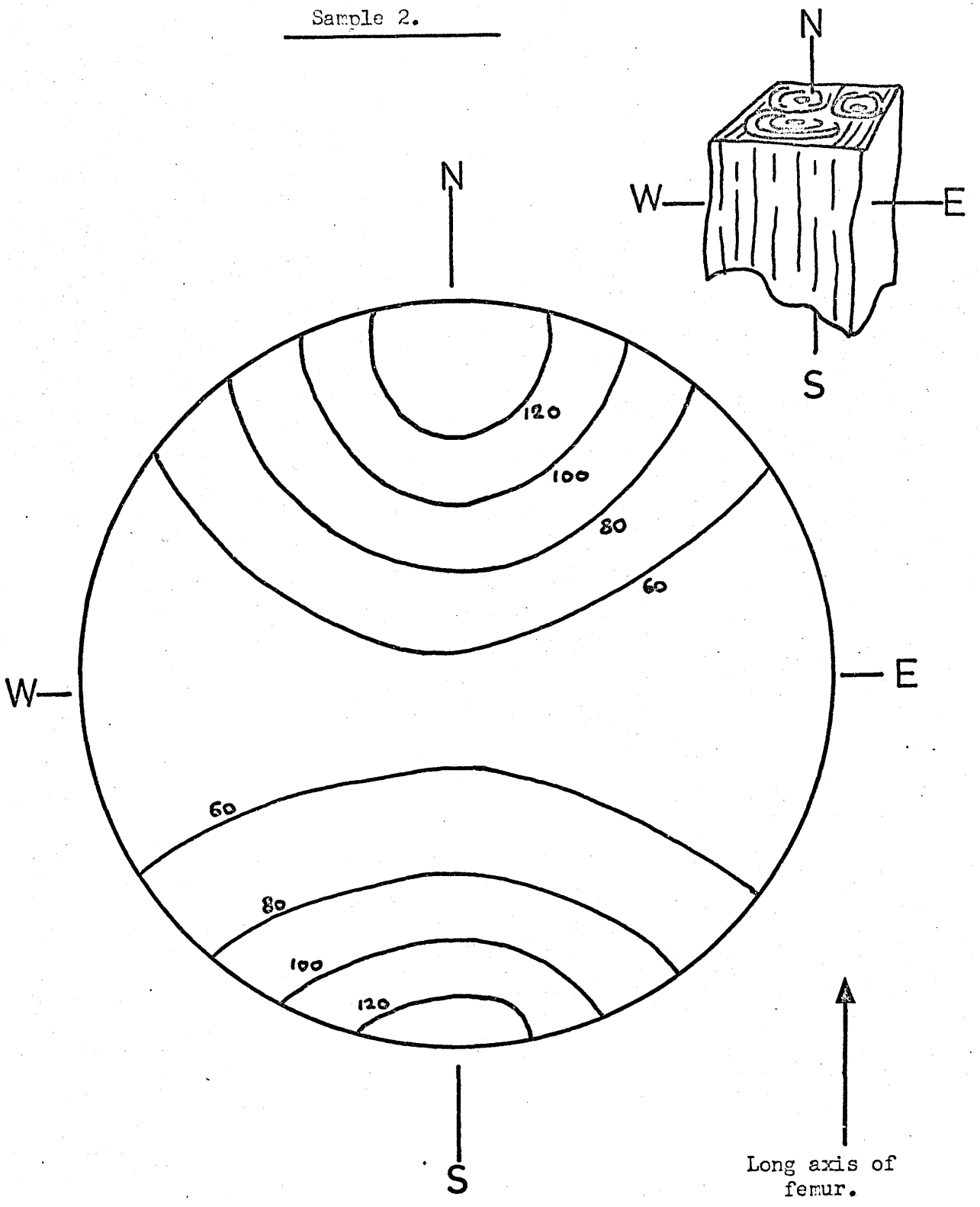

Figure 9·13

(002) Pole Figure. Secondary Type Bone.

Sample 3.

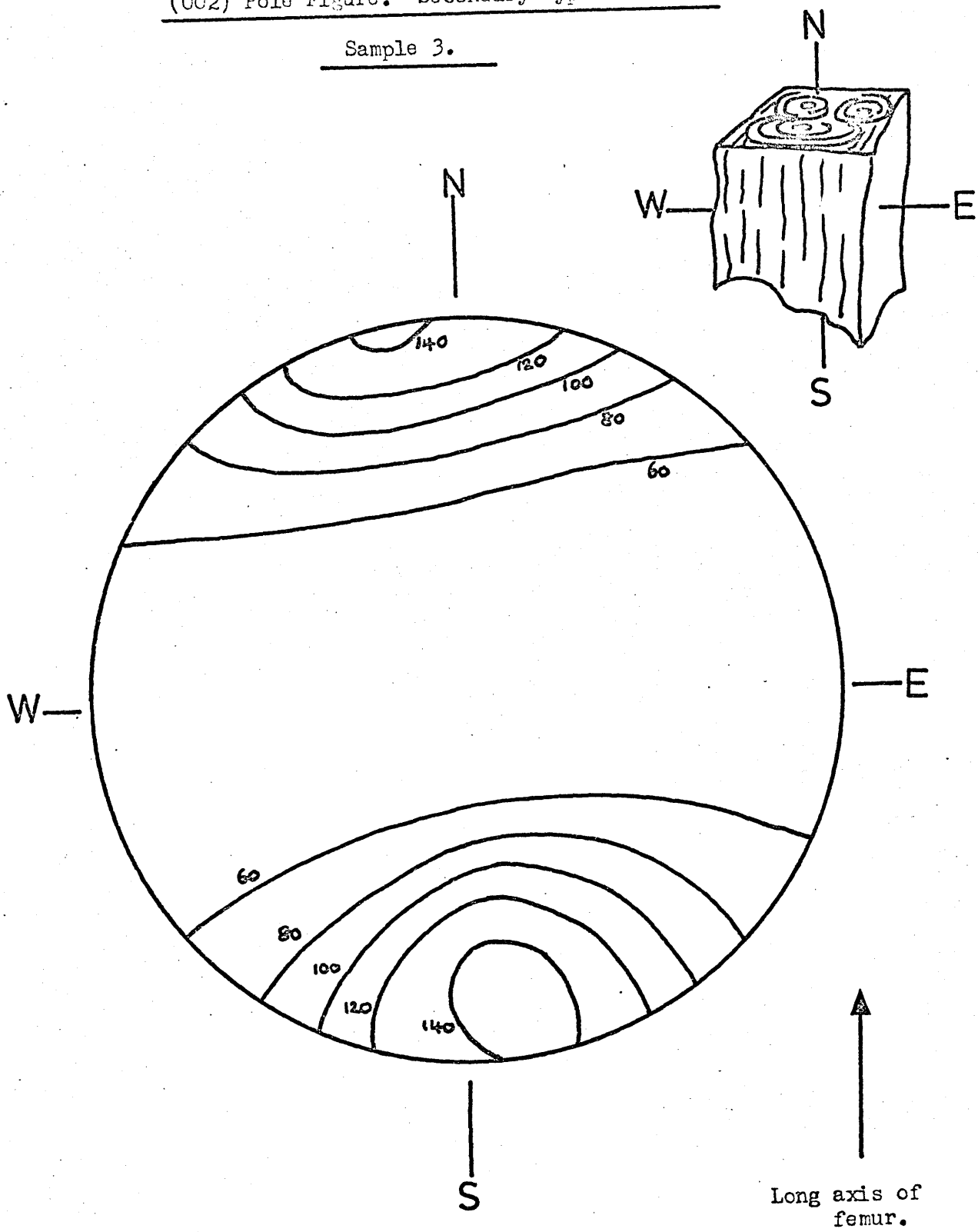

Figure 9·14

9.2.3. Secondary Bone - Summary

The three pole figures represent bone mineral c-axial orientation in three separate samples, taken from the mid-femural region of a human femur. The bone is characterised by systems of osteons, and therefore, typical of secondary type bone structure. Each pole figure shows essentially the same features.

a) The main fibrous orientation is aligned with the long axis of the femur

b) There is an even distribution of orientation about the major fibre axis. This can be seen since the T.S. sections show no orientation, and also since the contours of equal intensity tend to follow the shape of the lines of latitude.

The finding of an even distribution about the femural long axis is consistent with the fact that the osteon has rotational symmetry about this axis. Thus, it would be feasible that the fibrous structure of the laminations is similar to primary type bone, the symmetrical distribution about the long axis being produced by the histological structure.

9.3. Traebecular Bone

9.3.1. Material and Methods

The structure and orientation of traebecular, or cancellous bone is of interest since it has been suggested that the traebecular orientation is closely associated with the forces experienced by the traebeculae, Roux (1895), Pauwels (1948).

As a preliminary investigation on this type of bone, three mutually perpendicular sections were taken from the femural head of a Red Devon ox, aged 2-3 years, the bone had been deep frozen but otherwise untreated, see figure 9,15. Both thick and thin sections were cut from the femural head and examined by light microscopy. In the thick sections, the traebeculae appeared to be laminar structures, very densely packed and showing no obvious orientation within the sections. It was only in the cancellous bone adjacent to the femural shaft that rod-like traebeculae were found, several of these were dissected and examined initially by the film method.

In the region of the femural head where the shell is formed the traebecular density increases to such an extent that the solid bone structure is produced. The orientation of bone mineral within the shell was examined by the flat film method, and the goniometer was used to examine the traebeculae immediately beneath the shell.

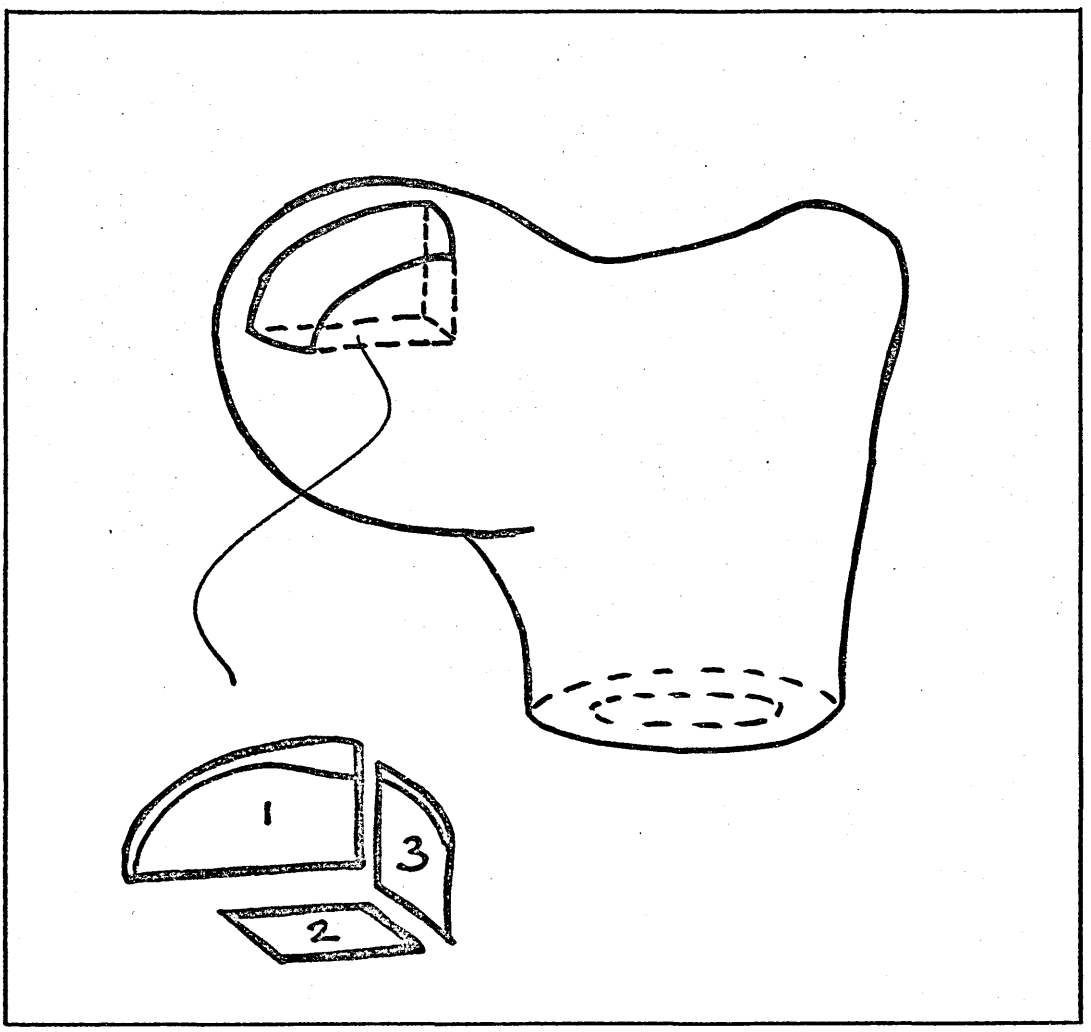

Figure 9.15

The three sections of traebecular bone were cut from the femural head as shown.

9.3.2. Results

The first section of traebecular bone as shown in figure 9.16 was examined by both the flat film and goniometer methods. The dense bone comprising the shell layer was examined by the film method at positions indicated, using Ni. filtered Cu. radiation, and a collimated beam of 1mm diameter. All diffraction patterns produced gave no indication of preferential orientation of the bone mineral c-axes, as shown in figure 9.16.

Results of examinations using the goniometer at positions, 4, 5 and 6, as indicated in figure 9.16 are shown superimposed in figure 9.17. Intensity readings were taken in angular steps of $18^{o}(\emptyset)$ for these samples. Figures 9.18. and 9.19 show in graphical form the results obtained from the other two sections, the positions of examination being indicated in the figures.

Figure 9.20 shows a diffraction pattern typical of those produced by the rod-like traebeculae, the uneven (002) ring indicating a certain degree of c-axial orientation along the long axis.

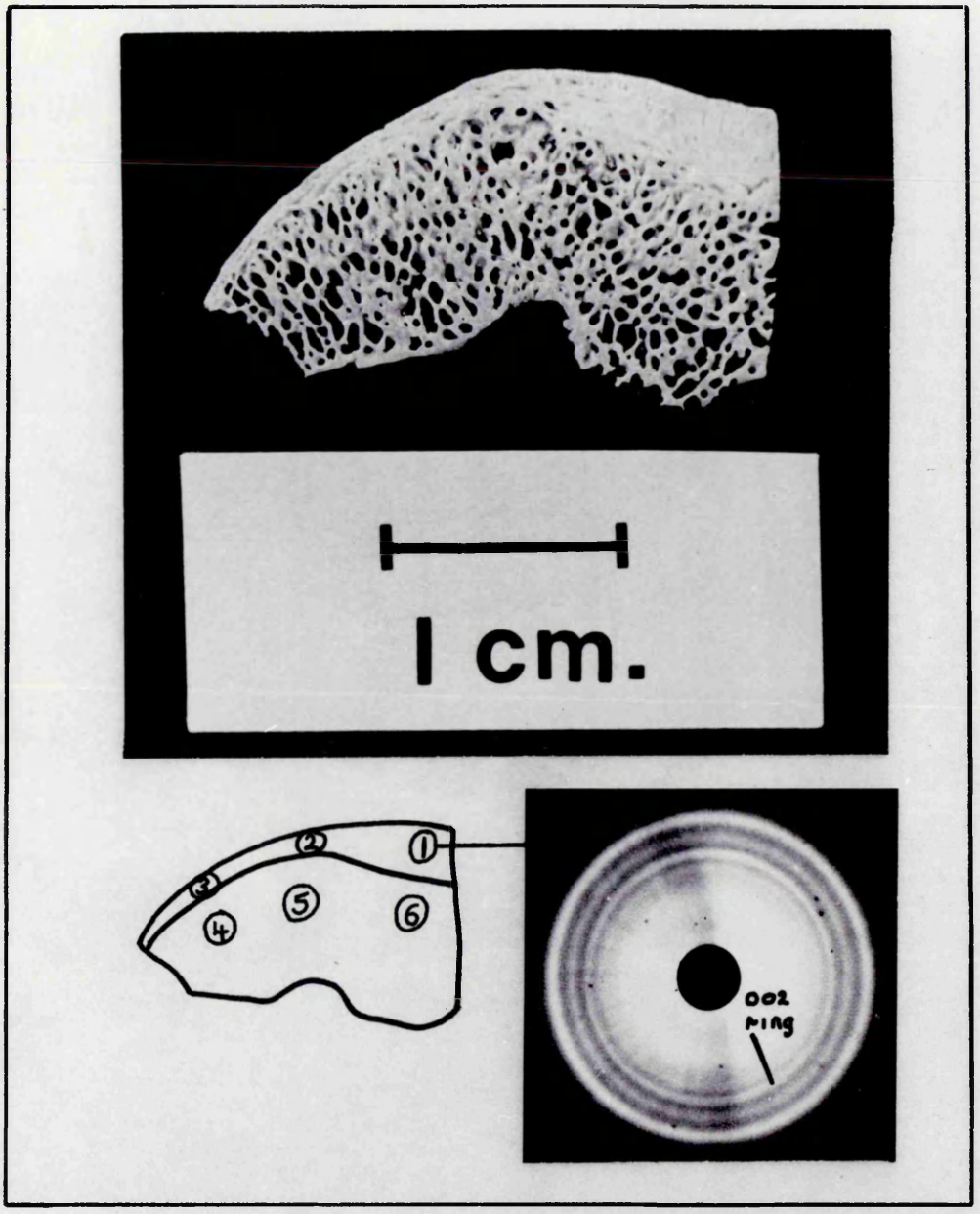

Figure 9.16

Positions 1,2,&3, were examined using the flat film method. The diffraction pattern of site 1, shows no prefered orientation and is typical of all patterns produced from the shell layer.

Positions 4,5,&6, were examined using the goniometer, see text for details.

(002) Beam Intensity
(c.p.s.)

Section 1.

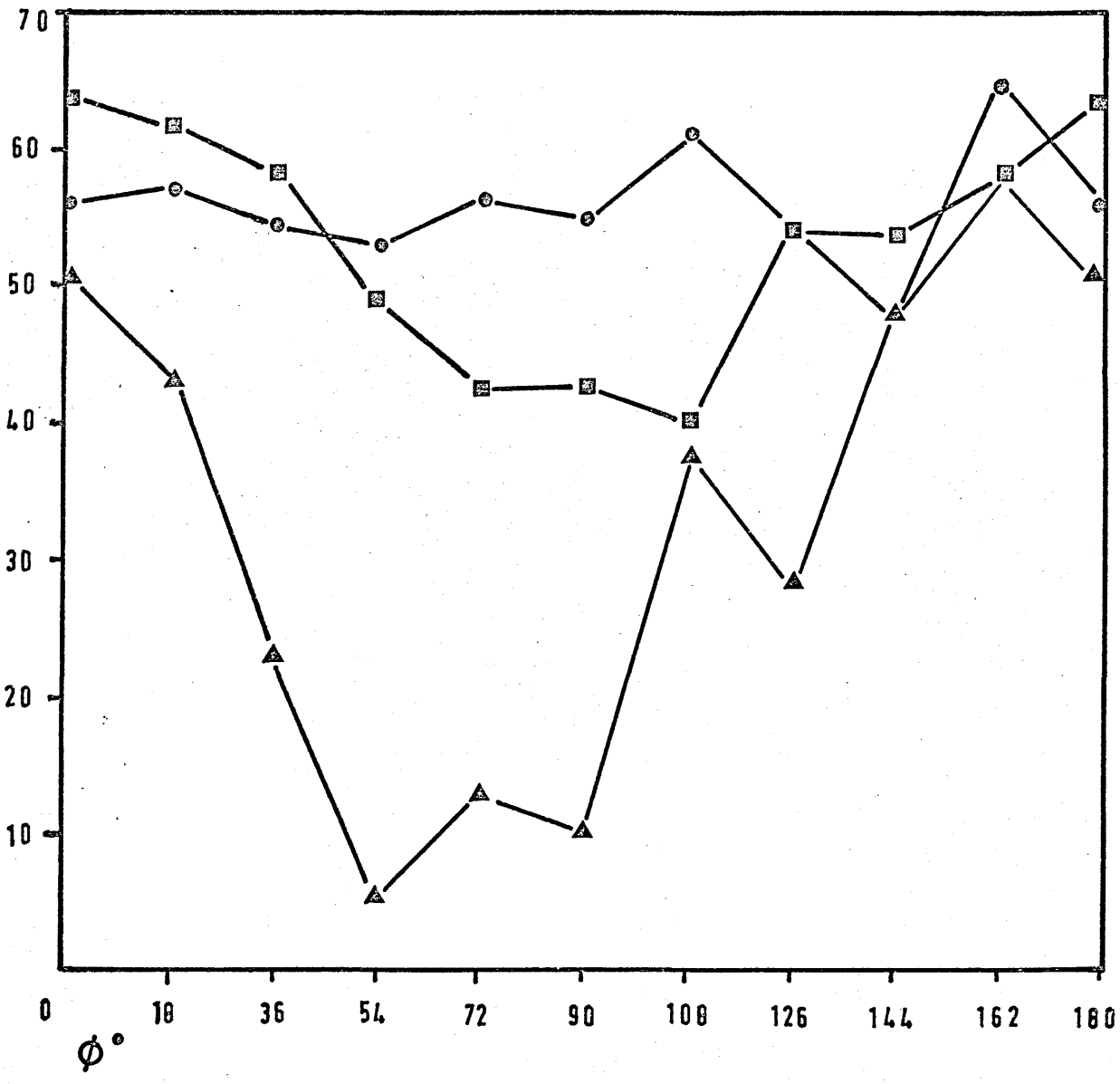

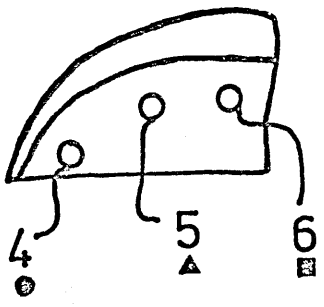

Figure 9·17

Section 2.

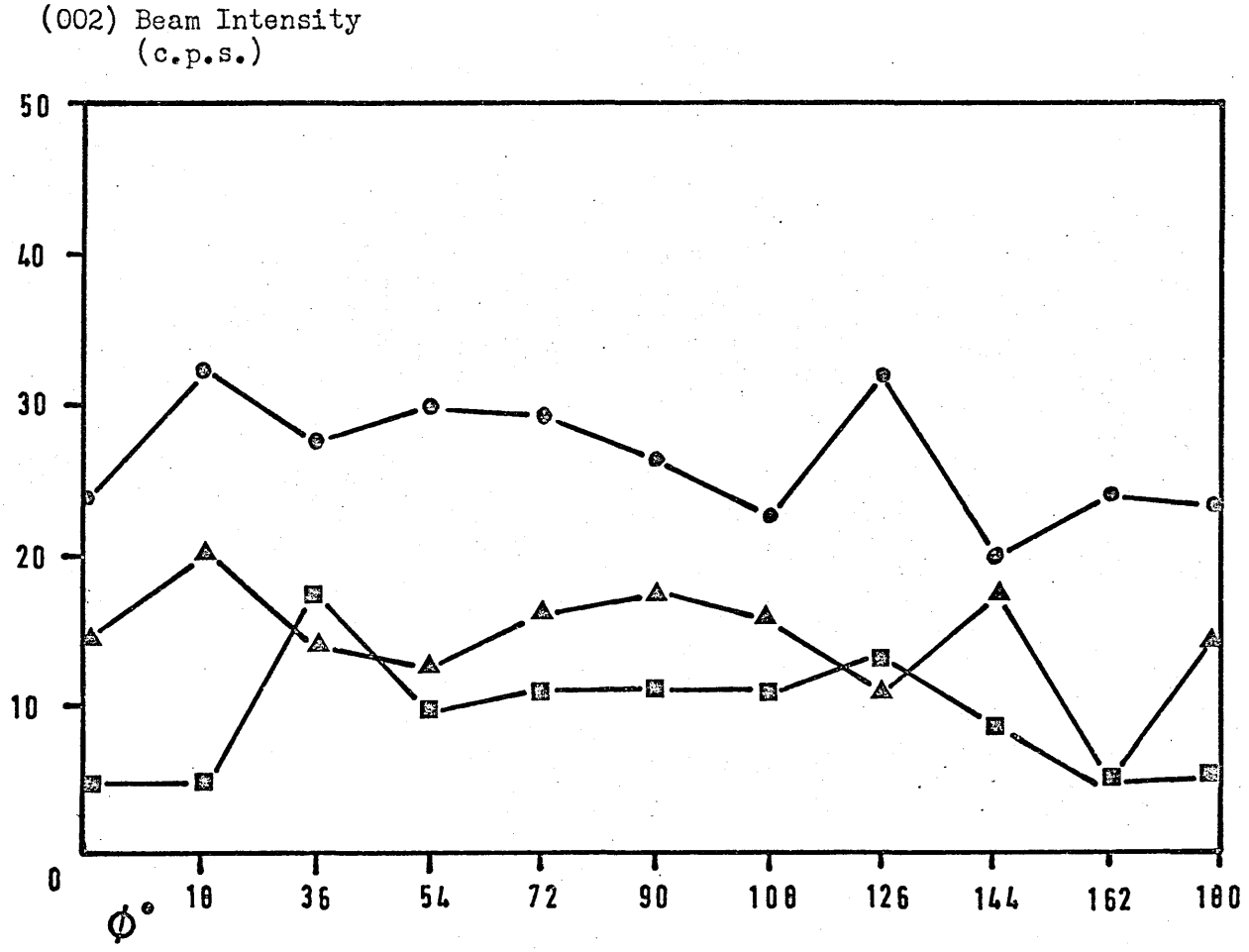

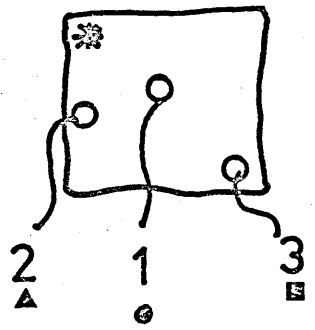

Figure 9-18

Section 3.

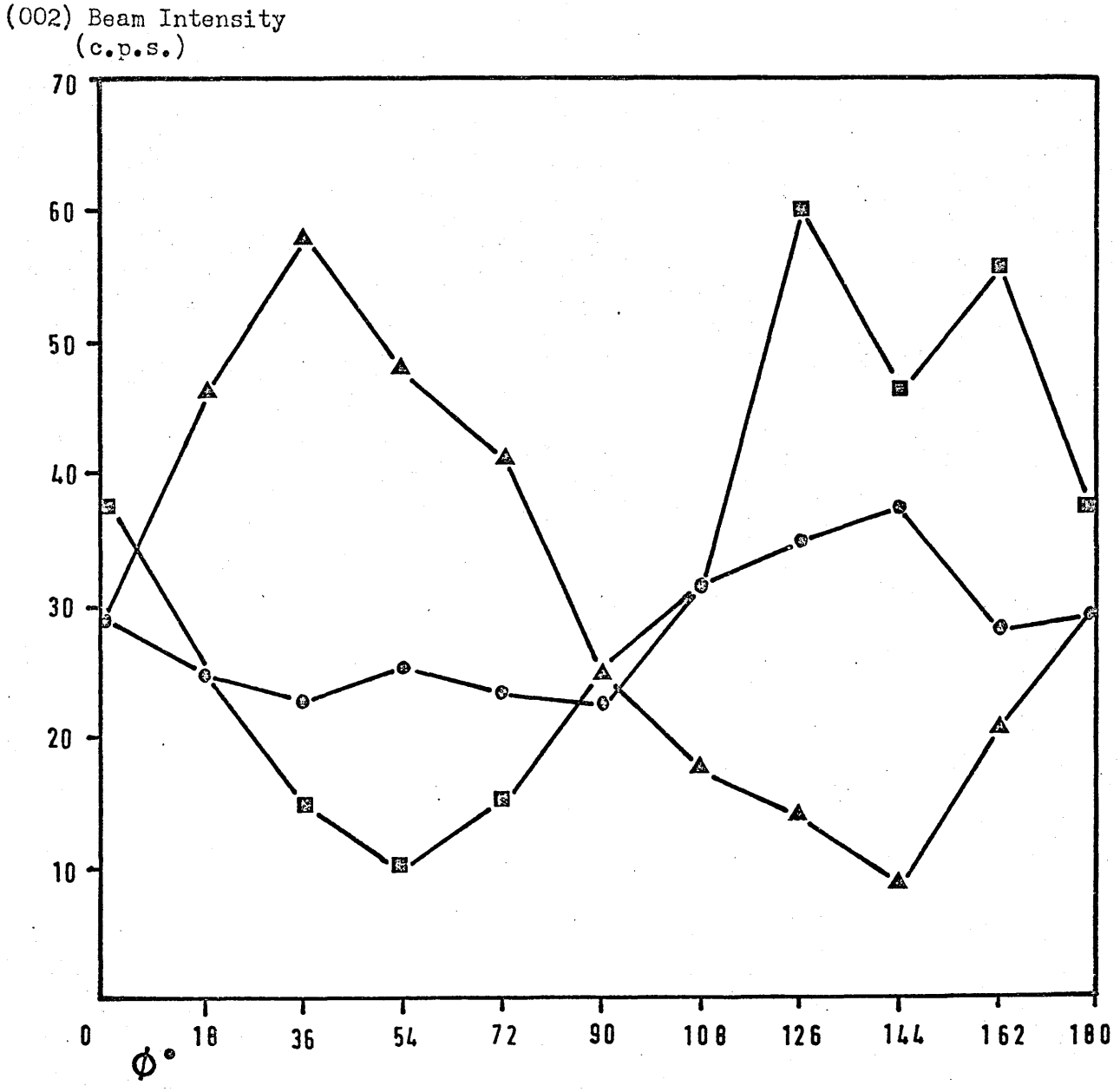

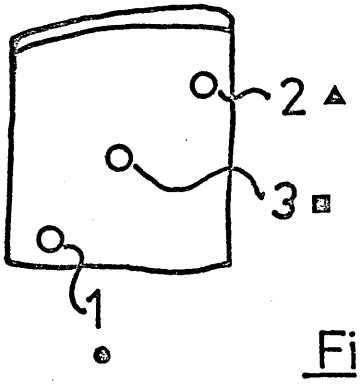

Figure 9.19

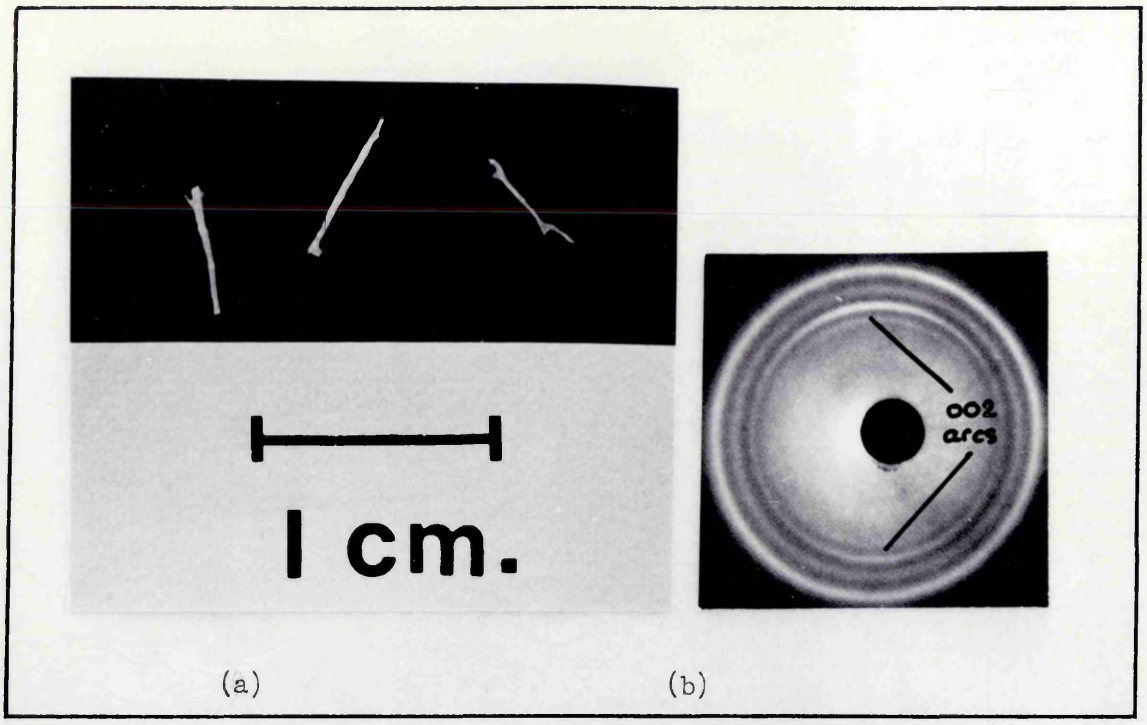

Figure 9.20

(a) Three rod-like traebeculae dissected from an ox femur.

(b) Diffraction pattern of one such traebecula, showing (002) arcs, thereby indicating a degree of c-axial alignment with the long axis.

9.3.3. Traebecular Bone - Summary

The traebecular structure within the femural head of an ox femur has been briefly investigated. Three sections were cut mutually perpendicular and examined in several positions. Under the optical microscope the traebeculae appear as sheet-like structures which show no preferential orientation. The traebeculae appear to increase in density at the shell to form solid bone. The shell structure itself shows no preferred c-axial orientation.

At the sites examined using the goniometer, the traebecular bone showed no preferential c-axial orientation.

The single rod-like traebeculae which were dissected from the cancellous bone in the region near the proximal end of the femural shaft were examined by the film method, and diffraction patterns were produced which indicated that c-axial orientation did exist in the direction of the traebecular long axis.

Hence, from the samples examined, only the well defined rod-like traebeculae showed any preferential fibrous orientation.

9.4. Discussion

The x-ray goniometer has proved to be a useful tool and (002) pole figures have been constructed for both primary and secondary bone types. The pole figures describe the fibrous structure of the bone samples in a quantitative way and this will be useful when selecting samples for physical testing to ensure uniformity of structure.

It must be emphasised that the pole figures produced so far have been constructed from only three lines on the stereographic projection. It was mentioned earlier that the contours could be drawn with a fair degree of confidence because of the large amount of information provided by film work which has preceeded this particular work. However, this will not always be possible, especially when studying bone with a non-uniform structure and many more measurements will be needed to enable the pole figure contours to be drawn accurately.

At this stage it was decided that rather than investigating many different types of bone with varying structures and functions, it would be better to confine the study to simpler forms of bone such as cortical primary and secondary types which have a well defined histology. Since most of the physical testing in the past has been performed on these types of bone this decision can be justified.

Although film work can provide a quick and qualitative measure of c-axial orientation, the goniometer produces more accurate quantitative results, and the following chapter shows how the goniometer can be used in isolation, i.e., without back-up film work, to produce pole figures in which the contours are plotted over the whole of the projection, thereby eliminating the need for any assumptions.

CHAPTER TEN

FULL POLE FIGURE DETERMINATION

10.1 Method

In a practical situation, when the microstructure of a bone sample needs to be determined, it is desirable to have a quick and accurate method which does not rely upon any other techniques. This chapter describes one such method, using the x-ray goniometer developed for this work to determine the full (002) pole figure of bone samples, and as before, primary and secondary type bone have been used since these types have been most commonly studied in the past.

In order to obtain an accurate representation of the (002) pole figure it is necessary to plot many points on the stereographic projection, so that the contours can be drawn with precision. This object can be achieved by rotating the specimen about its' long axis and thus examining a different plane within the sample. Because of this specimen rotation, the sterographic projections of the (002) poles are moved to different positions on the pole figure, as shown in figure 10.1 for RS and LS sections with $\pm$ 30° rotation about the long axis, with respect to the normal position.

All the bone samples examined so far have been in the form of thin plaques, aligned in the goniometer so that the plane of the plaque remains in the same orientation as the specimen is rotated through the angle ($\emptyset$). However, when the sample is rotated about its long axis through an angle (α), see figure 10.2, the movement through 180° ($\emptyset$) produces an apparent orientation in a randomly oriented sample. To measure this effect, a sample of bone with random c-axial orientation was prepared by compacting a fine bone powder, which was produced by filing, mixed with epoxy resin into a polythene mould. When the resin had cured, the bone powder was in the form of a solid block from which three mutually perpendicular sections were cut, approximately 70 microns thick. These sections were examined

Stereographic Projection of

Reference Sphere.

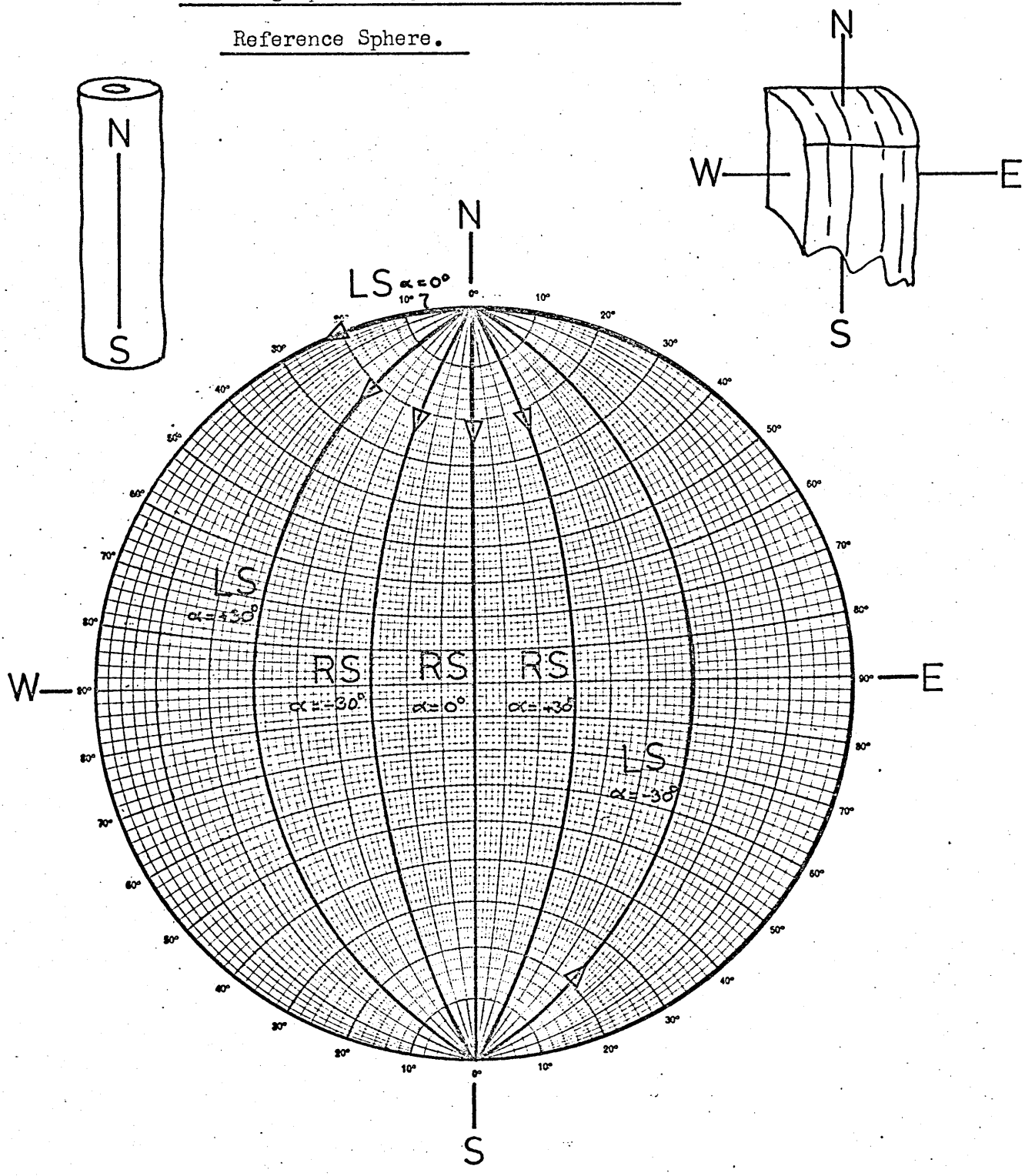

Figure 10·1

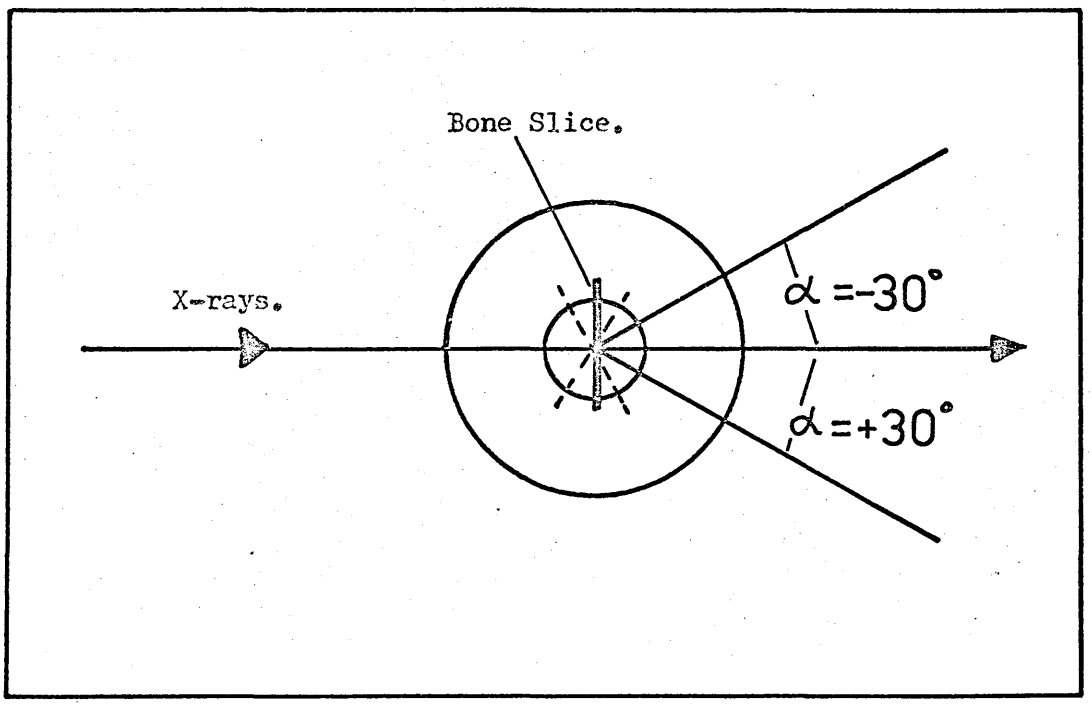

Figure 10.2

The specimen holder, viewed from above and showing rotation of $\alpha = \pm 30^{\circ}$ about the vertical axis, (N/S on the pole figure).

by the flat film and goniometer methods, an evenly distributed (002) ring indicated a random orientation of the bone mineral within each section. Figures 10.3 and 10.4 show the (002) diffracted beam intensity v ($\emptyset$) for a randomly oriented bone sample which was set with $\pm$ 30° (α) rotation about its long axis. The background intensity at angular positions above and below the $2\Theta_B$ (002) setting are also shown.

The intensity variation is attributed to two factors:-

a) absorption
b) diffracting volume

When the sample is displaced by the angle (α), a rotation through ($\emptyset$) causes variation in the amount of material being irradiated, this is because the orientation of the sample plane is no longer constant with respect to the incident and diffracted x-ray beams. Hence the change in diffracting volume alters the diffracted beam intensity. Also the path length of x-rays in the sample now varies with ($\emptyset$) when $\alpha \neq 0°$, and thus a combination of these two effects produce the apparent orientation in randomly oriented samples. To overcome this difficulty, a correction factor can be calculated using figures 10.3 and 10.4, for each position of ($\emptyset$) and (α) used. Figure 10.5 shows the correction factor by which the count rate has to be multiplied to obtain a true orientation pattern, for values of (α) set at $\pm$ 30° from the normal position.

(002) Diffracted Beam Intensity v (φ) for Sample with Random c-axial Orientation, $\alpha = +30°$.

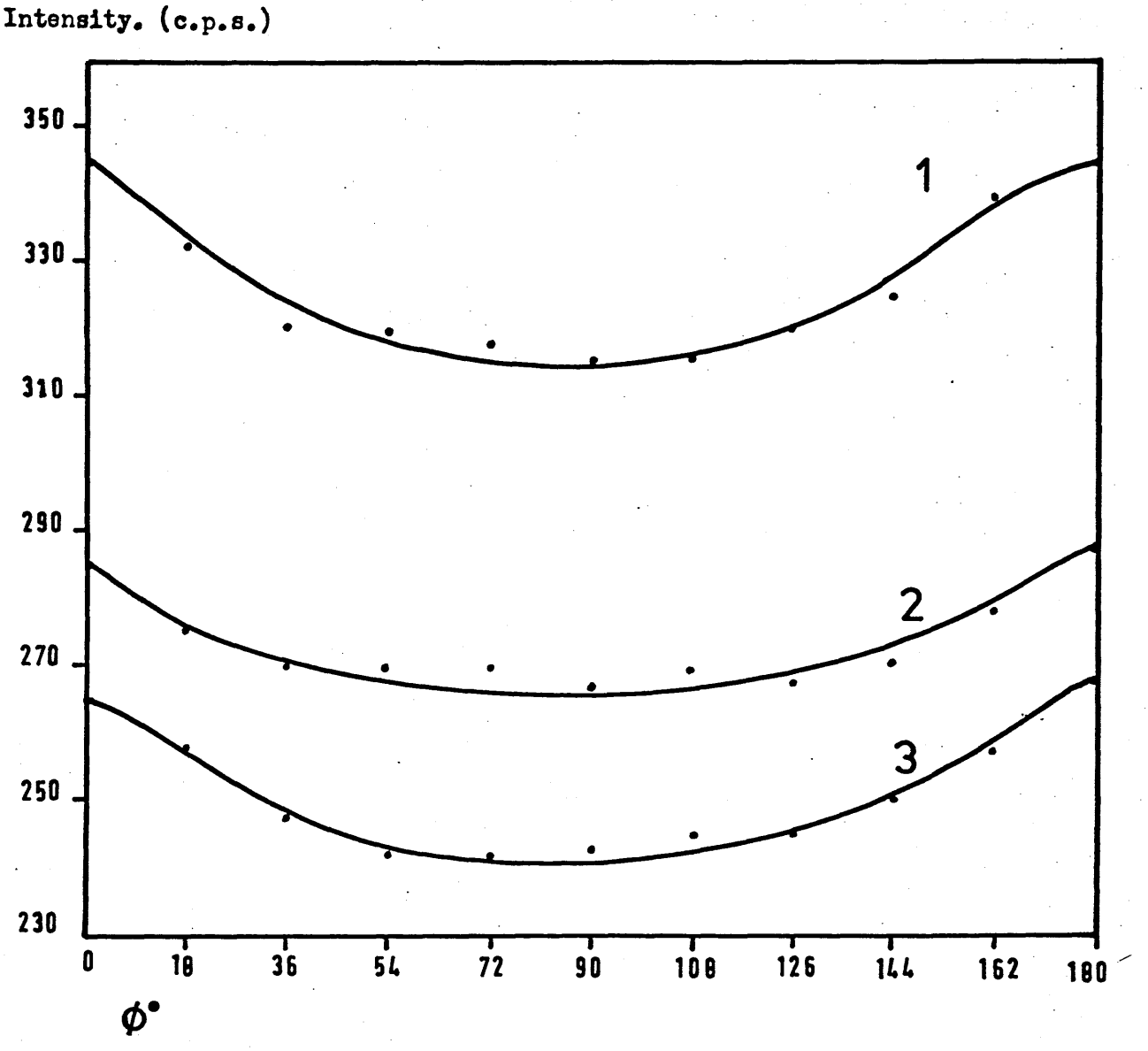

1 Total Count. (002) Beam + Background.

2 Background Count Below 2θ (002).

3 Background Count Above 2θ (002).

Figure 10·3

(002) Diffracted Beam Intensity v (ϕ) for Sample with Random c-axial Orientation, $\alpha = -30°$.

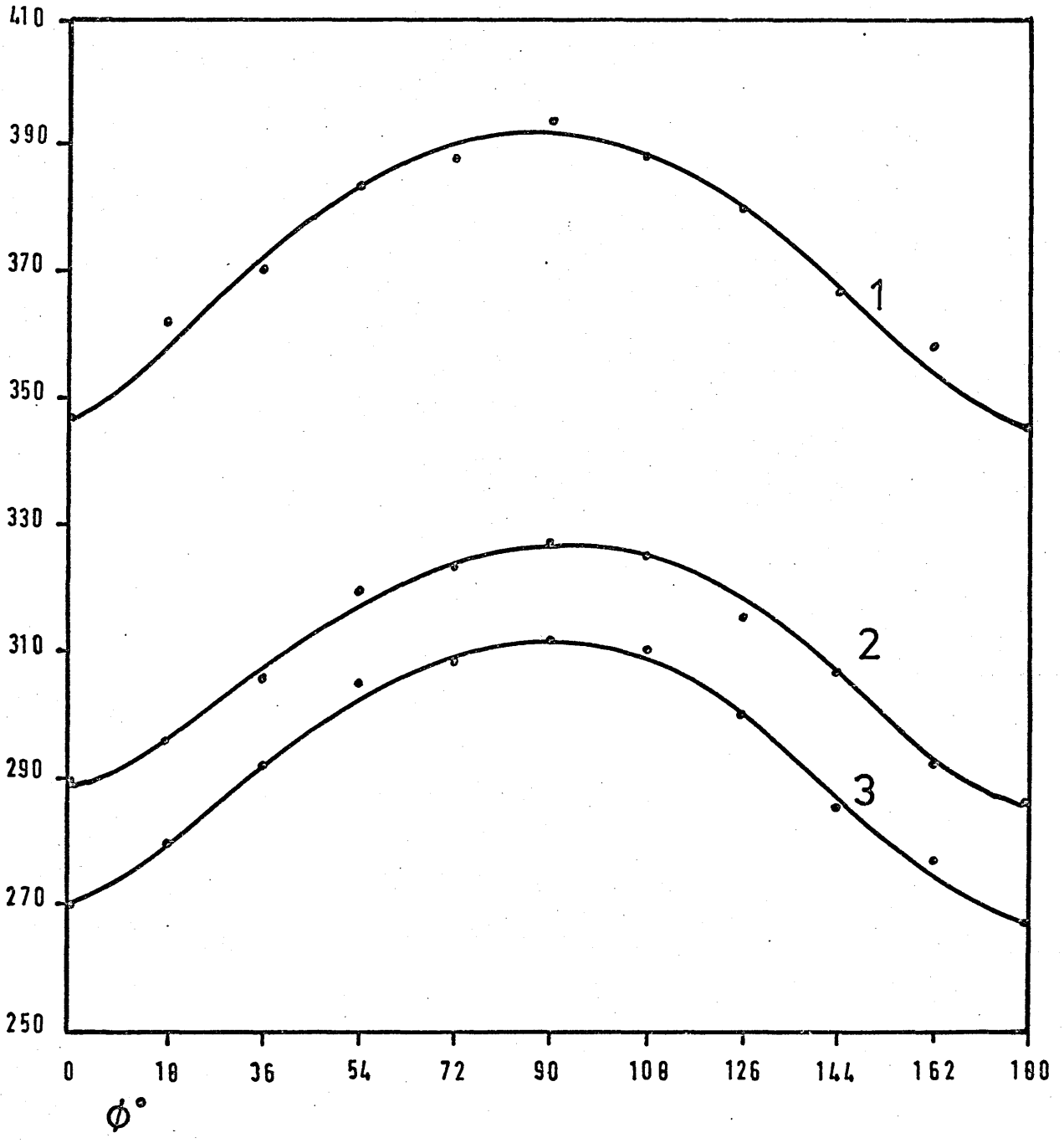

1 Total Count. (002) Beam + Background.

2 Background Count Below 2θ (002).

3 Background Count Above 2θ (002).

Figure 10·4

(002) Diffracted Beam Intensity Correction Factor.

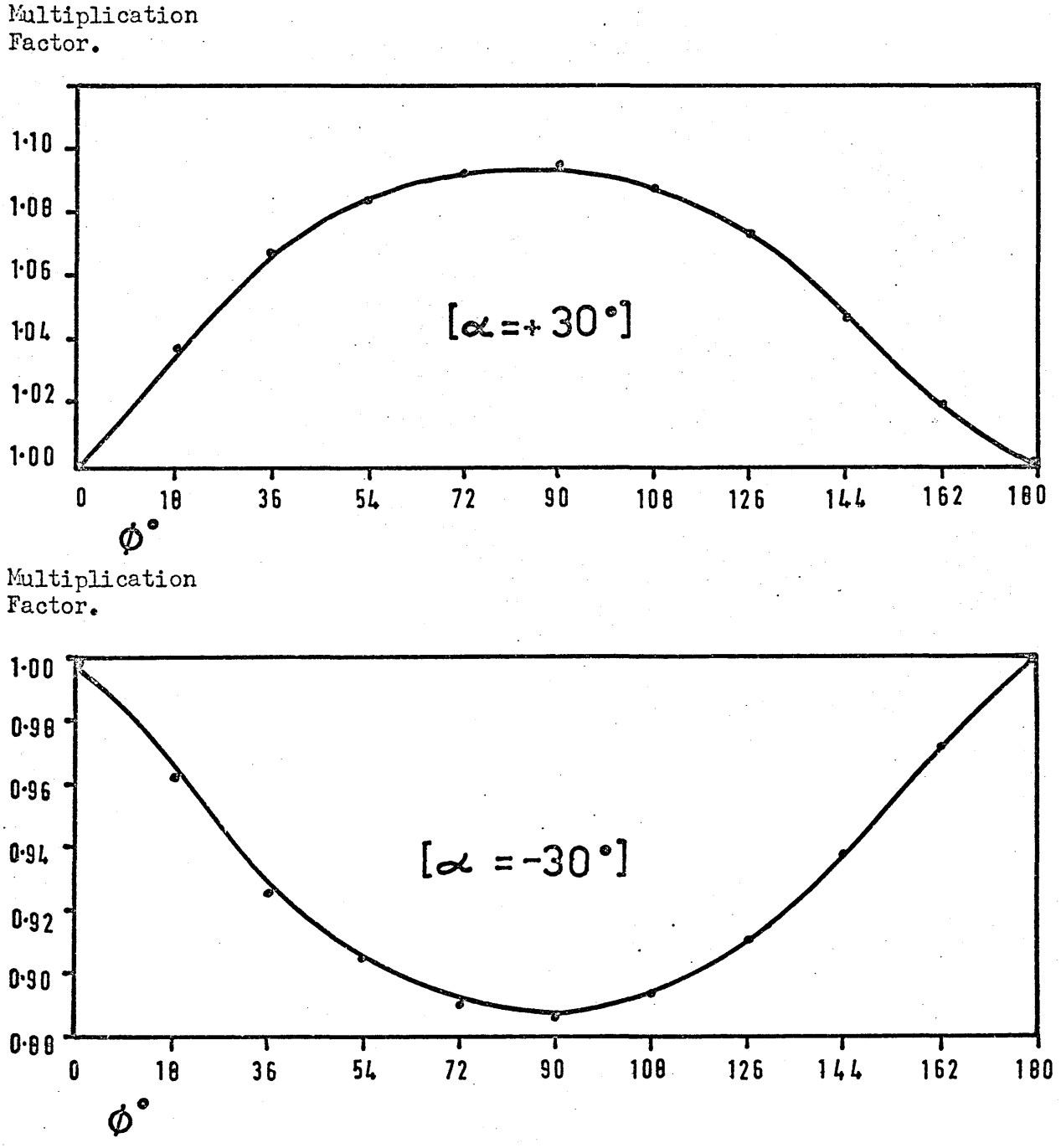

Figure 10·5

10.2 Primary Type Bone

Sections LS1 and RS1 of the ox femur described in 9.1 were used for this experiment. The (002) diffracted beam intensity as a function of (ϕ) with $\alpha = 0^{o}$ has already been determined for these sections, and figures 10.6 - 10.9 show this relationship for each section when set with $\alpha = \pm 30^{o}$ from the normal position. The intensity is also shown in each figure multiplied by the appropriate correction factor. These corrected curves are then used to plot the (002) pole figure shown in figure 10.10, after the final correction has been applied to equalise intensities at points of intersection.

Longitudinal Section (LS1) $\alpha = +30°$

(002) Beam Intensity.
(c.p.s.)

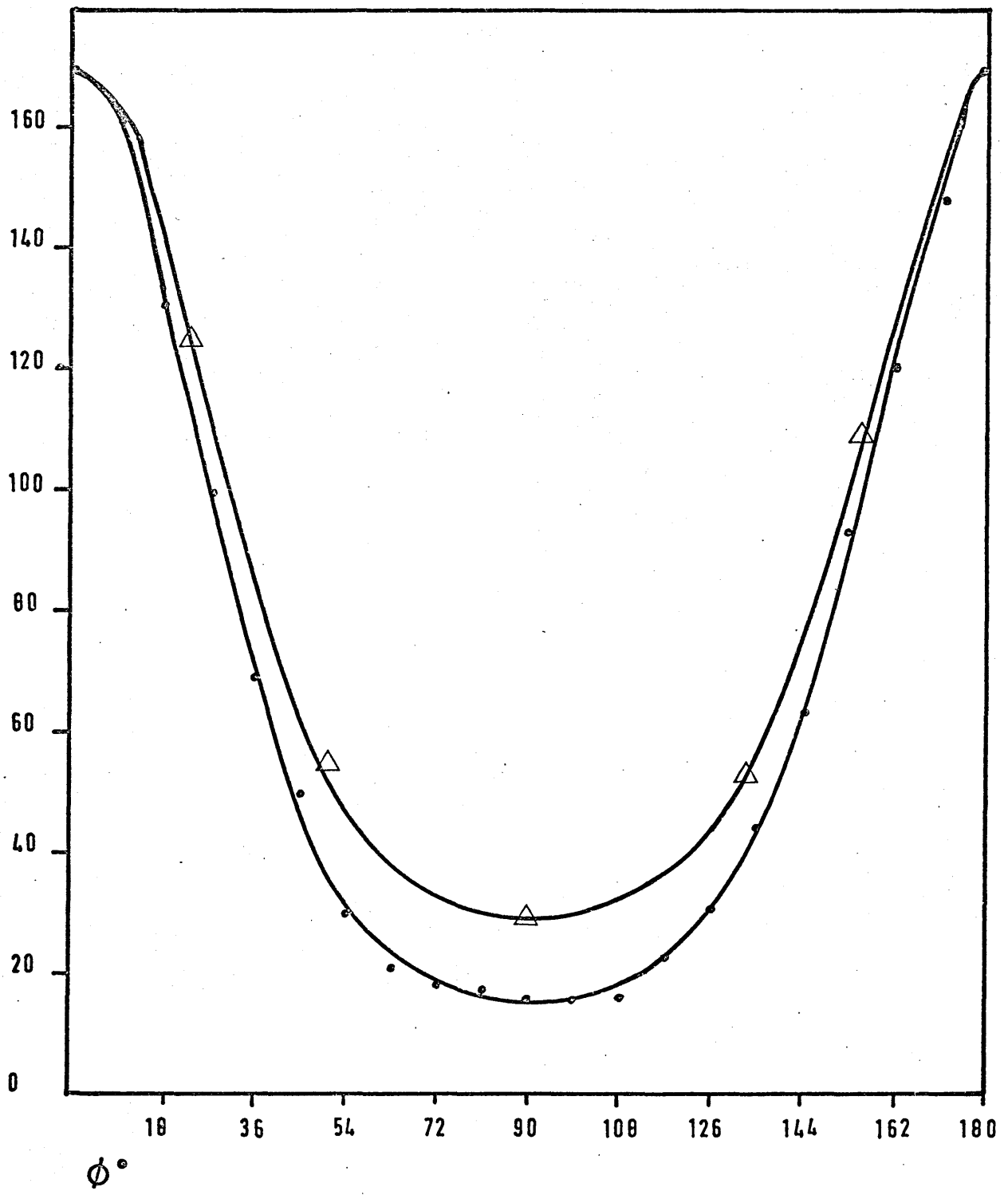

△ Intensity Corrected for α.

Figure 10·6

Longitudinal Section (LS1) $\alpha = -30°$

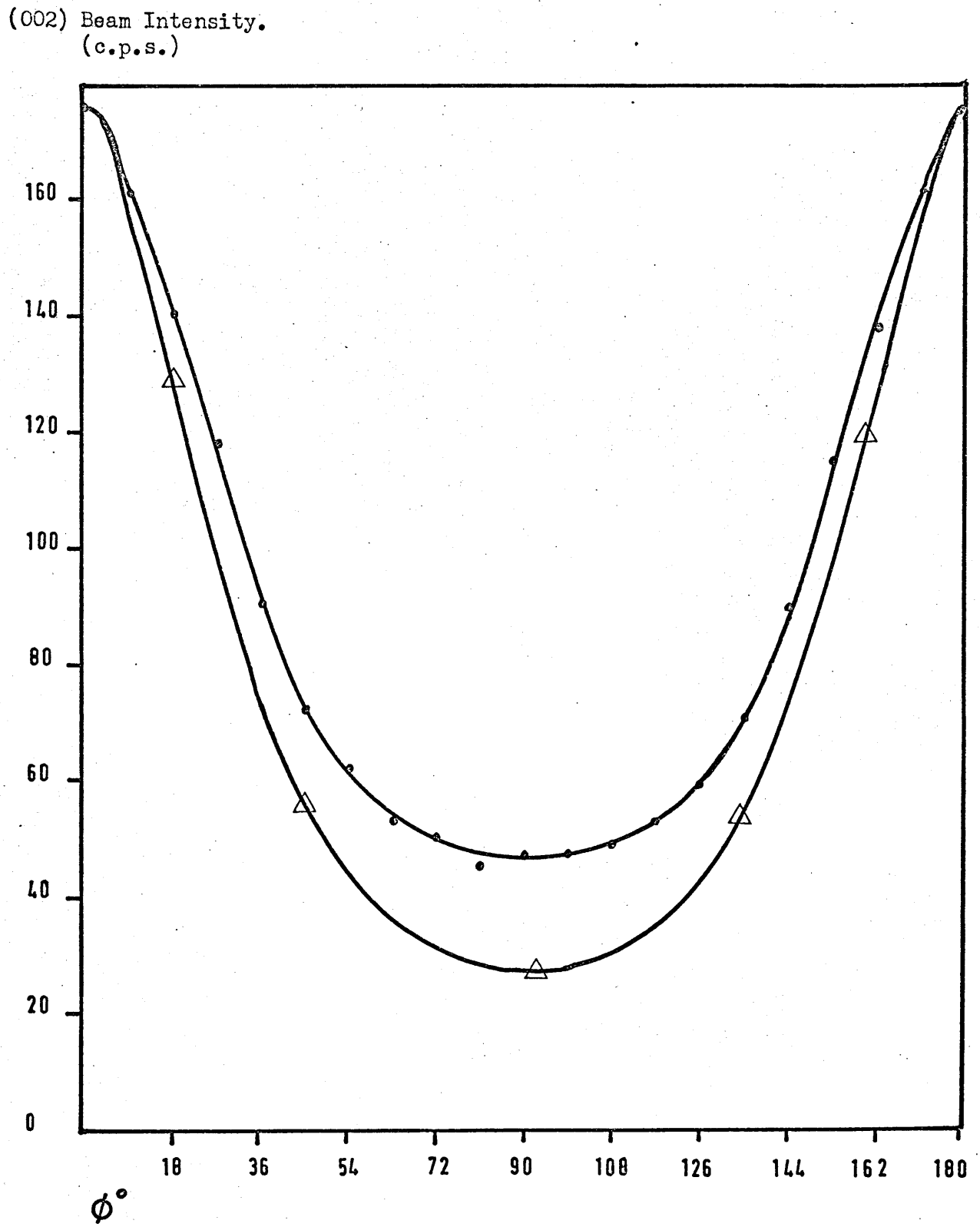

△ Intensity Corrected for α.

Figure 10·7

Bone Mineral c-axial Orientation, Primary Type Bone.

Radial Section (RS1), $\alpha = +30°$.

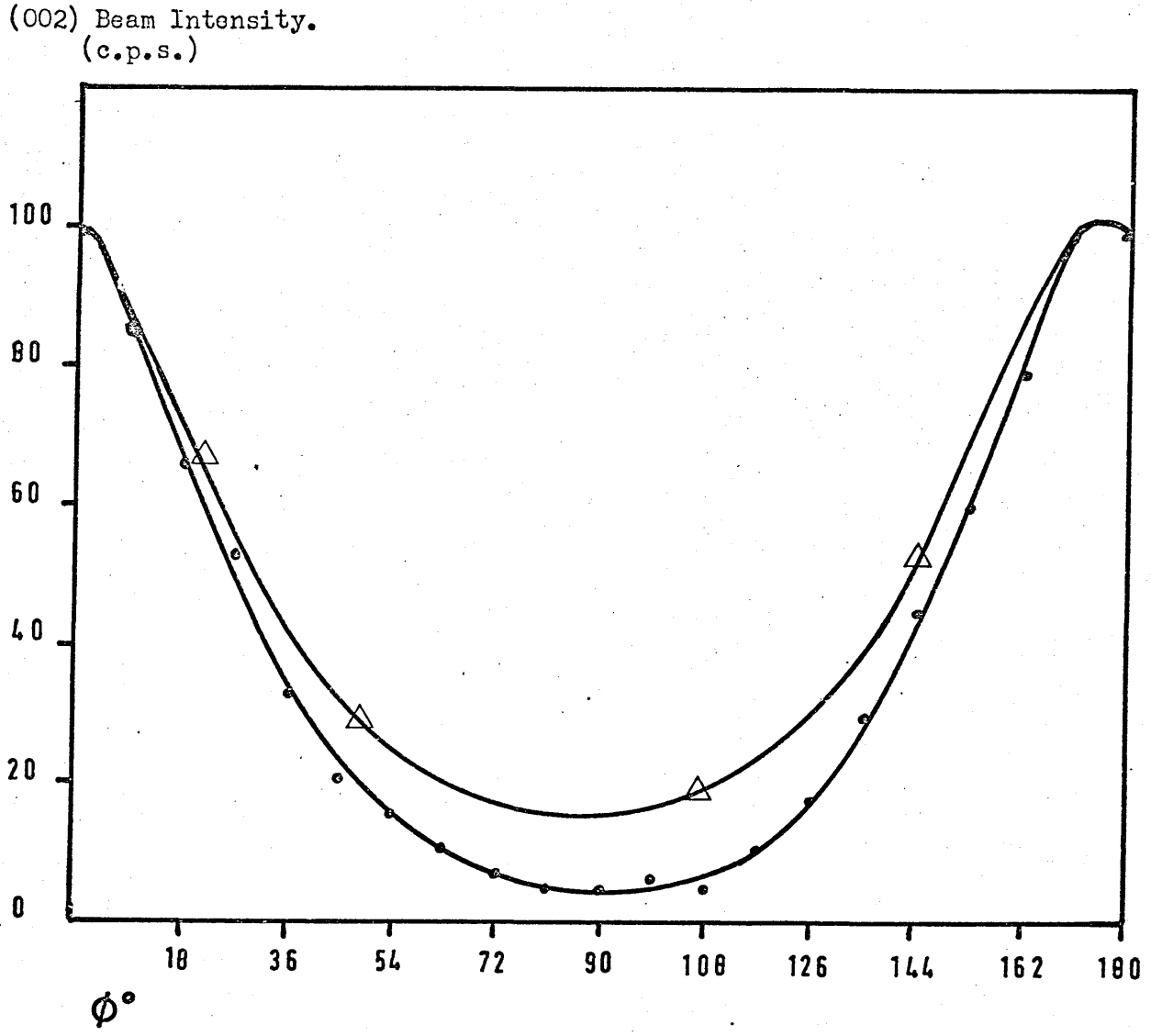

△ Intensity Corrected for α.

Figure 10·8

Bone Mineral c-axial Orientation, Primary Type Bone.

Radial Section (RS1), $\alpha = -30°$.

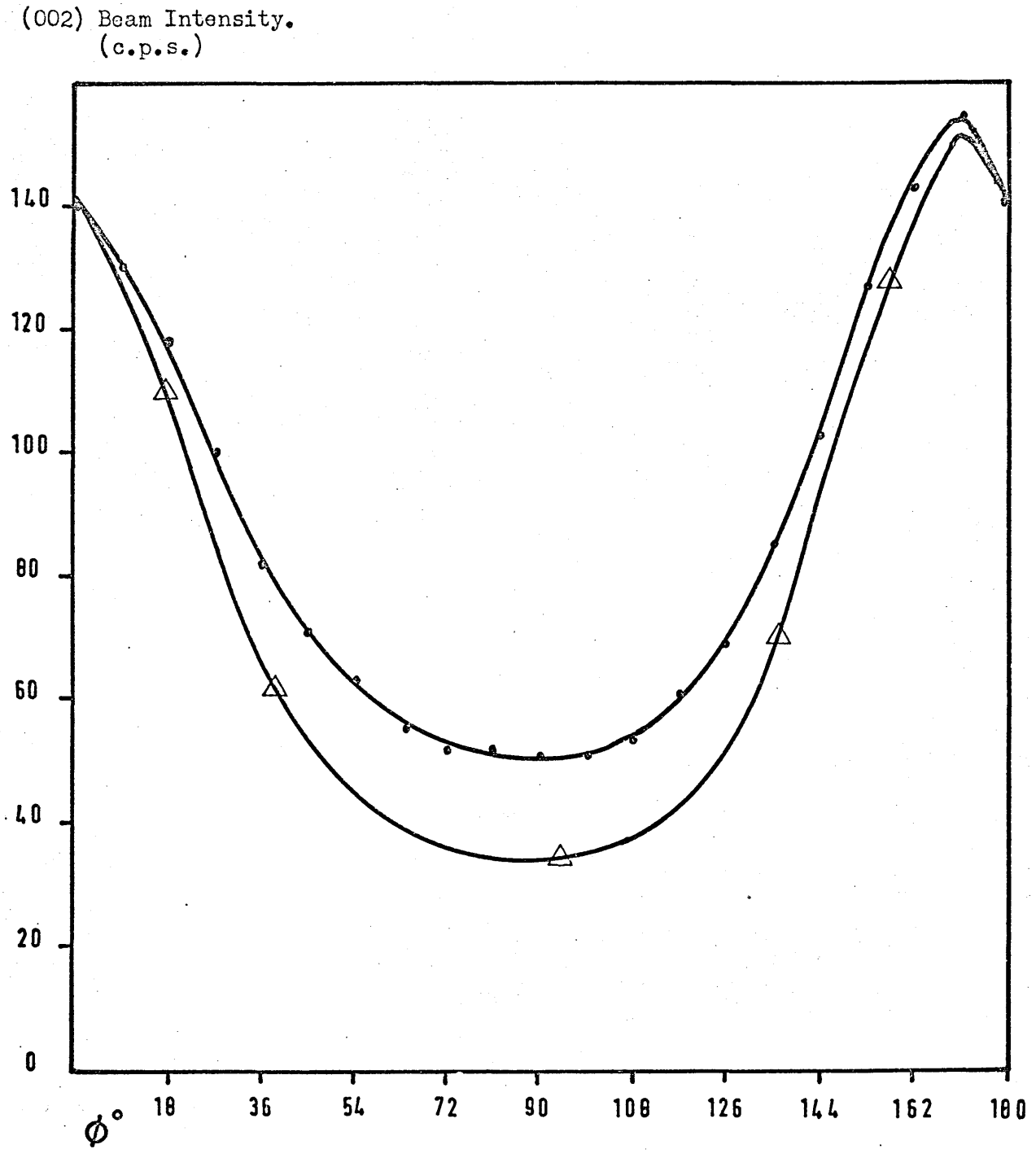

Figure 10·9

(002) Pole Figure. Primary Type Ox Bone.

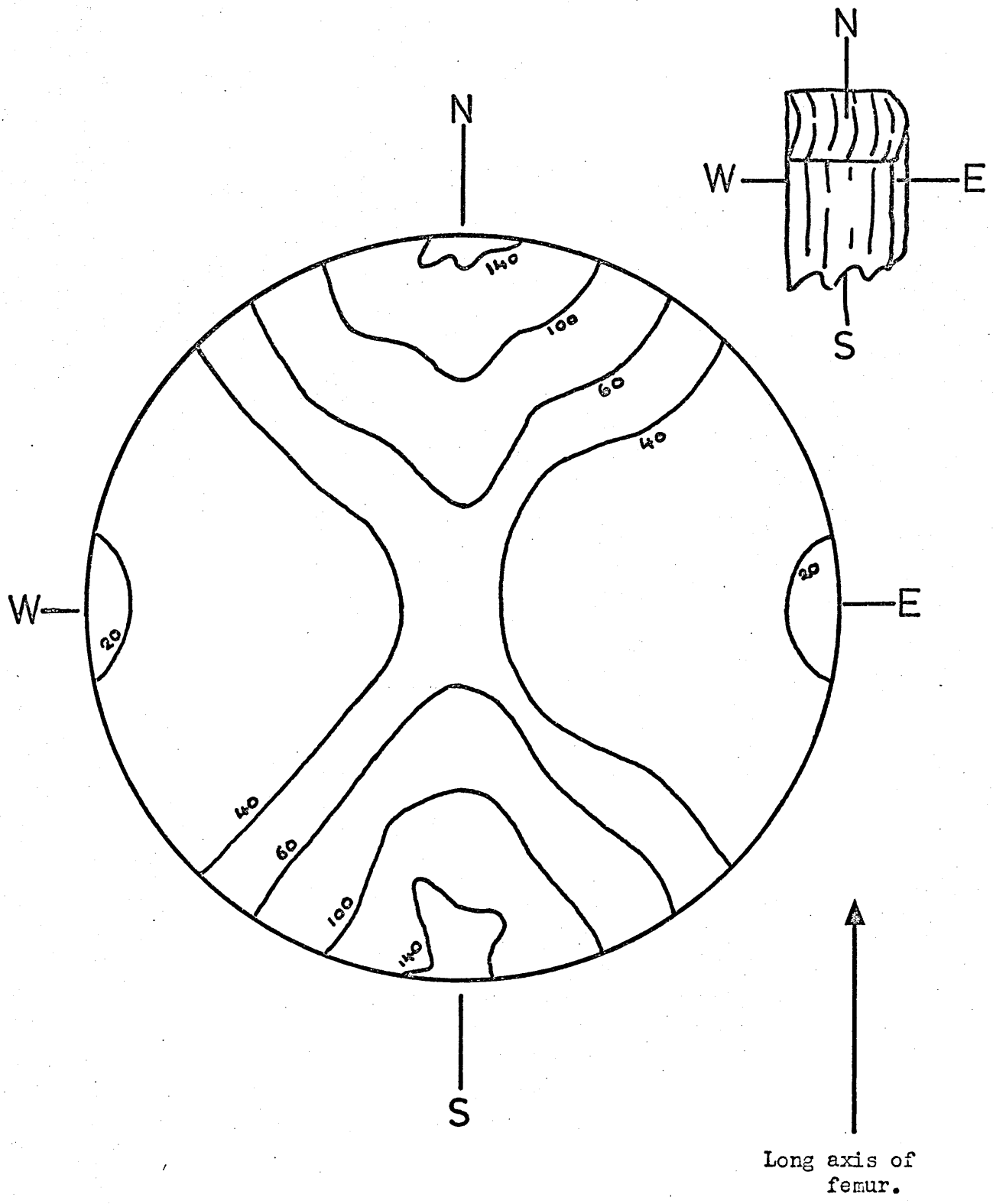

Figure 10·10

10.3 Secondary Type Bone

Sections LS2 and RS2 of the human femur described in 9.2 were used for this experiment. Figures 10.11 - 10.14 show the corrected and uncorrected (002) beam intensity versus (ϕ) distributions for $\alpha = \pm 30^{\circ}$, which are combined with the previously determined distributions with $\alpha = 0^{\circ}$, to produce the (002) pole figure as shown in figure 10.15.

Bone Mineral c-axial Orientation, Secondary Type Bone.

Longitudinal Section (LS2) $\alpha = +30°$

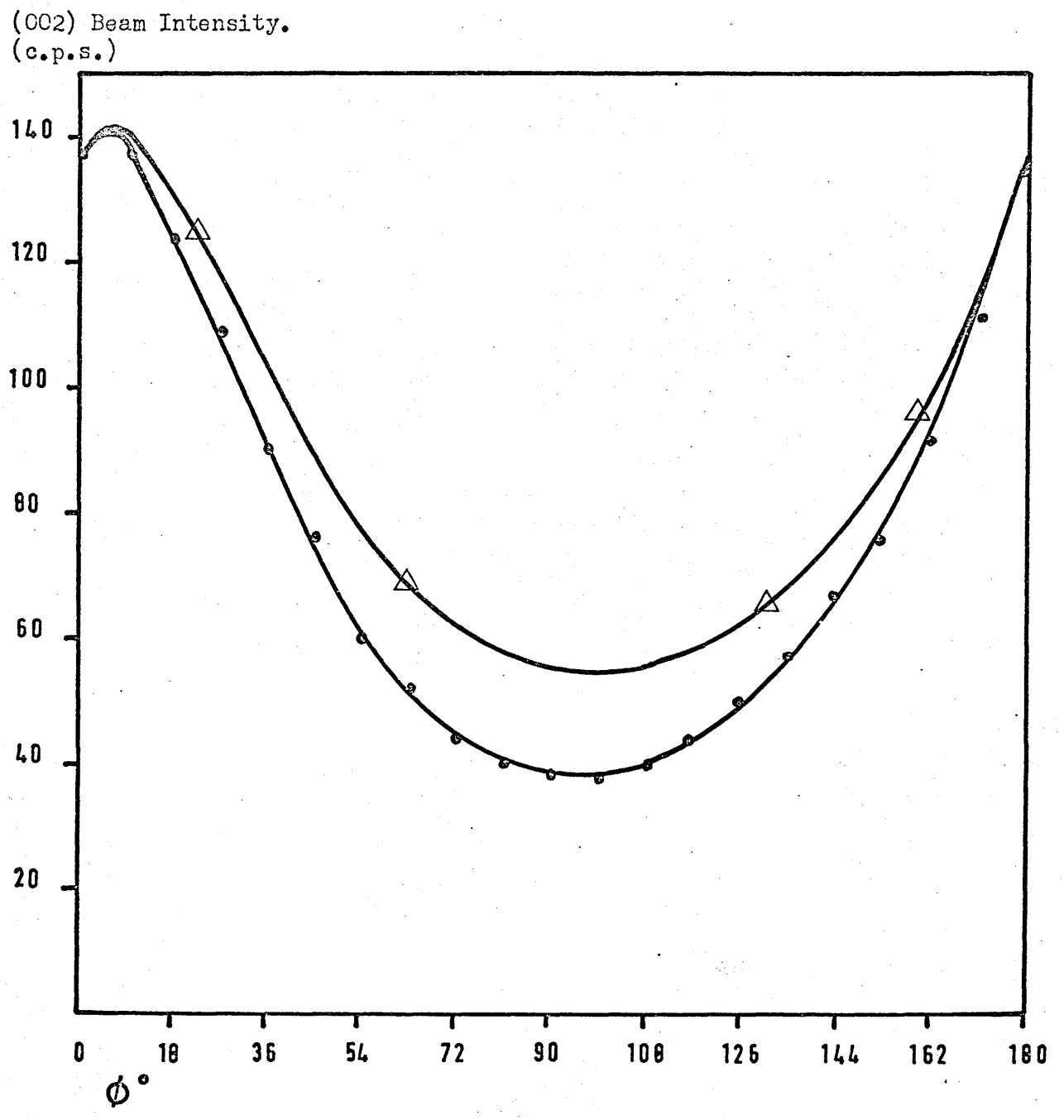

△ Intensity Corrected for α.

Figure 10·11

Longitudinal Section (LS2) $\alpha = -30°$

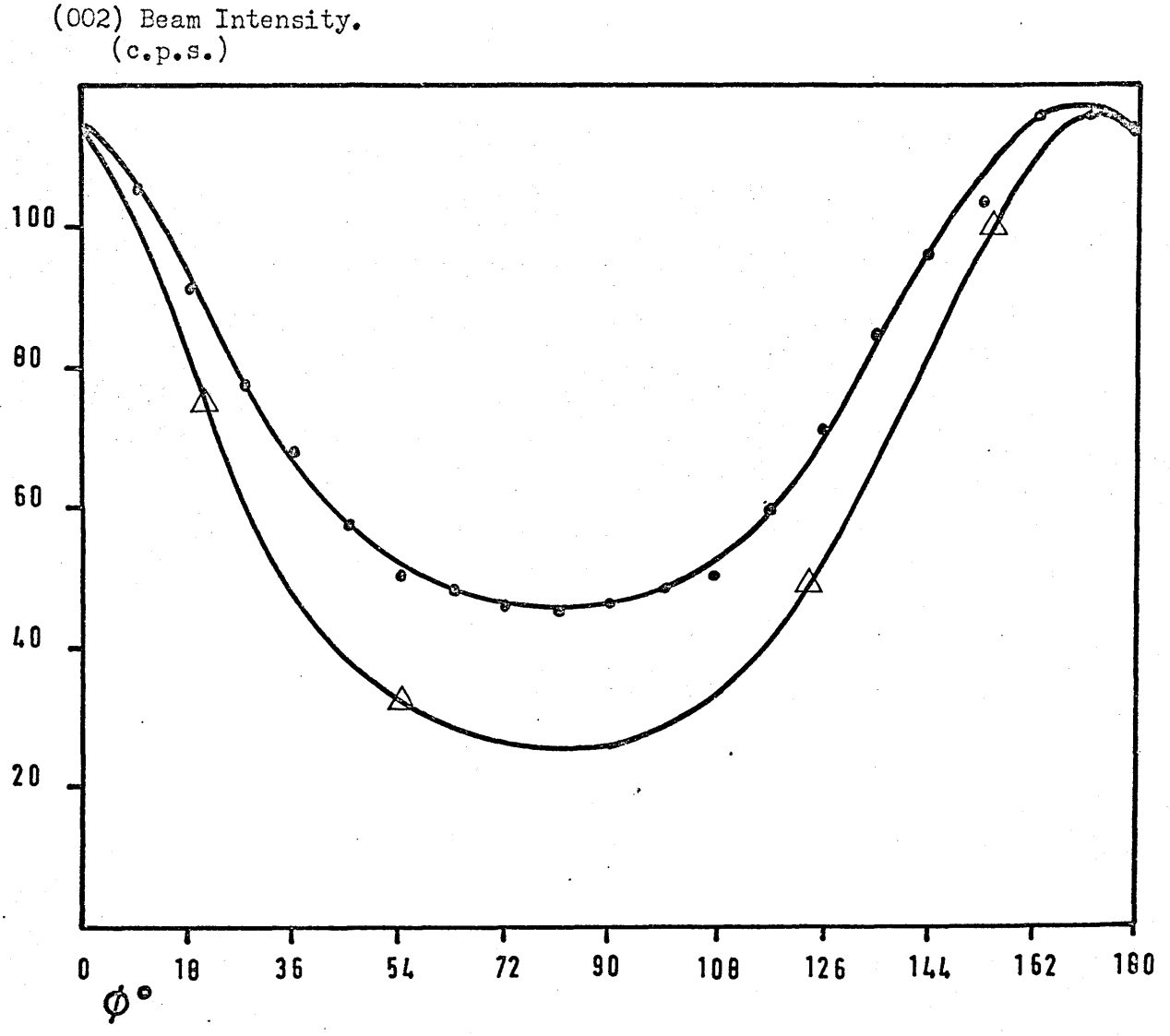

△ Intensity Corrected for α.

Figure 10·12

Bone Mineral c-axial Orientation, Secondary Type Bone.

Radial Section (RS2) $\alpha = +30°$

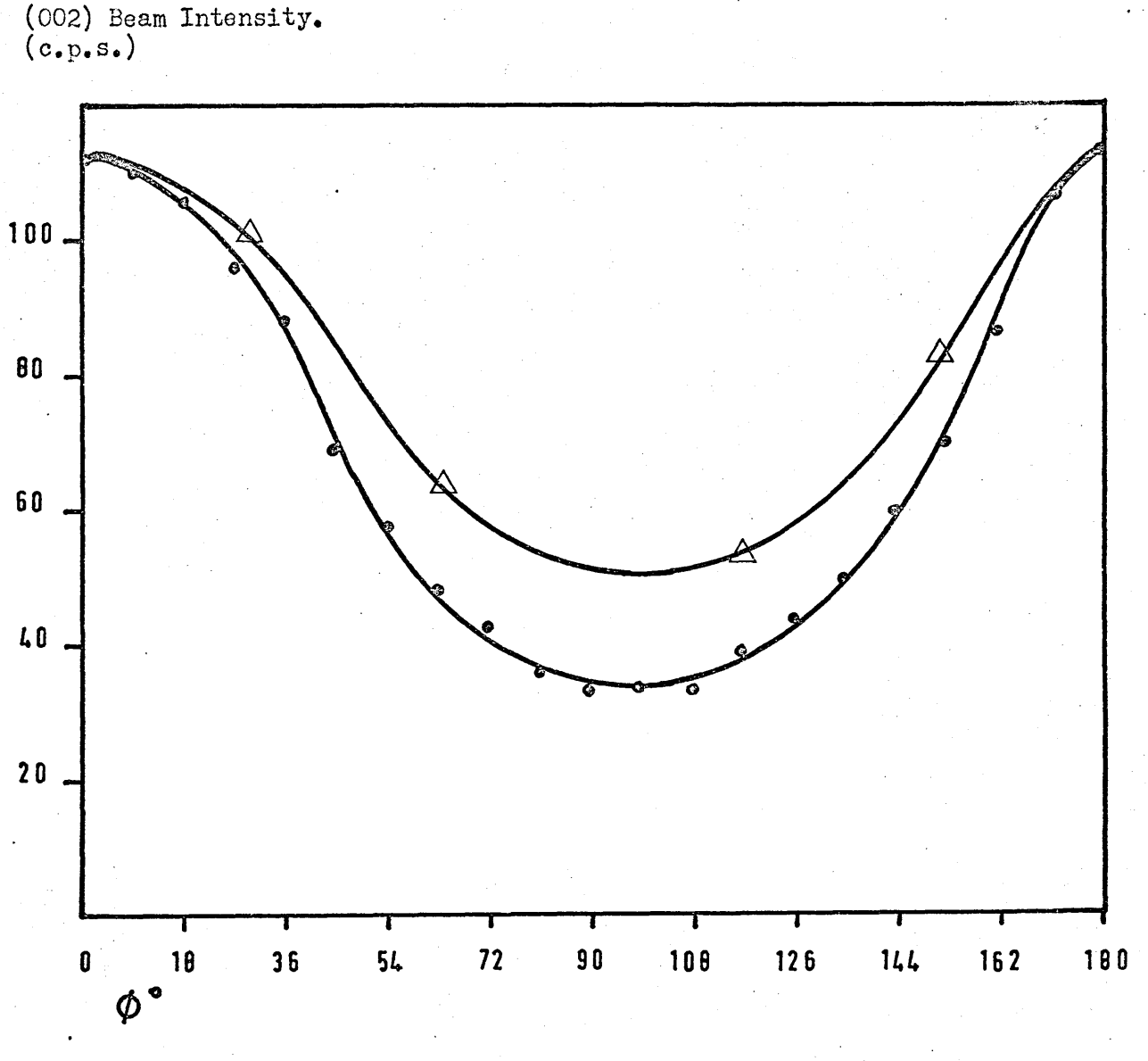

△ Intensity Corrected for α.

Figure 10·13

Bone Mineral c-axial Orientation, Secondary Type Bone.

Radial Section (RS2) $\alpha = -30°$

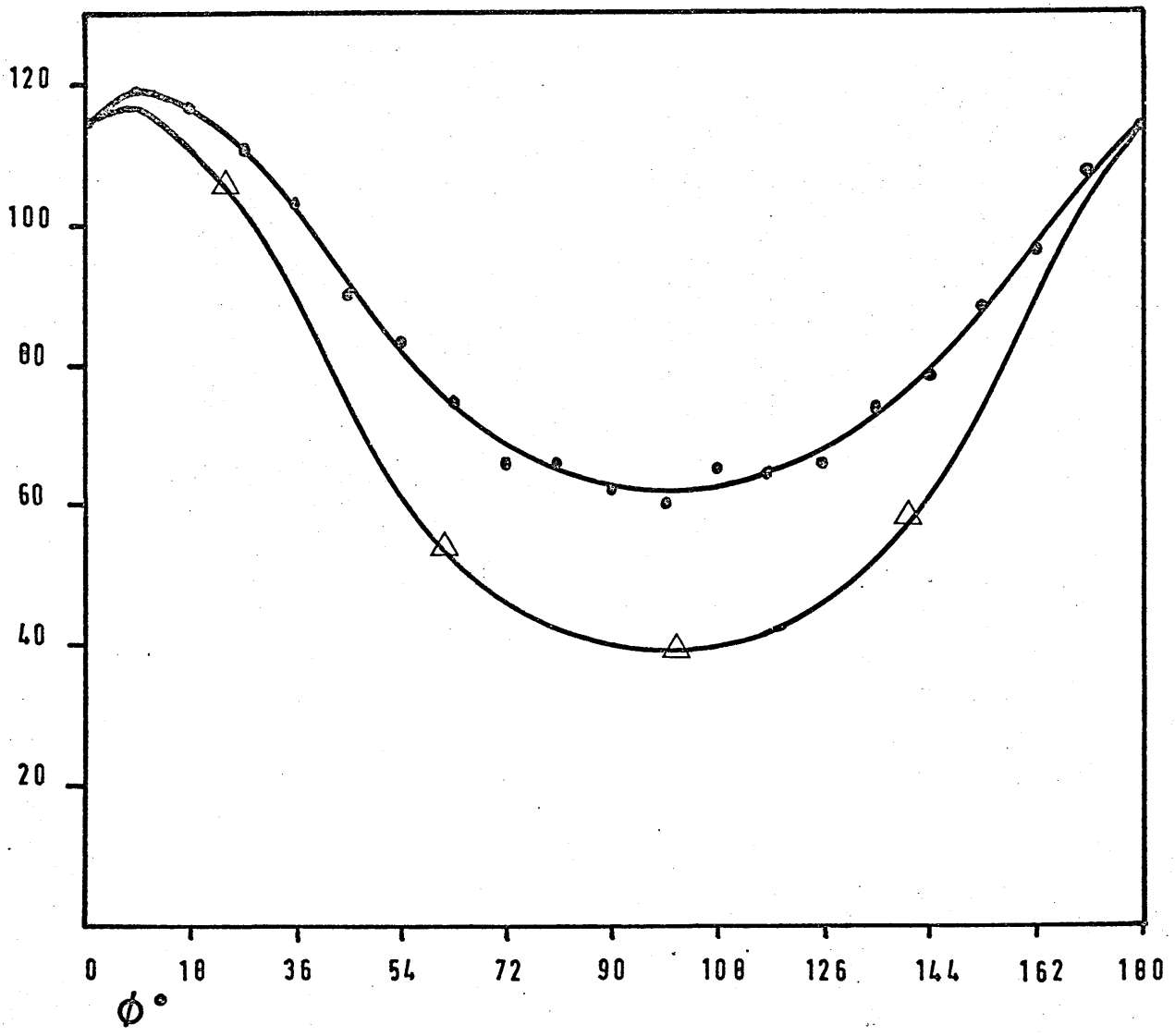

△ Intensity Corrected for α.

Figure 10·14

(002) Pole Figure. Secondary Type Human Bone.

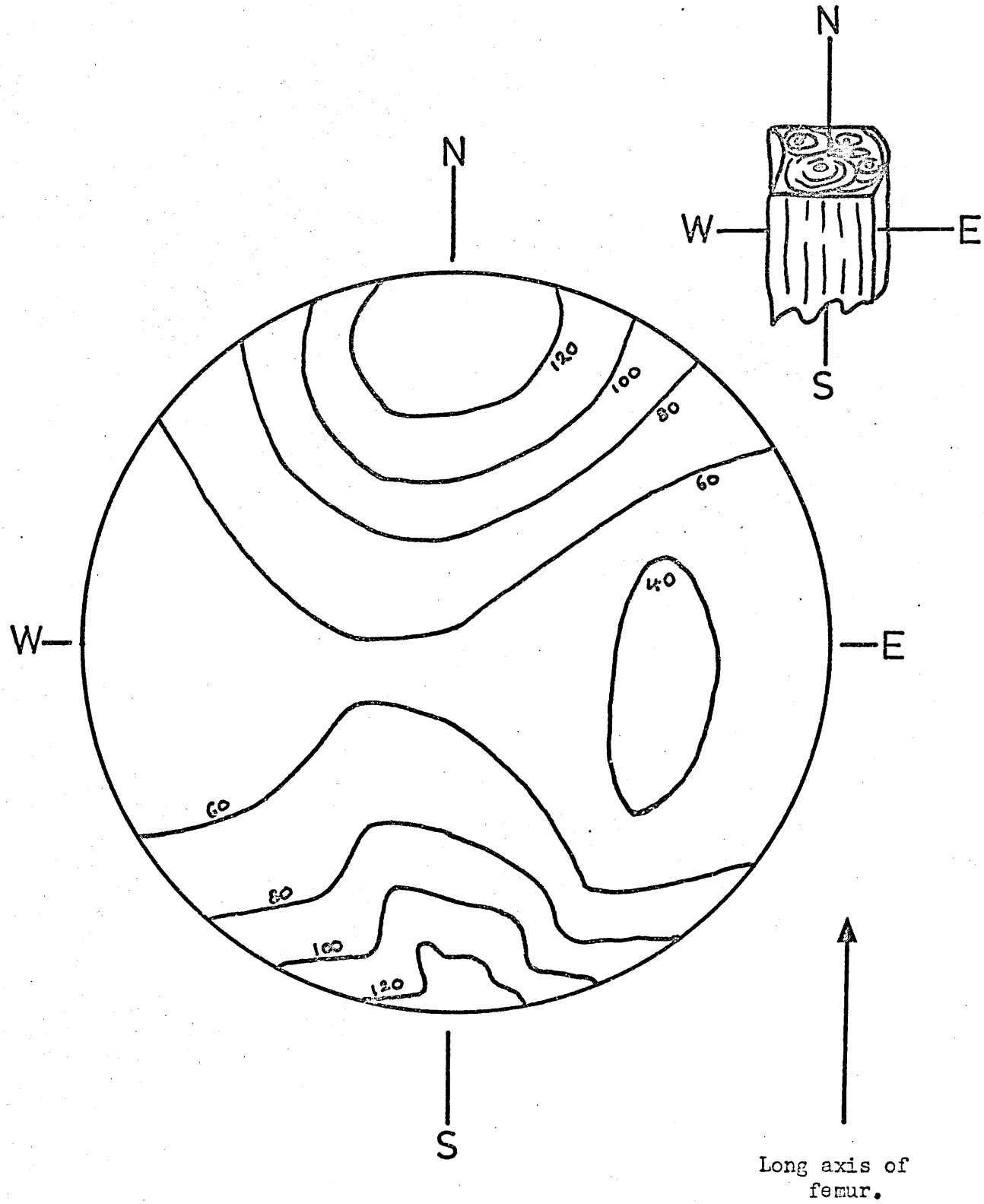

Figure 10·15

10.4 Summary

The x-ray goniometer developed for this orientation study has proved to be effective in producing (002) pole figures of small bone samples without the aid of other techniques. Therefore, this technique could be used for a study of bone microstructure itself, or in a routine manner where a determination of the microstructure is required.

The samples used to date have been thin plaques (approximately 70 microns thick), with an area of examination approximately 2mm in diameter. The size of area examined is determined by beam collimation, and a finely collimated beam could be used to examine the orientation variation within a single bone sample, and it is feasible that by using a microfocus x-ray set with suitable optical equipment, structural variation between distinct histological structures such as osteons and interstitial lammellae could be examined.

The pole figures plotted in this chapter have been produced by joining points of equal intensity between six lines of longitude covering the stereographic projection, hence allowing the contours to be drawn with more precision than for the previous pole figures. The accuracy ultimately depends upon the number of lines used to construct the figure, and this is determined by the experimental conditions.

In both primary and secondary type bone taken from the mid-femural region of bovine and human bones respectively, the major axis of preferred c-axial orientation is aligned on average with the long axis of the femur. The primary type bone shows a planar orientation in the laminar direction, whilst the secondary type bone exhibits an even c-axial distribution about the main fibre axis, hence confirming the findings of

chapter 9 and the large amount of film work which has preceeded this particular study.

The above statement of results appears qualitative, but does in fact, describe the quantitative data expressed in the pole figures, and it is the pole figures which yield detailed information about bone mineral orientation and hence the fibrous structure of a material whose structure has been in general described only qualitatively.

It is envisaged that the pole figures and the techniques developed for their determination will play a significant part in the future studies on structural aspects of bone, their significance is discussed with the rest of this work in the following final chapter.

CHAPTER ELEVEN

SUMMARY AND SUGGESTIONS FOR FUTURE WORK

11.1 Introduction

Bone is a complex living tissue having many functions. It is the host for the body's store of calcium and it is the presence of this mineral in the form of small crystals, which enables bone to perform its structural function. Before the behaviour of bone, in both normal and abnormal situations can be understood, many aspects of its structure and metabolism need to be studied. This work has examined bone as a material and attempted to clarify aspects of its microstructure which have not been well defined. Specifically, the shape and size of bone mineral crystals have been examined, and also the three-dimensional orientation of these crystals has been determined, which provides information about the fibrous structure of the sample. These aspects, in particular the techniques developed, the results obtained, and suggestions for further work will now be discussed in detail.

11.2. Specimen Preparation

Before any relevance can be attached to in-vitro experiments on any biological material, it is important to know what changes have occurred after death, whether by autolytic action or by the specimen preparation technique itself. Previous workers, see 3.1.2., concluded that bone mineral morphology and composition are not significantly changed between unfixed bone, and bone which has been fixed by a variety of methods. However, these results tended to be qualitative, and lacking in quantities which could be measured and compared. Since materials and techniques were being used in this study which had not been specifically used in the past, it was decided to determine if either the shape, size or composition of the bone mineral crystals in fixed and unfixed samples were significantly different.

The first investigation, see 3.1., used the x-ray powder method to compare the crystalline structure of bone samples fixed by four different techniques, to an untreated sample. The bone mineral was assumed to have the generally accepted crystalline structure of hydroxyapatite, and the diffraction patterns produced by all five samples fitted this model. The crystal d-spacings were calculated from measurements taken from each diffraction pattern and compared by the t-test. No significant differences were found at the 5% level between the five samples, indicating that the bone mineral composition was not significantly affected by any of the preparations used.

Bright field electron microscopy was used to examine fixed and unfixed samples of bone, and difficulties were encountered, as mentioned later in obtaining accurate measurements of the crystal size and shape. However, the general appearance of many micrographs examined throughout this work has shown bone mineral crystals to have varying size and shape within each sample, and no evidence was found to suggest that bone mineral crystal morphology is affected by any of the preparations used.

The technique of dark field imaging has allowed the c-axial length of bone mineral crystals to be measured, and this parameter has been used to assess the effect of specimen preparation. Of the three samples of bone examined, see 5.2., two were prepared by different routine biological preparations, and the other received no treatment at all. The data presented in 5.2.2., was analysed by a computer programme using a one-way analysis of variance, and the measured crystal size distributions showed no significant difference at the 5% level. Hence the techniques used in this study have failed to find any significant differences in the shape, size or composition of bone mineral crystals between treated and untreated samples. This result justified the use of untreated bone for this work, and meant that sample preparation time was reduced to a minimum.

The ultramicrotomy of unfixed, unembedded bone proved to be a relatively simple operation with the aid of a diamond knife. The bone sections were quite often fragmented, however, the fragments were ususally sufficient for investigation. The technique of ultramicrotomy has been criticised, (A. Boyde, personal comm.) as possibly damaging the bone mineral crystals through the deformation associated with a cutting mechanism. However, no evidence has been found, in this work or elsewhere, to substantiate this criticism, and it is therefore, assumed that samples prepared for electron microscopy by the techniques used in this work contain bone mineral crystals unchanged from their natural form, and are therefore representative of viable tissue.

11.3. Bone Mineral Shape and Size

The shape and size of bone mineral has been investigated in the past by two techniques, x-ray diffraction and bright field electron microscopy. The results produced by these two methods have not been consistent with each other, and have not succeeded in delineating either the shape or size of the bone mineral crystals. Both of the above methods have been used in this work, which has been applied and developed specifically in an attempt to explain past discrepancies and hence obtain an accurate measure of the crystal size and shape. These three techniques, their results and interpretation will now be discussed in detail.

Bright Field Imaging

Many bright field micrographs of bone have been presented in Chapter 4, the general appearance of a bone section shows many irregular shaped, densely packed overlapping crystals, with dimensions varying from approximately 5.0nm, to over 100.0nm. There appears to be both rod and plate-like forms of the crystals, which, since a bright field image is a two-dimensional projection of a three-dimensional object, could mean that the rods are images of plates on edge, or that the two types of structure are actually present. The technique of specimen tilting has been applied to this problem, and results are consistent with the rod-like images being plates on edge. However, the technique suffers from several disadvantages which, whilst not invalidating results do preclude accurate measurements. Firstly, the small size of a bone mineral crystal, and the fact that it is overlapping with many of its neighbours make isolation difficult. Secondly, as the specimen is tilted, diffraction contrast changes the image and this makes individual crystals difficult to follow. Thirdly, unless the crystal being studied is actually on the axis of tilt, a vertical displacement occurs and this changes the magnification factor of the microscope. However, it is envisaged that these problems could be overcome in the following way.

Figure 4.3. shows a section of bone which has torn and buckled during sectioning. It is worthy of note that no rod-like images are present in the very thin region around the tear, and only where the section has buckled and is thicker, do the rod-like images appear. It is precisely this type of bone section which is required for specimen tilting experiments since individual plate-like crystals can be identified and followed throughout the movement. It would be important in this case to provide support for the section to prevent movement or breaking caused by the pressure of the electron beam, and this can be accomplished by using carbon coated grids. Finally, some of the more recent electron microscopes, (e.g., JEM100c) are now fitted with a tilting stage which incorporates a 'Z control'. As the specimen is tilted, a vertical adjustment is made to keep the image in focus, thereby insuring that the object in view maintains a fixed position in the microscope. Hence the magnification factor remains constant and accurate measurements can be made.

Various morphological features have been observed throughout this work which have been reported in the past. Figure 4.4. shows examples of the double lined structures observed by D. Steve-Bocciarelli, (1969). The interpretation of these images is not yet clear, although it is possible that they could be images of two crystals growing epitaxially, this again is a topic in which specimen tilting could be used for further investigation.

Bone mineral has been visualised in a non-crystalline or amorphous form. This type of mineral has only been found adjacent to bone cells (type unknown) spreading for 3-4 microns from the cell border into the matrix.

The high resolution micrographs shown in figures 4.6., 4.7. and 4.10 were made possible because of the excellent thin sections produced by the diamond knife (thickness estimated to be less than 60.0nm). The lattice images are mainly of the (100) planes of the hydroxyapatite model, which have a spacing of 0.8169nm. The fact that these 'lattice lines' can be seen to extend over distances of several tens of nanometres suggests that crystals of this size are not composed of smaller units, or have been fragmented by the process of ultramicrotomy, as mentioned in 11.2. Some of the high resolution micrographs show irregularly shapped crystals, although angular features are sometimes present, and the variation in electron density over a single crystal could indicate that structural imperfections are present and this would give rise to internal lattice strain, as mentioned later.

There are two main conclusions to be drawn from the bright field work:-

a) That microscopic evidence strongly suggests that bone mineral crystals are in the form of thin plates, approximately 5.0nm in thickness, with an irregular shape and a variable maximum dimension, but occasionally extending to several tens of nanometres.

b) Measurements of crystal dimensions from bright field micrographs cannot be related to the crystal axes since the crystal orientation cannot be determined from any bright field image.

Whilst many previous workers have assumed the largest dimension of bone mineral crystals seen in the bright field to be c-axial this last conclusion gives little meaning to these measurements. Hence, to obtain accurate measurements of bone mineral crystals their orientation has to be known, consequently the dark field imaging technique was applied to the problem since it fulfilled this requirement.

The Dark Field Method

The dark field imaging technique uses diffracted rather than transmitted beams to form the image. Since crystals have to be specifically oriented to produce diffracted beams, this orientation can be determined in cases where the planes producing the diffracted beams have a unique d-spacing within that crystal. For example, crystal planes in bone mineral with Miller indices (001) have a unique d-spacing, however, since the (a) and (b) axes of the crystal lattice have equal lengths, planes with indices (h k l) have equivalent spacings to planes with indices (k h l). It is known from previous x-ray work that the (002) planes of bone mineral are perpendicular to the longest dimension of the crystal, which is the c-axial direction, and therefore dark field images produced using the (002) beams are images of crystals whose c-axes are in the plane of the section. It is fortunate that the (002) diffraction is strong and well isolated, and this has meant that using a special 10 micron diameter objective aperture, pure (002) dark field images could be produced, thereby reducing Moiré fringe effects, as discussed in Chapter 5.

The general appearance of the dark field images shows bone mineral cyrstals to have irregular shapes and sizes. The dimension measured perpendicular to the c-axial direction varies from approximately 5.0nm to dimensions approaching that of the c-axial length in some instances. Since an (002) dark field image would still be produced if the crystal was rotated about its c-axis, this observation once again suggests a plate-like form for bone mineral, with a thickness of approximately 5.0nm.

The dark field image possess two advantages over the bright field image; the illuminated crystal is isolated from its neighbours, and its c-axial orientation is known. From many dark field micrographs c-axial measurements were taken for three bone types. For rabbit, ox and human bones the mean c-axial

length was found to be 32.6nm, 36.2nm and 32.4nm respectively. The size distributions having standard deviations of 12.8nm, 19.0nm and 16.3nm. for rabbit, ox and human bones respectively are shown in Chapter 6. The dark field technique has allowed meaningful c-axial measurements to be made and also enabled the distribution of crystal sizes to be measured. The main disadvantage of the method is that crystals have to be selected from a photograph for measurement and hence there is a possibility of personal bias affecting the result. However, being aware of this possibility should reduce any such effect to a minimum.

In the past, bright field estimations of c-axial length have tended to be two or three times greater than those of the x-ray methods, probably because only the larger crystals could be seen in isolation. This fact, together with the inaccuracy of bright field estimations, invalidates any comparison between the two methods. Also the two methods tended to be used in isolation with various types of bone sample, and this makes comparison of results difficult. Consequently, the next stage of this work was to measure c-axial length by an x-ray method in the same samples as used for the dark field measurements, and hence obtain a valid comparison.

X-ray Line Broadening

The x-ray method of line broadening was chosen because of its widespread use in the past. The technique, which is relatively quick and simple and which requires the minimum of specimen preparation, is described in Chapter 6. Initially, when calculating the mean c-axial length the simplest formulation was used, i.e., assuming that the line broadening effect was due only to small crystal size. The mean c-axial lengths measured were 27.9nm, 28.3nm and 26.7nm for rabbit, ox and human bones respectively. Whilst these results are of the same order as the dark field measurements, a t-test shows a significant difference at the 5% level. If the line broadening

was caused by effects other than crystal size then the above treatment would produce an under-estimate of the mean c-axial length. These results are in fact smaller than the dark field measurements and hence it was suspected that other factors were involved. It is known that lattice imperfections cause a variation in the crystal d-spacings, and hence a spread of the diffraction profile, and the subsequent analysis accounted for this effect. In retrospect, since bone mineral crystals are formed in a dynamic environment, variation in composition and hence lattice strain are likely to occur. The high resolution micrographs discussed earlier show images where the electron density and lattice resolution lines are not consistent over the entire crystal, and this indicates structural imperfection which could cause lattice strain.

Using a formulation which allowed for lattice strain the mean c-axial lengths were calculated to be 33.2nm, 36.1nm and 32.2nm for rabbit, ox and human bones respectively, which, when compared with the dark field measurements showed no significant difference at the 5% level. The internal strain was also calculated and it was found that the maximum tensile or compressive component had a value of approximately 0.3% in all samples. This finding was important since it meant that the crystals were basically straight in the c-axial direction, and the dark field images were therefore, of the whole crystal and not just of a small section of a large curved cyrstal.

The line broadening technique gives information not only about crystal size but also about crystal perfection, and for this reason it was decided to investigate the development of bone mineral with age. The maturation of bone mineral has been recently studied, see Chapter 7, although no measurements of crystal perfection have been made. The mean c-axial lengths of the rabbit bone samples aged 7 weeks, 6 months and 12 months were 34.6nm, 33.4nm and 35.3nm with lattice strain factors (ε) 0.67%, 0.66% and 0.70% respectively. There is no significant

difference at the 5% level in these factors for the three samples, indicating a stable situation. However, the mean c-axial lengths of the 1 and 2 week old samples were 23.0nm and 34.6nm, with strain factors of 1.63% and 1.33% respectively, indicating that the youngest bone had the smallest and most imperfect crystals, and the 2 week old sample having the mature crystal size but still an 'imperfect' structure. The work of Termine (1966) indicates a crystal maturation process in which the crystalline component of bone mineral matures after 7 weeks at the expense of the amorphous component. These results would be consistent with that process, whereby the mature crystal size and structure are attained after approximately 7 weeks, but clearly these results are very tentative and further work is needed to confirm these findings. One disadvantage of the line broadening technique is that the result tends to be weighted in favour of the larger crystals. This is because the amplitude of a diffracted beam is proportional to the volume of the crystal and the number of lattice planes, but the intensity, which is the measured parameter is proportional to the square of the amplitude. Therefore, if the amplitude of a diffracted beam from a crystal with n planes is A, the intensity will be A^2, but for a crystal twice the size with 2n planes, the intensity will be $4A^2$. The close agreement between the two methods used could mean that either the dark field technique is also overestimating the mean c-axial length, or that the x-ray method is affected by other factors which cancel out the weighting effect. For instance, Berry (1947) has shown that for samples containing crystals with a size distribution approximating to a Gaussian, the theoretical diffraction profile is not significantly different to that produced by a sample with cyrstals of a single size. Unfortunately a variation in the crystal shape also affects the diffraction profile making the evaluation of these finer points impractical in the case of bone mineral.

In addition to the suggestions already made, the difficulties of past workers in producing consistent measurements of c-axial length using x-ray and microscopsical methods, could have been due to the fact that lattice strain was not always taken into account. Since consistent results have now been produced, and there is no evidence to suggest that either technique is inaccurate, both the dark field and line broadening methods can now be used in isolation to measure bone mineral size, size distribution, and crystallite perfection.

11.4. Crystal Orientation

The second aspect of this work was concerned with the development of a technique to determine the three-dimensional orientation of bone mineral quantitatively. Since the crystal c-axes are aligned on average with the collagen fibre axes, the x-ray diffraction patterns of bone mineral describe the fibrous arrangement of the sample. The technique was developed to examine small samples, with dimensions of mm, since this is the scale on which the physical testing of bone is usually carried out. Hence it would be possible to determine the microstructure of test samples, and also to examine structural variation within the whole bone. Existing goniometers such as the Schulz, are designed to be used with large samples (Cm), and hence only large bones can be used. The design and construction of the goniometer for this work is fully described in Chapter 8. The two main difficulties were:

a) Since small samples were being used only weak diffracted beams were produced. However, this point was overcome by building a stepping mechanism into the goniometer movement which allowed sufficient counts to be recorded.

b) Difficulty was encountered in producing the bone sample itself. A thin plaque (50-100 microns) produces a suitable diffracted beam since the x-ray absorption is small, but for each angle of rotation (α) used, (see Chapter 10), a separate correction is required for the diffracted beam intensity as a function of ($\emptyset$). Also, for $\alpha > 50^{o}$ the diffracted beam is severely attenuated. Therefore, only a limited coverage of the pole figure can be obtained from one plaque. A thin rod-like specimen would not require any correction for a rotation (α) but would require a correction of the diffracted beam intensity for each value of ($\emptyset$); this is because of different absorption within the specimen due to the path length of the diffracted beams. Attempts were made to

produce small rod-like specimens by turning, but unfortunately with diameters less than 200 microns, the samples fractured in the process. Even with samples of this size the x-ray beam was severely attenuated making this shape of sample impractical. The compromise solution was to take two plate-like samples cut at right angles, with their long axes parallel to the long axis of the femur. By rotating each sample $\pm 30^{o}$ about its long axis the whole pole figure was determined. The main assumption however being that each sample exhibits a c-axial orientation which is representative of the whole bone in the direction from which the sample was cut. The large amount of film and polarised light work which has preceeded this study justifies the assumption for the types of sample used.

The goniometer was found to perform satisfactorily and fulfil its design requirements, producing the pole figures shown in Chapters 9 and 10. The pole figures themselves are quantitative descriptions of the three-dimensional c-axial orientation of bone mineral, and hence represent the fibrous structure of the sample, however their interpretation is still somewhat qualitative.

A preliminary examination of traebecular bone indicated that preferred orientation only exists in the well defined rod-like traebeculae. However, it is envisaged that work on cancellous bone would be more usefully performed using a microfocused x-ray beam (0.1mm dia) which could probe the individual traebeculae.

The pole figures of primary type bone show one major axis of orientation which is aligned on average with the long axis of the femur. The contours of the pole figures show that primary bone has a planar orientation, with the c-axes spreading within the laminations. This finding is consistent with a fibrous spread within the laminations but not from one lamination to the next.

Secondary type bone also exhibits one major axis of orientation which is aligned on average with the long axis of the femur. However, the pole figure contours tend to follow the lines of latitude, indicating that the degree of preferred orientation has a rotational symmetry about the main fibre axis. Since the osteon, which is the predominant feature of secondary type bone has rotational symmetry, it is feasible that the laminar orientation is similar to that of primary type bone, with the symmetrical distribution of orientation produced by the histological structure.

The technique developed in this work has enabled the three-dimensional orientation of bone mineral crystals to be determined quantitatively. Past results have tended to be qualitative, and many works on physical properties have assumed bone to be isotropic and not allowed for structural variation. It has been shown that bone is anisotropic, with a degree of preferred orientation which can be measured from the pole figures. It is envisaged that pole figures, and the techniques developed for their determination, will play a significant part in interpreting future tests on the physical properties of bone.

11.5. Suggestions for Future Work

Throughout this work it has become clear that many topics exist for further research, which include further developments or use of the techniques described in this thesis. Using the bright field technique, the high resolution micrographs showing lattice images could be used to investigate structural imperfections within the crystals in both normal and abnormal conditions, and this could give information about factors which influence the mineralisation process itself. The technique of specimen tilting could be used to investigate the morphology of bone mineral crystals more accurately than has been attempted, by using the suggestions outlined in 11.3.

The dark field technique could also be used to investigate crystal imperfections since Moire fringes produce magnified images of crystal faults, as shown in figure 5.5. Dark field imaging could also be used to investigate the suggestion that large crystals seen in the bright field are actually aggregations of smaller units, this being another possible source of discrepancy between c-axial measurements in the past.

Since consistent measurements of crystal size have been made using an x-ray and a microscopical method, the relatively quick x-ray technique can now be used in isolation. Further work is needed to confirm the tentative findings of Chapter 7, dealing with the maturation of bone mineral crystals in size and perfection. It would be useful to measure these factors in pathalogical samples to gain information relating to the physical or chemical conditions within the bone which influence the mineralisation process. It is interesting to note that the low angle diffraction work of Engström, (1972) estimated a mean c-axial length of 33nm-35nm for fish bone, which is approximately the range of values measured in this work. It would, therefore, be useful to use this technique in conjunction with the dark

field and line broadening methods, to either confirm or refute the findings of this work.

The pole figures produced in the orientation work give quantitative descriptions of the fibrous structure of the sample. These pole figures, and the techniques developed for their determination will enable the degree of anisotropy within a test sample to be measured and allowed for in the subsequent analysis. The goniometer technique could also be used to investigate the bone microstructure itself, structural-functional relationships, and variations of structure in traumatic or pathological conditions. As already mentioned, a microfocus x-ray set would be valuable for the further study of traebecular bone, and could possibly be used to examine the structural variation between histological features such as osteons and interstitial lamellae within the same sample. Finally, the goniometer technique itself is open for further development. By automating the total movement of the sample, and by having an on-line computer to analyse, correct and plot the data, the pole figure determination could be reduced to a single process.

It is clear that a great deal of further research has yet to be done in the field of bone structure before the function and behaviour of bone can be understood. However, it is hoped that the techniques developed and results produced in this work, will have a role in the future study of bone as a structural material, and as a living tissue.

APPENDIX I

An X-ray Examination of Viable and Non-viable Bone

Introduction

It is generally accepted that bone mineral exists in two forms, a crystalline form which resembles hydroxyapatite, and an amorphous form. (see 1.7.8.). It has been suggested by Pautard (1970), that all bone mineral may be in the amorphous form in-vivo, and only becomes crystalline after death. The experiment performed by Pautard which led to this suggestion consisted of rapidly removing a sample of mouse calvarium and bathing it in culture medium whilst packing it between cellulose or polythene membranes, and examining it by x-ray diffraction. This sample, assumed to be in a viable state, produced a non-crystalline diffraction pattern similar to the upper trace of figure A1. However, after removal from the culture medium, the air dired, non-viable sample produced a diffraction pattern typical of bone mineral. The sample was then re-wetted with culture medium and still produced a recognisable diffraction pattern, typical of bone mineral.

Since the implications of this result would seriously affect the relevance of in-vitro experiments on bone, it was decided to investigate Pautards suggestion, and this was done by basically repeating the experiment using rabbit bone.

Method

A longitudinal section was removed from the mid-femural region of an eight week old femal dutch rabbit immediately after death, care being taken to keep the bone constantly bathed in T.C.199 physiological medium. The sample which was assumed to be in viable condition was examined by x-ray diffraction, using a J.E.O.L. microfocus x-ray set. The x-ray beam was collimated to 0.1mm diameter to minimise cellular damage by the x-rays. The sample was bathed in a continuous drip of physiological medium whilst being irradiated, by using the specimen holder shown in figure A2. The exposure time was three hours.

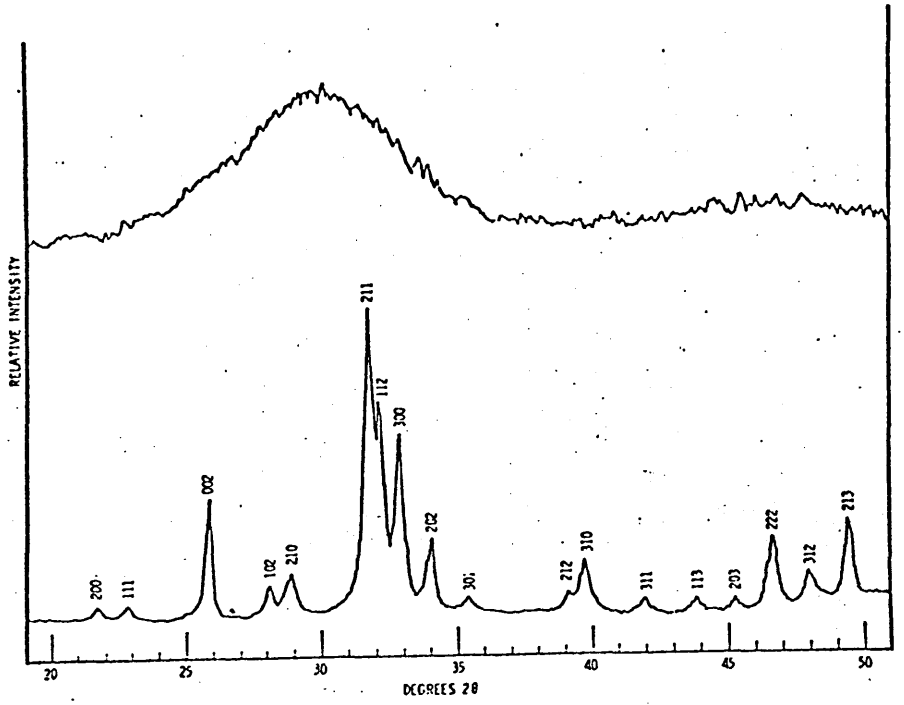

X-ray diffraction patterns of amorphous calcium phosphate (upper) and synthetic hydroxyapatite (lower); Copper K-alpha radiation. The Miller indices are shown on the crystalline pattern. (Reference: Bienenstock, A. and Posner, A. S. (1968) Archives of Biochem. and Biophys. 124, 604-607)

Figure A1.

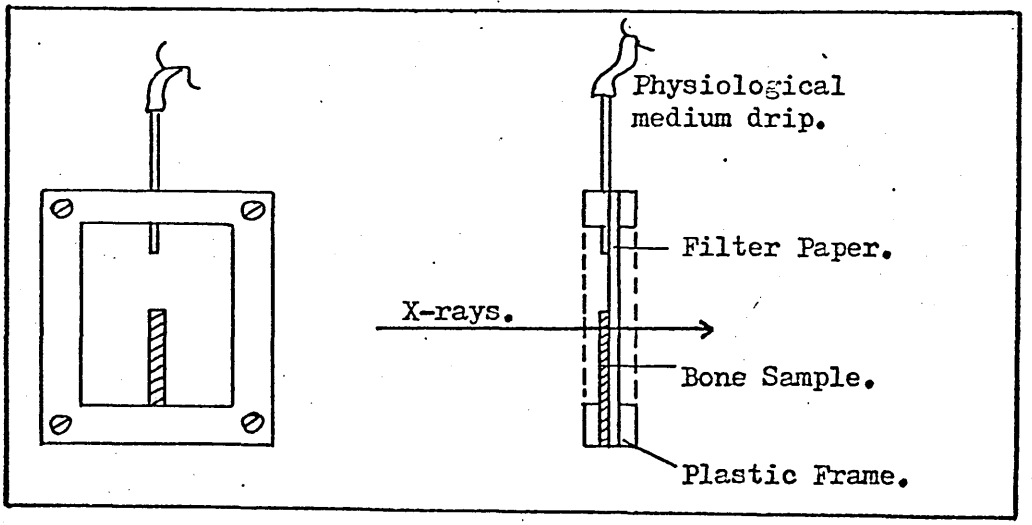

Figure A2.

The specimen holder used to keep the sample of bone bathed continually in physiological medium whilst being irradiated with X-rays.

After the first examination, the sample was washed in distilled water for three hours to remove any culture medium, air dried, and examined by x-ray diffraction, approximately 24 hours later. This sample was assumed to represent non-viable bone.

Results and Conclusion

The experiment was performed twice, and results were the same in both cases, i.e., typical bone mineral diffraction patterns were obtained in each exposure as shown in figure A3. Provided that the bone sample was in a viable state for the first exposure, this would indicate that crystalline bone mineral was certainly present in the sample.

Since no evidence has been published to support Pautards suggestion, and since this investigation also provides no support, it has been assumed that results of in-vitro experiments on the crystalline aspects of bone are representative of viable tissue.

Reference.

PAUTARD.F.G.E.

Biophysical properties of connective tissues.
In: The Comparative Molecular Biology of Extracellular Matrices.
Ed, H.C.Slavkin. New York:Academic. 440, (1970).

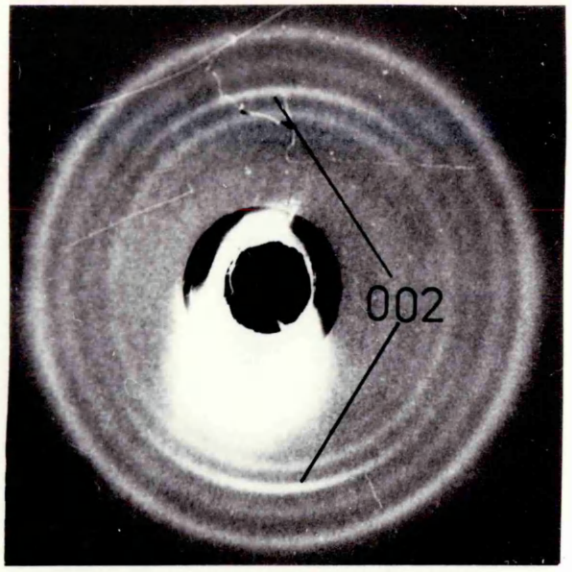

(a) Diffraction pattern of rabbit femur, examined immediately after death whilst bathed in physiological medium.

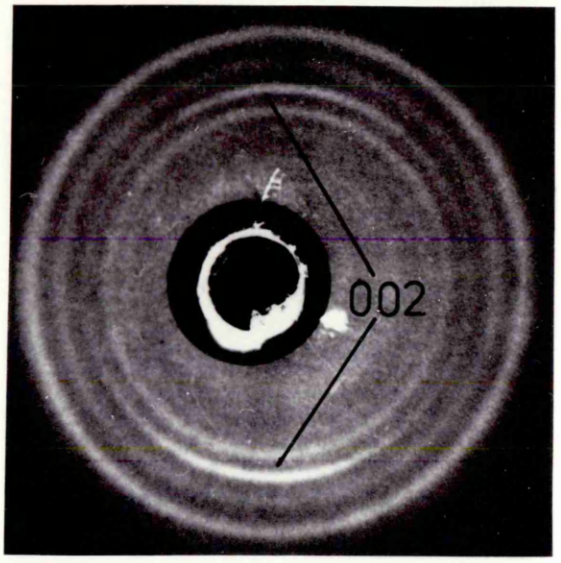

(b) Diffraction pattern of same sample as above after washing in distilled water and drying overnight.

Figure A3.

APPENDIX II

This program performs a statistical analysis on a set of n data values. Output is in the form of a histogram and printed values of:-

Minimum.

Maximum.

Range.

Mean.

Median.

Standard Deviation.

Variance.

Kurtosis..

Skewness.

Card input takes the form:-

nnnnnn xxxxxx TITLE* DATA DATA.....

Where (nnnnnn) is the number of data values.

(xxxxxx) is the histogram interval.

The program will accept as many sets of data as required.

```
'COMMENT'      ****  INPUT FROM DOC SOURCE  ****  ;

   'COMPACT DATA'
   'PMD'(ED,MSJADUMP)
   'PROGRAM'(MSJA)
   'INPUT' 3=CR0
   'INPUT' 0=TR0
   'OUTPUT' 0=LP0,45
   'OUTPUT' 2=LP2,45
   'OUTPUT' 3=CP0
   'OUTPUT' 1=TP0
   'SPACE' 100
   'TRACE' 2
   'COMMENT' END OF PROGRAM DESCRIPTION, SOURCE PROGRAM FOLLOWS:

   'BEGIN''INTEGER'A1,A2,A3,I,J,K,K1,M,N,JOB,RUN,CNT;
BLOCK     1
          'REAL'A,B,L,MIN,MAX,SCALE,STEP1,STEP2,H,X1,X2,X3;
          SELECT INPUT (3);
   JOB:=READ;
          'FOR'RUN:=1'STEP'1'UNTIL'JOB'DO'
   'BEGIN'
   SELECT INPUT (3);
   N:=READ;H:=READ;
   M:=0;
   WRITETEXT('('''('2C40S')'SPECIMEN'('6S')''')');
   COPYTEXT('('*')');
   NEWLINE(5);
          'BEGIN''ARRAY'X[1:N];
BLOCK     2
   SELECT OUTPUT (0);
                'FOR'I:=1'STEP'1'UNTIL'N'DO'
                     X[I]:=READ;
                'FOR'I:=1'STEP'1'UNTIL'N'DO'
                'BEGIN'K:=I;MIN:=X[I];
                       'FOR'J:=I+1'STEP'1'UNTIL'N'DO'
                       'IF'X[J]<MIN'THEN'
                       'BEGIN'K:=J;MIN:=X[J];'END';
                       'IF'K#I'THEN''BEGIN'X[K]:=X[I];X[I]:=MIN'END
                'END';B:=X[N];
          A1:=1;
          A2:=0;
   NEXT:
          'FOR'A3:=A1'STEP'10'UNTIL'A1+90'DO'
          'BEGIN'
                'IF'(A3+A2)>N'THEN''GOTO'REPEAT;
                PRINT(X[A2+A3],2,2);
                SPACE (4);
          'END';
   REPEAT:
          'IF'A2=9'THEN''GOTO'AGAIN;
          A2:=A2+1;
          NEWLINE(1);
          'GOTO'NEXT;
   AGAIN:
          'IF'(A2+A3)'GE'N'THEN''GOTO'OUT;
          A1:=A1+100;
          A2:=0;
          NEWLINE(3);
          'GOTO'NEXT;
```

```
   OUT;
   NEWLINE (1);
   A:=0;
   'IF'B=ENTIER(B)'THEN'L:=B 'ELSE'
   'IF'B>ENTIER(B)+0.5 'THEN' L:=ENTIER (B)+1 'ELSE'
   L:=ENTIER (B)+0.5;
                'BEGIN''ARRAY'C[1:(L-A)/H+10,0];
BLOCK    3
                          'REAL''PROCEDURE'SUM(I,A,B,X);
BLOCK    4
                          'VALUE'A,B;'INTEGER'I,A,B;
                          'REAL'X;'ALGOL';
      'COMMENT' PLOT HISTOGRAM;
   MAX:=-1; I:=K:=0;
      'FOR'STEP1:=A'STEP'H'UNTIL'L'DO'
      'BEGIN'
         CNT:=0; STEP2:=STEP1+H; I:=I+1;
         'IF' K+1>N 'THEN' 'GOTO' SKIP;
       'FOR'K:=K+1'STEP'1'UNTIL'N'DO'
       'IF'X[K]'LE'STEP2'THEN'CNT:=CNT+1;
         M:=M+CNT;
         K:=M;
   SKIP: 'IF' CNT>MAX 'THEN' MAX:=CNT; C[I]:=CNT;
      'END';
   SCALE:=N'/'300;
   SCALE:=(SCALE-(SCALE-1)/2);
   K1:=100*SCALE;
   NEWLINE(10);SPACE(35);
         K:=0;
   WRITETEXT('('('5C')'%RANGE%%NUMBER'('C8S')'OF'('C8S')'
   OBJECTS'('C8S')'IN'('C8S')'RANGE'('4C')'')');
   SPACE (11);WRITETEXT('('000')');
   SPACE (15);
   PRINT (K1/5,3,0);
   'FOR'M:=2'STEP'1'UNTIL'5'DO'
      'BEGIN'
   SPACE (14);
   PRINT (M*K1/5,3,0);
      'END';
   'FOR'CNT:=1'STEP'1'UNTIL'4'DO'
   'BEGIN'
   NEWLINE(1);
   SPACE (12);
   PRINTCH(26);
   'FOR'J:=1'STEP'1'UNTIL'5'DO'
   'BEGIN'
   SPACE (K1/(SCALE*5)-1);
   PRINTCH (26);
      'END';
   'END';
   NEWLINE (1);
      'FOR'STEP1:=A'STEP'H'UNTIL'L'DO'
      'BEGIN'
         K:=K+1; PRINT(STEP1,2,2);
   NEWLINE(2);
   SPACE(7);
   PRINT(C[K],3,0);
         'FOR'MIN:=SCALE'STEP'SCALE'UNTIL'C[K]'DO' PRINTCH(26);
```

```
    NEWLINE(1);
    NEWLINE(1);
        'END';
        'COMMENT'  COMPUTE STATISTICS;
        WRITETEXT('('''('30')'MINIMUM%=%')'); PRINT(X[1],0,8); SPACE(4);
        WRITETEXT('('MAXIMUM%=%')'); PRINT(X[N],0,8); SPACE(4);
        WRITETEXT('('RANGE%=%')'); PRINT(X[N]-X[1],0,8); NEWLINE(2);
        MAX:=SUM(I,1,N,X[I])/N; WRITETEXT('('MEAN%=%')'); PRINT(MAX,0,8);
        WRITETEXT('('''('8S')'MEDIAN%=%')'); PRINT(X[ENTIER(N/2+0.5)],0,8);
        MIN:=SQRT(SUM(I,1,N,(X[I]-MAX)↑2)/N);
        WRITETEXT('('''('4S')'STANDARD%DEVIATION%=%')'); PRINT(MIN,0,8);
        WRITETEXT('('''('2C')'VARIANCE%=%')'); PRINT(MIN↑2,0,8); SPACE(4);
        STEP1:=SUM(I,1,N,((X[I]-MAX)/MIN)↑4)/N-3;
        WRITETEXT('('KURTOSIS%=%')'); PRINT(STEP1,0,8); SPACE(4);
        STEP2:=SUM(I,1,N,((X[I]-MAX)/MIN)↑3)/N;
        WRITETEXT('('SKEWNESS%=%')'); PRINT(STEP2,0,8);
        PAPERTHROW
    'END'
    'END'
    'END';
    'END';
```

REFERENCES

ASCENZI. A. et al
The Fine Structure of Bone Mineral in Different Experimental Conditions. IV European Regional Conf. on Electron Microscopy. Rome. 431-433, (1968)

BACHRA. B.N.
Calcification of Connective Tissue. Int. Rev. of Connective Tiss. Res. 5: 165, (1970)

BASSETT. C.A.L.
The Biological Significance of Piezoelectricity. Calc. Tiss. Res. 1: 252-272, (1968)

BASSETT. C.A.L. and BECKER. R.O.
Generation of Electric Potentials by Bone in Response to Mechanical Stress. Science. 137: 1063-1064, (1962)

BERRY. C.R.
The Shape of X-ray Diffraction Lines from Colloidal Magnesium Oxide. Phys. Rev. 72: 942, (1947)

BONUCCI. E.
The Locus of Initial Calcification in Cartilage and Bone. Clin. Orthop. 78: 108-139, (1971)

BRADDOCK. G.
An Investigation of Bone Mineral Substance by Transmission Electron Microscopy, Incorporating Electron Diffraction and Dark Field Imaging. MSc Thesis University of Surrey. (1973)

BRADFIELD. J.R.G.
Phosphatase Cytochemistry in Relation to Protien Secretion. Exp. Cell. Res. Supp. 1: 338-350, (1949)

BROWN. W.E.
Octacalciumphosphate and Hydroxyapatite. Nature. 196: 1048, (1962)

BROWN. W.E. et al
Crystallographic and Chemical Relations Between Octacalciumphosphate and Hydroxyapatite. Nature. 196: 1050, (1962)

CARLSTROM. D.
X-ray Crystallographic Studies on Apatites and Calcifled Structures. Acta Radiologica. Supp. 121 Stockholm. (1955)

CARLSTROM. D. and FINEAN. J.B.
X-ray Diffraction Studies on the Ultrastructure of Bone. Biochim. Biophys. Acta. 13: 183, (1954)

CARLSTROM. D. and GLAS. J.E.
X-ray Diffraction Studies on the Ultrastructure of Bone. Biochim. Biophys. Acta 35: 46, (1959)

CLARK. J.H.
A Study of Tendons, Bones and Other Forms of Connective Tissues by means of X-ray Diffraction Patterns. Am. J. Physiol. 98: 328, (1931)

CURREY. J.D.
The Adaptation of Bones to Stress. J. Theor. Biol. 20: 91, (1968)

DE-JONG. W.F.
La Substance Minerale dans les Os. Rec. trav. chim. 45: 445, (1926)

EANES. E.D. and POSNER. A.S.
Amorphous Calcium Phosphate in Skeletal Tissues. Clin. Orthop. 53: 223-235, (1965)

EANES. E.D. et al
An Amorphous Component in Bone Mineral. Fourth European Symp. on Calcified Tissues. ed. P.J. Gaillard, A. Van den Hoof, R. Steedijk. Amsterdam. Excerpta Med. 24-26, (1966)

EANES. E.D. and POSNER. A.S.
The Formation and Structure of Bone Mineral. In: Biological Calcification. ed. H. Schraer, N.Y. Appleton-Century-Croft. (1969)

ENGSTROM. A.
Aspects of The Molecular Structure of Bone. In: The Biochemistry and Physiology of Bone. Vol. 1 Structure, 2nd ed. Ed. G.H. Bourne. Acad. Press. (1972)

ENGSTROM. A. and FINEAN. J.B.
The Low Angle X-ray Diffraction of Bone. Nature. 171: 564, (1953)

ENGSTROM. A. and ZETTERSTROM. R.
Studies on the Ultrastructure of Bone. Exp. Cell Res. 2: 268, (1951)

FERNANDZ-MORAN. J. and ENGSTROM. A.
Electron Microscopy and X-ray Diffraction of Bone. Biochim. Biophys. Acta. 23: 260-264, (1957)

FITTON-JACKSON. S. and RANDALL. J.T.
Fibrogenesis and the Formation of Matrix in Developing Bone. In: Bone Structure and Metabolism. Ed. G.E.W. Wolstenholme and C.M. O'Conner. Boston: Little, Brown. 47-64, (1956)

FUKADA. E. and YASHUDA. I.I.
On the Piezolectric Effect of Bone. J. Phys. Soc. Japan. 12: 1158-1162, (1957)

FUNG. Y.C.

Functional adaption of bone.
In: Biomechanics. Ed. Fung. Y.C. et al. Prentice Hall Inc. 261 (1972)

GLIMCHER. M.J.

Molecular Biology of Mineralised Tissues with Particular Reference to Bone. Rev. mod. Phys. 31: 359, (1959)

GLIMCHER. M.J.

Recent Studies of the Early Mineral Deposits in Bone and Enamel. Calc. Tiss. Res. 2: Supp. 1, (1968)

GRANT. R.A. et al

A New Model for the Tropocollagen Molecule and its Mode of Aggregation. Nature. London. 207: 822-826, (1965)

GROSS. J.

Collagen. Sci. American. 204: 121-129, (1961)

HARPER. R.A. and POSNER. A.S.

Measurement of Non-Crystalline Calcium Phosphate in Bone Mineral. Proc. Soc. Exp. Biol. Med. 122: 137, (1966)

HERMAN. H. and DALLEMAGNE. M.J.

The Main Mineral Constituent of Bone and Teeth. Arch. Oral Biol. 5: 137, (1961)

HODGE. H.C. et al

The Subunit Structure of the Tropocollagen Macromolecule, and its Relation to Various Ordered Aggregation States. In: Structure and Function of Connective and Skeletal Tissue. Butterworths. London 31-41, (1965)

HOHLING. H.J. et al
Electron Microscopy of Bone. 3rd European Symp. on Calcified Tissues. Springer-Verlag. Berlin. 145-151, (1966)

IRVING. J.
Bone Matrix, Lipids and Calcification. Calc. Tiss. Proc. 2nd Symp. Ed. L.J. Richelle, and M.J. Dallemagne. Collection des colloques de l'universite de Liege. 313-324, (1965)

JACKSON. S.A.
The Orientation of the Mineral Phase of Bone With Respect to the Organic Phase, and the Bone as a Whole. MSc. Thesis. University of Surrey. (1973)

JOHANSEN. D.M.D. and PARKS. H.F.
Electron Microscopic Observations on the 3-Dimensional Morphology of Apatite Crystallites of Human Dentine and Bone. J. Biophys. Biochem. Cytol. V7, No. 4: 743-745, (1960)

JOHNSON. C.
Morphologic Analysis in Pathology. In: Bone Biodynamics. Ed. H.M. Frost. Little, Brown. Boston. 543-654, (1964)

KAUFFMAN. A.
An Electron Microscopic Study of Bone Mineral. MSc. Thesis. University of Surrey. (1973)

KLEMENT. R.
Die Zusammensetzung der Knochenstutzsubstanz. Hoppe-Seyler's Z. Physiol Chem. 183: 132, (1929)

KLEMENT. R. and TROMELL. G.
Hydrozylapatit der Hauptbestandtell der Anorganishen Knochen und Zahnsubtanz. Hoppe-Seyler's Z. Physiol. Chem. 213: 263, (1932)

LANG. S.B.

Ultrasonic Method for Measuring Elastic Coefficient of Bone, and Results on Fresh and Dried Bovine Bones. I.E.E.E. Trans. Biomed. 17: 101-105, (1970)

LENART. G.

Use of X-ray Diffraction Method in Investigations on Mineral Substances of Bone and Callus. Acta. biochim. biophys. Acad. Sci. Hung. 3: 305-316, (1968)

LENART. G.

Bone Mineralisation Investigated by Electron Diffraction. Acta biol. Acad. Sci. Hung. 22(4): 431-434, (1971)

MOLNAR. Z.

Development of the Parietal Bone of Young Mice/ Crystals of Bone Mineral in Frozen-Dried Preparation. J. Ultrastruct. Res. 3: 39, (1959)

MOLNAR. Z.

Additional Observation of Bone Crystal Dimension. Clin. Orthop. 17: 38-42, (1960)

MYERS. H.M. and ENGSTROM. A.

A Note on the Organisation of Hydroxyapatite in Calcified Tissue. Exp. Cell Res. 40: 182, (1965)

NEUMAN. W.F.

Surface Absorption. Atomic Energy Project Report No. U.R.238. University of Rochester. (1953)

NEUMAN. W.F. and NEWUMAN. M.W.

In: The Chemical Dynamics of Bone Mineral. Chicago University. Chicago Press (1958)

NEWESELY. H.

Die Realstrucktur von Oktacalciumphosphat. Mh. Chem. 95: 94-101, (1964)

OWEN. M.
Cell Population Kinetics of an Osteogenic Tissue. J. Cell Biol. 19: 19-32, (1963)

PAUTARD. F.G.E. and ARNOTT. H.J.
Osteoblast Function and Fine Structure. Israel. J. Med. Sci. 3: 657-670, (1967)

PAUWELS. F.
Bedeutung und Kausale Erklarung der Spongiosaarchitekture in neuer Auffassung. Arztl. Wschr. 3: 379, (1948)

PETRUSKA. J.A. and HODGE. A.J.
A Subunit Model for the Tropocollagen Macromolecule. Proc. Natn. Acad. Sci. U.S.A. 51: 871-876, (1964)

POSNER. A.S. and PERLOFF. F.A.
Refinement of the Hydroxyapatite Structure. Acta. Cryst. 11: 308, (1958)

POSNER. A.S. et al
The Effect of Fluoride on the X-ray Diffraction Pattern of the Apatite of Human Bone. Biochem. Biophys. Acta 59: 255, (1962)

POSNER. A.S. et al
X-ray Diffraction Analysis of the Effect of Fluoride on Human Bone Apatite. Arch. Oral. Biol. 8: 549, (1963)

POSNER. A.S. et al
Small Angle X-ray Diffraction Analysis of the Effect of Fluoride on Human Bone Apatite. Arch. Oral Biol. 10: 161, (1965)

POSNER. A.S. et al
Crystal Chemistry of Bone Mineral. Physiol. Rev. 49: 760, (1969)

RAMACHANDRAN. G.N. and KARTHA. G.
The Structure of Collagen. Nature 174: 269, (1954)

RAMACHANDRAN. G.N. and KARTHA. G.
The Structure of Collagen. Nature 176: 593, (1955)

RICH. A. and CRICK. F.H.C.
The Molecular Structure of Collagen. J. mol. Biol. 3: 483-506, (1961)

ROBINSON. R.A.
The Possible Significance of Hexosephosphoric Esters in Calcification. Biochem. J. 17: 286-293, (1923)

ROBINSON. R.A.
An Electron Microscopic Study of the Crystalline Inorganic Component of Bone and its Relationship to the Organic Matrix. J. Bone and Joint Surg. 34a: 389, (1952)

ROBINSON. R.A. and WATSON. M.L.
Collagen-Crystal Relationships in Bone as seen in the Electron Microscope. Anat. Rec. 114: 383, (1952)

ROBINSON. R.A. and WATSON. M.L.
Crystal-Collagen Relationships in Bone as observed in the Electron Microscope. Ann. N.Y. Acad. Sci. 60: 596, (1955)

ROUX. W.
Gesammelte Abhandlungenuber Entwicklungsmechanik der Organismen. Iu. II. Engelmann, Leipzig. (1895)

SCHERRER. P.
Bestimmung der Grosse und der inneren Strucktur von Kolloidteilchen mittels Rontgenstrahln. Nachr. Gottingen Gesell. 2: 98, (1918)

SOBEL. A. et al
Calcification of Teeth. J. Dent. Res. 28: 61, (1949)

SOGNNAES. R.
Fluoride Protection of Bones and Teeth. Science. N.Y. 150: 989-993, (1965)

STEVE-BOCCIARELLI. D.
The Morphology of Crystallites in Bone. Calc. Tiss. Res. 5: 261, (1969)

STUHLER. R.
Die Lagerung der Onorganischen Kristallite im Knochen. Naturwissenschaften. 24: 523, (1936)

STUHLER. R.
Uber den Feinbau des Knochens Eine Rontgen-Feinstruktur-Untersuchung. Fortschr Gebiete Rontgenstrahln. 57: 231, (1938)

TERMINE. J.D.
Amorphous Calcium Phosphate: The Second Mineral of Bone. PhD Thesis Cornell University. (1966)

TERMINE. J.D. and POSNER. A.S.
Amorphous/Crystalline Inter-relationships in Bone Mineral. Calc. Tiss. Res. 1: 8-23, (1967)

TERMINE. J.D. and POSNER. A.S.
Comparative Chemistry of Amorphous and Apatitic Calcium Phosphate Preparations. Calc. Tiss. Res. 10: 171-197, (1972)

VAUGHAN. J.M.
In: The Physiology of Bone. Clarendon Press. Oxford. 43-50, (1970)

WARREN. B.E.

X-ray Diffraction Methods. J. Appl. Phys. 12: 375, (1941)

WARREN. B.E. and BSICOE. J.

The Structure of Silica Glass by X-ray Diffraction Studies. J. Am. Ceram. Soc. 21: 49-54, (1938)